Peptide-Assisted Cancer Cell Migration Along Engineered Surfaces

Thesis by

Rodolfo TONDO

Under the supervision of

Prof. Davide BONIFAZI

Presented to the School of Chemistry of Cardiff University in partial fulfilment of the Requirements for the degree of Doctor of Philosophy (PhD) in Chemistry

Cardiff University, 2019

Ordo ab Chao

Acknowledgements:

I have countless people to thank, starting from Prof. Bonifazi for the patience through all these years. Prof. Alain Krief for his Menschkeit, Prof. Carine Michiels, Sophie Ayama, Antoine Fattaccioli and all the people from URBC Namur.

I would like to thank Valentina and Riccardo, Valentina and Laure-Elie, but also Lou for their precious advice and guidance during my PhD.

I would like to thank my colleagues, PTSD/PhD veterans still in the trenches for fighting scientific and non-scientific battles alongside. It was a pleasure. Cataldo, Jacopo, Tommaso, Santa Gavina, Draga Lepa Tanja, Oliwia, Andrea F., Andrea C., Anaelle, Aurelie, Andrea S., Riccardo, Antonio, Davide, Francesco, Maria, Antoine, Andrey, Alex, Lucia.

I would like to thank Pittini staff Edi, Tony, Daniela for their help and understanding when it comes to PhD matters. A big merci goes to Andrea Cucchiaro, for his enlighting help in the lab.

And a special thanks goes to you. Grazie.

Table of contents

Abstract

Cell migration is a key process in human biology and the understanding of its complex mechanisms has a crucial importance in biomaterials,[1] engineering, medicine,[2] cell biology and immunology. This important feature is predominant in biochemical processes such as tissue regeneration, cancer metastasis and embryogenesis. Cells can detect chemical and physical gradients both on surface and in solution and respond to them with oriented movement therefore controlling such processes could potentially result in major advances in cancer metastasis treatment and many other cell migration-related diseases. It has been described that specific peptide sequences such as Ile-Gly-Asp (IGD, see Fig. 0-1) and Gly-Arg-Gly-Asp (GRGD) interact with the extracellular matrix (ECM), in particular with Fibronectin protein domains inducing adhesion and migratory behaviour on model cells (MDA-MB-231 metastatic breast cancer cells).[3] Such peptides can be tethered onto Au surfaces by means of self-assembled monolayers (SAMs). It is widely known that alkanethiols on Au surfaces form well-ordered and stable SAMs, which represent nowadays the most used model substrate for studying cell behaviour.[4] Recent studies performed in our group proved that IGD-bearing peptides induce adhesion and then migratory behaviour on metastatic breast cancer cells.[5,6] The goal of this research project is to use such tuneable scaffolds to mimic the extracellular environment, being able to induce and control cell migration towards an anisotropic surface, for a reversible migration movement.

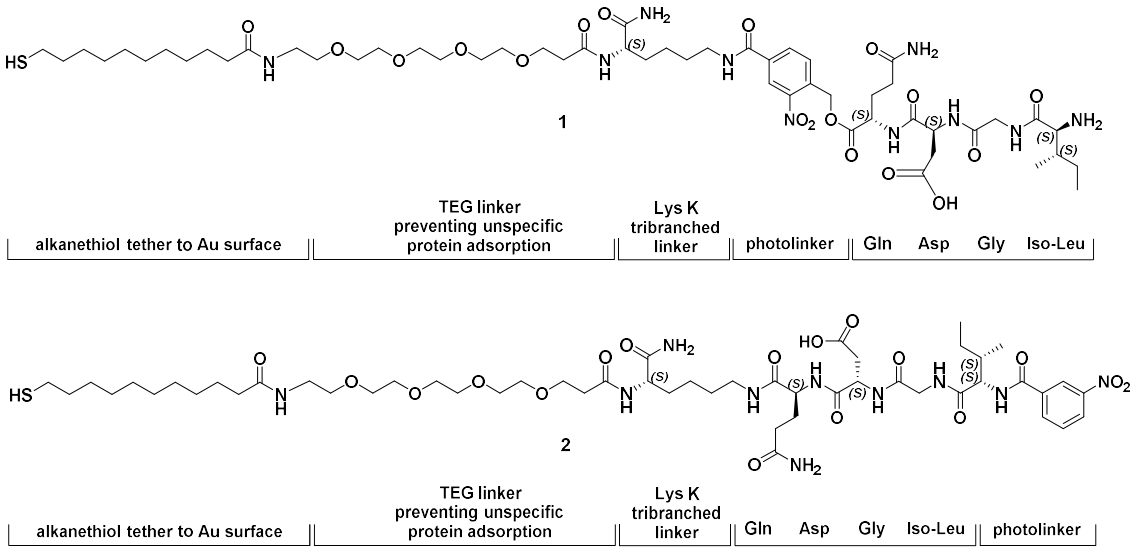

Figure 0-1 – Molecular structures of thiolated peptides bearing the motogenic motif IGDQ (IsoLeu-Gly-Asp-Gln; respecting the biological readability of the sequence) and respective nitrobenzyl photolabile linkers.

Two different IGD-bearing peptides will be used to pattern Au surface with two concentration gradients in the opposite direction. A photolabile protecting group will be

employed in both peptides. The first peptide will induce the first migration and light irradiation at a specific wavelength will remove the protecting group with its motogenic sequence, therefore exposing the opposite gradient towards the surface, for the second migration to occur.

Abstract bibliography

1. K. G. Sreejalekshmi, P. D. Nair, *J. Biomed. Mater. Res. - Part A* **2011**, *96 A*, 477–491.
2. A. Aman, T. Piotrowski, *Dev. Biol.* **2010**, *341*, 20–33.
3. I. R. Ellis, S. J. Jones, D. Staunton, I. Vakonakis, D. G. Norman, J. R. Potts, C. M. Milner, N. A. G. Meenan, S. Raibaud, G. Ohea, et al., *Exp. Cell Res.* **2010**, *316*, 2465–2476.
4. M. Mrksich, G. M. Whitesides, *Annu. Rev. Biophys. Biomol. Struct.* **1996**, *25*, 55–78.
5. F. De Leo, R. Marega, V. Corvaglia, R. Tondo, M. Lo Cicero, S. Silvestrini, D. Bonifazi, *Langmuir* **2017**, *33*, 7512–7528.
6. V. Corvaglia, R. Marega, F. De Leo, C. Michiels, D. Bonifazi, *Small* **2015**, *12*, 321–329.

Abbreviations

1D, 2D, 3D Mono, Bi, Tridimensional
AA Amino acid
Abs Absorbance
AFM Atomic Force Microscopy
Asp Aspartic Acid
Au Gold surfaces
BOC *tert*-Butoxycarbonyl
Cbz Benzyloxycarbonil
DCC *N*,*N*'-Dicyclohexylcarbodiimide
DIEA *N,N*- Diisopropylethylamine
DMF Dimethylformamide
ECM Extra-Cellular Matrix
EDT 1,2-Ethanedithiol
EGF Epidermal Growth Factor
ESI Electrospray Ionization

FAs Focal Adhesions
Fmoc Fluorenylmethyloxycarbonyl
Fn Fibronectin
GBD Gelatin-Binding Domain
Gln Glutamine
Gly Glycine
HATU *O*-(7-Azabenzotriazol-1-yl)-*N*,*N*,*N*',*N*'-tetramethyluronium hexafluorophosphate
HBTU *O*-(Benzotriazol-1-yl)-N,N,N',N'-tetramethyluronium hexafluorophosphate
IGD Isoleucine-Glycine-Aspartic Acid
IGDQ Isoleucine-Glycine-Aspartic Acid-Glutamine
IGDQK-SH L(+)-isoleucine-glycine-L(-)-asparticacid-L(-)-glutamine-L(-)-lysine-1-thiol decanoic acid
IGDS Isoleucine-Glycine-Aspartic Acid-Serine
Ile Isoleucine

IR Infrared Spectroscopy
Lys Lysine
MALDI Matrix-Assisted Laser Desorption-Ionization
µ-CP Microcontact Printing
MHz MegaHertz
MSF Migration Stimulating Factor
NMP *N*-Methyl-2-Pyrrolidone
MUA Trityl-Mercaptoundecanoic acid
NVOC Nitro-Veratryloxycarbonyl
PBS Phosphate Buffered Saline
PDMS Polymethylsiloxane
PE Polyethylene
PEG Poly-Ethylene Glycol
PNA Peptidic Nucleic Acid
PP Polypropylene
PS Polystirene

PVC PolyVynil Chloride
r.t Room Temperature
Rg Gyration Radius
RGD Arginine-Glycine-Aspartic Acid
RMSD Root-Mean-Square Deviation
ROCK Rho Kinase
RP-HPLC Reverse-Phase HPLC
RV Reaction Vessel
SAMs Self-Assembled Monolayers
SASA Solvent Accessible Surface Area
SPPS Solid Phase Peptide Synthesis
STM Scanning Tunneling Microscope
TEG Tetra-(Ethylene-glycol)
TFA Trifluoroacetic Acid
TIPS Triisopropylsilane
TM-AFM Tapping Mode Atomic Force Microscopy
TOF Time of Flight
UHV Ultra High Vacuum
UV-Vis Ultraviolet-Visible
VEGF Vascular Endothelial Growth Factor
WASP Wiskott-Aldrich Syndrome Protein
WAVE Wiskott-Aldrich Veprolin
WCA Water Contact Angle
XPS X-Ray Photoelectron Spectroscopy

1. Introduction

This first chapter deals with cell migration as part of the wider and ongoing research on cancer metastasis. Cell movement is described and discussed in the metastasis context with a brief insight on the factors contributing to 2D cell motility such as motogenic peptide sequences from the Extra-Cellular Matrix (ECM), focal complexes and integrin receptors. Sections 1.2 and 1.3 lay down a general introduction to cancer cell migration. Sections 1.3 to 1.5 address the key actors that allow cell movement, transmitting the chemical signal from the ECM to the cytoplasm. A short overview on the literature investigating for novel devices to study cancer cell migration is discussed from section 1.6, concluding with the aim of the project and the approach employed in this PhD Thesis to tackle such issue. Moving on to the next chapters, the characterisation of the peptide gradient that triggers and sustains cell migration on self-assembled monolayers (SAMs) is presented and discussed extensively. Chapter 3 discusses the synthesis of the motogenic peptides with different features and designs, while Chapter 4 deals with the microscopy results when imaging MDA-MB-231 breast cancer cells on our tailored substrates.

1.1. General account on metastasis

Metastasis is the primary cause of death in patients diagnosed with cancer.[1] Cells migrate into blood vessels and then invade other organs were they -if not caught by the immune system- adhere to the new tissue and proliferate in such environment. Metastasis process is very low and inefficient[1] because of the poor compatibility between invasive cells and the so-called distal site where the nesting is performed. As a first distinction, migration and invasion are in fact two different processes. Both mechanisms are present in biological systems.[2–4] Migration can be seen as cell movement in the same biological system, e.g. the same organ or tissue. Invasion is enacted when a cell squeezes through a tissue, generically a stromal barrier, to get past and adhere into a new environment. As the tumour mass grows, cell migration in the nearby tissues is performed. To move from the main tumour, epithelial-to-mesenchymal transition is performed by the outer cells. Thanks to this transition, cells can now form invadopodia and squeeze into the surrounding tissue. Invadopodia are cell protrusions with the purpose of degrading the surrounding stromal ECM tissue via proteolytic activity. Specifically, degradation is performed by proteins like MT1-MMP that is a transmembrane-multidomain Zinc-protease endopeptidase. Such proteins remodel the ECM for cell-cell signalling, proliferation, migration, morphogenesis and

differentiation.[5] Cancer cell movement is characterised by mesenchymal and amoeboid motility. Migration mode seems to be influenced by ECM's tumour surrounding. According to each scenario, cells are able to use invasive protrusions (invadopodia) or motility protrusions (lamellipodia) to move. While invadopodia seem to have primarily proteolytic activity, lamellipodia seem to serve more as anchorage points connecting the substrate to the focal adhesion complex. This complex deals with cell polarisation and subsequently movement. Rac GTPase protein system seems to be one of the factors responsible for migration mode switching. Amoeboid migration can be described as a rapid gliding of the cell over the surface. A mesenchymal movement is performed in stages of cell rolling and dragging towards a direction, anchoring itself with lamellipodia and filopodia and retracting its rear end (Fig. 1-1). Mesenchymal migration involves strong focal attachment to the ECM, cytoskeletal contractility with actin polymerisation and degradation and elongated spindle-like cell bodies. The two movement patterns are at the opposite, but the practical event is never one or the other, but a blend. Mesenchymal 3D migration is likely to have also ECM degradation by extracellular proteolytical activity. Fibroblasts and other cells transform from epithelial to mesenchymal migration mode employing focal adhesions (FAs) and integrins. Integrins are transmembrane receptors that enable substrate-to-cytoplasm (and viceversa) signalling, cell movement, proliferation. There are also migration modes induced by other factors, without the involvement of integrins to cluster the FAs. Cytokines, growth factors and other small proteins are responsible for cell migration without integrin activation.[6] As one example among many of integrin-independent cell migration the reader is addressed to the work of Lämmermann et al.[7]

1.2. Cellular migration

After the first glance on cell migration and invasion, where the partners that coordinate the movement are hundreds and biology regulate exquisitely this equilibrium with smooth transitions between one mechanism and another, an introduction on cell migration modes is presented and discussed. Cell migration pattern is not random but follows physical or chemical messengers that are sensed in the ECM. Physical stimuli such as traction and electrical stimuli migration modes are called Durotaxis and Electrotaxis, respectively.[8,9] Chemical messengers triggering cell migration can be tethered on a surface or can be in solution e.g. the bloodstream. The former migration mode is called Haptotaxis, while Chemotaxis is the latter.[10,11] Migration can be triggered by the ECM but also can be activated intracellularly.[12] In this thesis, attention will be focussed on ECM-triggered cell migration thanks to integrin receptor activation.

As shown in Fig. 1-1, cell migration is performed in 4 steps such as sensing and cell protrusion towards the migration direction, adhesion, migration and retraction of the rear end.[13,14] Actin polymerisation is triggered by Cdc42 and the Arp2/3 complex.[15–18] The most interesting G-proteins belonging to the Rho group are Rac1 and Cdc42. RhoA, -B and -C (isoforms) organise the focal adhesions, while Cdc42 the filopodia and Rac1 the lamellipodia. Lamellipodia are biomolecular cell "feet" at the leading edge of a polarised cell, protruded towards a migration direction. Podosomes consisting of invadopodia but also lamellipodia and filopodia are therefore differently involved in cell migration. Cell "feet" are named after their shape, therefore filopodia (tiny wire-like) are elongated, lamellipodia are flat and spread on surfaces and pseudopodia have a round shape, as the 3D version of lamellipodia. Pseudopodia sense the ECM and drive the migration during chemotaxis.[19] Invadopodia are generally smaller than lamellipodia, not necessarily pointing to the direction of migration. Interestingly Rho-C is directly connected with invadopodia formation in breast cancer invasion, triggering downstream Rac1. Such proteins trigger actin formation via the Actin Related Protein (Arp2/3) that serves as mold and sustains the polymerisation process. Actin is set on tension through ROCK proteins (Rho-associated coiled-coil containing kinase) that generate contractile forces to pull the cell forward. Conversely, actin disassembly is regulated by Cofilin proteins that cleave the polymer chains recycling the monomers, enabling the rear cell retraction, towards the movement direction.

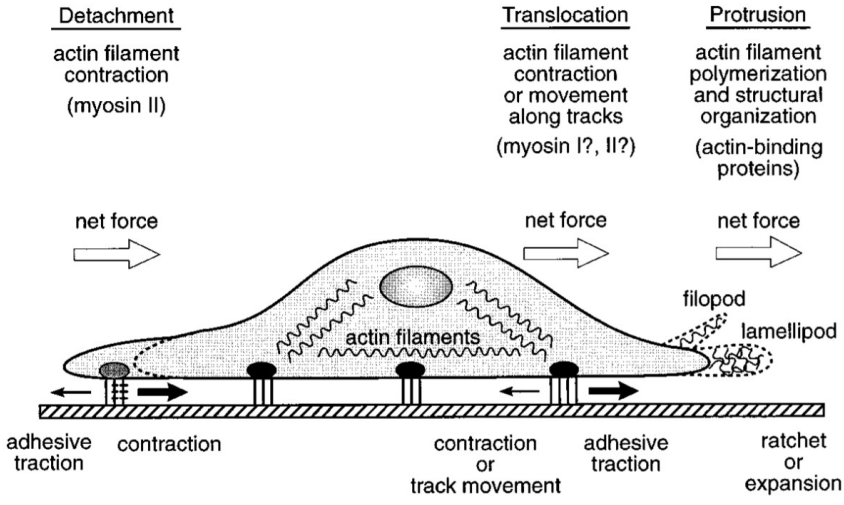

Figure 1-1 - Cell migration mechanism: Migration process starts with ECM sensing with lamellipodia protrusions, polarisation, focal complex formation and adhesion, migration and rear retraction. Image taken from reference.[14]

The adhesion/traction points connect the substrate *via* integrin receptors to the focal complexes, therefore transmembrane receptors called integrins enact the role of biochemical clutch converting a chemical clue into mechanical forces.[20,21] Tumour

invasiveness is enhanced thanks to heightened actin polymerisation that supports membrane protrusions for cell movement.[18] Actin polymerisation is regulated by several factors including the phosphorylation of Cortactin so it binds to proteins like NCK1 and Cofilin to form the invadopodia.[22] Furthermore, Caveolin regulates invadopodium formation at the membrane level, as suggested by the work of Caldieri and coworkers.[23] Invadopodia could have more than just proteolytic function, since it can be found in leading edges of MDA-MB-231 cancer cells, and might have a role in cell orientation sensing.[24] This latter cancer cell type was used in this research project as a reliable model for highly invasive breast cancer cell line. Specifically such cell line is known to move with micro-adjustments around its adhesion positions but is also able to perform cm-scale movements as previously demonstrated in our research group.[25]

1.3. ECM proteins: Fibronectin

One of the most important biomolecules present in the ECM is Fibronectin (Fig. 1-2).[26,27] Fibronectin (Fn) is a multi-domain glycoprotein responsible for cell adhesion, migration and differentiation. Soluble Fn can be found in plasma, while the insoluble variant is present in the ECM. Fn protein is a dimer of two similar subunits of around 250 kDa each. This protein is constituted by 3 types of domains (namely I, II and III) and can be translated in up to 20 variants due to alternative splicing, indicating an important regulatory function with such abundant isoforms. Each variant has different domains for a multitude of target proteins.

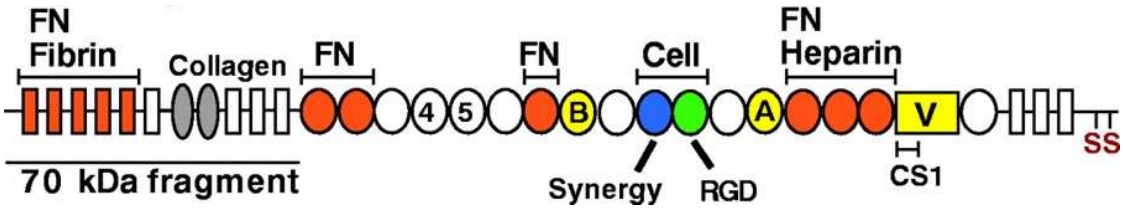

Figure 1-2 – Fibronectin structure: FN type I (rectangles), type II (ovals) and type III (circles) repeats. Sets of repeats constitute binding domains for fibrin, FN, collagen, cells and heparin, as indicated. The three alternatively spliced segments, EIIIA, EIIIB and V (or IIICS), are in yellow. The assembly domain and FN-binding sites are highlighted in orange. SS indicates the C-terminal cysteines that form the disulphide dimer. Image reported from references 26 and 27.

Domain $I_{1\text{-}5}$ are responsible for Fn matrix assembly (rectangles in Fig. 1-2). Other domains bind collagen and other structural proteins. Between B and A type III region (Fig. 1-2) resides the well-known RGD-binding domain (Arginine-Glycine and Aspartic acid) responsible for triggering cell adhesion.[28,29] Specifically, Fn domain III_{10} represented in green and bearing the RGD loop interacts with integrin subtypes α5β1 and αVβ3 triggering cell adhesion.[28,30] The important finding that integrins could be activated by oligopeptides mimicking Fn and triggering a biological response was very

interesting for the spatio-temporal control of cancer cell migration. It was found that RGD-tethered ECM-mimicking surfaces induced adhesion in deposited cells over the substrates. Another remarkable discovery by Schor and co-workers was that IGD-bearing peptides (Iso-Leucine-Glycine-Aspartic acid) are responsible for sustaining and enhancing cell migration in fibroblasts, later demonstrated in this group for MDA-MB-231 cancer cells on gold surfaces.[25,26,31,32] The IGD motif was found to be a highly conserved sequence present into 4 of the 9 type I Fn domains.

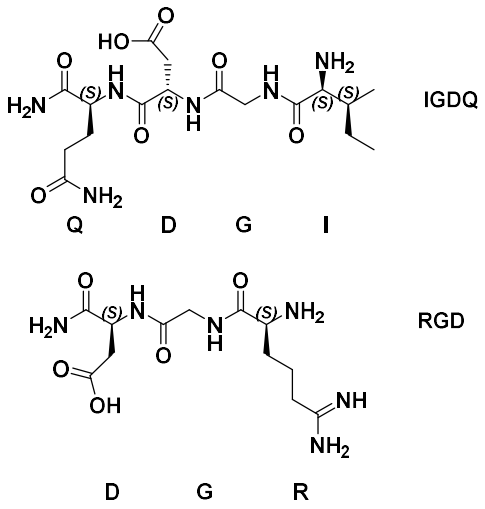

Figure 1-3 – Integrin-binding peptide sequences IGDQ and RGD. Since biological binding occurs from IsoLeu (I) to Gln (Q), such versus was kept in the sequence name, even though molecules are drawn from left to right.

In his pioneering study, Schor assessed the activity of different peptides such as IGD, IGDQ, IGDS, RGDS and the scrambled SDGI. He found that IGDS was the most active in stimulating fibroblast migration. Walking down the reactivity scale, IGDQ and IGD went second and third in the chart, while SDGI and RGDS did not induce migration. Interestingly, the study found that cell activation is correlated to integrin αvβ3 activation with the phosphorylation of focal adhesion kinase (FAK) protein complex and even more interestingly is down regulated when integrin α5β1 is active. A more recent paper by Ellis and co-workers used a smaller isoform of Fn called Migration Stimulating Factor (MSF).[31–33] This protein induces migration in fibroblast, while the native Fn does not. In the study, it was demonstrated that two IGD-bearing modules belonging to the 3rd and 5th type I domains were able to trigger motogenic activity in fibroblasts. As they previously demonstrated when mutations in 7th and 9th modules on type I Fn are produced, MSF is then devoid of any motogenic activity. The study was carried out in collagen gels and with transmembrane migration assays. The mechanism of interaction between Fn exposed amino acids and integrin receptors is still not clear, also because a large number of integrin receptor dimers can interact to the numerous isoforms of Fn.

Thanks to their work, new light was shed on the importance of integrin-binding peptides controlling cell activity. Controlling cell behaviour is crucial for potential treatments in a wide variety of diseases since cell migration is implicated in a large number of physiological and pathological processes.

1.4. Integrin transmembrane receptors

This following section on Integrin transmembrane receptors portraits the signalling pathways from the ECM to the focal complex, establishing a physical connection between the cytoplasmic organelles and the substrate. Integrins are heterodimeric receptors that interact with the ECM and trigger the intracellular cascade for cell movement. Integrins have α and β dimers that lie in an inactive position.

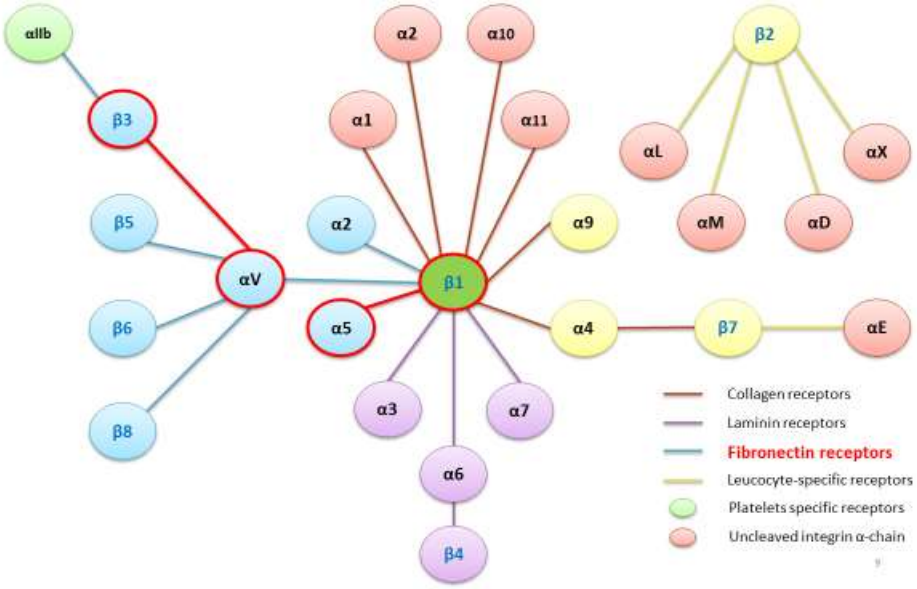

Figure 1-4 - Integrin receptor heterodimers' matching pattern. Image adapted from Ref.[34]

Upon activation, integrins switch to the extended "open" conformation enabling cell signalling (ECM to cytoplasm and *viceversa*). This PhD work exploits a relatively unknown interaction between some Integrin subtypes and a highly conserved tripeptide section of Fibronectin from the ECM with IsoLeucine-Glycine-Aspartic Acid (IGD in the one-letter code for Aminoacids) that was found to trigger cell migration on cancer cells in an *in vitro* setup. Integrins are transmembrane receptors with a multitude of functions and activation modes. Depending on the two α and β subunits that couple, a different function is performed. Integrins possess extracellular binding regions capable of binding collagen, fibronectin, laminin and also the Ig superfamily, that are all components of the ECM.[35] For example, the α5β1 and α4βl integrins mediate migration on fibronectin[36], and the α2β1 integrin mediates migration on collagen.[37] αvβ3 implied in metastasis and angiogenesis[38] is associated with persistent migration, and it is likely

to be responsible for the migration of our model cells on our cell-instructing surfaces.[39],[25,40] Ligand binding induces integrin clustering that forms multiprotein complexes comprised of intracellular signalling and adaptor proteins that connect to the actin cytoskeleton. Binding specificity is determined by different extracellular integrin domains, that bind different proteins. The affinity of integrin for its ligands is regulated by intracellular signalling that leads to integrin activation.[41] In the scheme above the integrin heterodimer matching is shown. 9 different integrins bind to the RGD (Arg-Gly-Asp) cell-adhesion motifs in the Fibronectin multi-domain protein of the ECM. If the ECM contains Fibronectin and there is cell adhesion, it is likely induced and influenced mainly by the fibronectin binding of corresponding integrins. An alteration in integrin expression or even knock-out experiments can influence the migration mode, speed and signalling. One integrin can replace another, handling part of the signalling burden. Alterations in integrin expressions can lead to different phenotypes, that in the context of metastasis and cell invasion can trigger a more aggressive phenotype.[42] Because of such numerous coupling possibilities, a fine tuning of cellular functionalities is enabled. On the other hand, altered integrin signalling, unbalance and overexpression, and such anomalies are found in a multitude of pathological diseases, from inflammation, dysfunctional embryonic morphogenesis, tissue regeneration but also cancer and metastasis.[43] As a direct implication that complicates the system even more, there is likely to be some cross-talk between integrins, that influence each other.[44][45][46]

Ligand binding on integrins causes protein clustering and therefore receptor activation. Different protein clustering regulates ligand affinity.[41] αvβ3 can be activated in lamellipodia of migrating cells, and it is likely involved in cell migration as a main receptor heterocouple.[39] Rho GTPases are also involved in adhesion/migration regulation, downstream with the protein binding cascade.

1.5. Focal Adhesions

Focal adhesions (FAs) are the dynamic linkage between the actin bundles and the substrate *via* integrins. A multitude of cytoskeletal proteins constitute the focal adhesions, connecting the actin bundles to the underlying substrate, balancing the traction points created in the ECM. Focal adhesions are therefore a biological clutch for mechano-transduction, balancing the adhesion forces at the front and the rear of the migrating cell, preventing the retrograde flow. Actin polymerization in cell protrusions that are not fast enough lead to retrograde flow. The protrusion rate is therefore the difference between the advancing lamellipodia and the retrograde flow, finely tuned by

FAs that act as molecular clutches for cell migration. Many pathological diseases can be associated with altered cell adhesion and migration regulated by integrin activation. FAs have structural function as well as signalling, with the Focal Adhesion Kinase (FAK) phosphorylation, the Protein Kinase C (PKC) and others. It is now clear that there are multiple FAs and different stages in the focal adhesion turnover. A classification of FAs is provided with detailed images by Zaidel-bar and co-workers but also by Vicente-Manzanares that elucidate the complexity of this system.[47–49] This kind of protein clustering event can be divided into nascent adhesions, but consequent maturation leads to the evolution of the system in focal complexes and focal adhesions. This results in different types of integrins, clustering different FAs that have a multitude of functions, being able to finely tune the cellular activity. Turnover of assembly/disassembly of FAs is a dynamic process for cell migration. As extensively explained by Huttenlocker et al. and lately discussed by us from a peptide SAM point of view, the optimum of adhesion and migration speed is an intermediate situation of dynamic FA clustering and disruption, enabling traction forces to drag the cell and retain directionality.[40,50]

1.6. *In-vitro* cancer cell migration

Although the broad and multidisciplinary character of this topic, this section focusses on *in vitro* substrates to study tumour invasion for future therapeutics. Such biocompatible substrates face the challenge of perfect biocompatibility of the device, with preferably cheap and easy chemical functionalization. Moreover, unambiguous characterization is needed together with fast analysis outcome, with simple but cutting-edge techniques to be able to investigate intracellularly the biological pathways that trigger such complex and yet not fully understood response. As a second implication of this research, industrial applications for high-throughput screening scale-up should be considered as are much more convenient than in vivo testing, at least for early stage research and development on the subject. Substrate patterning with widely known techniques such as μ-contact printing (μ-CP) and soft lithography with poly-dimethylsiloxane (PDMS) could be employed and therefore extended to an industrial scale. Massive screening of vast libraries of compounds to develop new therapeutics for cancer would become possible with appropriate chip technology patterning and infrastructures, and in principle will be beneficial not only for cancer treatment but also for many other related pathologies, since cell migration is crucial for numerous biological processes such as embryo development, wound healing but also inflammation. Comprehensive reviews on this medical side of the issue can be found

at the end of this Chapter.[51],[2,43,52] There are many examples of migration studies in literature, and it is useful to divide the research in sub-categories. Sutherland et al.[53] tackle wound healing, with an insight on growth factors that enable both proliferation and migration on different cell lines. Their substrates of polyacrylamide gels are micropatterned for Durotaxis according to the procedures by Itoga and Hartman.[9,54] Most of the devices for cell migration are made with microfluidic technology[55] and photolithography patterning. An overview of one of the possible applications is detailed in the work of Zhang on skin reconstruction scaffold with different biocompatible polymers.[56]

1.7. Cell migration assays

A comprehensive overview on the migration and invasion assays is discussed in depth by Kramer and co-workers[2] describing the Boyden chamber assay[57–59] with a porous membrane for the cells to cross both regarding single-cell and collective movements. Another cheap and useful experiment is the “scratch assay” that is performed over a confluent cell culture that is scratched with a pipette tip and cohort regrowth and reoccupation of the missing space is monitored by microscopy techniques. The zone-exclusion assay derives from this principle, and is typically based on a physical obstacle that contains the seeded cells at confluence and afterwards is removed.[60] This experiment aims to evaluate the migration of the seeded cell line filling in the physical barriers that have been removed. The fence assay follows the same idea, with a Teflon ring positioned on the Petri dish, that is conveniently removed for the cells to grow and proliferate radially while monitored in the same fashion. Justus et al. provided a useful video library of different migration tests and their outcomes that can be helpful when comparing procedures and kits available on the market.[61] Another assay developed in 1990 was the microcarrier bead experiment developed by Rosen et al.[62] Beads of dextran or similar materials serve as support for cell growth. Beads are then transferred onto culture plates where the cells migrate and adhere onto the Petri surface. Before the imaging step, the beads are removed to be able to analyse the population that moved to the Petri. The spheroid migration assay is set with tumour cells that must be able to form such aggregate. The spheroids are deposited on a culture plate and monitored by microscopy techniques. Cells will then migrate and spread over the culture plate while monitored, increasing the size and the contact with the plate. The spreading through spheroids has the advantage of a more accurate mimicking of tumour invasion.[63] Cells can also be encapsulated into alginate beads[64] that could be used in applications for tissue regeneration in the vascular system. The last migration

assay described is the microfluidic chamber assay[65–68]. In the first pit the cells are deposited and the second one is filled with both medium and chemo-attractants. Cells will move towards the gradient and the event can be observed by common microscopy techniques. There are several models and variants of such tests, and the most interesting point relies on the scale they are performed, that makes them suitable of high throughput in industry. Another cheap and easy-to-handle assay is capillary tube migration test[69,70], that can be easily observed by common microscopy techniques. There are more tests developed for invasion[71,72] rather than cell migration that will not be covered here. After this overview on biological assays to study cell migration, self-assembled monolayers (SAMs) will be introduced.

1.8. SAMs for studying *in vitro* cell migration

The interface between a living organism and an organic, inorganic or hybrid material is currently object of study to find the best substrate and functionalization to match its biological counterpart, for therapeutics and prosthetics[73]. As nowadays' material research is growing upon 30 years of efforts and achievements, bioengineering and regenerative medicine are pushed for higher quality of biocompatible substrates, with always better technological properties, lower rejection at a minimal cost. SAMs[74] on gold are in use since the 90s and still a landmark of reliability, biocompatibility and flexibility for surface imaging, cell culturing and chemical processability. SAMs are a system of self-rearranging molecules that tether on a metallic surface in a solvent, over

a certain time. The potential for SAMs used for cell-based screening devices is remarkable because of the easy protocols and manipulation.

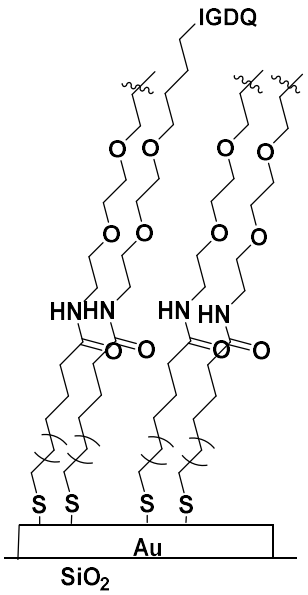

Scheme 1-1 – Alkanethiol-PEG chains of a self-assembled monolayer (SAM). IGDQ motogenic sequence is covalently bound on top of the monolayer.

From a pharmaceutical point of view, cell adhesion and migration with cancer cell models can be studied for future therapeutics. Mechanistic pathways of adhesion and migration can be characterised with such tool to understand the crosslinked pathologies related to cell movement. SAMs on gold have the advantage of easy functionalisation with thiolated molecules. Surfaces could be simply dipped into the solution for a certain time to obtain the monolayer. After a gentle washing, the monolayer is ready for cell seeding without further manipulation. When chemical modification is needed, surfaces are immersed in the solution of chemicals or irradiated to perform the reactions. An important tool while customising a SAM for a certain biological function is the use of bio-inert tags (Scheme 1-1).[75] This peculiar strategy employs poly(ethylene glycol) (PEG) that prevents unspecific protein adsorption.

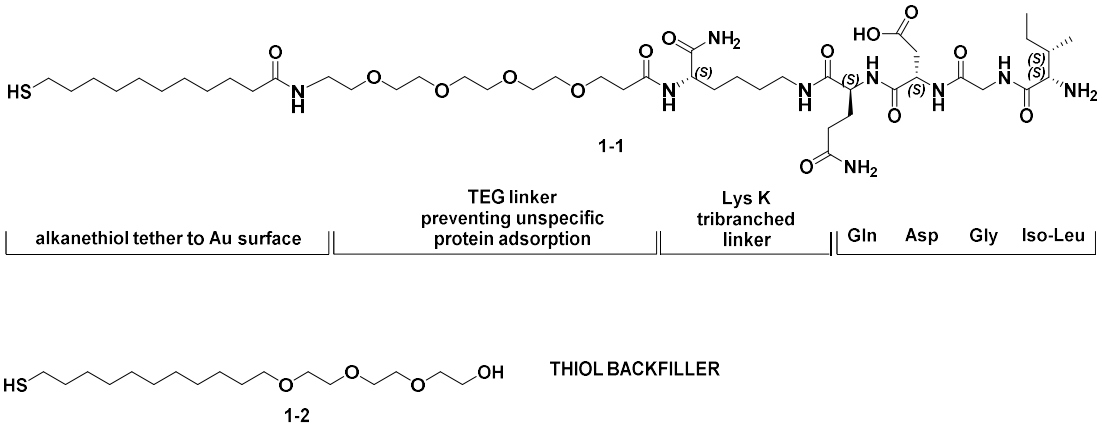

Scheme 1-2 - IGDQ-bearing peptide 1-1 with its matching backfiller 1-2.

The chosen peptides in this thesis work were tailored with an oligo-TEG chain for this reason (Scheme 1-2). Pioneering works of Liu and co-workers employed integrin-binding peptide RGD to induce cell adhesion.[76] Interestingly this work was elegantly performed with the use of azobenzene that controlled the readability of the integrin-binding peptide RGD, that could be photochemically switched. Other research groups pioneered this approach with more elaborate techniques such as photolithography and μ-Contact printing. Different strategies and techniques to control adhesion and release of cell populations over dynamically controlled substrates were employed, however, the maximum distance covered with such devices is 1 mm at best, while the distances of migrating cells over the substrates fabricated within this PhD Thesis are at the cm-scale.[75–77] The work of Zheng was remarkable, concerning the phototriggered cell differentiation.[78] A very interesting application was the laser-guided cell migration on pre-patterned surfaces. A laser beam would modify the adhesive properties of the substrate guiding the advancement of the migrating cell population. Another remarkable landmark for phototriggered substrates for cell adhesion and migration was the work of Salierno et al. in which they had a two-step phototriggered adhesion and migration with a cyclic RGD peptide and an NVOC-derived photolinker.[79] Yousaf and co-workers pioneered the microfluidic photolithography to generate a Fn gradient along a gold surface (Fig. 1-5), directing cell migration toward a specific direction.[80] Another interesting example of SAM application in biosensing is shown by the work of Revzin and co-workers. Mixed SAMs of alkanethiols with antibodies were covalently tethered on gold electrodes.[81] T-lymphocytes were then bound to the antibody-presenting monolayer. Desorption of the SAM occurred when applying an electric potential, for cell cleavage and further analysis or sorting. Such cytometric device has potential

application in the field of diagnostics and sensing for diseases affecting the immune system, e.g. HIV that alters the immune response.

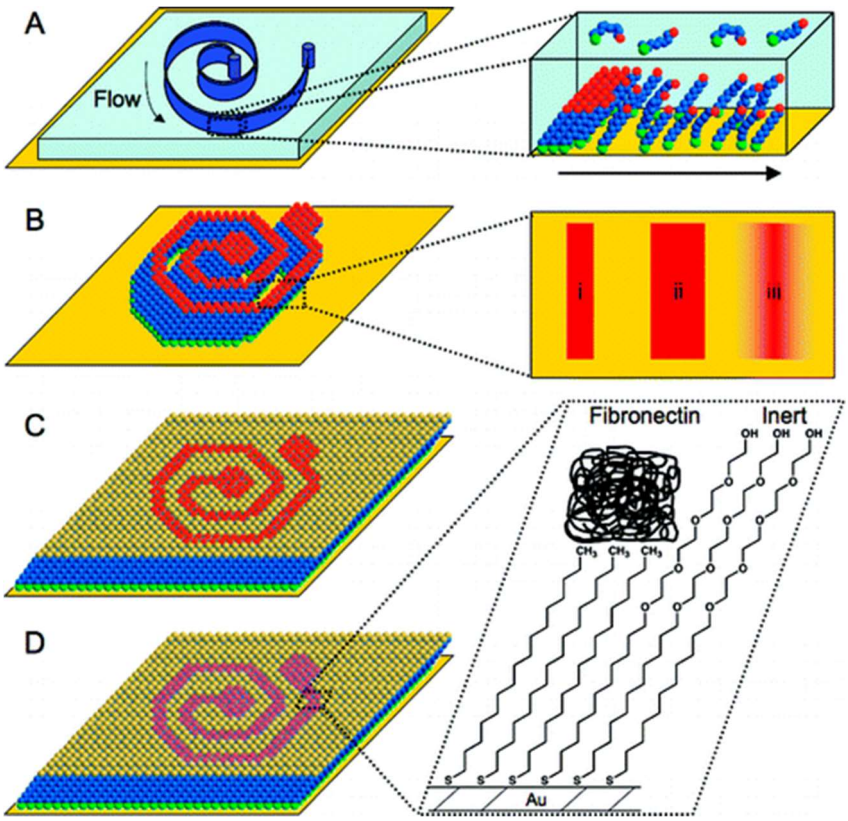

Figure 1-5 – Microfluidic-fabrication of a SAM gradient. Image reported from Ref.[80]

The work of Yousaf and co-workers was chosen as pivotal example of potential applications of SAM technology for the spatiotemporal control of cancer cell migration. Gradients of Fibronectin (Fn) were used to guide cells along the spiral gradient on the chip. Our approach replaces Fn with IGDQ-bearing peptides (Scheme 1-2) that are responsible for triggering cell migration (See section 1.4). It is now clear that cells follow chemical gradients on surface, and 2D spatiotemporal control can be achieved by fabricating a motogenic gradient on a suitable substrate. The common components of the monolayers presented so far employ alkanethiols bound to oligo-ethylene glycol chains, that are a useful tool that can be employed in solid phase synthesis for the purpose of this project and PhD Thesis. As a conclusion of this overview on SAMs, their wide range of application, easy manipulation and functionalisation makes them the ideal biomimicking support to host cell culturing for multiple functions such imaging, sensing and screening. In the next section, fabrication of the peptide gradient with the two-step immersion protocol will be discussed.

1.9. Isotropic and anisotropic fabrication of SAMs

The approach of this PhD Thesis exploited the mixed SAM technology for the fabrication of anisotropic gradients of IGDQ-bearing peptides on gold surfaces. Following the work of Morgenthaler and Spencer[82–85], our group first reported on the preparation of SAMs exposing IGDQ peptides (Scheme 1-2) by simply dipping a gold surface into the IGDQ-bearing peptide solution. A second backfilling immersion was also performed to enhance the monolayer packing, maximising peptide readability for integrin biorecognition.[84] The peptide structure is tailored to ensure monolayer packing thanks to the alkanethiol chains and the TEG moiety would provide resistance to unspecific protein adsorption, preventing irreversible cell binding, blocking the migration movement. Integrin-binding motifs such as IGDQ-bearing peptides were used to mimic the role of Fn in the ECM. Such simple method shown in Fig. 1-6 enabled the production of concentration gradients of motogenic peptides (Scheme 1-2) on gold surfaces. The fabrication of an anisotropic gradients of thiolated peptides on gold surfaces is performed by the technique showed in Fig. 1-6. The thiolated peptide is dissolved into a μM EtOH solution. The surface is cleaned by ozone treatment for 15 minutes and then dipped into the first solution. Monolayer production is performed via a linear motor clamping the gold surface for a speed-controlled dipping (15 min, 17 $\mu m \cdot s^{-1}$ speed, 1 μM EtOH solutions). This protocol was the standard procedure for the monodirectional concentration gradients fabricated in this project and PhD Thesis. After the first controlled dipping, the surface was washed to remove any trace of physi-sorbed material and then immersed completely for 10 minutes into the backfilling solution of a shorter molecule, that helps packing the system up, exposing the peptide towards the surface, assuring the maximum readability of the IGDQ sequence. Due to the dipping procedure, the part of the surface that lies longer into the thiol solution has a higher concentration of molecules adsorbed. Conversely, the part of the surface closer to the clamp lies for shorter time into the thiol solution therefore has a lower concentration of molecules packed in the monolayer. As adsorption occurs immediately, the longer peptide chains tend to lie flat on the metal surface, due to charge-transfer interactions.[86,87] The monolayer has therefore a non-defined architecture, with disordered and not periodic structure and a rather shallow gradient, confirmed by XPS experiments shown later in Chapter 2.[40]

After the dipping, PVC masks were applied to the surfaces. This step facilitates imaging and cell seeding, since the masks have a cell-deposition spot that makes it easier to pipette the cell suspension. The masks were always applied placing the cell-seeding

spot at the lowest point of the chemical gradient. Once seeded the cells, sensing process would start, guiding the cells towards the migration channel, that would be parallel to the fabricated gradient on the substrate. Different self-adhesive PVC masks were tested, with different patterns, although optimisation is not reported in this Thesis. Xurography cutting/printing of the PVC mask designs with 3 migration channels *per* surface were fabricated.

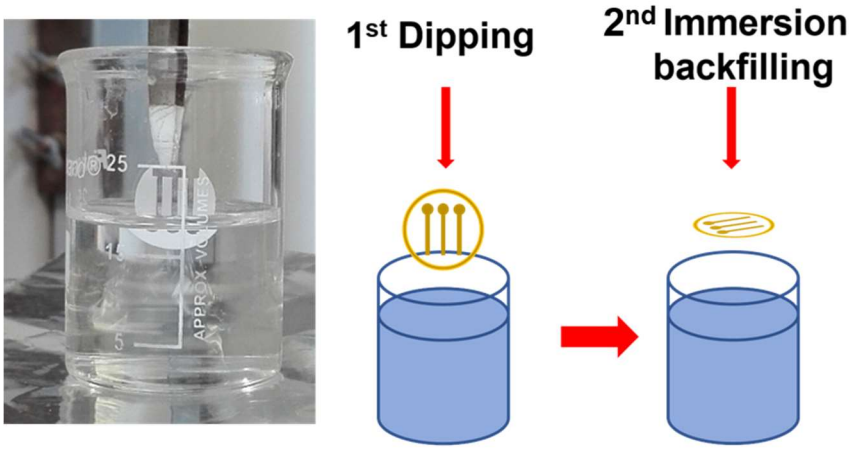

Figure 1-6 - Two-step immersion protocol for the fabrication of anisotropic gradients on surface.

Extensive confocal and phase-contrast imaging were performed for a systematic characterisation of cell movement on surface. Cells seeded on such chemical gradients having the chemoattractant molecules on surface were monitored for over 5 days, tracking cell movement along pre-designed migration channels on adhesive PVC masks.[25] On the other hand, isocratic SAMs were also fabricated by simply immersing overnight a clean gold surface into the thiol solution. Surfaces can be tethered with any thiolated peptide. Such surfaces showed no evidence of migration because of the lack of chemical gradient guiding the cell population.

1.10. Nomenclature for isotropic and anisotropic gradients on surface

A conventional labelling method for gold surfaces was established.[25] Isotropic SAMs on gold were named according to their composition. A single-component SAM of peptide **1-1** (Scheme 1-2) fabricated by overnight dipping into a μM EtOH solution of the peptide was named IPS100%·Au or in short IPS100%, standing for IGDQ-bearing peptide with PEG chain (see structure in Scheme 2-1 below) and thiol-terminus (S). Mixed monolayers were named after their peptide present in the mixture: a 10% molar ratio of peptide **1-1** into 90% molar ratio of backfiller **1-2** was labelled as IPS10%·Au or in short IPS10%. Regarding the anisotropic gradients of peptide **1-1** a δ was included

to indicate the incremental concentration along the scan direction, so for a coverslip SAM gradient of peptide **1-1** and backfiller **1-2** the name referenced in this thesis was δIPS/PS·Au, referring to the standard 15' dipping conditions applied.

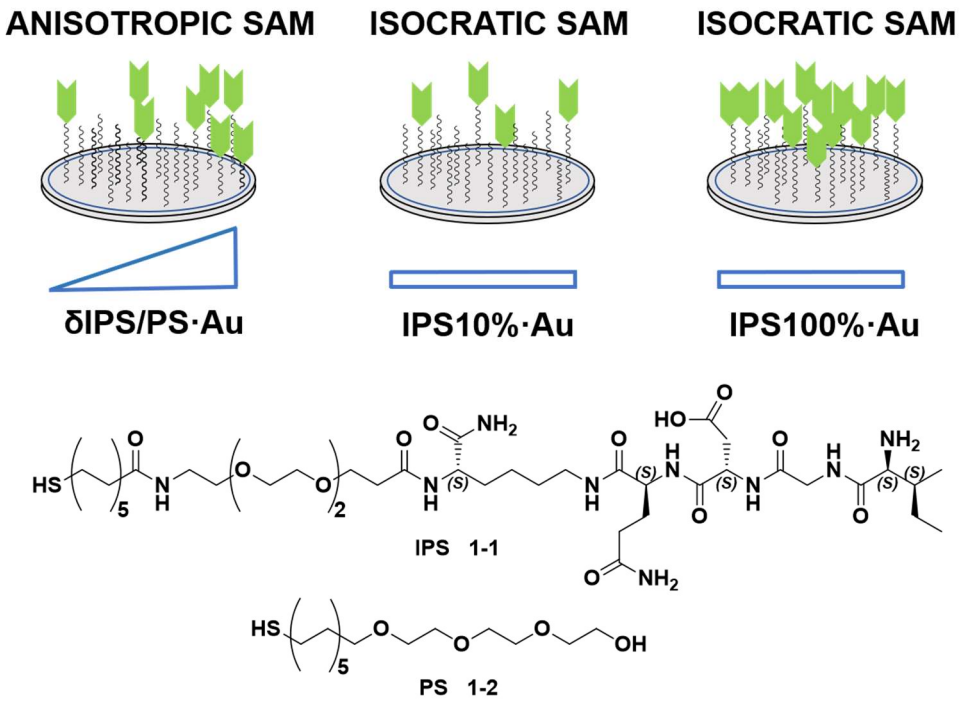

Scheme 1-3 – TOP: SAM nomenclature and corresponding representation: 1 anisotropic and 2 isotropic SAMs. Colour code: green tip = IGDQ-bearing peptide **1-1**; wobble chain = backfiller structure **2-2** (Scheme 2-1). BOTTOM: IGDQ-bearing peptide **1-1** backfiller **1-2**.

1.11. Cell migration experiment – spatiotemporal control of cancer cells on SAMs

In this previously reported experiment, chemical gradients of IGDQ and RGD peptides were fabricated on round coverslips. MDA-MB-231 cells were seeded on both sets of surfaces, and imaged daily. The IGDQ-bearing substrate is showed on the left, while the RGD in displayed on the right (Fig. 1-7). MDA cells were monitored over 5 days. The results of such experiments are remarkable, because it was proven that the anisotropic functionalisation of integrin-binding peptides could guide cell migration along a 1.4 cm pathway of patterned gold.[25] Different conditions were applied, but only the 15' dipping into the IGDQ-bearing peptide with a 10' immersion into the backfiller enabled the cm-scale single cell migration. Hydrophobicity and chemical gradient steepness were specifically explored and tuned to obtain the best migration results with an extensive monolayer characterisation, focussing on SAM biorecognition with tailored monolayer architectures.[40]

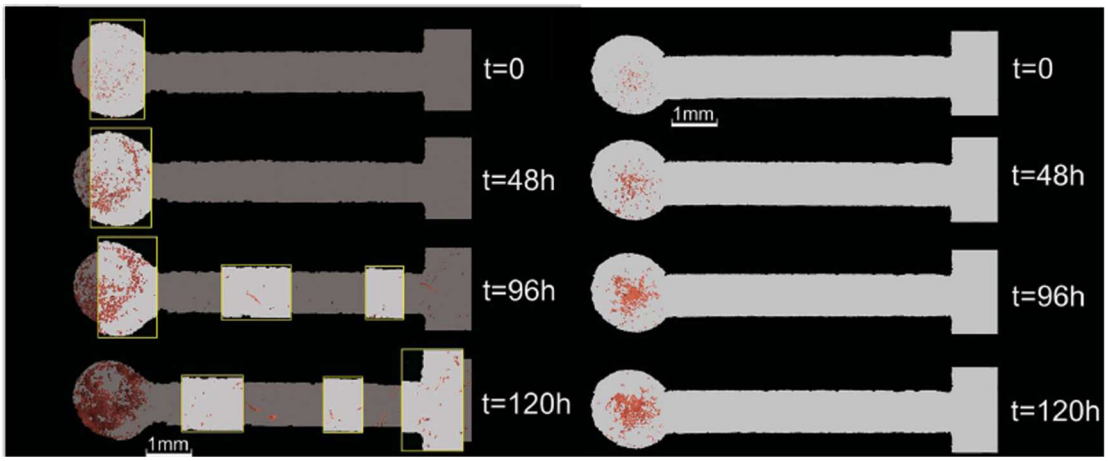

Figure 1-7 - Edited optical microscopy snapshots of the time-dependent migration of MDA-MB-231 cells on left: IGDQ gradient; RIGHT: RGD gradient.

1.12. Aim of the project

These findings built a solid foundation on the technology for the fabrication of ECM-mimicking substrates to study cancer cell migration. However, among the several investigations covered in this project, the architectural and structural aspects of the monolayers were not addressed. To fill this gap, one of our goals was to investigate the cell-substrate interface, specifically by the monolayer side. An extensive microscopy characterisation was performed to assess peptide readability brought by the monolayer packing, corroborated by Molecular Dynamics and coupled with confocal imaging on in vitro model cells (MDA-MB-231 cancer cells). After the investigation of the structural features of SAM monolayers that could mimic the ECM, our curiosity moved to build up a more complex system with improved features. Many works were taken into consideration, regarding cell control on tailored substrates. Dynamic control of SAM adhesion with light and motogenic peptides in microfluidics to guide migration were investigated by important scientists such Feringa, Mrksich and del Campo, however none of them had our gradient fabrication method and a correspondent cm-scale migration with plenty of room for other surface modifications.[75,77,88] To fill this gap and expand our knowledge over cancer cell migration, a more elaborate substrate with two series of tethered messengers that could shift chemical gradients upon shining light has not been studied with our tuned gold surfaces. Photolabile peptides were employed for a chemical-free design that could switch the anisotropic gradient by shining light over the substrate. Surfaces tethered with integrin-binding peptides were used with the purpose of mimicking to a greater extent the complex environment of a tissue or an organ and study the corresponding cell behaviour. Having such dynamic substrate tool could lead to a huge number of possible applications, from screening to bio-devices,

with the potential of unveiling the crucial aspects of cancer cell migration, for future therapeutics.[89]

1.13. Bibliography

[1] F. Van Zijl, G. Krupitza, W. Mikulits, *Mutat. Res. - Rev. Mutat. Res.* **2011**, *728*, 23–34.

[2] N. Kramer, A. Walzl, C. Unger, M. Rosner, G. Krupitza, M. Hengstschläger, H. Dolznig, *Mutat. Res. Mutat. Res.* **2013**, *752*, 10–24.

[3] P. Friedl, K. Wolf, *Nat. Rev. Cancer* **2003**, *3*, 362–74.

[4] M. Mak, C. A. Reinhart-King, D. Erickson, *PLoS One* **2011**, *6*, e20825.

[5] C. Bonnans, J. Chou, Z. Werb, *Nat. Rev. Mol. Cell Biol.* **2014**, *15*, 786–801.

[6] D. J. Sieg, C. R. Hauck, D. Ilic, C. K. Klingbeil, E. Schaefer, C. H. Damsky, D. D. Schlaepfer, *Nat. Cell Biol.* **2000**, *2*, 249–256.

[7] T. Lämmermann, B. L. Bader, S. J. Monkley, T. Worbs, R. Wedlich-Söldner, K. Hirsch, M. Keller, R. Förster, D. R. Critchley, R. Fässler, et al., *Nature* **2008**, *453*, 51–55.

[8] A. Ortega-Carrion, L. Feo-Lucas, M. Vicente-Manzanares, *Encycl. Cell Biol.* **2016**, *13*, 720–730.

[9] C. D. Hartman, B. C. Isenberg, S. G. Chua, J. Y. Wong, *Proc. Natl. Acad. Sci.* **2016**, *113*, 11190–11195.

[10] S. V. Plotnikov, A. M. Pasapera, B. Sabass, C. M. Waterman, *Cell* **2012**, *151*, 1513–1527.

[11] M. Bailly, L. Yan, G. M. Whitesides, J. S. Condeelis, J. E. Segall, **1998**, *299*, 285–299.

[12] C. De Pascalis, S. Etienne-Manneville, *Mol. Biol. Cell* **2017**, *28*, 1833–1846.

[13] D. A. Lauffenburger, A. F. Horwitz, *Cell* **1996**, *84*, 359–369.

[14] R. Ananthakrishnan, A. Ehrlicher, *Int. J. Biol. Sci.* **2007**, *3*, 303–317.

[15] E. Tzima, W. B. Kiosses, M. A. Del Pozo, M. A. Schwartz, *J. Biol. Chem.* **2003**, *278*, 31020–31023.

[16] Y. G. Ko, C. C. Co, C. C. Ho, *Soft Matter* **2013**, *9*, 2467–2474.

[17] M. Innocenti, *Cell Adh. Migr.* **2018**, 01–41.

[18] W. Wang, J. B. Wyckoff, S. Goswami, Y. Wang, M. Sidani, J. E. Segall, J. S. Condeelis, *Cancer Res.* **2007**, *67*, 3505–3511.

[19] J. Condeelis, J. E. Segall, *Nat. Rev. Cancer* **2003**, *3*, 921–930.

[20] L. S. Prahl, M. R. Stanslaski, P. Vargas, M. Piel, D. J. Odde, **2018**, 1–30.

[21] B. T. Helfand, L. Chang, R. D. Goldman, *J. Cell Sci.* **2004**, *117*, 133–141.

[22] E. T. Roussos, J. S. Condeelis, A. Patsialou, *Nat. Rev. Cancer* **2011**, *11*, 573–587.

[23] G. Caldieri, G. Giacchetti, G. Beznoussenko, F. Attanasio, I. Ayala, R. Buccione,

J. Cell. Mol. Med. **2009**, *13*, 1728–1740.

[24] J. J. Bravo-Cordero, L. Hodgson, J. Condeelis, *Curr. Opin. Cell Biol.* **2012**, *24*, 277–283.

[25] V. Corvaglia, R. Marega, F. De Leo, C. Michiels, D. Bonifazi, *Small* **2016**, *12*, 321–329.

[26] C. J. Millard, I. R. Ellis, A. R. Pickford, A. M. Schor, S. L. Schor, I. D. Campbell, R. Pickford, A. M. Schor, S. L. Schor, I. D. Campbell, et al., *J. Biol. Chem.* **2007**, *282*, 35530–35535.

[27] R. Pankov, K. M. Yamada, *J. Cell Sci.* **2002**, *115*, 3861–3863.

[28] E. Ruoslahti, *Annu. Rev. Cell Dev. Biol* **1996**, *12*, 697–715.

[29] M. D. Pierschbacher, E. Ruoslahti, *Nature* **1984**, *309*, 30–33.

[30] R. Pytela, M. D. Pierschbacher, E. Ruoslahti, *Cell* **1985**, *40*, 191–198.

[31] S. L. Schor, I. R. Ellis, S. J. Jones, R. Baillie, K. Seneviratne, J. Clausen, K. Motegi, B. Vojtesek, K. Kankova, E. Furrie, et al., *Cancer Res.* **2003**, *63*, 8827–8836.

[32] I. R. Ellis, S. J. Jones, D. Staunton, I. Vakonakis, D. G. Norman, J. R. Potts, C. M. Milner, N. A. G. Meenan, S. Raibaud, G. Ohea, et al., *Exp. Cell Res.* **2010**, *316*, 2465–2476.

[33] G. Solinas, S. Schiarea, M. Liguori, M. Fabbri, S. Pesce, L. Zammataro, F. Pasqualini, M. Nebuloni, C. Chiabrando, A. Mantovani, et al., *J. Immunol.* **2010**, *185*, 642–652.

[34] R. O. Hynes, *Cell* **2002**, *110*, 673–687.

[35] K. T. Chan, C. L. Cortesio, A. Huttenlocher, **2007**, pp. 47–67.

[36] C. Wu, A. J. Fields, B. A. Kapteijn, J. A. McDonald, *J. Cell Sci.* **1995**, *108 (Pt 2*, 821–829.

[37] B. M. Chan, N. Matsuura, Y. Takada, B. R. Zetter, M. E. Hemler, *Science* **1991**, *251*, 1600–1602.

[38] Y. Zhao, R. Bachelier, I. Treilleux, P. Pujuguet, O. Peyruchaud, R. Baron, P. Clément-Lacroix, P. Clézardin, *Cancer Res.* **2007**, *67*, 5821–5830.

[39] H. Truong, E. H. J. Danen, *Cell Adhes. Migr.* **2009**, *3*, 179–181.

[40] F. De Leo, R. Marega, V. Corvaglia, R. Tondo, M. Lo Cicero, S. Silvestrini, D. Bonifazi, *Langmuir* **2017**, *33*, 7512–7528.

[41] S. J. Shattil, C. Kim, M. H. Ginsberg, *Nat. Rev. Mol. Cell Biol.* **2010**, *11*, 288–300.

[42] R. E. Seftor, E. A. Seftor, K. R. Gehlsen, W. G. Stetler-Stevenson, P. D. Brown, E. Ruoslahti, M. J. Hendrix, *Proc. Natl. Acad. Sci. U. S. A.* **1992**, *89*, 1557–61.

[43] P. Friedl, D. Gilmour, *Nat. Rev. Mol. Cell Biol.* **2009**, *10*, 445–457.

[44] J. S. Bauer, C. L. Schreiner, F. G. Giancotti, E. Ruoslahti, R. L. Juliano, *J. Cell Biol.* **1992**, *116*, 477–487.

[45] J. C. Puigvert, S. Huveneers, L. Fredriksson, M. op het Veld, B. van de Water,

E. H. J. Danen, *Mol. Pharmacol.* **2009**, *75*, 947–955.

[46] S. Huveneers, E. H. J. Danen, *J. Cell Sci.* **2009**, *122*, 1059–1069.

[47] R. Zaidel-Bar, M. Cohen, L. Addadi, B. Geiger, *Biochem. Soc. Trans.* **2004**, *32*, 416–20.

[48] M. Vicente-Manzanares, C. K. Choi, A. R. Horwitz, *J. Cell Sci.* **2009**, *122*, 199–206.

[49] R. Zaidel-Bar, S. Itzkovitz, A. Ma'ayan, R. Iyengar, B. Geiger, *Nat. Cell Biol.* **2007**, *9*, 858–867.

[50] A. Huttenlocher, A. R. Horwitz, *Cold Spring Harb. Perspect. Biol.* **2011**, *3*, 1–16.

[51] H. Yamaguchi, J. Wyckoff, J. Condeelis, *Curr. Opin. Cell Biol.* **2005**, *17*, 559–564.

[52] A. Aman, T. Piotrowski, *Dev. Biol.* **2010**, *341*, 20–33.

[53] J. Sutherland, M. Denyer, S. Britland, *J. Anat.* **2005**, *207*, 67–78.

[54] Kazuyoshi Itoga, Jun Kobayashi, Yukiko Tsuda, and Masayuki Yamato, T. Okano*, K. Itoga, J. Kobayashi, Y. Tsuda, M. Yamato, T. Okano, *Anal. Chem.* **2008**, *80*, 1323–1327.

[55] F.-Q. Nie, M. Yamada, J. Kobayashi, M. Yamato, A. Kikuchi, T. Okano, *Biomaterials* **2007**, *28*, 4017–4022.

[56] S. P. Zhong, Y. Z. Zhang, C. T. Lim, *Wiley Interdiscip. Rev. Nanomedicine Nanobiotechnology* **2010**, *2*, 510–525.

[57] M. Falasca, C. Raimondi, T. Maffucci, *Methods Mol. Biol.* **2011**, *769*, 87–95.

[58] Y. H. Li, C. Zhu, *Clin. Exp. Metastasis* **1999**, *17*, 423–429.

[59] M. M. M. Woo, C. M. Salamanca, A. Minor, N. Auersperg, *Vitr. Cell. Dev. Biol. - Anim.* **2007**, *43*, 7–9.

[60] M. Poujade, E. Grasland-Mongrain, A. Hertzog, J. Jouanneau, P. Chavrier, B. Ladoux, A. Buguin, P. Silberzan, *Proc. Natl. Acad. Sci.* **2007**, *104*, 15988–15993.

[61] C. R. Justus, N. Leffler, M. Ruiz-Echevarria, L. V Yang, *J. Vis. Exp.* **2014**, *752*, e51046.

[62] E. M. Rosen, L. Meromsky, E. Setter, D. W. Vinter, I. D. Goldberg, *Exp. Cell Res.* **1990**, *186*, 22–31.

[63] K. Hattermann, J. Held-Feindt, R. Mentlein, *Ann. Anat.* **2011**, *193*, 181–184.

[64] T. P. Kraehenbuehl, L. S. Ferreira, P. Zammaretti, J. A. Hubbell, R. Langer, *Biomaterials* **2009**, *30*, 4318–4324.

[65] C. M. Wells, A. J. Ridley, *Methods Mol. Biol.* **2005**, *294*, 31–41.

[66] S. Chaubey, A. J. Ridley, C. M. Wells, *Methods Mol. Biol.* **2011**, *769*, 41–51.

[67] D. Zicha, G. A. Dunn, A. F. Brown, *J. Cell Sci.* **1991**, *99*, 769–775.

[68] S. H. Zigmond, *Methods Enzymol.* **1988**, *162*, 65–72.

[69] G. Han, J. J. Cooney, *J. Ind. Microbiol.* **1993**, *12*, 396–398.

[70] R. Bainer, H. Park, P. Cluzel, *J. Microbiol. Methods* **2003**, *55*, 315–319.

[71] A. Valster, N. L. Tran, M. Nakada, M. E. Berens, A. Y. Chan, M. Symons, *Methods* **2005**, *37*, 208–215.

[72] K. I. Hulkower, R. L. Herber, *Pharmaceutics* **2011**, *3*, 107–124.

[73] D. Campoccia, L. Montanaro, C. R. Arciola, *Biomaterials* **2013**, *34*, 8533–8554.

[74] M. Mrksich, G. M. Whitesides, *Annu. Rev. Biophys. Biomol. Struct.* **1996**, *25*, 55–78.

[75] J. Robertus, W. R. Browne, B. L. Feringa, *Chem. Soc. Rev.* **2010**, *39*, 354–378.

[76] D. Liu, Y. Xie, H. Shao, X. Jiang, *Angew. Chem. Int. Ed.* **2009**, *48*, 4406–4408.

[77] V. Sriraghavan, R. A. Desai, Y. Kwon, M. Mrksich, C. S. Chen, S. Raghavan, R. A. Desai, Y. Kwon, M. Mrksich, C. S. Chen, *Langmuir* **2010**, *26*, 17733–17738.

[78] Y. Zheng, A. Farrukh, A. del Campo, *Langmuir* **2018**, 34, 14459–14471.

[79] M. J. Salierno, A. J. García, A. Del Campo, *Adv. Funct. Mater.* **2013**, *23*, 5974–5980.

[80] B. M. Lamb, D. G. Barrett, N. P. Westcott, M. N. Yousaf, *Langmuir* **2008**, *24*, 8885–8889.

[81] A. Revzin, K. Sekine, A. Sin, R. G. Tompkins, M. Toner, *Lab Chip* **2005**, *5*, 30.

[82] S. M. Morgenthaler, S. Lee, N. D. Spencer, *Langmuir* **2006**, *22*, 2706–2711.

[83] S. Morgenthaler, C. Zink, N. D. Spencer, *Soft Matter* **2008**, *4*, 419.

[84] S. Morgenthaler, S. Lee, S. Zürcher, N. D. Spencer, *Langmuir* **2003**, *19*, 10459–10462.

[85] E. Beurer, N. V. Venkataraman, A. Rossi, F. Bachmann, R. Engeli, N. D. Spencer, *Langmuir* **2010**, *26*, 8392–8399.

[86] Y. Arima, H. Iwata, *Biomaterials* **2007**, *28*, 3074–3082.

[87] Z. Futera, J. Blumberger, *J. Chem. Theory Comput.* **2019**, *15*, 613–624.

[88] B. M. Lamb, S. Park, M. N. Yousaf, *Langmuir* **2010**, *26*, 12817–12823.

[89] Y. Yang, W. Gao, *Chem. Soc. Rev.* **2019**, *48*, 1465–1491.

2. Chemical gradient characterisation on patterned gold surfaces

In this chapter different experiments performed for the morphological characterisation of Self-Assembled Monolayers (SAMs) of thiolated peptides on gold are reported and discussed. The aim of this chapter is therefore to investigate the morphology of the cell-substrate interface from the surface-chemistry side, focussing on the monolayer architectures of our tailored SAMs on gold.

The first section reports results from Water contact angle (WCA) experiments, starting from the previous work from Dr. Corvaglia and Dr. Marega and then moving on to the new ultra-flat gold surfaces employed for this project. After the wettability on surface section, Atomic Force Microscopy (AFM) results are reported and discussed from Section 2.3. Experiments were carried out on the round coverslips used for biological testing but also on ultra-flat chips for a better understanding on the SAM architectures. As a further investigation, summarised results from the *in-silico* studies of Dr. Federica de Leo are reported in section 2.10. The chapter concludes with X-ray photoelectron spectroscopy (XPS) characterisation. This latter technique was used to characterise the chemical gradient functionalisation. Different researchers worked on this project and performed the experiments reported in this chapter. Details over the experiments and the techniques used are reported in the experimental part.

2.1. Wettability of engineered surfaces with motogenic peptides.

Wettability is a property of a material and can be evaluated from the angle that a solvent drop forms when deposited on a surface.[1] Such solvent is typically water or octadecane. The measured angle *θ* is mathematically bound to interface tensions between the solid (substrate), the liquid (solvent drop) and the gas (ambient air) and can be found in *Young's equation* expressed as the following: $\gamma SV = \gamma SL + \gamma LV \cdot cos\theta$ where *γSV* is the tension between Solid-Vapour, *γSL* for Solid-Liquid and *γLV* for Liquid-Vapour (Fig. 2-1, top). Surface free energy can also be calculated however such specific calculations were not performed in this thesis. Another type of contact angle measurement called dynamic contact angle gives a qualitative indication over the packing degree of a monolayer (Fig. 2-1 bottom R/L). A droplet is deposited over the surface, and the needle is kept in the drop. Solvent is pumped in and out cyclically in a hysteresis: the difference between the contact angle of the advancing droplet

(increasing) and the receding droplet (solvent withdrawal) is the dynamic contact angle (advancing and receding contact angle ARCA-WCA). The greater this difference is, the worse is the packing. If the monolayer is well packed the difference between advancing and receding angles is around 10°.

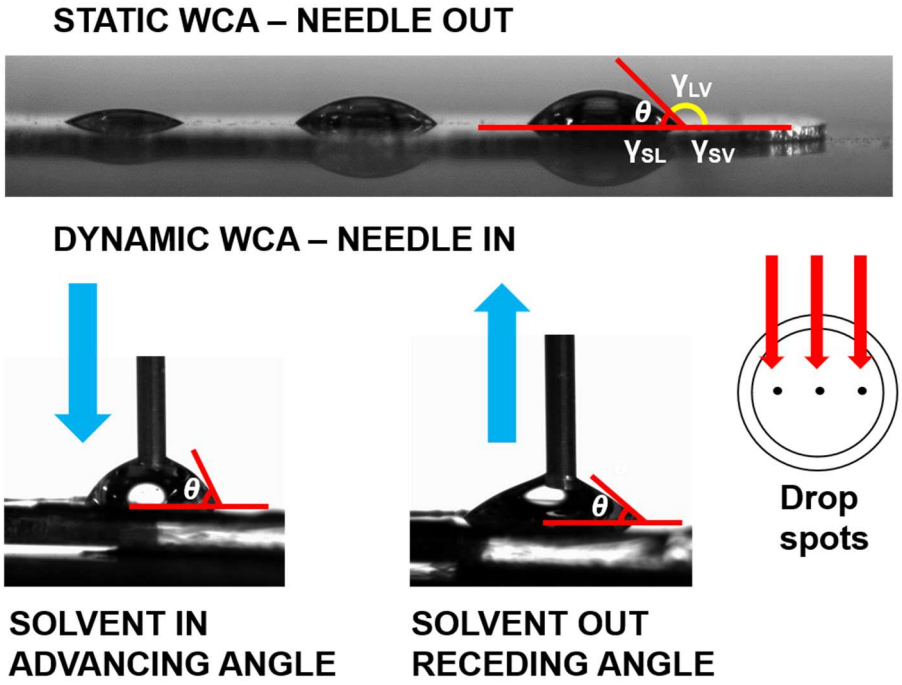

Figure 2-1 – Static (top) and dynamic WCA measurements (bottom): dynamic WCA design from Ramé-hart instruments co.

A well-packed system has isotropic properties around the droplet. Conversely, in a poorly packed SAM advancing and receding angle gap would be higher, increasing the ΔWCA. One qualitative and quick assessment of the surface functionalisation can be performed with a WCA experiment.[4] A droplet of solvent is deposited on a surface and the angle between the surface and the drop is measured by a goniometer. Hydrophilic materials tend to maximise contact with polar solvents. Conversely, hydrophobic materials would maximise contact with oils. Wettability test is a routine experiment performed for the characterisation of coated substrates. WCA studies started at the beginning of the century with the pioneering work of Young. As soon as SAM technology was invented, WCA characterisation was adopted as an important investigation tool for surface chemists. In the early ages of SAM technology, Bain and Whitesides published in 1989 a study in which they characterised a SAM by WCA.[2] In this remarkable study, SAMs were functionalised with different thiols and characterised by WCA. Water and hexadecane were used for the WCA experiments. The monolayer properties were assessed, and a rationale between surface disorder, chain mobility and WCA was established. It was shown that mixed monolayers were bringing more surface disorder, therefore increasing the WCA because of the loose hydroxyalkane chains that

were speculated to be hanging on top of the monolayer. Many years have passed, and WCA is still used nowadays for the characterisation of superhydrophobic surfaces and novel applications in coatings. Si and Guo described extensively the high number of applications of superhydrophobic surfaces, from corrosion resistance to anti-bacterial and drag-reducing coatings. In all of these applications, WCA is always a primary tool for surface characterisation.[3] The importance of such simple experiment resides in the need for controlling hierarchical molecule organisation to the nanometre level. Wettability evaluations were performed on freshly patterned surfaces, as a qualitative assessment analysis of the functionalisation. Water contact angle (WCA) measurements of 15 mm round coverslips were performed on isocratic and anisotropic SAMs of thiolated peptides as previously reported.[5] In addition to that, novel ultra-flat gold-coated chips (1x1 cm of 100 nm Au [111] layer on Silicon wafer substrate, Platypus technologies) were patterned and afterwards their wettability was checked by WCA experiments.[6] Both static and dynamic WCA measurements are necessary to understand the monolayer properties concerning wettability and packing.

2.2. WCA results on ultra-flat gold chips

Here shown in Fig. 2-2 the WCA results of a series of isotropic and anisotropic substrates. Three drops were deposited from the lowest gradient point (drop at 1 mm) to the highest (drop at 9 mm, Fig. 2-1 from left to right). Static water contact angle measurements were performed on isotropic and anisotropic SAMs of **1-1** peptide and **1-2** backfiller (Scheme 1-2) according to the optimised procedure for two-step immersion protocol.[5,7] Results of WCA experiments on freshly-prepared gold chips with a monodirectional concentration gradient are summarised in Fig. 2-2. After replacing the already characterised coverslips, novel ultra-flat gold substrates were used. Ultra-flat surfaces were initially chosen as a replacement for round coverslips for

the microscopy characterisation, with a better surface quality and a known local morphology.[6] Ultra-flat chips were used without ozone cleaning.

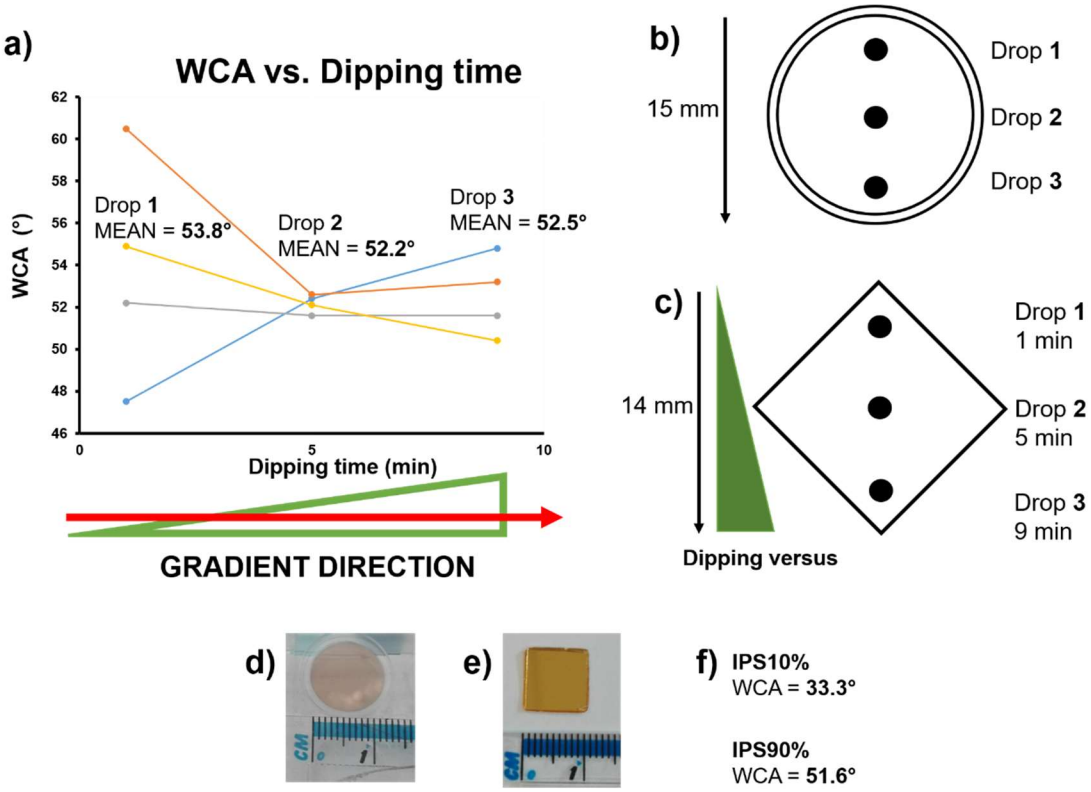

Figure 2-2 – a) static WCA results on anisotropic ultra-flat gold chips; b) drop deposition map on round surface; c) drop deposition map on ultra-flat chips; d) coverslip; e) ultra-flat chip; f) static WCA on isotropic ultra-flat chips.

Figure 2-2 shows a summary of WCA measurements on ultra-flat chips (a). The two schematics on the right (b and c) compare the drop deposition spots on both substrates and the black dots represent the water droplets (1 µL as a standard quantity for static WCA) deposition points. Three drops were deposited on both isocratic and anisotropic SAMs and WCA values were measured. Concerning the anisotropic surfaces, the first droplet was deposited in the low-functionalisation zone, the middle in the centre, and the last one in the high-concentration spot. The left chart (Fig. 2-3) shows 4 replicates of static WCA measurements on ultra-flat chip gradients of peptide **2-1** (Scheme 1-3). Each experiment was carried out using a pristine surface, without any pre-treatment. The first point, corresponding to low-concentration region shows an average value of 53° ranging from 47° to 61°. The middle point seems to be the intermediate situation that is very reproducible as WCA measurement. The high-concentration region seems to be similar to the middle one with a slightly higher value oscillation ranging from 51° to 55°. It seems that in these ultra-flat gold surfaces the kinetic nature of the SAM is heightened thanks to the smoother metal substrate. Further experiments with ozone pre-treatment gave the same outcome and no ΔWCA similar to the one showed in

Table 2-1 were found. Pristine gold chips had a WCA on clean surface of around 50° and this fact might had caused the offset of the chips, compared to the coverslips. Two isocratic mixed SAMs (10% and 90% molar ratio of IPS peptide in PS backfiller, respectively, µM EtOH solutions, overnight immersion) were prepared using ultra-flat chips. Isotropic SAMs on chips gave the same WCA results as the coverslips (see Fig. 2-3 f), with 33° of WCA on IPS10% SAM and 51.6° on the IPS90%. Dynamic WCA experiments were then performed on ultra-flat surfaces and ultra-flat monolayer packing was disclosed. SCA20 software (*Dataphysics*) was used to automatically detect and track the water drop dispensed on the surface. Dynamic WCA experiments were performed dispensing and withdrawing 5 µL at a rate of 0.1 $\mu L \cdot s^{-1}$ for 50 s with a delay between the steps (5 s to 10 s). Advancing and Receding Contact Angle (ARCA) measurements of each surface were repeated several times (5 to 10). Dynamic WCA charts are listed below in Fig. 2-3.

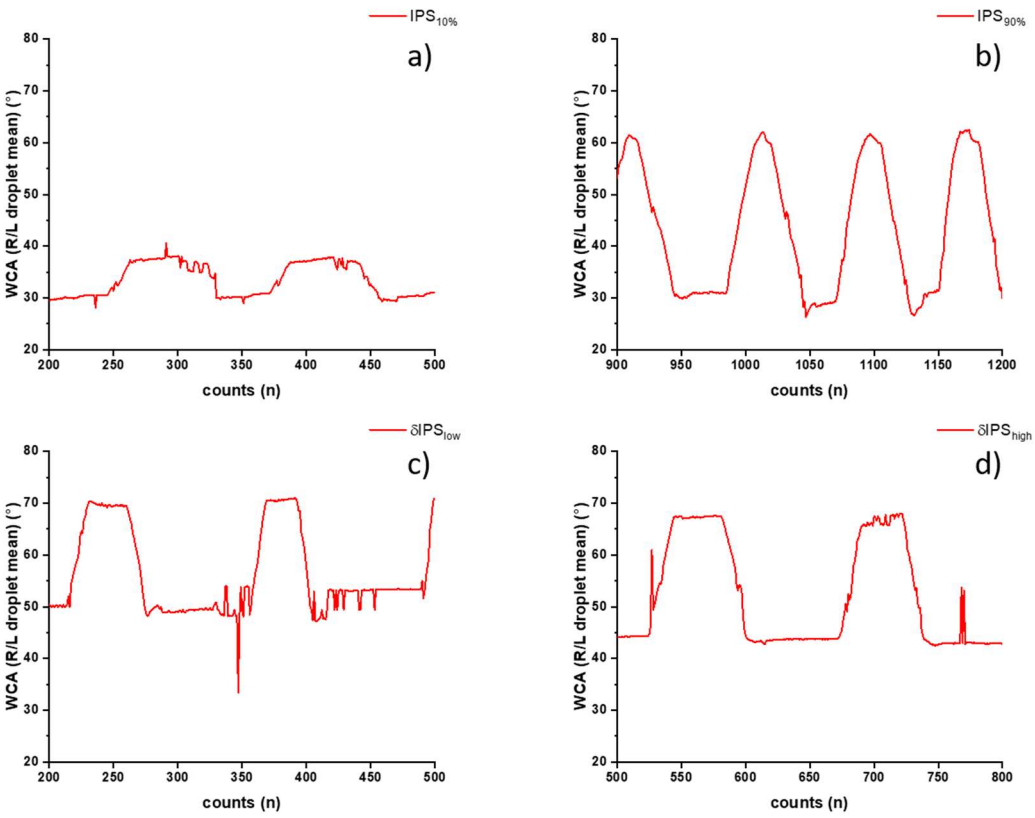

Figure 2-3 - Dynamic WCA of a) IPS10%, b) IPS90%, c) dIPS-low and d) dIPS-high concentration region. Outliers excluded from dataset.

IPS10% (a) has the lowest ΔWCA-ARCA value of around 10°, thanks to the preponderant effect of the backfiller, packing up the monolayer. The highest value of ΔWCA-ARCA was found for IPS90% setting the ΔWCA-ARCA value at 30°. Peptide 2-1 in a 100% single-component SAM does not form ordered architectures, due to its

structure and flexibility. Interestingly, IPS90% showed 51° of static WCA, that does not match the advancing and receding values, showing local disorder, conformational freedom that allows the droplet to “comb” the monolayer during the hysteresis. In conclusion, the chemical gradient of thiolated peptides on ultra-flat gold seems to be very shallow, with a high amount of local disorder and low monolayer packing. This is due to the 15-minute dipping technique that is used, that produces a kinetic type monolayer, far from the well-packed system that can be obtained with an overnight immersion. Nevertheless, when this system is put in cell culture medium, and model cells are deposited over, not only allows cell adhesion and proliferation, but this shallow gradient seems to be responsible for triggering and sustaining cell migration along such anisotropic patterning.[5] Given these premises, a deeper insight into the monolayer architecture with greater magnification on thiol chains and their interactions is necessary, aimed at understanding biological readability of the motogenic sequence of IPS peptide. For this reason, XPS and AFM investigations were carried out to discover more information on monolayer composition and architectures.

2.3. AFM characterisation of gold surfaces

AFM is one of the most popular tools of surface scientists amid the scanning probe microscopy (SPM) techniques, including scanning electron microscopy (SEM), scanning tunnelling microscopy (STM) and many more[8–10][11]. Academia is now enriched by projects employing such imaging techniques, that enables both routine profiling analyses but also sensing and manipulation of material at the micro- and nanometric level. AFM principle is briefly explained: the scanning tip (commonly silicon nitride, but can vary depending on the analysed material), connected to a cantilever maps the substrate that is mounted on a motorised stage. In these instruments the tip oscillates only vertically while the stage is moved for the mapping. A laser focussed on the cantilever shines light that is being reflected from the cantilever to the detector, converting a physical oscillation to electrical signal. When the tip interacts with the sample, the cantilever deviates from its set oscillation therefore the beam is deflected, and such movement is recorded on the detector. This principle allows surface profiling, matter manipulation[12],[13] but most importantly it is possible to detect different materials with different phase plots. The different signal detected on the phase channel is due to a difference in mechanical properties of the substrate, indicating that a different material can be present on the sample. Phase plot is used when detecting different materials on a substrate, that shift the phase oscillation of the cantilever, because of the difference in mechanical properties. Tip scanning mode can be in air, ultra-high vacuum

(UHV) or even in a liquid medium, for soft or biological samples. Scanning mode, among these main modes can be contact mode, tapping mode or non-contact mode. Each technique performs best with different materials. Hard materials can be mapped with tapping and non-contact mode, while soft materials can be scanned with contact mode, dragging the tip into the material. Magnetic and conductive tips can be employed for magnetic force microscopy and to measure electrostatic surface potential with Kelvin probe microscopy respectively.[14,15]

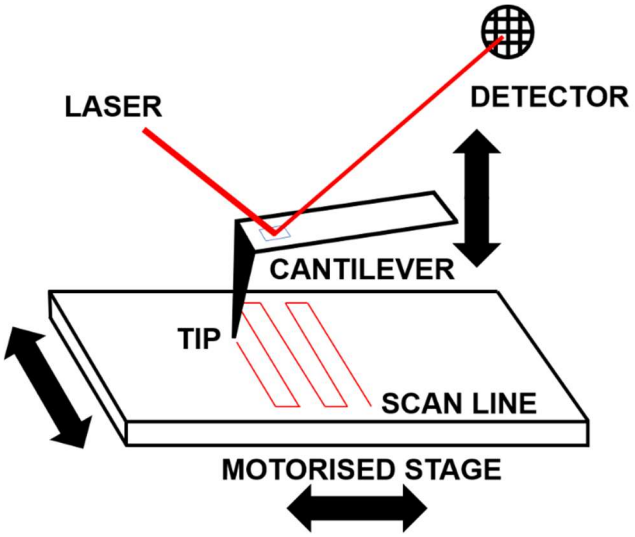

Figure 2-4 – Drawing of AFM principle.

Images presented below were recorded in tapping mode in ambient air. The aim of this paragraph is to probe the monolayer interface and detect the morphology of the thiols responsible for the cell migration on engineered surfaces. AFM imaging technique was therefore used to scan a different number of SAMs for the understanding of thiol architectures on gold.

2.4. AFM results on round coverslips – bare gold

The first image (Fig. 2-6) shows the result of an AFM scan of a bare gold coverslip, without a SAM. This first experiment was set to investigate the nature of the substrate so peptide architectures could be unambiguously identified. Figure 2-6a shows one of the images recorded over the bare gold. Images were scanned twice, mapping the surface from left to right and vice-versa, to exclude artefacts or image drifts caused by the tip scooping material from the monolayer. Since the right and left images used to overlap, only one is reported. After the mapping, a profile scanline is exported from the image, chosen as representative of the sample. Figure 2-6b) shows the chosen scanline from the blank: Z axis shows a relative height, not an absolute value, because of no reference points. Profile plot shown in section b) shows that the substrate is not

flat but rough with hills ranging from 0.5 nm to 2 nm, comparable with peptide length. Peptide and backfiller (Scheme 2-1, **2-1** and **2-2** respectively) length in an extended conformation were calculated to be around 1.1 nm and 0.8 nm respectively.

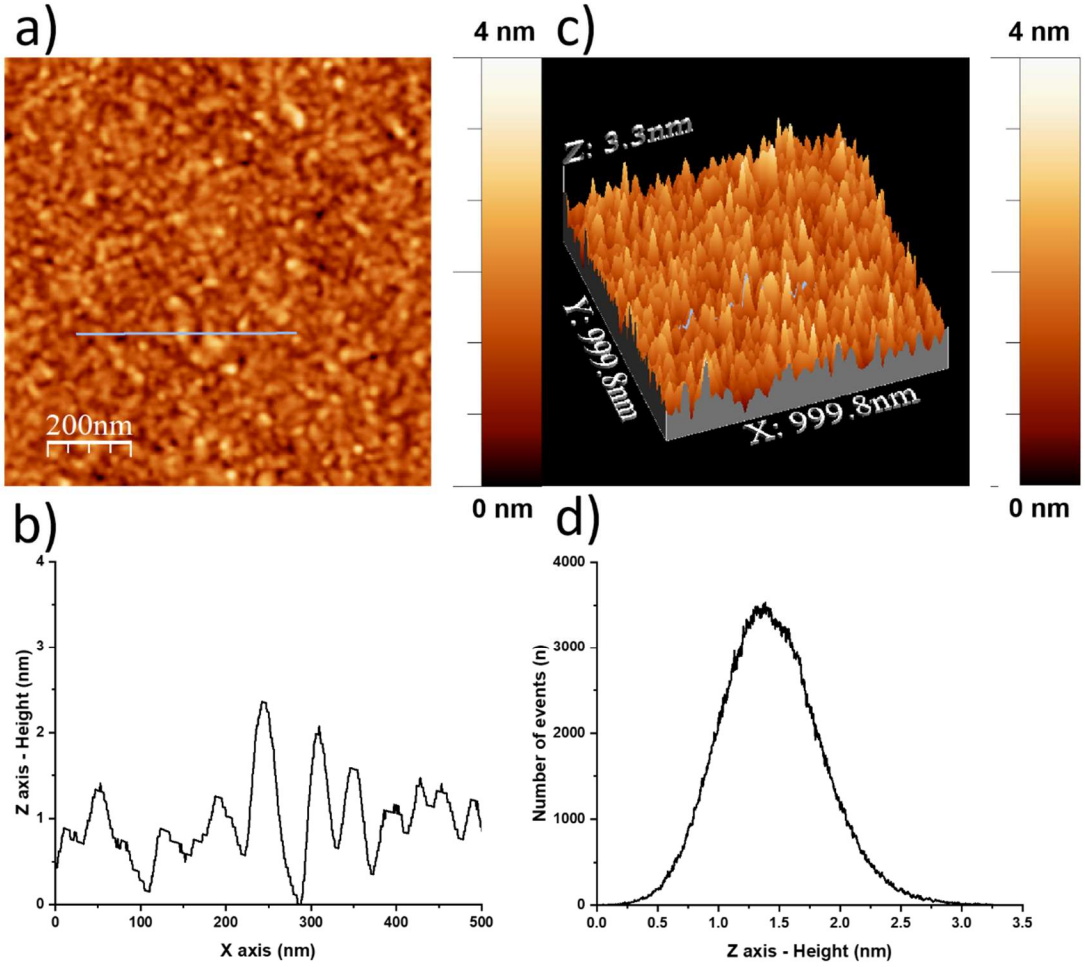

Figure 2-5 - AFM (air, tapping mode, 298 K) of clean Au-coated coverslip (Platypus). a) 1x1 μm^2 image, b) scanline profile, c) 3D rendering, d) average height plot.

Average roughness of the gold coverslip seemed to be of the same magnitude of the peptide length. One possible way to determine the absolute monolayer height could be etching the SAM with the tip in contact mode until the gold layer and then profiling the defect, however this experiment was not performed. As a third section c) the 3D rendering of the surface scan is shown. Colour scale is the same as the mapping a). The 3D scan reveals the intrinsic roughness of the bare coverslips, showing that the height of the asperities is comparable to the peptides. The last chart d) shows the average roughness found, which is around 1.5 nm.[16] Investigation on IPS10% and IPS90% mixed monolayers but also δIPS/PS·Au chemical gradient on coverslips are reported in the next sections.

2.5. AFM results on gold coverslips – isotropic mixed monolayers

IPS10% is a mixed monolayer of 10% molar ratio IPS peptide in 90% backfiller (Scheme 1-3, molecules **2-1** and **2-2** respectively, overnight immersion in a μM EtOH solution). Figure 2-6b shows a profile scanline with many aggregates identified as peptide bundles extending from the surrounding shorter backfiller. Adding 10% of peptide **2-1** in a monolayer enables the tailoring of SAM architecture, having the aggregates of longer molecules assembling with H-bonding interactions.

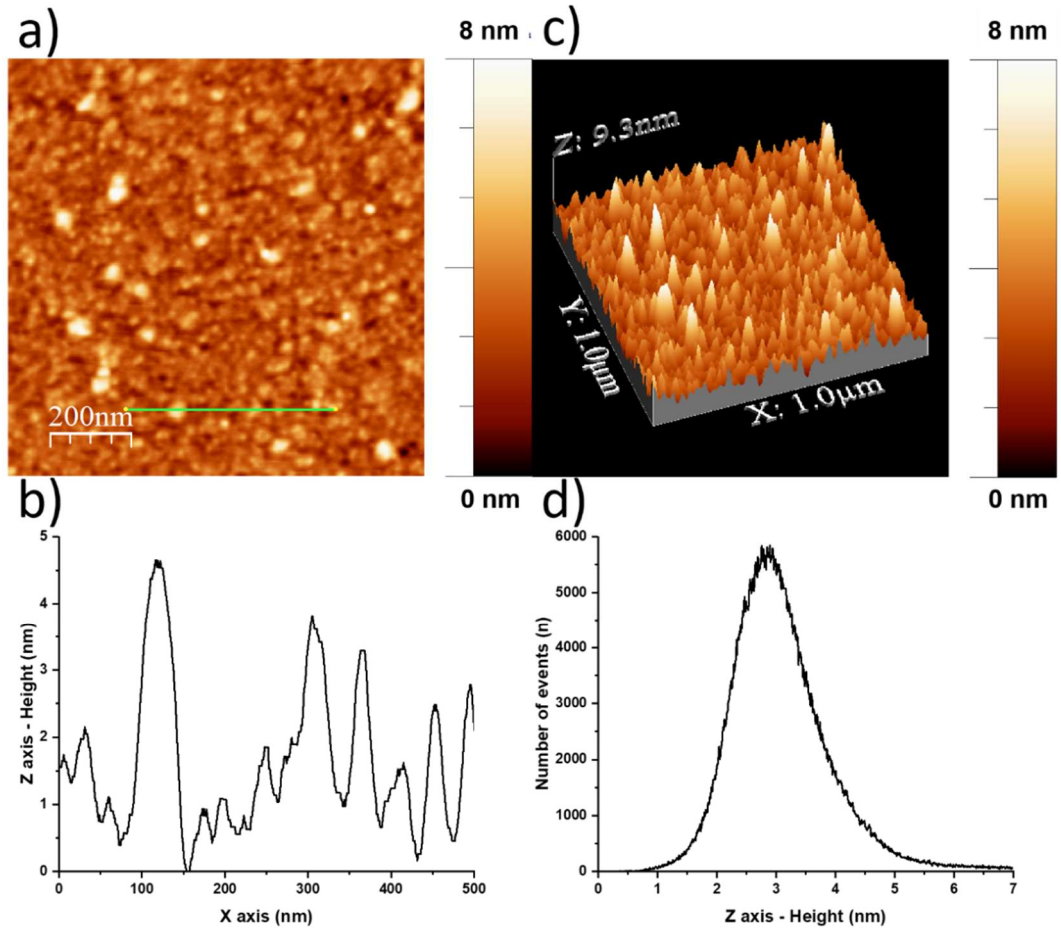

Figure 2-6 - AFM (air, tapping mode, 298 K) of IPS/PS·Au coverslip (Platypus). a) 1x1 μm^2 image, IPS10%, b) scanline profile, c) 3D rendering, d) Roughness analysis: average height plot.

IPS10% shows a relatively higher monolayer, compared to the bare gold. Relative height scale for the images is higher, up to 8 nm. 3D rendering shows clearly the presence of material on the substrate. Peptide bundles influenced the SAM architecture and its overall roughness that shifted up to 3 nm. Furthermore, hill diameter also

increased in size. The second isocratic SAM analysed was IPS90% with the opposite molar ratio of peptide and backfiller. The texture is thicker than IPS10% with a denser plot. Scanline shows shorter architectures with a more uniform monolayer. This is due to the higher percentage of peptide **2-1**. With a higher percentage of peptide, stabilisation occurs through all the monolayer, without the formation of higher and isolated bundles of peptides. 3D rendering of IPS90% shows a substrate that can be compared to the bare gold surface.

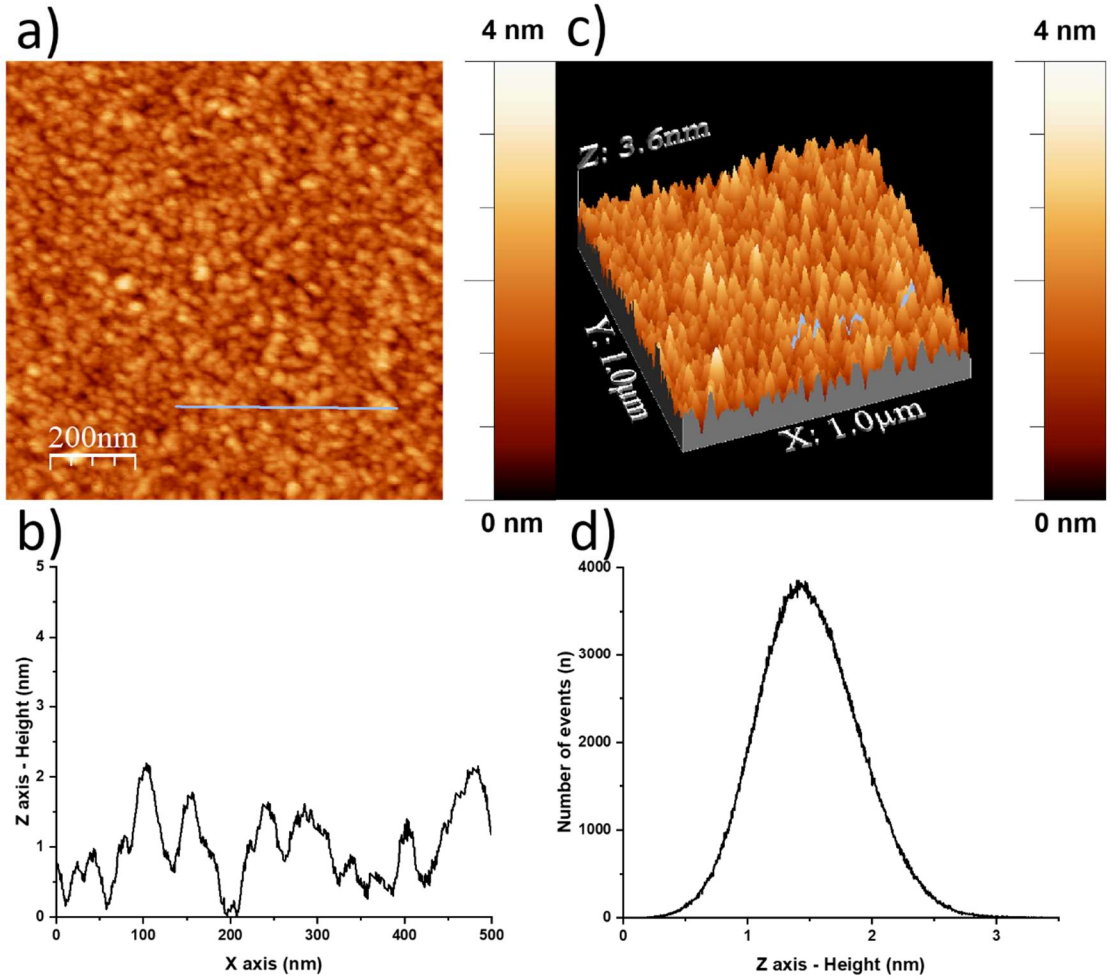

Figure 2-7 - AFM (air, tapping mode, 298 K) of δIPS/PS·Au coverslip (Platypus). a) 1x1 μm^2 image, IPS90%, b) scanline profile, c) 3D rendering, d) Roughness analysis: average height plot.

Peptide **2-1** covering 90% of the surface (assuming 100% adsorption) produced a "blanket effect" covering the layer underneath. Average roughness shown is around 1.5 nm. The lack of peptide bundles shifts down the roughness value for a more homogeneous SAM.

2.6. AFM results on gold coverslips – anisotropic monolayers

Regarding the δIPS/PS·Au anisotropic SAM shown in Fig. 2-8, AFM imaging shows a SAM similar to IPS90% (Fig. 2-7), if comparing abundance of surface asperities, hill height and distribution. Low-concentration region of the gradient is the surface part with a lower peptide percentage.

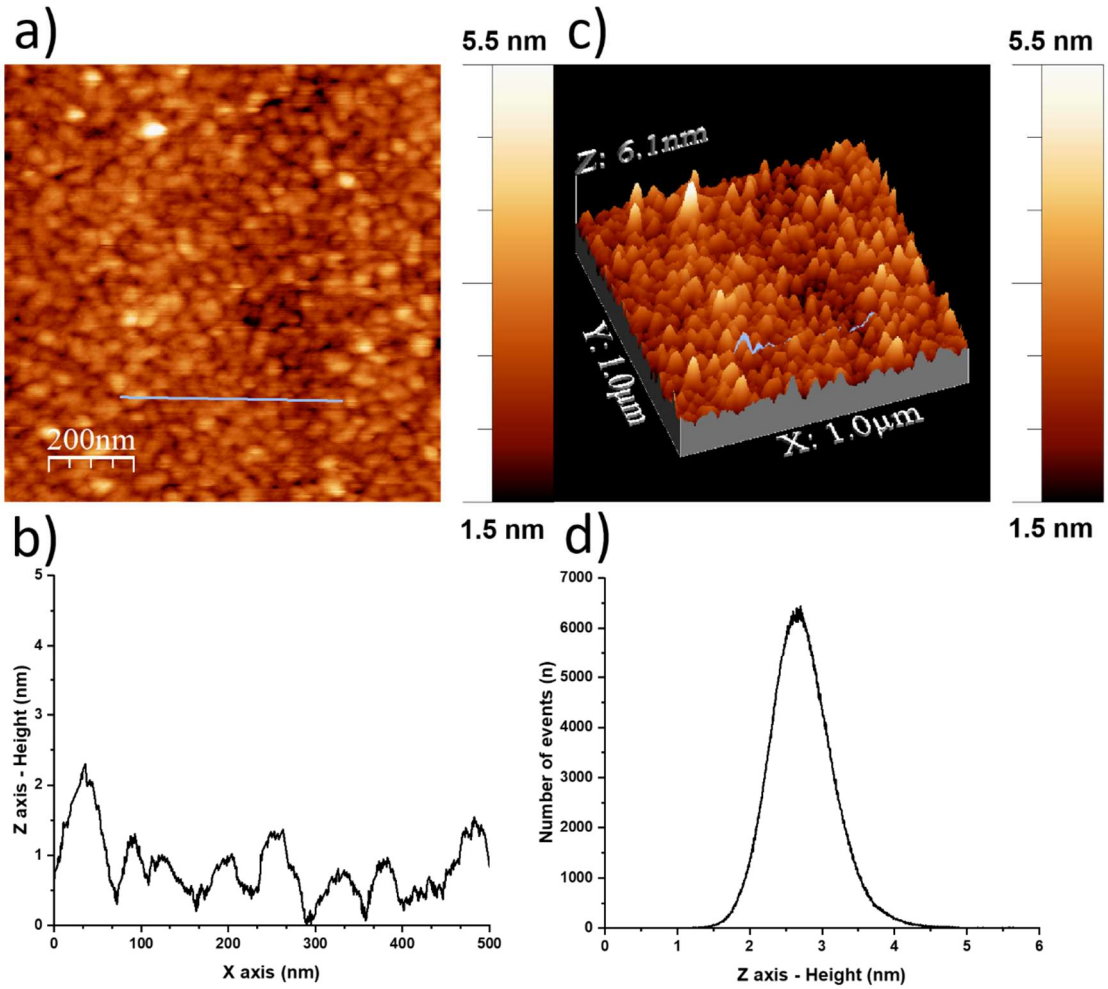

Figure 2-8 - AFM (air, tapping mode, 298 K) of δIPS/PS·Au coverslip (Platypus). a) 1x1 μm^2 image, low-concentration zone, b) scanline profile, c) 3D rendering, d) Roughness analysis: average height plot.

This is due to the shallow nature of the chemical gradient on surface, confirmed by XPS experiments shown later in this chapter. Surface scanline shows peaks and asperities within 1.3 nm of relative height, that can be attributed to peptides covering the existing substrate roughness. 3D rendering confirms the hypothesis of having a surface with similar features of IPS90%. Interestingly surface roughness is different from IPS90%, indicating a fair level of disorder and surface aggregates peaking at 3 nm as IPS10%. This indicates that not only the gradient is shallow, but peptide concentration is remarkably low, forming again bundles as seen in IPS10%.

Medium-concentration region of the gradient (Fig. 2-10) shows an intermediate situation, with a rather uniform monolayer without remarkable hills or aggregates with a length comparable to target molecules **2-1** and **2-2**.

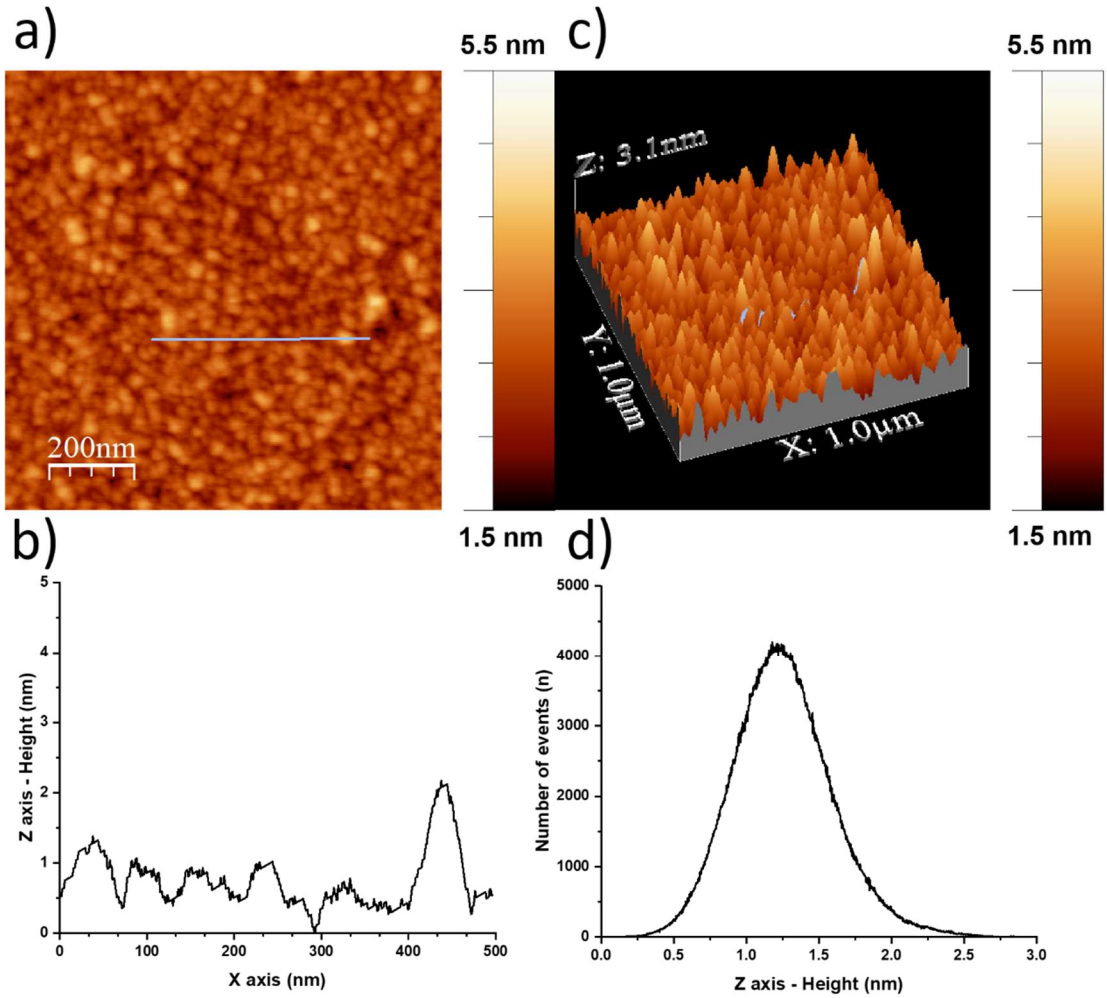

Figure 2-9 - AFM (air, tapping mode, 298 K) of δIPS/PS·Au coverslip (Platypus). a) 1x1 μm^2 image, medium-concentration zone, b) scanline profile, c) 3D rendering, d) Roughness analysis: average height plot.

Surface scanline is very regular, with asperities below 2 nm, as it was confirmed by the roughness plot d). Roughness value is below 1.5 nm showing a homogeneous monolayer. 3D rendering c) shown in the picture above confirms the fairly low abundance of IGDQ-bearing peptides for chemical readability of the motogenic sequence. As a last experiment, AFM of a high-concentration zone on a coverslip is reported below (Fig. 2-11). Surface scanline shows the presence of architectures as peptide aggregates with around 1 nm in relative height. Surface roughness decreased below 2 nm indicating a peculiar SAM condition. High-concentration zone seemed to have the characteristics of IPS10% when looking at the aggregates on surface, with an intermediate monolayer roughness. In the high-concentration region the aggregates

are larger than those found on IPS10% but peptide concentration is higher. Because of the increased peptide concentration, peptide bundles could interact with each other and stabilise in between themselves with intra-chain H-bonds for less protruding hills, but with enhanced stability.

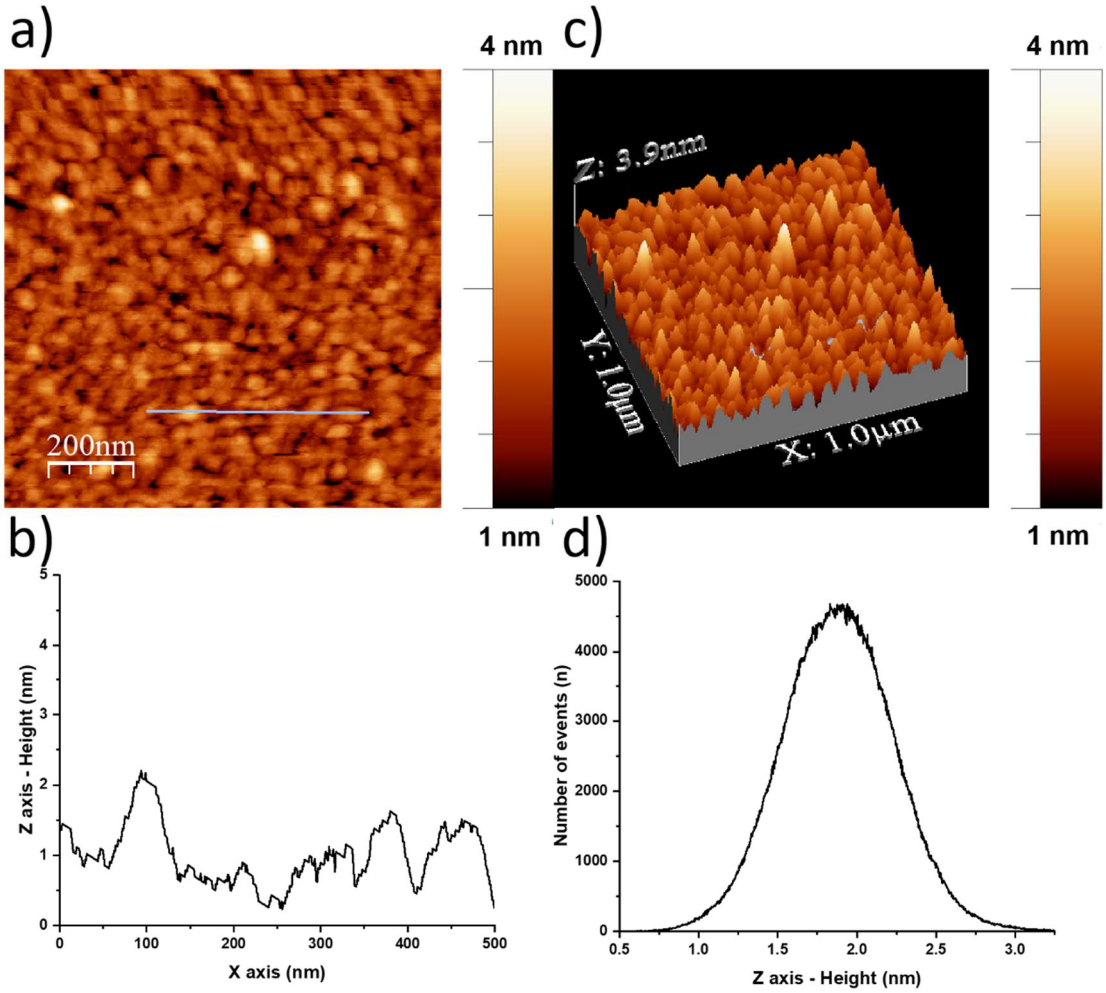

Figure 2-10 - AFM (air, tapping mode, 298 K) of δIPS/PS·Au coverslip (Platypus). a) 1x1 µm^2 image, high-concentration zone, b) scanline profile, c) 3D rendering, d) Roughness analysis: average height plot.

2.7. AFM results on ultra-flat gold chips – bare gold

AFM imaging on gold chips is shown in Fig. 2-11 with the same presentation style: blank gold, IPS10%, IPS90% and the anisotropic surface, with only low- and high-concentration region reported. In addition to the usual imaging provided, phase image is added to the characterisation. As previously reported, the phase plot indicates a deviation from the tips' oscillation, due to material with different mechanical properties. For such high-quality surfaces this could be very useful to detect peptide aggregates extending from the monolayer. Clean ultra-flat gold is very different from the coverslips

in almost every aspect. Profile scanline ranges around 0.5 nm, with gold islands surrounded by pits of about 3 nm. Surface roughness is influenced by the pits and is 3.5 nm. 2D imaging and 3D rendering shows very well the morphology of ultra-flat islands.

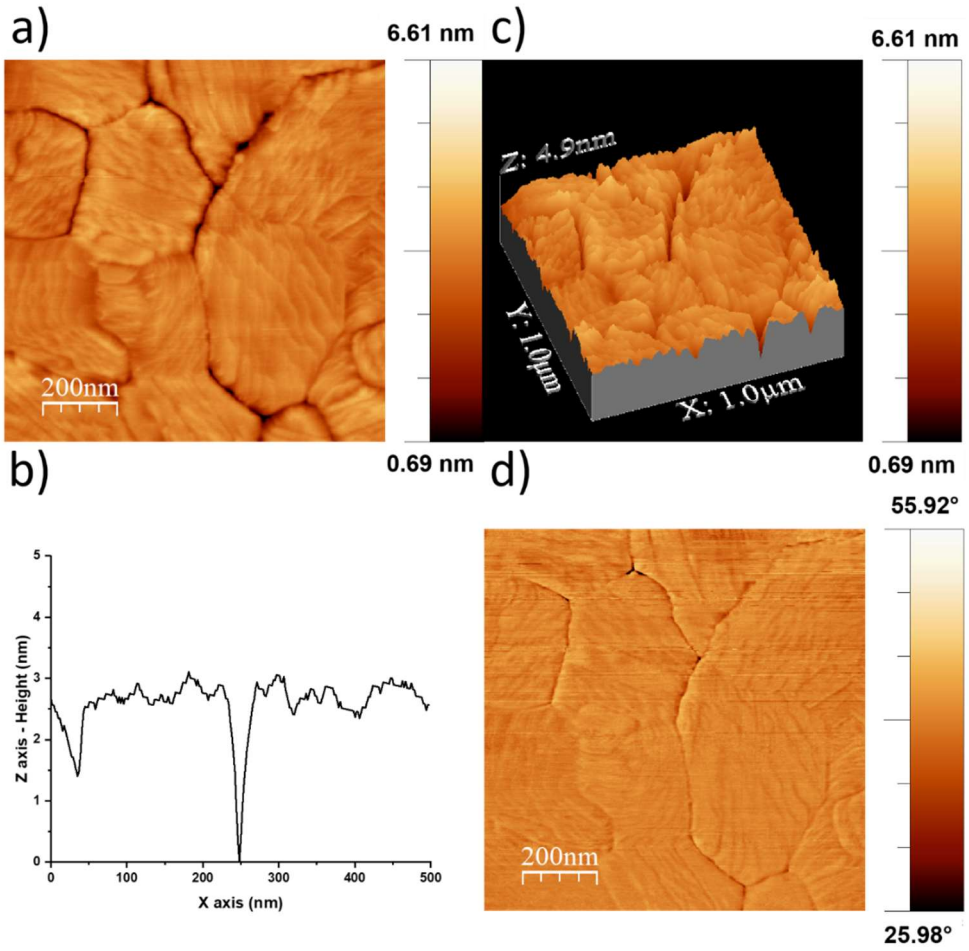

Figure 2-11 - AFM (air, tapping mode, 298 K) of a clean ultra-flat Au[111] (Platypus). a) 1x1 μm^2 image (flattened, horizontal offset subtracted in rows direction), b) scanline profile, c) 3D rendering, d) phase plot.

2.8. AFM results on ultra-flat gold chips – isotropic mixed monolayers

Concerning IPS10% on ultra-flat gold, it is possible to see peptide bundles already from the first image (Fig. 2-13a). 3D rendering shows the aggregates extending from the upper left part of the image. Surface scanline presents aggregates of around 1.5 nm of relative height, with an average roughness of 5 nm. This value is remarkably influenced by the pits in between the islands of gold and the aggregates on them. The phase shows the aggregates of a different colour, indicating that a different material is present on the surface. Peptide bundles extending from the surface are interacting more with

the AFM tip therefore a different signal is recorded. Concerning IPS90% on ultra-flat gold, roughness analysis is still influenced by the gold islands on surface, and its value reaches 4 nm.

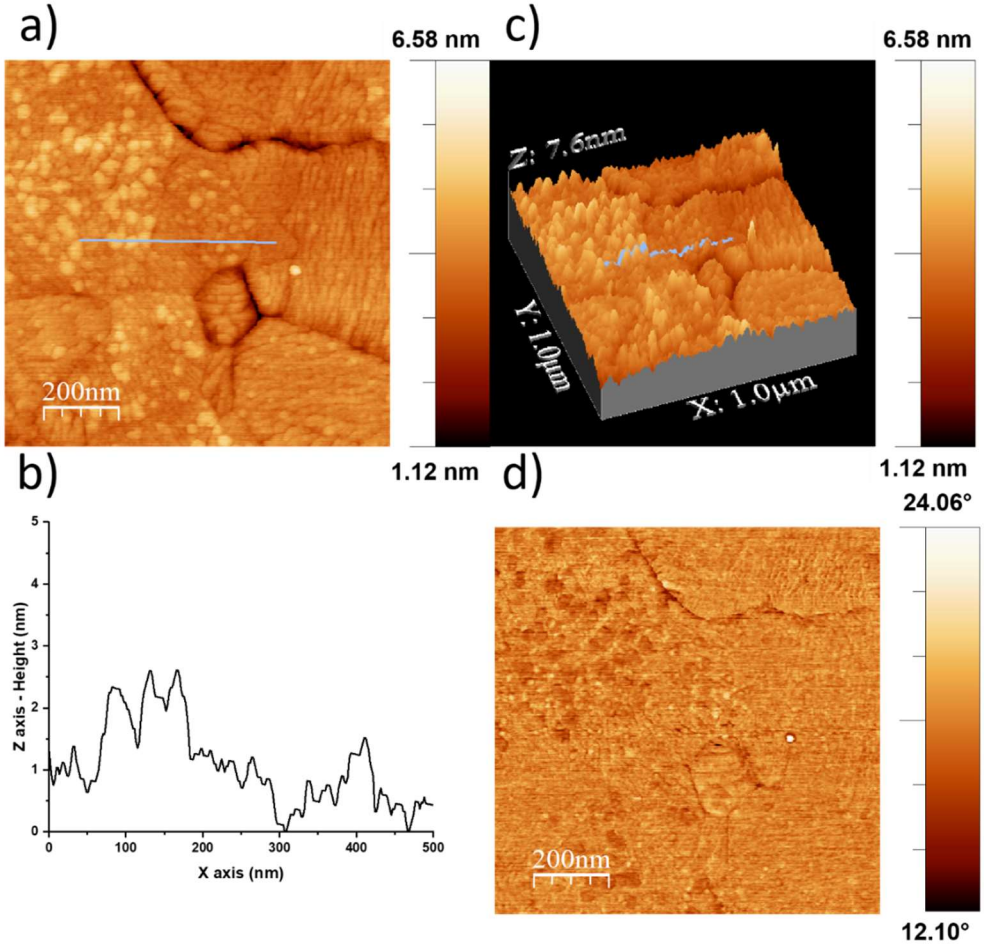

Figure 2-12 - AFM (air, tapping mode, 298 K) of IPS10% on ultra-flat Au[111] (Platypus). a) 2x2 μm^2 image (flattened, horizontal offset subtracted in rows direction), b) scanline profile, c) 3D rendering, d) phase plot.

Surface scanline shows pits of about 3 nm and a surface profile of about 0.5 nm. 2D and 3D rendering show a surface full of small aggregates and asperities, while the phase shows a very homogeneous monolayer in which the island pits are very distinct from the rest.

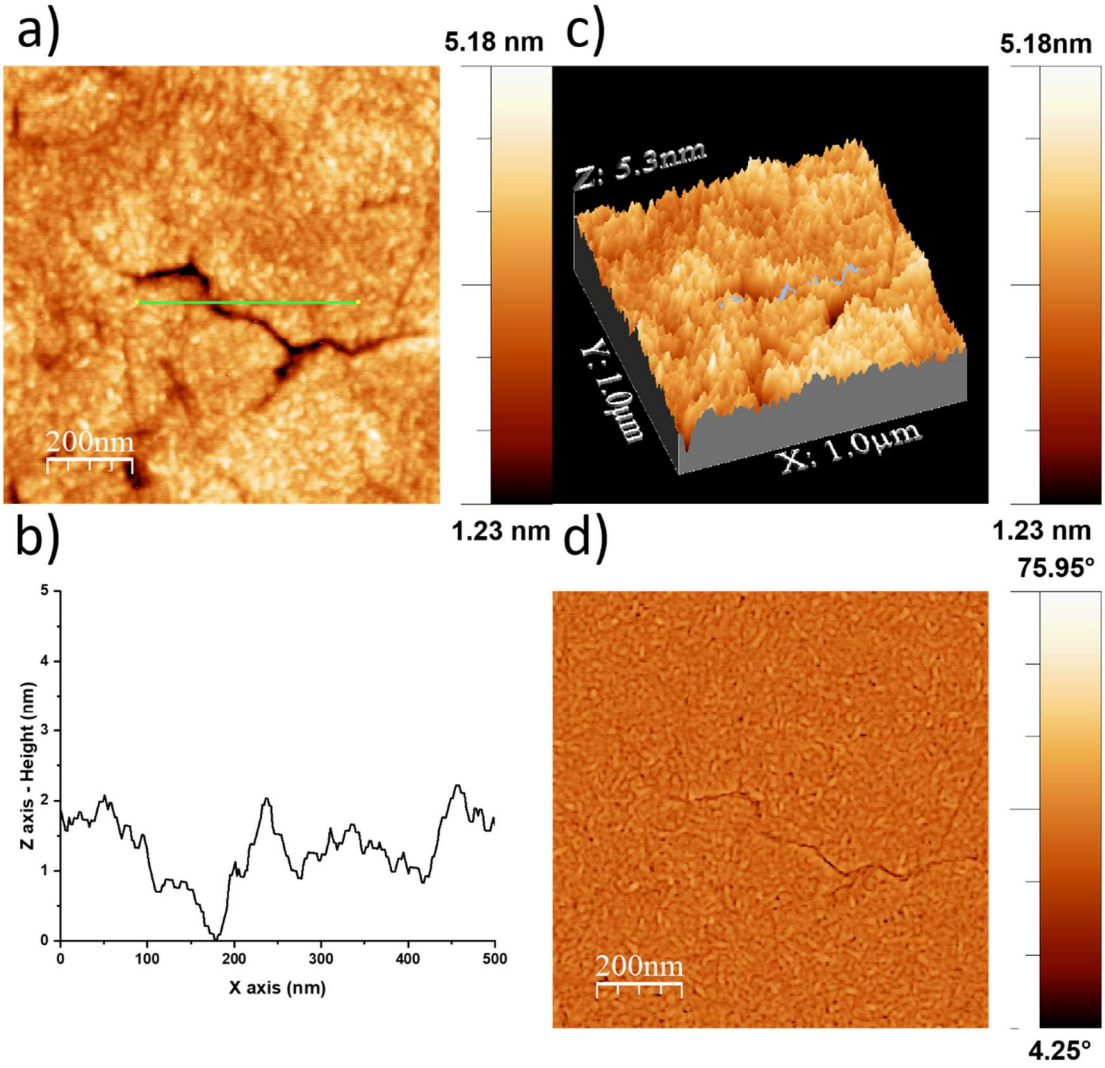

Figure 2-13 - AFM (air, tapping mode, 298 K) of IPS90% on ultra-flat Au[111] (Platypus). a) 2x2 μm^2 image (flattened, horizontal offset subtracted in rows direction), b) scanline profile, c) 3D rendering, d) phase plot.

Remarkably, a higher number of aggregates is seen on surface when the peptide concentration is increased, indicating that the peptide bundles aggregate in units that could stabilise with intra-chain H-bonds interactions. Increasing the peptide concentration does not produce more aggregates as seen in IPS10% but a more densely packed monolayer. The aggregates have a diameter of around 20 nm, indicating that multiple peptide bundles could be winded up together.

2.9. AFM results on ultra-flat gold chips – anisotropic monolayers

Concerning the low-concentration region on an ultra-flat chemical gradient of peptide **2-1**, the monolayer seems to resemble IPS90%. Monolayer is very homogeneous,

around 1 nm in relative height. The Phase plot (Fig. 2-15d) confirms the homogeneity of the monolayer.

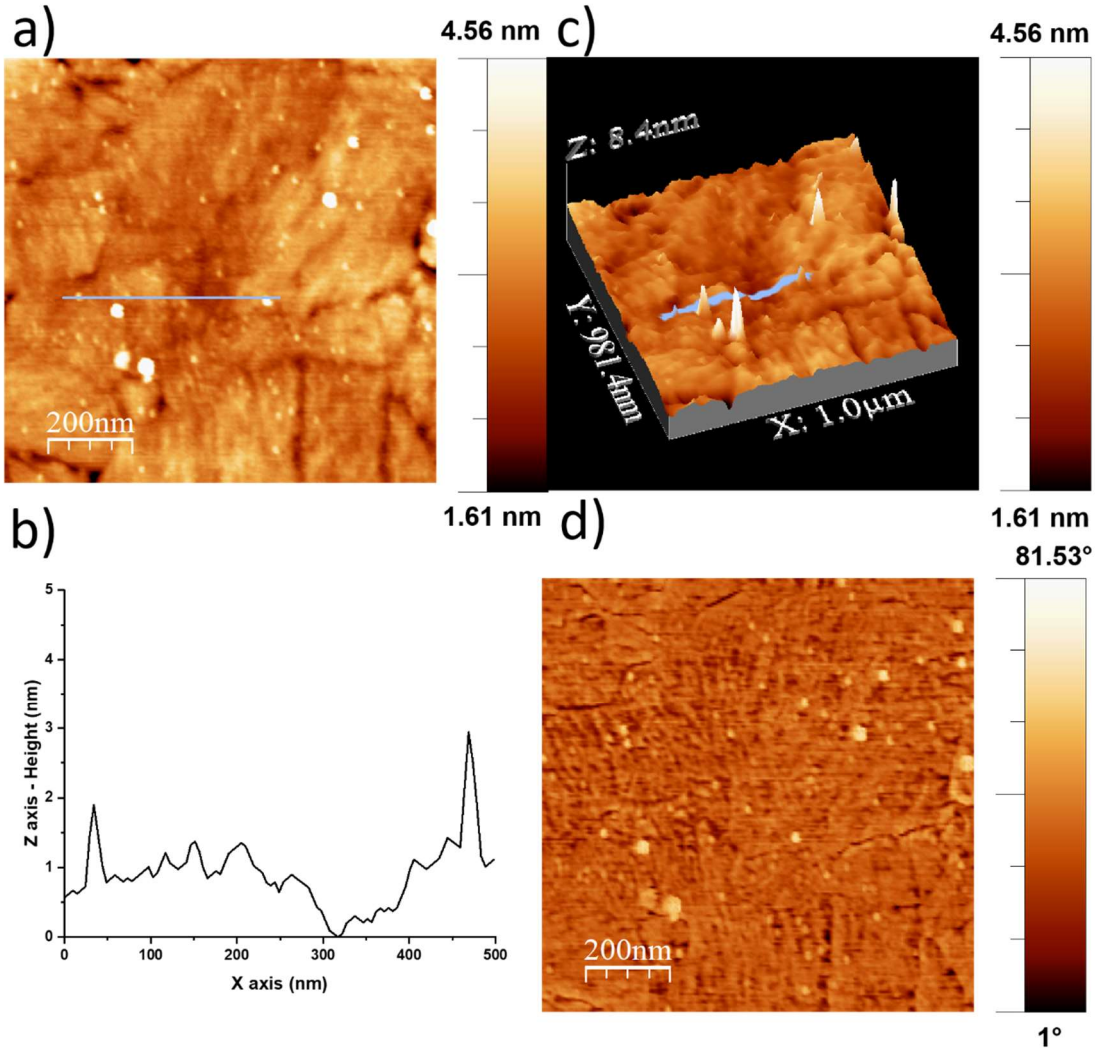

Figure 2-14 - AFM (air, tapping mode, 298 K) of δIPS/PS·Au on ultra-flat Au[111] (Platypus). a) 1x1 µm^2 image on a low-concentration zone (flattened, horizontal offset subtracted in rows direction), b) scanline profile, c) 3D rendering, d) phase plot.

2D and 3D rendering show a homogeneous monolayer with a few aggregates probably due to dust (white hills in 3D rendering c)). Surface roughness of the low-concentration region was found to be just below 4 nm, thanks to the ridges dividing the islands of gold. Interestingly the phase shows aggregates on the substrate, in darker colour.

After the low-concentration scan on ultra-flat gold, the high-concentration region was mapped. Sub-nanometric asperities can be seen over the gold islands, separated by very defined pits. 2D and 3D rendering show a remarkably flat surface, with no peculiar features except for the ridges. Surface roughness was found to be around 3 nm.

Surface scanline was very homogeneous with a profile of 0.5 nm. High-concentration gradient can be compared to IPS90% imaging, with an even smoother profile.

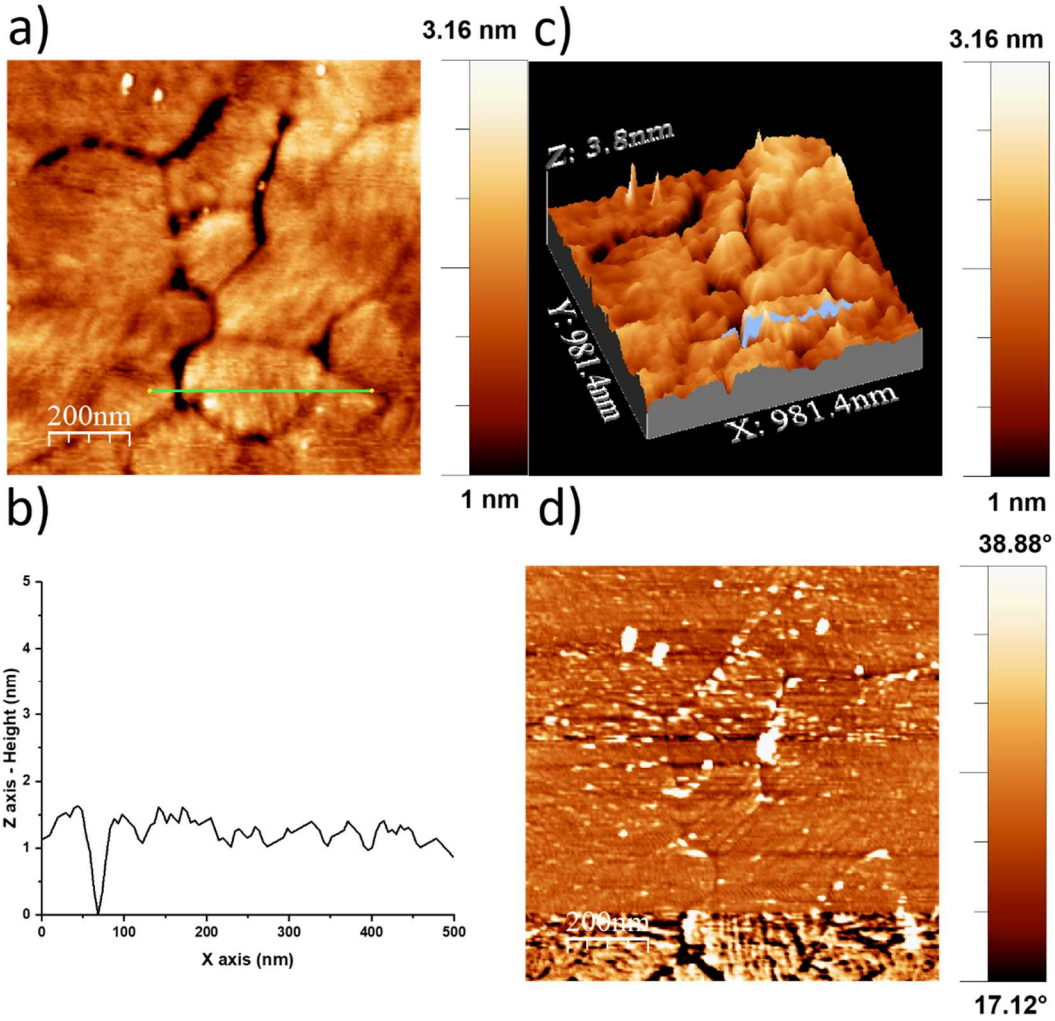

Figure 2-15 - AFM (air, tapping mode, 298 K) of δIPS/PS·Au on ultra-flat Au[111] (Platypus). a) 1x1 μm^2 image on a high-concentration zone (flattened, horizontal offset subtracted in rows direction), b) scanline profile, c) 3D rendering, d) phase plot.

The high-concentration region on an ultra-flat chip was zoomed from a 5x5 μm^2 image, in search for features and peculiarities of the SAM gradient. As a final image, a further processed collection of images of the high-concentration gradient is shown. With the aim of characterising the morphology of the IPS/PS·Au monolayer, zoom of the high gradient is reported. Sub-nanometric structures can be seen with an unfortunately high level of noise, as expected. Figure 2-16 reports the amplitude instead of height. Amplitude is a different parameter correlated to tip oscillation current and sometimes can give more details.

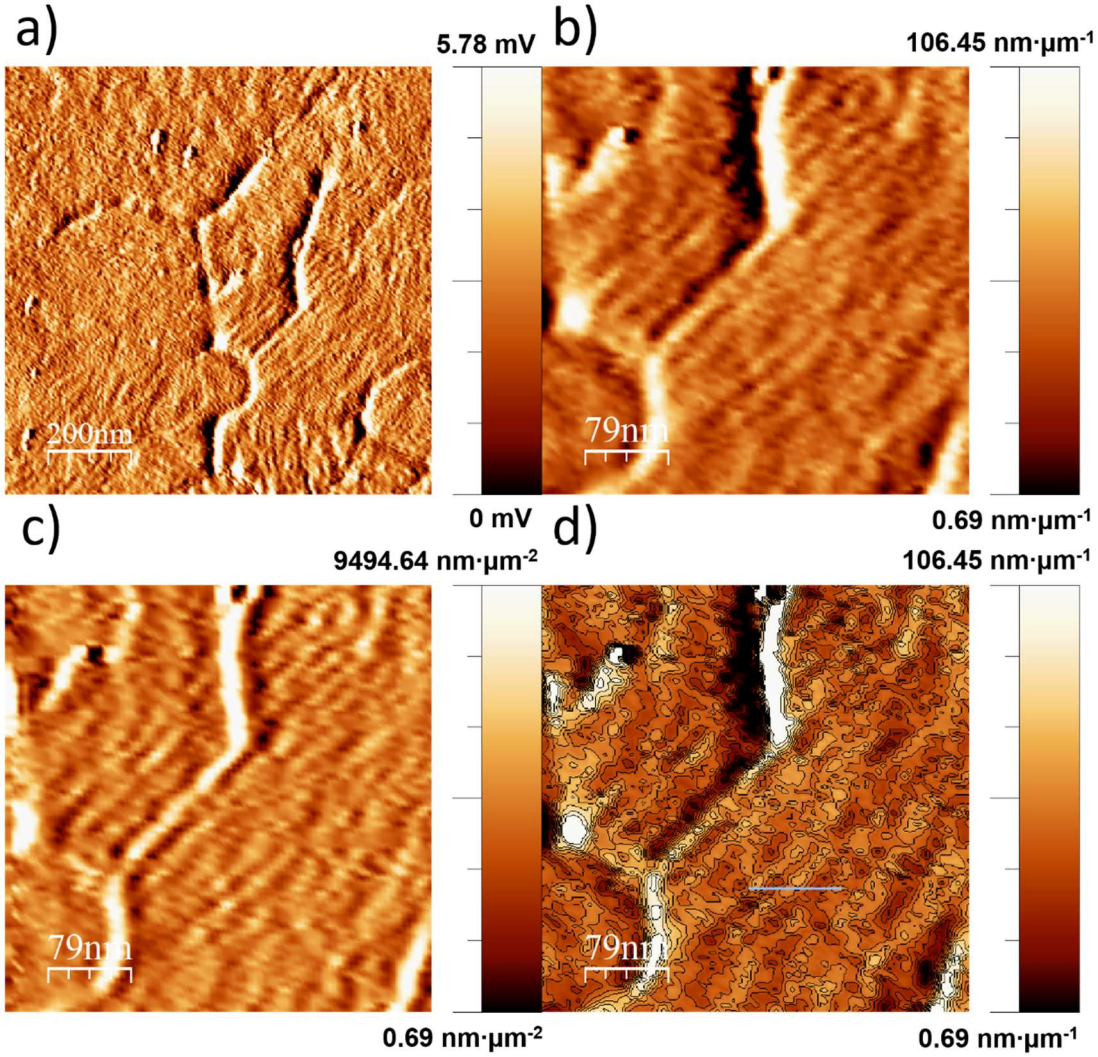

Figure 2-16 – AFM (air, tapping mode, 298 K) zoom from of δIPS/PS·Au on ultra-flat Au[111] (Platypus). a) 1x1 µm^2 Amplitude image on a high-concentration zone (flattened, horizontal offset subtracted in rows direction), b) zoom with smoothing, equalisation c) derivative and successive smoothing and flattening filter, d) contour plot.

Image a) has greater contrast and gold functionalisation can be seen. Zoom b) shows the edge of an island, but the corrugated material is seen with less contrast. Parallel trends are often tip artefacts or noise. By further processing, the mirror image in colour code has higher contrast and thiol architectures can be seen, without parallelism due to tip drift. Contour plot was added to show that peptide aggregates and hills are around 20 nm in diameter.

2.10. Theoretical simulation of the IGDQ-confined SAMs

The purpose of this work was to predict how the peptide would rearrange in aqueous medium exposing the 4 amino acids IGDQ that extend on top of the monolayer and trigger a biological response on MDA-MB-231 model cells plated over the anisotropic SAM. Two systems were simulated, with two peptides namely IPS and IS in solution and on surface, with H_2O and MeOH as solvents. Several experiments were performed

with 1, 2 or a set of 30 peptides in 7 lines simulating a surface anisotropic chemical gradient. Backfiller presence in the monolayer was also studied. The investigation was carried out aiming at finding intra-peptide interactions that could stabilise the system and ensure amino acid extension from the top of the monolayer. Conformational contributions of the amino acids were also taken into consideration. Simulation with and without the backfiller were carried out to probe monolayer packing strength and integrity. As a first step, peptide flexibility was evaluated calculating the Root Mean Squared Deviation (RMSD) of the Cα, N and C atoms of the backbone. Another important parameter considered was the Gyration radius G_R evaluating molecular flexibility in solution. H-bonds, the key feature for peptide readability were also estimated. Comparison between IPS and IS (Scheme 1-3, molecules **2-1** and **2-3** respectively) peptides was performed. IPS peptide tends to have a more compact conformation having a smaller G_R. IPS peptide seems to be locked in one conformation because of H-bond interactions. IS peptide seems to alternate between conformations and together such findings corroborate the experimental results that found no biological activity of the IS peptide. As a consequence, the more compact conformation of IPS compared to IS ensures higher peptide readability that is then reflected on its biological activity. After peptide simulation in solution, H_2O and MeOH solvents were introduced in the algorithm. MeOH solvent results will not be reported as the biological medium for cell culturing is H_2O. Single peptide simulations will not be reported and only more complex systems (30 peptides arranged in 7 rows) will be discussed. Interestingly, despite the longer structure of molecule **2-1** compared to **2-3**, the former has still the most rigid structure. Peptide structure on surface was found to be tilted and not flat, especially in H_2O. This conformation is favoured by inter- and intra-chain H-bonds. Conversely, the collapsed conformation of IS recalls a low degree of surface organisation, in agreement with the wettability results found for δIS·Au. Another important parameter calculated was the Solvent Accessible Surface Area (SASA). The SASA profile was assessed for 3 simulated structures describing the exposed peptide. SASA profile calculated for IS peptide decrases over time because of its flatter conformation aquired over time. Such findings seem to corroborate the poor motogenic activity of **2-3** peptide. SASA results are also explained by interchain H-bonds that favour a packed conformation with little solvent access to the monolayer. It also shows a predominance of H-bonds over Van der Waals (VdW) interactions that influence the overall SAM architecture

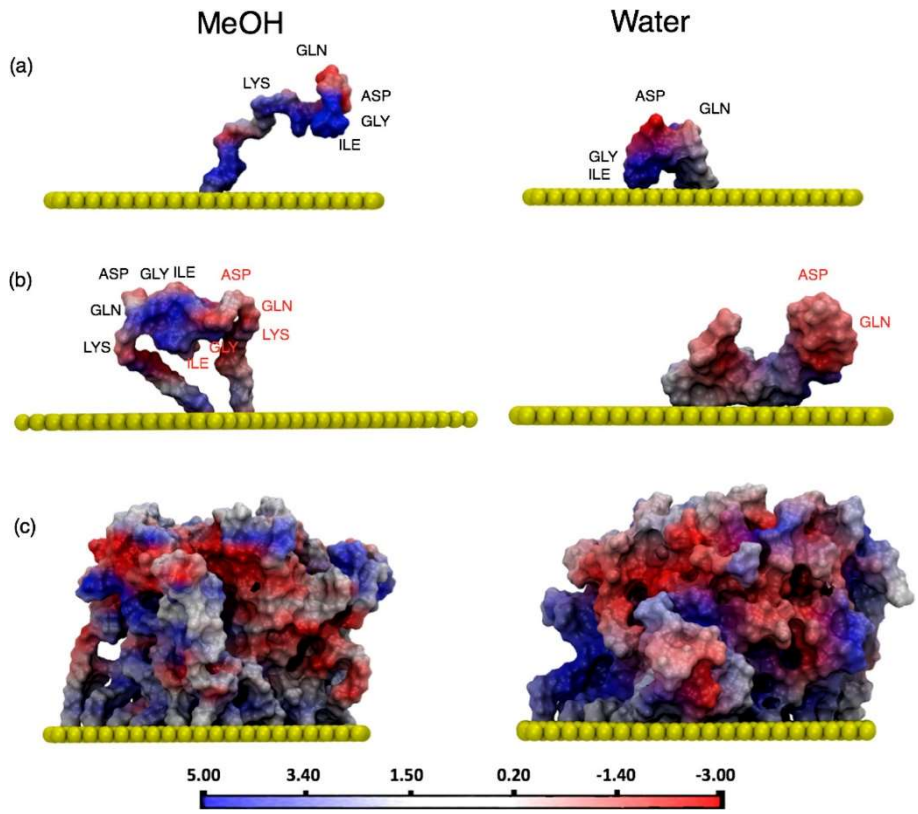

Figure 2-17 - Front view of the electrostatic surface potential plotted on the last snapshot of the 1- (a), 2- (b), and ∂IPS·Au (c) MD simulations in MeOH (left column) and water (right column). The scale bar at the bottom is also reported. The aa residues within the peptide structure are labelled with their symbol names, namely isoleucine (Ile), glycine (Gly), aspartic acid (Asp), glutamine (Gln), and Lysine (Lys).

Electrostatic surface potential (ESP) in both MeOH and H_2O shows that the adsorbed peptides on surface seem to point hydrophilic amino acids towards the solvent. Conversely, hydrophobic residues seem to point to the gold substrate. In addition to these findings, Molecular Dynamics (MD) were also performed by Dr. De Leo to explore the behaviour of chemisorbed peptides on gold substrates. Even in this last MD simulation shown (Fig. 2-19), when complexity is added to the system, polar amino acids are pointing out from the monolayer. In conclusion, G_R, SASA and ESP parameters were calculated for different model systems simulated and peptide **2-1** was found to have more H-bonding interactions that could maintain the same conformation and statistically have a better exposition towards the top of the monolayer.

The second finding revealed how fillers (molecule **2-2**, Scheme 1-3) structurally sustain the monolayer. In the backfilled SAM, face-to-face H-bonds play a central role for peptide readability.

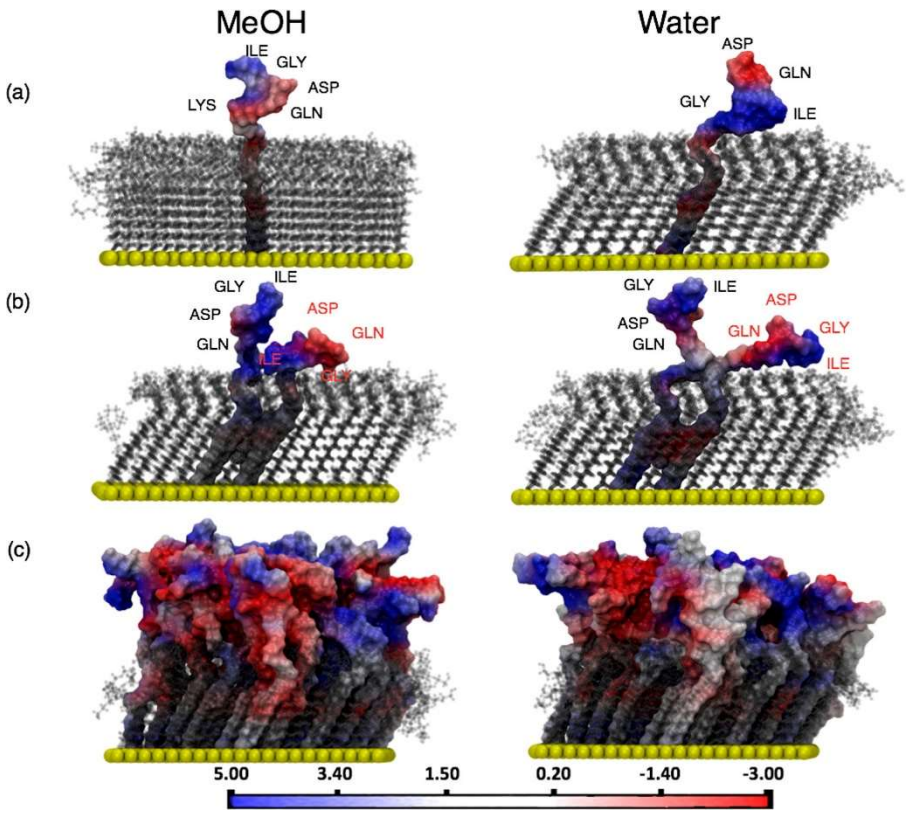

Figure 2-18 - Front view of electrostatic surface potential plotted on the last snapshot of the 1- (a), 2- (b), and ∂IPS/PS·Au (c) MD simulations in MeOH (left column) and water (right column). The scale bar at the bottom is also reported. The aa residues within the peptide structure are labeled with their symbol names: isoleucine (Ile), glycine (Gly), aspartic acid (Asp), glutamine (Gln), and lysine (Lys).

Furthermore, the anchoring points of H-bonds help the peptide extending itself from the monolayer. Since the actual peptide conformation when in contact with the cellular transmembrane receptor is not known so far, Radial Distribution Function (RDF) studies were then performed. RDFs express a measure of the H_2O-peptide interactions as a measure of the sequence exposition to the solvent. Peptide **2-1** has a greater RDF trend compared to molecule **2-3**. In conclusion, the *in-silico* studies gave as outcome the important role of H-bonds for peptide stabilisation. The backfilling process contributes remarkably to IGDQ sequence readability. All the other peptide properties such as gyration radius, SASA and electrostatic surface potential corroborate the hydrophilic amino acid exposition from the monolayer, enabling peptide exposition to the solvent.

2.11. X-Ray Photoelectron Spectroscopy of anisotropic gold surfaces

X-Ray photoelectron spectroscopy (XPS) is a semi-quantitative characterisation technique that employs X-rays to scan materials.[17] XPS together with WCA and AFM is a technique that is included in the bundle of surface characterisation protocol. Photoelectrons are emitted from an irradiated sample and are collected at the detector, therefore a spectrum is generated.

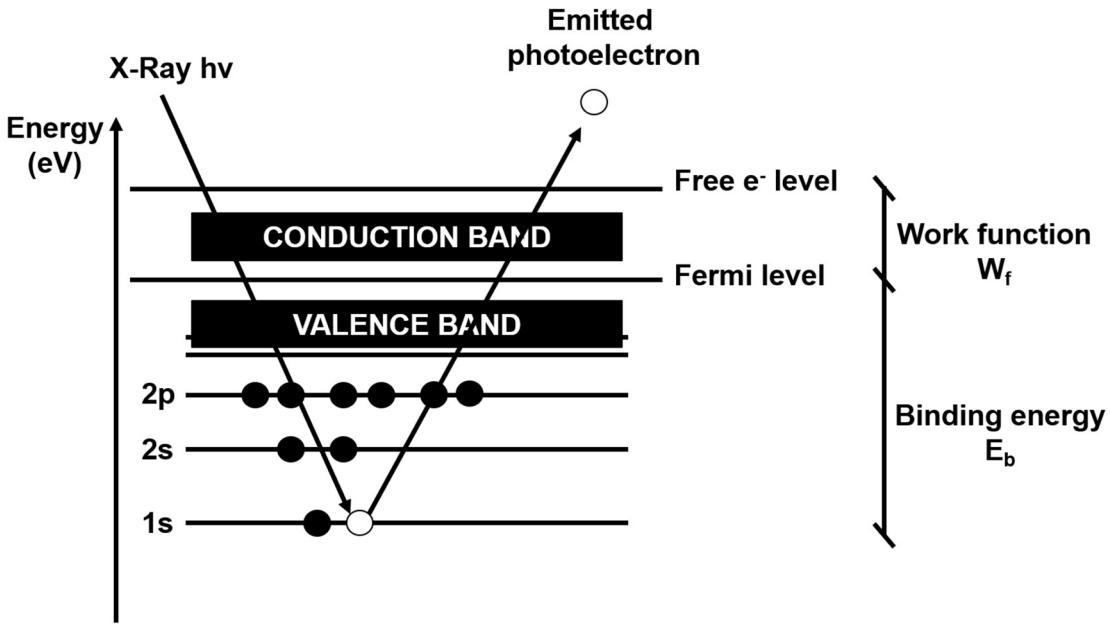

$$h\nu = Eb + Eki_n + Wf$$

Figure 2-19 - Schematic of the principle of XPS A typical XPS spectrum is a plot of the number of electrons detected. Figure adapted from Baruwati PhD Thesis 2007.[18]

Binding energy contributes to the total photoelectron energy, together with the work function and the photoelectron's kinetic energy. The work function is the minimum energy needed to extract one electron from a surface, under vacuum conditions. Photoelectron energies involved are around 1.2-1.5 keV and every photoelectron has a characteristic binding energy, that can be correlated to an element or compound. Chemical shifts of the core electrons are characteristic of the irradiated elements and their relative abundance can be detected. To map our model surfaces, a variable number of scan points were set along the anisotropic functionalisation axis. Such points were set at equal distance from each other, avoiding the edges, because of the possible damage caused by tweezers while handling the surfaces. Scan points at the extremities of the surfaces were strategically placed on the glass, as a control reference that would give zero Au4f signal. Multiple acquisitions (15 to 50) on the same point gave the same

outcome without any difference in intensity, leading to the conclusion that no desorption or photocleavage caused by the beam was occurring. Scanned elements for this chapter were Carbon C1s, Nitrogen N1s, Oxygen O1s, Gold Au4f and Sulphur S2p and the same colour code is reported throughout this thesis. Specifically, carbon C1s was represented in black squares, nitrogen N1s in blue circles, oxygen O1s red triangles, sulphur S2p yellow triangles, Au4f dark-yellow triangles, respectively. In addition to those already mentioned, Iron $Fe2p^3/_2$ and Fluorine F1s were also monitored for the proof of concept of the double chemical gradient and results are reported in the next chapter.

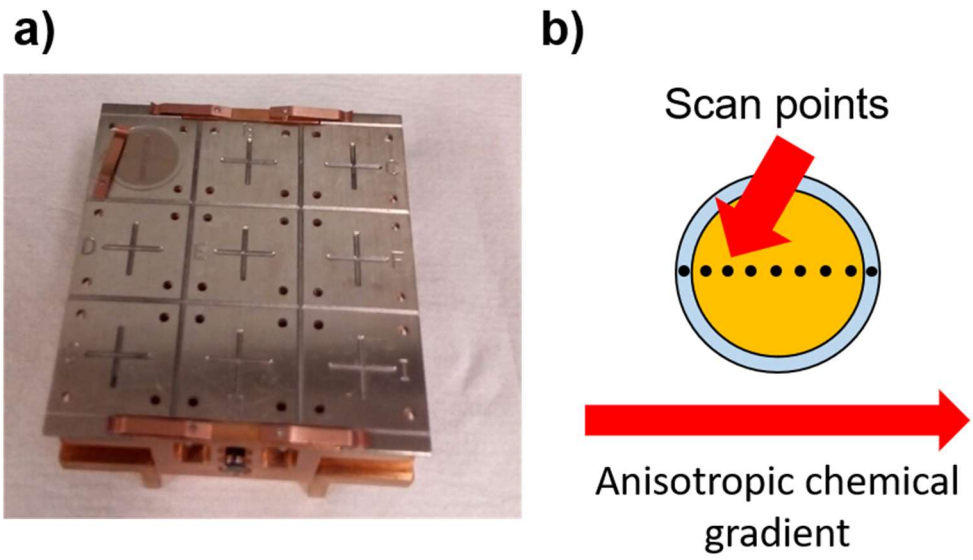

Figure 2-20 – a) XPS sample holder with a clipped round coverslip; b) scan point representation on an anisotropic gold coverslip.

Iron $Fe2p^3/_2$ At% XPS signals were represented in grey, while F1s in olive green. As a standard procedure, surfaces fabricated with the two-step immersion protocol were clamped onto the XPS sample holder (Fig. 2-21), placed in the chamber and vacuum was applied. Grid points were set starting the measurement from the low-gradient point to the highest. This surface mapping technique was used to map round coverslips and ultra-flat gold chips.[6] Spectra normalisation was performed using the Au4f signal (atomic percentage At%) corresponding to that specific scan point. Cross-section (CS) normalisation was also performed. The cross section represents the probability of a particle (photoelectron in this case) to be emitted from the sample. The first surface mapping experiment reported in Fig. 2-21a below was taken from the previously mentioned paper, representing the anisotropic gradient characterisation performed on gold coverslips.[6] The chemical gradient of the anisotropic functionalisation is can be seen in the three charts, from left to right (Fig. 2-21). Carbon C1s, oxygen O1s and

nitrogen N1s show a trend on increasing At% along the gradient direction, from left to right. Carbon content was up to 90% while oxygen and nitrogen were about 40% and 20%, respectively. Sulphur S2p showed a constant trend along the monolayer with around 10% of At%.

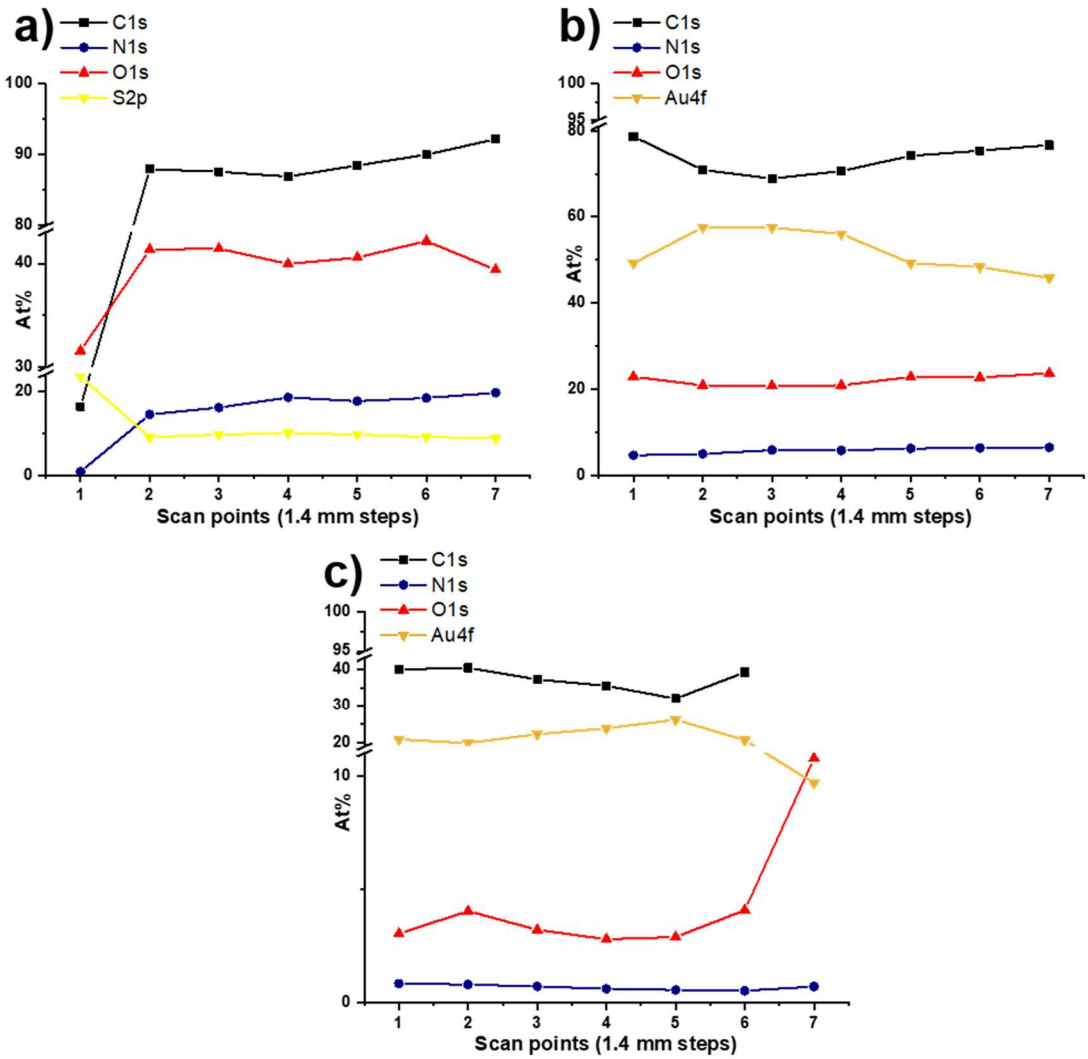

Figure 2-21 – XPS mappings on gold-coated surfaces. Colour code: carbon C1s black squares, nitrogen N1s blue circles, oxygen O1s red triangles, sulphur S2p yellow, gold Au4f dark yellow. a) Position-dependent chemical composition of δIPS/PS·Au on gold coverslip: b) Position-dependent chemical composition of δIPS/PS·Au on gold coverslip. c) Position-dependent chemical composition of δIPS/PS·Au on ultra-flat chip.

This reference experiment was then repeated on another set of coverslips and one representative result is shown in Fig. 2-21. Surprisingly when routinely analysing the gold Au4f At% it was found that this element was not constant along the gradient. This result was obtained with a different XPS facility (same instrument) and was attributed to the different detector settings. Carbon C1s content for chart b) 10% lower than the first reference experiment a). Oxygen O1s for b) content was half of the first one around 20% and nitrogen N1s below 10% of At%. Concerning the duplicate of the reference

experiment shown in Fig. 2-21b, the adsorption rates are remarkably low however a shallow gradient is present. As a third anisotropic gold surface characterisation, ultra-flat chips were mapped. Results of one XPS mapping of a chip are shown in Fig. 2-21c. Surprisingly adsorption was found to be even lower than the two reference experiments a) and b). This result was attributed to the higher substrate quality that could not carry the same rate of contaminants or dust. Ultra-flat gold layer with extremely flat isles could have also played an important role. Edges and asperities of the lower-quality counterpart seemed to have enhanced the adsorption rates of peptides, while this did not occur for the ultra-flat chips, resulting in a lower functionalisation. Carbon C1s content was found to be around 40% with 5% oxygen O1s content and 2% of nitrogen N1s content. Interestingly a shallow concentration gradient of carbon C1s and oxygen O1s was found, with a reverse trend for gold Au4f as in the previous surface Fig. 2-21b. The monodirectional gradient shown in three representative experiments was found to be shallow with Carbon C1s At% from 80% to 90% on coverslips, while just 40% on ultra-flat chip, due to the difference in substrate quality. Nitrogen N1s At% was found to be around 20% or less as a pivotal element indicating the presence of only peptide **2-1** (or IPS) on surface, and not being present in the backfiller. Oxygen O1s was present in peptide **2-1** and backfiller **2-2** but a shallow gradient was however observed for the three experiments a), b) and c).

2.12. Conclusions

Rationalising from the first paragraphs, wettability experiments showed that anisotropic peptide gradients of peptide **2-1** are very shallow and not well-packed. This lack of defined peptide architecture is the cause for such wettability results and high ARCA-WCA.

Regarding the AFM studies, peptide gradient presents aggregates in the low-concentration region of both ultra-flat chips and coverslips, indicating the presence of peptide bundles protruding from the monolayer. High-concentration region showed less aggregates and a smoother monolayer. This indicates that this type of SAM with a two-step immersion protocol has a remarkable disordered architecture. Peptide aggregates on surface seen on isotropic IPS10% did not depend the dipping time but the concentration. It can be concluded that the right peptide readability is set through a fine balance between the ideal peptide concentration and the corresponding stabilisation interactions. Increasing the peptide concentration results in a more densely packed monolayer that is however without a periodic and precise structure. Starting from the low concentration region, ideal conditions meet because of the favourable SAM

architecture promoting a sufficient peptide exposition towards the monolayer, enabling cell readability, triggering movement response.

XPS investigation showed the shallow nature of the gradients that is, however, not crucial for peptide readability, because of the higher sensing capacity of the model cells employed for this study.

The theoretical simulation corroborated the hypothesis of peptide bundles exposing the motogenic amino acids from the monolayer, thanks to the electrostatic surface potential comparison between different peptides, solvents and monolayers. Simulations showed that polar amino acids in water have more conformational freedom, monitored through several parameters such as gyration radius and SASA. Results showed that hydrophilic residues are more exposed to the solvent when simulating with water. This is due to the inter-chain stabilisation that the system undergoes, with H-bonding interactions between the peptide bundles. Another important finding was that simulation of peptide **2-3** led to the outcome that it possessed higher conformational freedom. Because of this fact, no motogenic activity was found for this peptide, also because of its hydrophilicity and not ideal length. Radial Distribution Function RDF was calculated, to determine that IGDQ sequence was more exposed to the solvent for peptide **2-1** rather than **2-3**. Furthermore, the investigation revealed the crucial role of the backfiller, packing the monolayer up, playing a central role in peptide readability, with lower alkyl chain VdW interactions and upper H-bonds.

In conclusion, a comprehensive morphology study over our ECM-mimicking substrates was performed. These results provide the link from surface science up to cell-monolayer interface. From the material science perspective, the reason behind the motogenic activity of ECM-mimicking SAMs was unravelled, however IGDQ mechanism of action remains undisclosed. Thanks to the disordered nature of the SAMs fabricated by the two-step immersion protocol, the motogenic activity is conferred through peptide aggregates in the low-concentration region. This region is the seeding bay for the cell culture, that is therefore in direct contact with the readable motogenic sequences extending from the monolayer. This granted success in the ECM-controlling experiment of single cell migration over a biocompatible substrate.

2.13. Bibliography

[1] R. J. Good, *J. Adhes. Sci. Technol.* **1992**, *6*, 1269–1302.

[2] C. D. Bain, G. M. Whitesides, *J. Am. Chem. Soc.* **1989**, *111*, 7155–7164.

[3] Y. Si, Z. Guo, *Nanoscale* **2015**, *7*, 5922–5946.

[4] Y. Arima, H. Iwata, *Biomaterials* **2007**, *28*, 3074–3082.

[5] V. Corvaglia, R. Marega, F. De Leo, C. Michiels, D. Bonifazi, *Small* **2016**, *12*, 321–329.

[6] F. De Leo, R. Marega, V. Corvaglia, R. Tondo, M. Lo Cicero, S. Silvestrini, D. Bonifazi, *Langmuir* **2017**, *33*, 7512–7528.

[7] S. Morgenthaler, S. Lee, S. Zürcher, N. D. Spencer, *Langmuir* **2003**, *19*, 10459–10462.

[8] S. Kalinin, A. Gruverman, *Scanning Probe Microscopy*, **2007**.

[9] P. K. Hansma, V. B. Elings, O. Marti, C. E. Bracker, *Science* **1988**, *242*, 209–216.

[10] R. Möller, A. Csáki, J. M. Köhler, W. Fritzsche, **2000**, *28*, 1–5.

[11] S. P. Microscopy, *Scanning Probe Microscopy Electrical and Electromechanical Phenomena at the Nanoscale*, **2007**.

[12] F. J. Rubio-Sierra, W. M. Heckl, R. W. Stark, *Adv. Eng. Mater.* **2005**, *7*, 193–196.

[13] O. Custance, R. Perez, S. Morita, *Nat. Nanotechnol.* **2009**, *4*, 803–810.

[14] L. Abelmann, in *Encycl. Spectrosc. Spectrom.*, **2016**.

[15] W. Melitz, J. Shen, A. C. Kummel, S. Lee, *Surf. Sci. Rep.* **2011**, *66*, 1–27.

[16] I. Horcas, R. Fernández, J. M. Gómez-Rodríguez, J. Colchero, J. Gómez-Herrero, A. M. Baro, *Rev. Sci. Instrum.* **2007**, *78*, 013705.

[17] P. S. Bagus, E. S. Ilton, C. J. Nelin, *Surf. Sci. Rep.* **2013**, *68*, 273–304.

[18] B. Baruwati, PhD Thesis, **2019**.

3. Double chemical gradients on gold surfaces

This chapter discusses the design and production of two orthogonal anisotropic gradients of photolabile peptides on gold-coated surfaces. The aim of this chapter is to produce a reliable biocompatible platform that could host cancer cell cultures and instruct cell movement along preferred directions. The system was designed to be responsive to light and change the anisotropic patterns upon irradiation. After the characterisation, photocleavage testing experiments in solution are presented and discussed. Paragraphs from 3.1 to 3.5 deal with the design and the peptide synthesis of probe peptides on solid phase. Paragraph 3.6 deals with the characterisation of the double gradient on surface via XPS. After the production of the double gradient with the probe peptides, paragraphs 3.7 and 3.8 introduce the synthesis of novel photolabile linkers and peptides. From paragraph 3.9 results from XPS characterisation of the double gradient with the photolabile peptides are presented. From paragraph 3.10 photolabile linkers and peptides are irradiated and their photocleavage is monitored, both in solution and on surface. WCA and XPS techniques are used to characterise the surface irradiation of photolabile monolayers. As a last experiment, double gradient of photolabile peptides is irradiated and results are discussed. Experiments were monitored with different techniques such as UV-Vis, RP-HPLC and LC-MS at Cardiff University. XPS characterisation shown in this chapter was performed with the precious help of Dr. Alexander Felten at the Université de Namur and at Cardiff University by Dr. Matteo Lo Cicero. Surface irradiation was first performed in Cardiff University, but afterwards was moved at Université de Namur thanks to Mr. Antoine Fattaccioli and Ms. Sophie Ayama under the supervision of Prof. Carine Michiels.

3.1. Designing a novel system for a two-stage cell movement

After accomplishing the spatio-temporal control on longitudinal chemical gradients of IGDQ-bearing peptides[1,2], a novel design inspired by the same technology was tackled.[3] In a tissue or organ, a multitude of chemical messengers flow through bloodstream and are also secreted to the extracellular matrix (ECM) for a fine-tuning of cellular activity. The goal of this project is to study cancer cell migration with an in-vitro substrate that resembles as much as possible the complexity that can be found in Nature. For this reason, a double gradient of motogenic peptides was designed and produced on a gold-coated surface. This novel design was produced to mimic the ECM

with two different chemical clues triggering a biological cascade of events that in the end generates cancer cell movement.

As a better and more accurate in-vitro model, this system was tailored to support the complete characterisation of cell migration in all its aspects, from imaging to cell sorting. Specifically, our design exploits the motogenic peptides containing the biologically active[4] IsoLeucine-Glycine-Aspartic Acid and Glutamine (IGDQ) motif (Scheme 3-1) in a system that aims for a stage-controlled cellular movement.

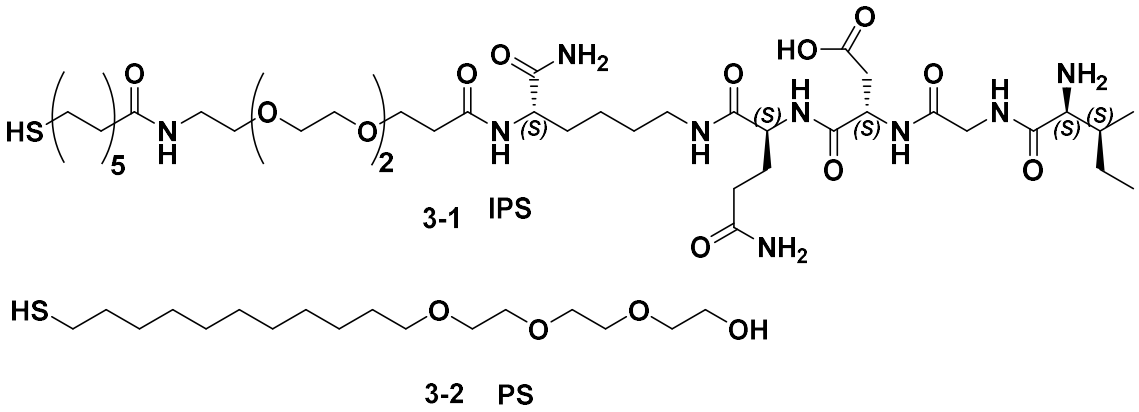

Scheme 3-1 – Motogenic peptide **3-1** or IPS and its backfiller **3-2** or PS.

Cell movement in two directions potentially requires two peptides and the same IGDQ-bearing sequence can be used along two different directions. Because of the different peptide structure chosen, the same sequence can be used for two movements without interference. Our strategy employs two photolabile linkers: the first one masking the other, enabling the first migration. At the end of the first movement, irradiation would cleave the first motogenic sequence uncaging the second one, for the second stage migration. The movement was designed to be in two different directions, typically 90° so the single cells are easier to detect and recognise with microscopy techniques. The use of photolabile groups enabled surface modification without the addition of any chemical reagent to the monolayer, preventing any toxicity issues to the cells. Moreover, two suitable photolabile linkers were specifically designed for such system. The peptides for the double gradient system will be chemically tethered with two photolabile groups using the same coupling technology employed for the other amino acids. Furthermore, a strict requirement dictates that surface irradiation should not damage the cell culture. For this reason, far-UV irradiation was provided with 350 nm to 365 nm wavelength range. As shown in the picture above (Scheme 3-1), the double gradient fabricated on surface is made by two IGDQ-bearing peptides that are tethered with two different photolabile linkers (blue and red cartoons) from left to right and vice versa respectively. One photolabile linker (blue cartoon) is placed prior to the IGDQ sequence, and the other (red cartoon) stands on top of the sequence, masking the

motogenic sequence. After the first migration along the exposed IGDQ-bearing peptide, irradiation and subsequent peptide cleavage is shown, removing the first gradient and exposing the second one, ready for the second migration. A system with such specifics for bio-processability and bio-compatibility results in a more complex ECM-mimicking substrate, suitable for a more in-depth cancer cell imaging throughout all its stages from adhesion to migration.

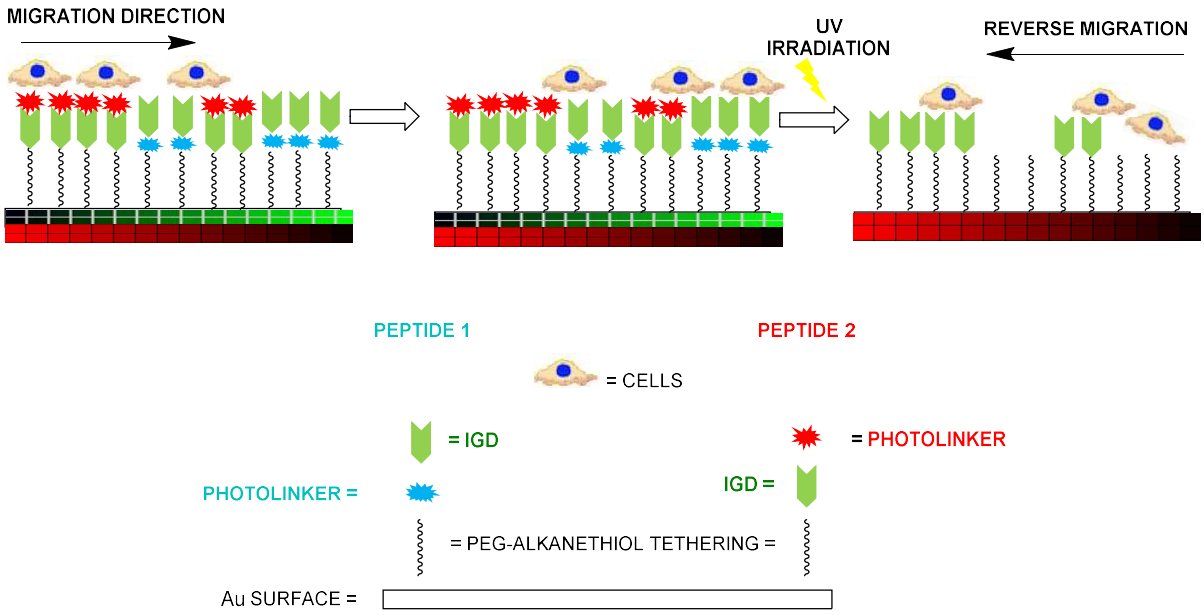

Figure 3-1 - Cartoon of the two-step cell migration on a double gradient of photolabile peptides.

3.2. Double gradient production – a three-step dipping process

Concerning the double gradient system, two different peptides and the same backfiller were employed. This novel strategy is inspired from the work of Beuer[3] and co-workers, having an orthogonal double gradient system with two different thiols on the same Au surface. A schematic representation of the chemical gradient patterning on surface is shown in Fig. 3-2. The double gradient is in fact the result of the production of two orthogonal gradients on a surface. The chemical gradients are represented by the two hypotenuses lying orthogonally to each other over the disc, the latter representing the gold-coated glass coverslip. As shown in picture Fig. 3-2, this three-step immersion consists of two gradual dippings into two different thiolated solutions. After the first dipping, a 90° twist is required so that the second gradient is orthogonal to the first. As the last step, full immersion in backfiller **3-2** solution (Scheme 3-2) is performed. Concerning the dipping times for the monodirectional gradient, 15' dipping at 17 $\mu m \cdot s^{-1}$ and 10' of full immersion were the optimum. Regarding the double gradient,

the dipping was faster to avoid early surface saturation and peptide displacement. Three conditions were screened: 10' dipping for both peptides at 25 $\mu m \cdot s^{-1}$ and 7' at 36 $\mu m \cdot s^{-1}$ that turned out to be the optimal speed for an even double gradient, thanks to the packing effect of the backfiller. Gradient optimisation was performed with two probe peptides made specifically for such task. Peptide synthesis introduction is covered in the following paragraphs, starting from the standardised synthesis of the probe peptides to the procedures for the photolabile ones.

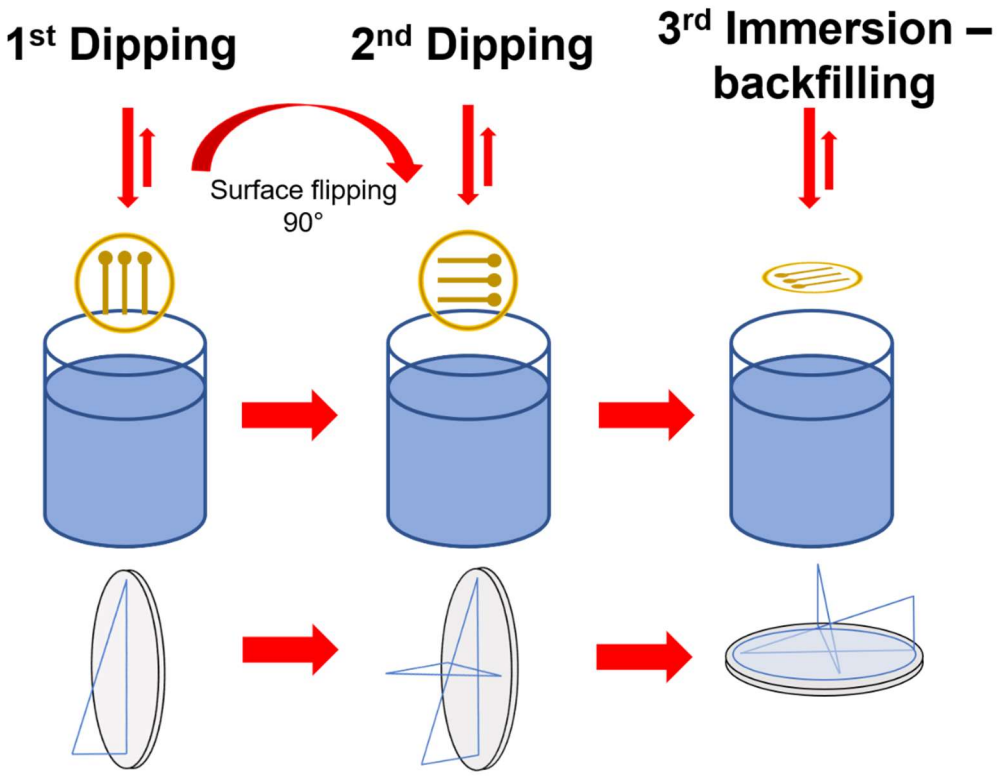

Figure 3-2 - Three-step immersion protocol for the production of double anisotropic gradients on gold surfaces.

3.3. Peptides for the double concentration gradient on surface

Before the production of the double gradients with photolabile peptides, two additional peptides were first synthesised as a proof of concept. The probe peptides designed for the production of the double-gradient on surface are shown below (see structures **3-5** and **3-6** in Scheme 3-2). Such peptides are not photolabile. Both peptides have the same IGDQ motogenic sequence, but the different head groups make them unequivocally distinct for XPS mapping, since two different elements were monitored. IPS-Fc has a carboxy-Ferrocene bound as amide to the Iso-Leucine amino group, and

in the same fashion, IPS-F respectively has a pentafluoroethyl benzoic acid (Scheme 3-2). Probe peptides were synthesised using pre-optimised solid-phase synthesis technique. Regarding the photolabile peptides, the structure is drawn in the same scheme as above. Both peptides share the nitrobenzyl group (see box, peptide **3-3** and **3-4**). Nitrobenzyl linker was very popular as a photolabile group for solid phase peptide synthesis (SPPS) and was very appealing for this project because of the possibility of being included in our automated protocols.[5–8] Peptide **3-3** with the exposed IGDQ sequence was designed to provide the first migration, meanwhile the second **3-4** was "caged". After the first migration to occur, surface irradiation would cleave the former exposed peptide **3-3** and uncage the latter **3-4**, triggering the second movement response.

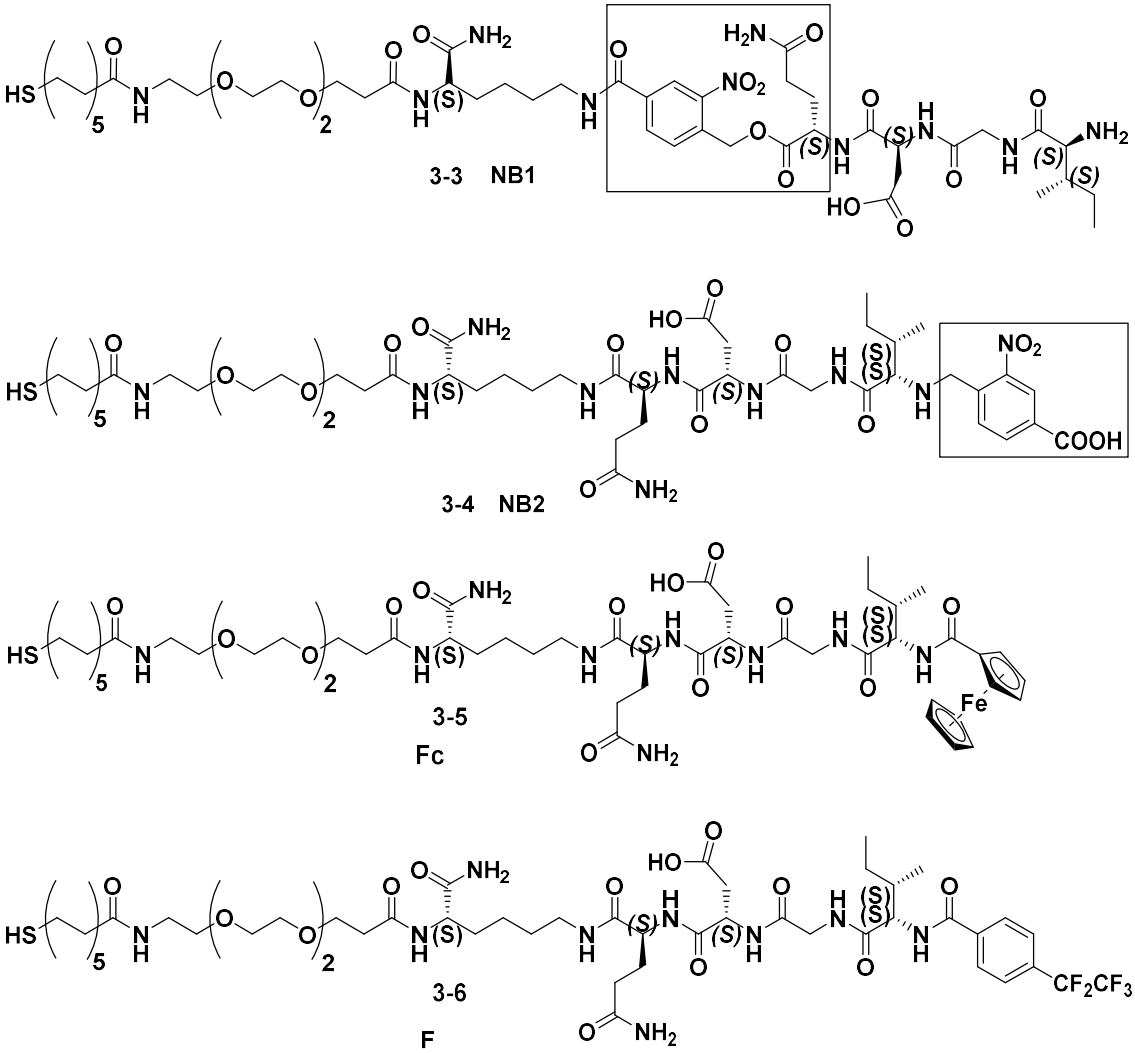

Scheme 3-2 - Photolabile peptides for the orthogonal cell movement. Photolabile groups are highlighted in each structure.

3.4. Nomenclature for the double concentration gradients

A conventional labelling method for gold surfaces was established taking inspiration from the first part of this project.[9] Double anisotropic gradients of peptides **3-5** and **3-6** (Scheme 3-2) shown later in this chapter are labelled as δFc/F/PS·Au whether there was a backfilling step, or simply δFc/F·Au with a specific dipping time in the caption. The twin experiment with the inverted dipping order of peptides was labelled as δF/Fc·Au and δF/Fc/PS·Au respectively. Surface flipping when coating peptides **3-5** and **3-6** was 180° while later in this chapter it was lowered to just 90° for peptides **3-20** and **3-26** as shown in Scheme 1-3. Double anisotropic gradients of peptides **3-20** and **3-26** are reported later in this chapter. Nomenclature was established as δNVOC1/NVOC2/PS·Au for the double gradient of peptide **3-20** and **3-26**, respectively. The twin experiment with the same peptides but with an inverted dipping order was labelled as δNVOC2/NVOC1/PS·Au or in short δ2/1/PS·Au. The isocratic mixed SAMs of peptides **3-20** and **3-26** were labelled as NVOC1/NVOC2 with a default molar ratio of 1:1. Isocratic single-component SAM of nitrobenzyl-bearing peptide **3-3** was labelled NB1-100%.

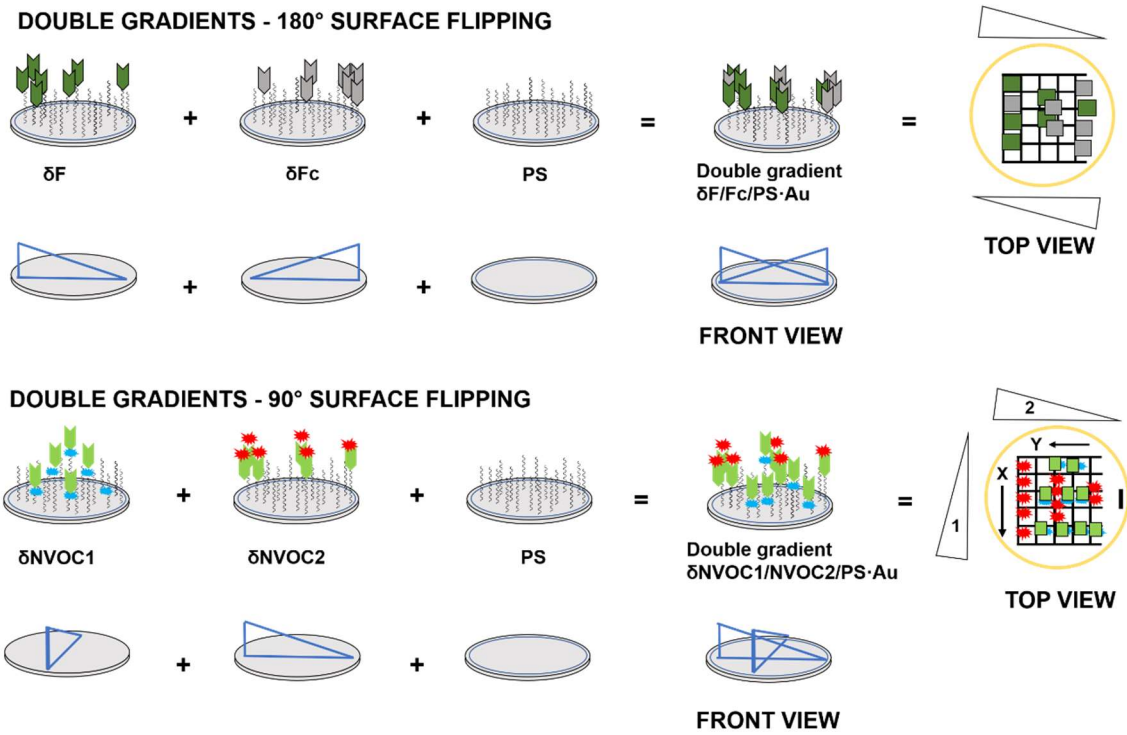

Scheme 3-3 – TOP: double gradients of peptides **3-5** and **3-6**, construction scheme. Colour code: peptide **3-5** grey tips, peptide **3-6** olive green; BOTTOM: green tip = IGDQ-bearing peptide **3-20**; red tip = peptide **3-26** (Scheme 3-14).

3.5. Solid-phase peptide synthesis (SPPS)

The strategy for peptide synthesis was inspired from the work previously done on this project[1] and employs the use of Fmoc-protected Rink amide methyl benzhydryl (MBHA) resin for peptide chain growth with Fmoc-protected L-amino acids via HATU-activated ester intermediate in the presence of diisopropylethylamide (DIEA) as a base. Several types of resins are shown in the scheme above (Scheme 3-4). Resin types can be divided into three categories namely poly-ethylene glycol (PEG) resins, polystyrene (PS) and PS-functionalised resins (crosslinked). Each category has several advantages and disadvantages towards peptide synthesis, solvent compatibility and swelling. Boc/Benzyl peptide syntheses require harsher cleavage conditions with HF and trifluoromethanesulphonic acid that were avoided.[10]

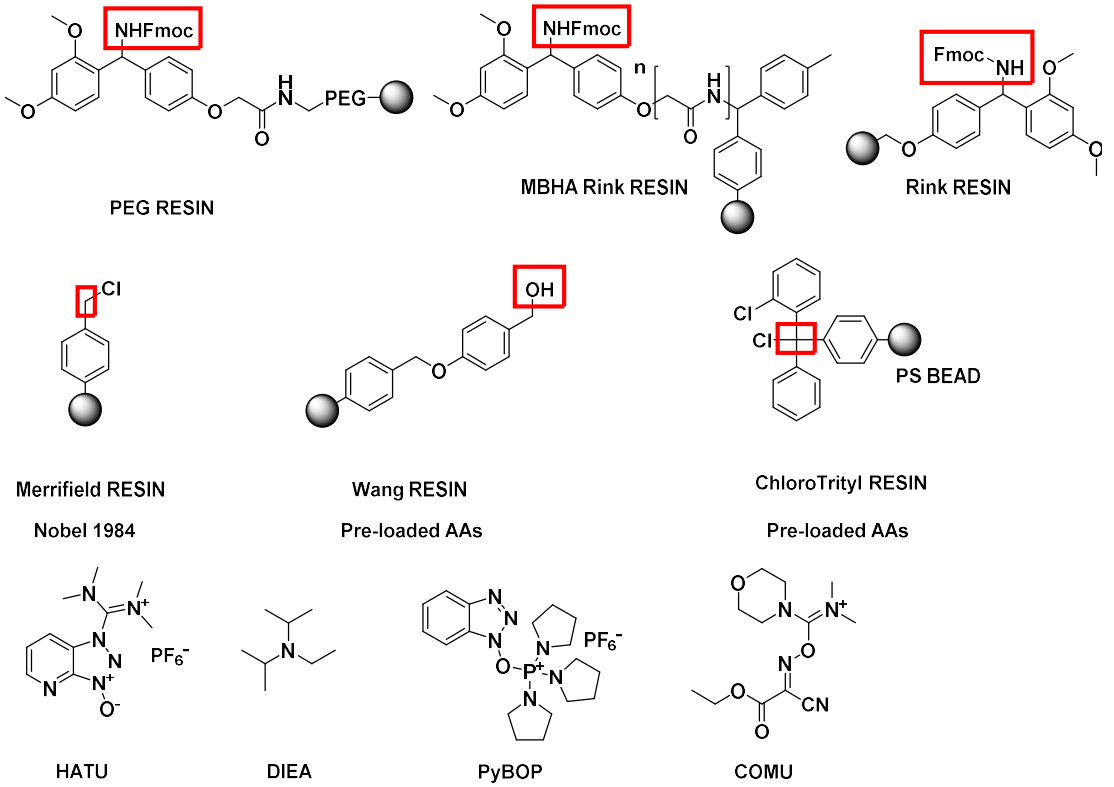

Scheme 3-4 - Resin types for solid phase synthesis and the chosen coupling agents for SPPS.

For our purposes, Rink PS resin with divinylbenzene crosslinking and MBHA linker can be employed since they are base resistant allowing Fmoc/*tert*-Butyl peptide synthesis with mild cleavage conditions with TFA. Rink linker is nowadays very commonly used to favour the peptide cleavage, thanks to its methoxy groups.[11] The selected acid-labile resin was the Fmoc-protected Rink Methyl-BenzHydril Amide (MBHA) that swells better in non-halogenated solvents like DMF and NMP. Since the chosen resin bears Fmoc-protected amino-terminal residues, the synthetic peptide chain growth was performed from the N-terminus to the newly inserted carboxy moiety. A variety of

coupling agents are available from the market, and each of them has different performances with different substrates. Synthetic protocols were tailored for the use of HATU with DIEA as a base, even if novel coupling agents and different solutions were adopted for the synthesis of modular peptides.[10,12,13] Peptide yields and reaction conversions were therefore not screened with novel amide coupling agents since the yields were considered adequate for the needs of this project. However, considering a scale-up on an industrial level for the surface production, microwave-assisted solid-phase synthesis novel coupling conditions need to be screened. Semi-automated peptide synthesis was performed with AAPPTEC peptide synthesizer, equipped with a sintered glass bottom filter shaking reactor, being able to hold the resin in place while operating the washing steps. The Fmoc-protected amino acids were dissolved in separate vessels and automatically delivered to the pre-activation/mixing vessel prior to each coupling step. Amide coupling reactions were carried out in the presence of DMF/NMP as solvents.

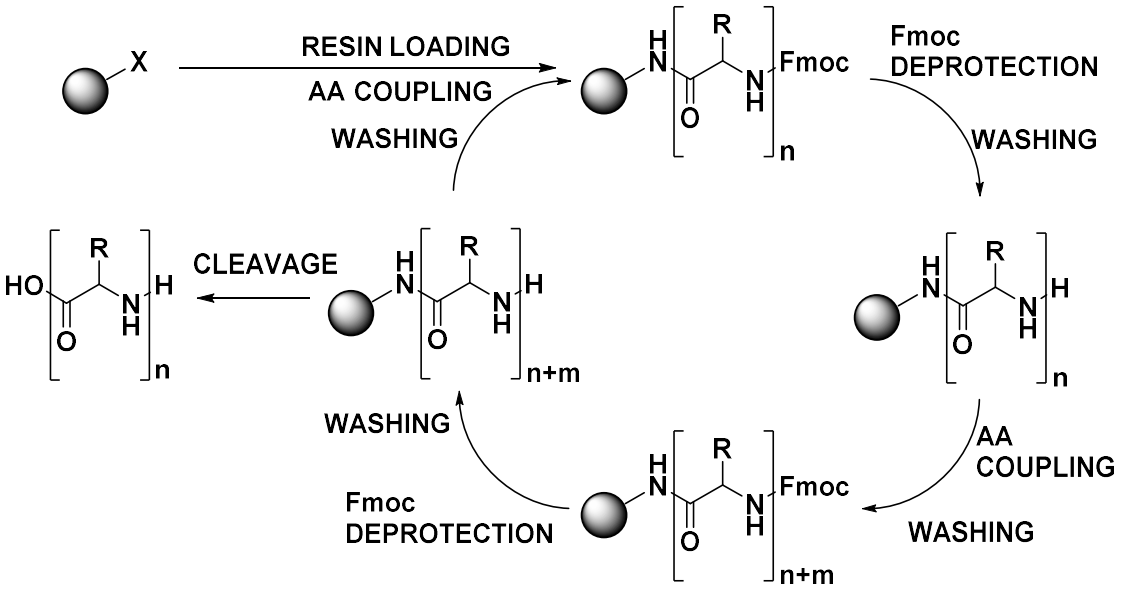

Scheme 3-5 - Solid-Phase Peptide Synthesis (SPPS) stepwise mechanism. NOTE: Resin bead is now representing both Polystyrene and Rink linker.

The general automated peptide synthesis pathway is shown above (Scheme 3-5). After the resin swelling and Fmoc deprotection of the resin, the first amino acid can be loaded. Separate carboxylic acid activation as ester is performed before every coupling. After the coupling, washing steps were performed to prevent side reactions with unreacted reagents and peptide aggregation.

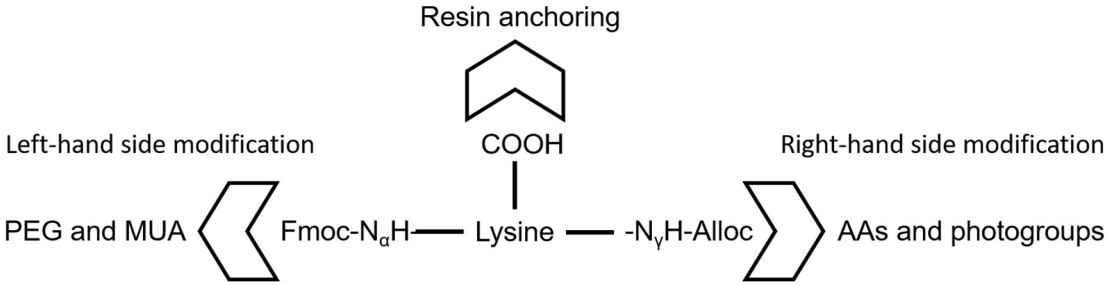

Figure 3-3 – Peptide synthesis strategy: orthogonal functionalisation of central trifunctional Lysine

After each iteration of Fmoc deprotection and coupling, a washing step is performed until the end of the sequence. After that, the resin was washed with CH_2Cl_2 and the peptide cleaved from the resin. Our synthetic strategy for SPPS was adapted from the general pathway shown in Scheme 3-5. Lysine was chosen as a suitable trifunctional amino acid that could enable orthogonal peptide chain growth. Carboxy Lysine was chosen as resin-anchorage amino acid because of being Fmoc-protected at the -Nα and Alloc protected at the -Nγ. These two different groups allow orthogonality with full tolerance to SPPS basic conditions. Furthermore, the Trityl-protection of 11-mercaptoundecanoic acid (Iris Biotech, MUA, Scheme 3-6, coupling c'') is chosen instead of acetyl because it can be cleaved with the same peptide cleavage conditions.

3.6. Synthesis of probe peptides 3-5 and 3-6 – General protocol

The first step was the resin swelling, followed by triple Fmoc deprotection and washing. Resin swelling is needed to expand the polymer beads allowing solvent and reagent access to the internal parts of the polymer.

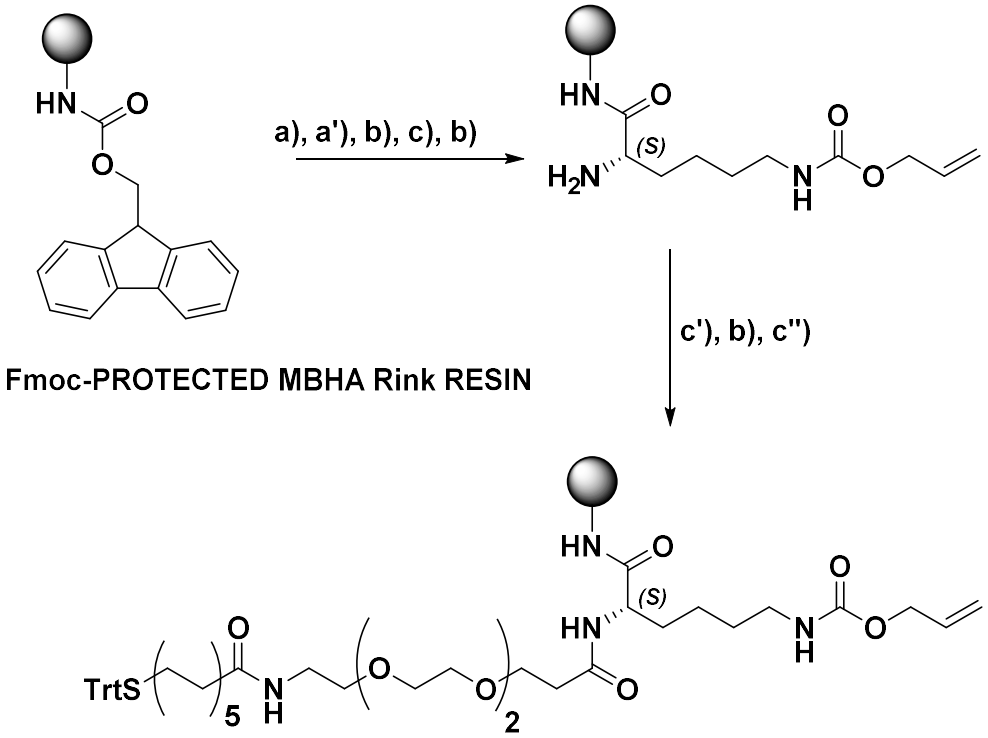

Scheme 3-6 – LEFT-HAND SIDE CHAIN GROWTH: Conditions: (a) NMP resin swelling, 10 mL x 30 min; (a') washing: 3 x 15 mL DMF, 3 x 10 mL NMP, (b) 20% piperidine/DMF, 6 mL × 4 min x 3, r.t; (c) Fmoc-Lys(Alloc)-OH (0.2 M), O-(7-Azabenzotriazol-1-yl)-N,N,N',N'-tetramethyluronium hexafluorophosphate (HATU, 0.4 M) and N,Ndiisopropylethylamine (DIEA, 2 M), N-methyl-2-pyrrolidone (NMP), r.t, 30 min; (c') Fmoc-NH-PEG(3)-COOH (0.2 M), HATU (0.4 M) and DIEA (2 M), NMP, r.t, 3 h; (c'') 11-Trityltioundecanoic acid (0.2 M), HATU (0.4 M) and DIEA (2 M), NMP, r.t, 3 h. NOTE: in between each step there is at least one washing, even if not mentioned.

After that, every amino acid of generally every carboxy-bearing molecule that is going to be added is separately activated with O-(7-Azabenzotriazol-1-yl)-N,N,N',N'-tetramethyluronium hexafluorophosphate (HATU, 0.4 M in DMF) and N,N-diisopropylethylamine (DIEA, 2 M in DMF) and mixed under N_2 stream for a minute. This step is required to form the more reactive ester that will undergo coupling reaction with deprotected amine groups from the resin. Standard peptide coupling reaction time was set for thirty minutes. Glutamine couplings after Alloc deprotection were set for 1 h and Fmoc-NH-PEG(2)-COOH or 11-Trityltioundecanoic acid (MUA) were set for 3 h after optimisation. All reaction conversions were initially monitored by Kaiser test. A second coupling called "double coupling" was performed for the inexpensive and

commercially available amino acids used in this project. After iterative HATU/DIEA couplings and Fmoc-deprotection reactions the left part of the IGDQ-bearing peptide was completed. The subsequent step was the Alloc deprotection. This reaction can be performed in CH_2Cl_2 but requires an appropriate washing and swelling of at least 45 minutes. The resin immediately shrinks when washed with CH_2Cl_2 and slowly starts to swell again after some time. Alloc deprotection reaction is routinely performed on solid phase with Tetrakis(triphenylphosphine)Palladium(0) and Phenylsilane as ligand/allyl scavenger.[14–16] The first part of the synthesis was carried out in automatic mode, which implies that the mixing, dispensing, washing and reaction steps are automated. The Alloc deprotection step was carried out in "manual mode" by manually adding Phenylsilane and then Palladium in dry/degassed CH_2Cl_2 to the resin. This synthesis can be carried out in a flask with traditional inert contitions, but due to the low mechanical resistance of the resin, shaking/N_2 bubbling was preferred to the magnetic stirring bar. Alloc deprotection was performed for thirty minutes. As a standard protocol, the reaction was performed twice. In between each deprotection, 3 x CH_2Cl_2 washings, 3 x DMF washings and again 3 x CH_2Cl_2 washings were performed to remove the side products formed. After the Alloc deprotection, the resin had to be washed thoroughly and swelled again in NMP for another thirty minutes. After the NMP swelling step, no deprotection reaction had to be carried out since the resin was already deprotected. The second part of the synthesis after the left-hand side chain elongation deals with its right-hand side counterpart. Two moieties can be coupled, producing two series of peptides. If the photolabile linker is coupled after the Alloc deprotection but prior to the same IGDQ sequence, molecule **3-3** would be obtained. Conversely, if Glutamine amino acid is coupled after the Alloc deprotection, molecules **3-5** or **3-6** would be obtained, with the same coupling conditions and strategy (see Scheme 3-2). This method gives flexibility towards the synthesis of different peptides by simply swapping the amino acid that can be loaded after the Alloc deprotection, since the left-hand side moiety is shared for both peptide series. Coupling reaction of Fmoc-Glutamine was performed as a double coupling and each one was extended to 1 h.

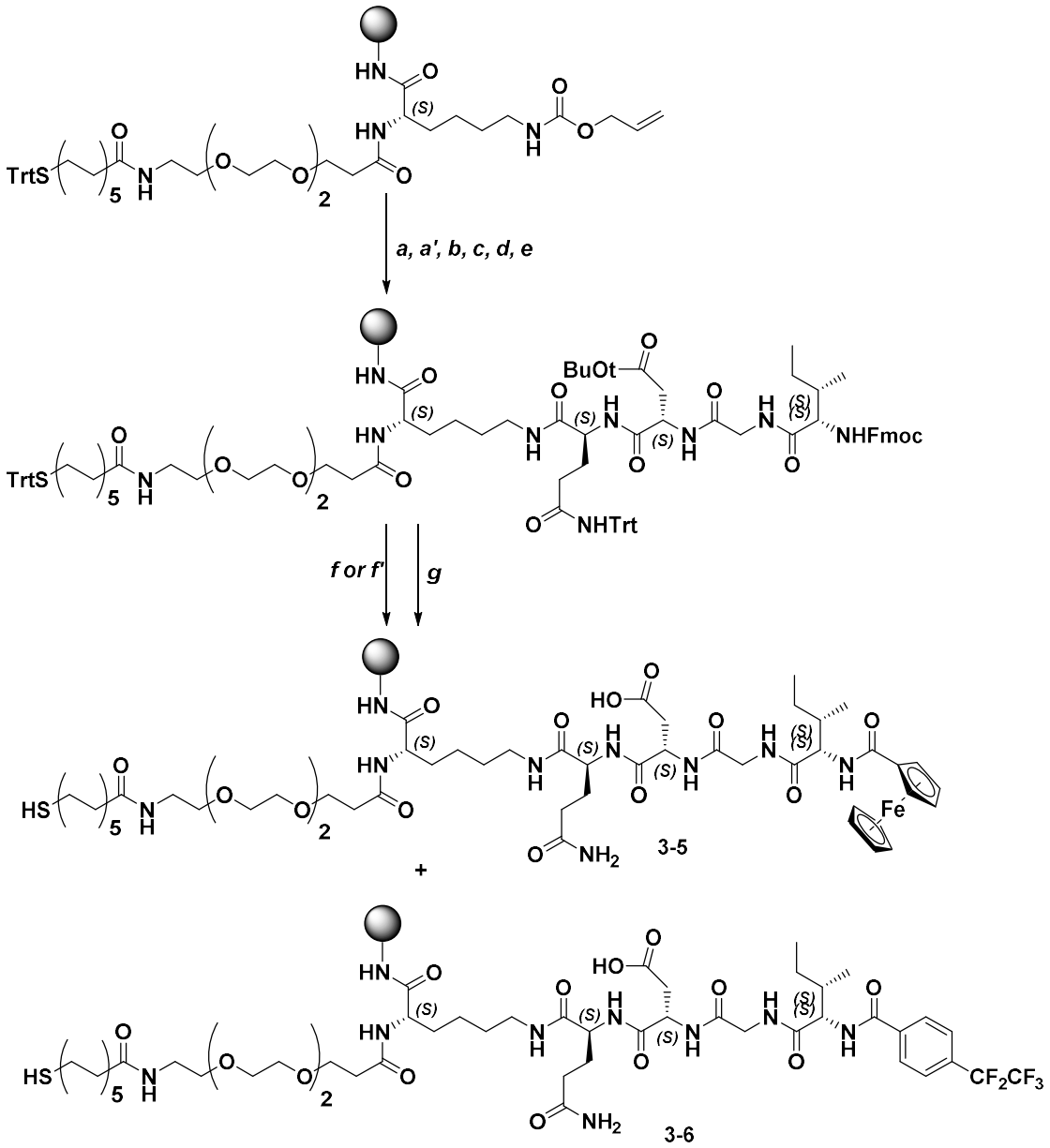

Scheme 3-7 - RIGHT-HAND SIDE ELONGATION: SPPS scheme for the synthesis of IGDQ-bearing peptides. Semi-automated Fmoc-based SPPS of **3-5** and **3-6**. Conditions: *a*: dry degassed CH_2Cl_2 resin swelling, 15 mL x 30 min under N_2; *a'*: washing: 5 x 15 mL CH_2Cl_2; *b*: phenylsilane, $[Pd(PPh_3)]_4$, CH_2Cl_2, r.t, 30 min x 2 + 3 x 10 mL DMF washing, 3 x 15 mL CH_2Cl_2 washing; NMP resin swelling, 15 mL x 30 min; (*c*) Fmoc-Gln(Trt)-OH (0.2 M), O-(7-Azabenzotriazol-1-yl)-N,N,N',N'tetramethyluronium hexafluorophosphate (HATU, 0.4 M) and N,Ndiisopropylethylamine (DIEA, 2 M), N-methyl-2-pyrrolidone (NMP), r.t, 1 h; (*d*) 20% piperidine/DMF, 6 mL × 4 min x 3, r.t; (*e*) I, G, D (0.2 M), HATU (0.4 M) and DIEA (2 M), NMP, r.t, 30 min; (f) CarboxyFerrocene, HATU, (0.4 M), DIEA, (2 M), N-methyl-2-pyrrolidone (NMP), r.t, 1 h; (*f'*) Pentafluoroethylbenzoic acid, HATU, (0.4 M), DIEA, (2 M), N-methyl-2-pyrrolidone (NMP), r.t, 1 h (*g*) TFA, triisopropylsilane (TIS), 1,2-ethanedithiol (EDT), H_2O, (95: 1: 2.5: 2.5) r.t, 3 h.

After that, iterative steps previously described in our group were performed, as a sequence of Fmoc deprotections and HATU/DIEA coupling reactions and washing, to achieve the IGDQ-bearing peptide scaffold. As a last step, Carboxy-Ferrocene was

coupled with the same procedure, but coupling time was extended to 1 h. The same was setup was set for the pentafluorobenzoic acid.

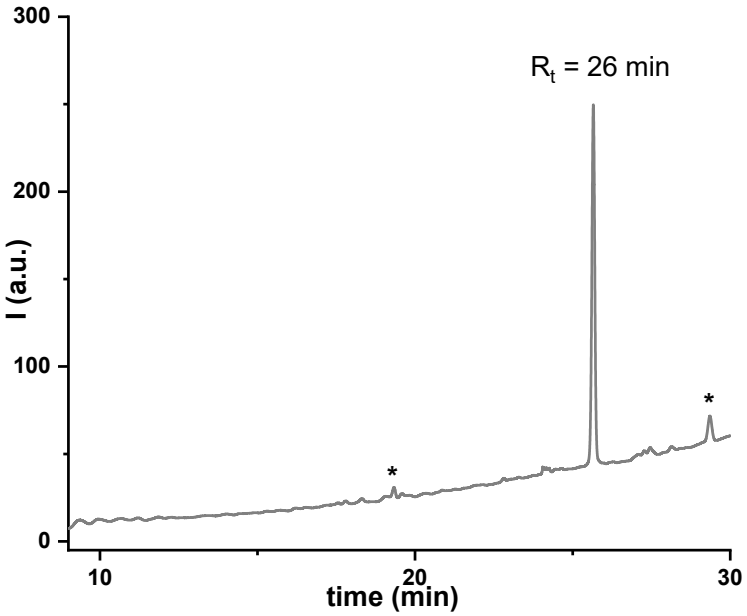

Figure 3-4 – RP-HPLC chromatogram of peptide **3-5** (R_t = 26 min). Processed spectrum. (*) column contamination. Colour code: LT grey for Ferrocene-bearing peptide **3-5**.

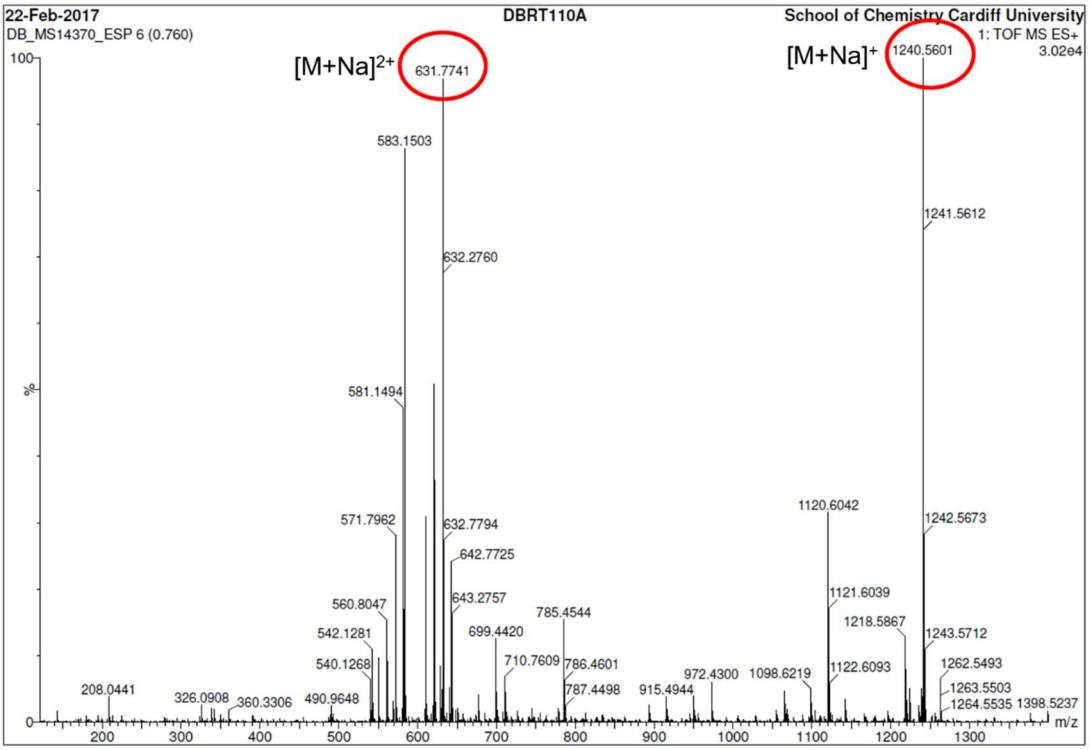

Figure 3-5 - HR-MS of peptide **3-5**.

Both peptides **3-5** and **3-6** were analysed and purified by RP-HPLC and show retention times (R_t) of 26 and 27 minutes respectively. ES-TOF HR-spectrometry was carried out, identifying in both cases the protonated molecular peak and the doubly-charged disulphide.

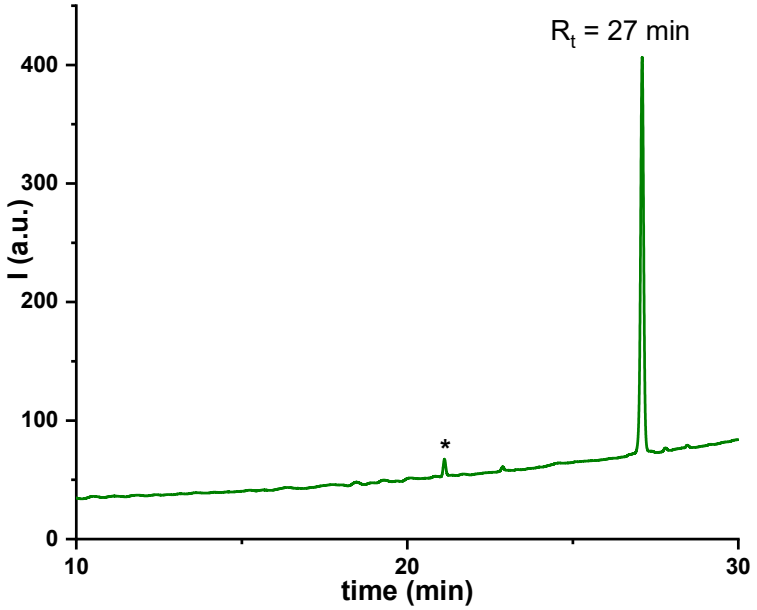

Figure 3-6 - RP-HPLC chromatogram of peptide **3-6** (R_t = 27 min). Processed spectrum. (*) column contamination. Colour code: Olive green for Fluorinated peptide **3-6**.

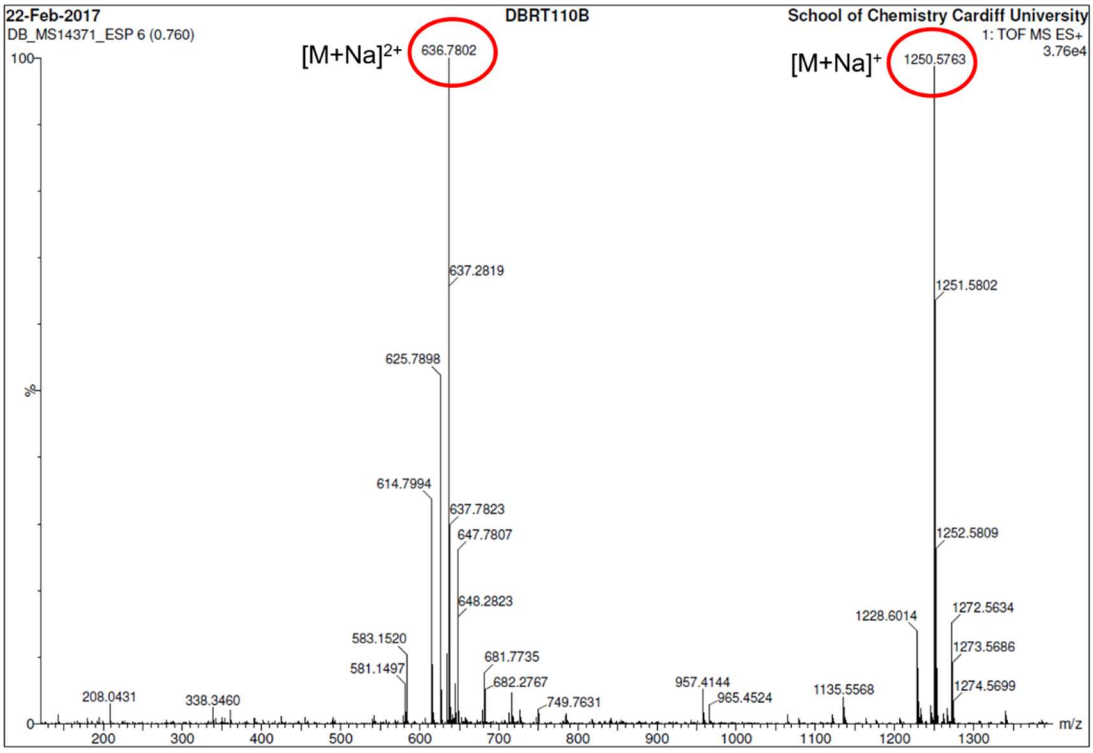

Figure 3-7 - HR-MS of peptide **3-6**.

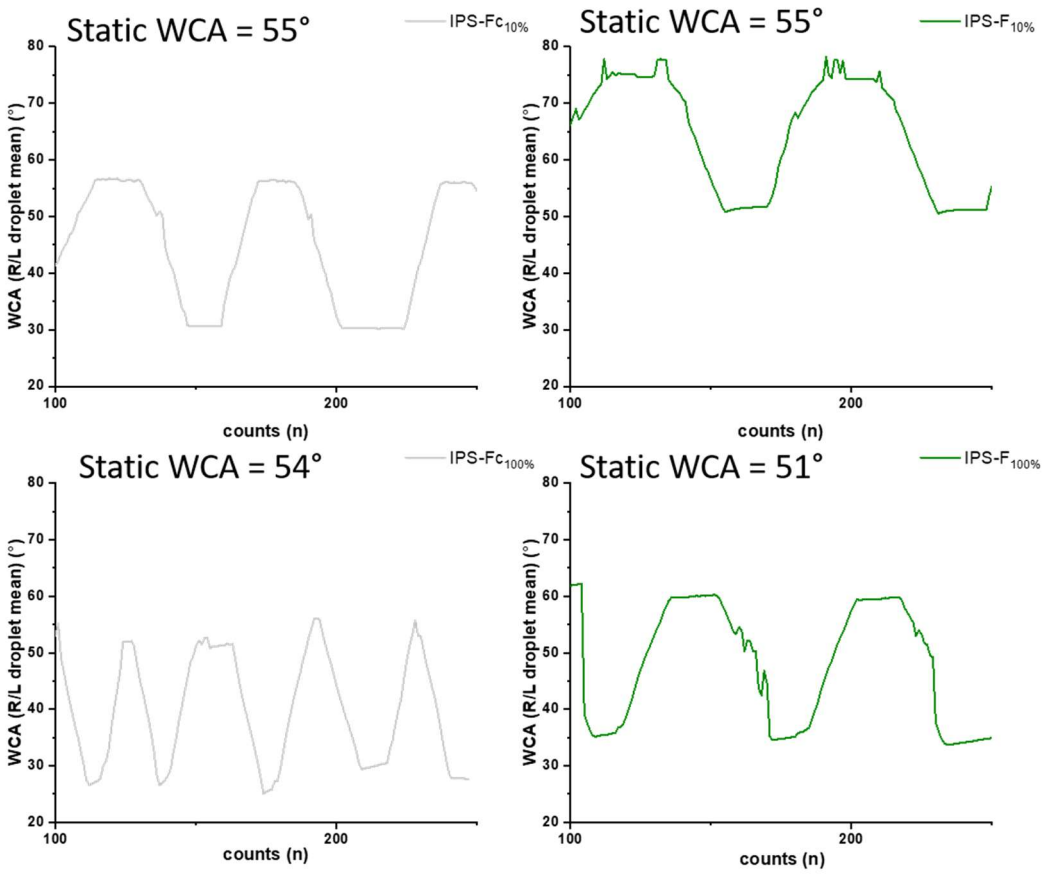

Figure 3-8 - Dynamic Water Contact Angle (WCA) of different SAMs.

The exact mass found for molecule **3-5** is m/z 1240.5601 and 631.7741, which corresponds to the $[M+Na]^+$ peak and $[M+Na]^{2+}$ peaks of $[C_{56}H_{91}FeN_9O_{15}S]$ having a calculated mass of m/z 1217.5705. The exact mass found for molecule **3-6** is m/z 1250.5763 and 636.7802, which corresponds to the $[M+Na]^+$ peak and $[M+Na]^{2+}$ peaks of $[C_{54}H_{86}F_5N_9O_{15}S]$ having a calculated mass of m/z 1227.5884. In Fig. 3-8 above are shown the results of the static and dynamic WCA experiments on two types of isocratic monolayers, namely mixed and mono-component. On the left (top and bottom) isocratic mono-component and 10% IPS-Fc SAMs are shown respectively. The 10% IPS-Fc is an isocratic SAM of 9:1 molar ratio of backfiller **3-2** (Scheme 3-2) and IPS-Fc 100% is the mono-component monolayer. On the right (top and bottom) the same experiments are shown for peptide IPS-F bearing the fluorinated head group. Static and dynamic WCA are reported (Fig. 3-8). Static WCA of the two isocratic SAMs of IPS-Fc and IPS-F are roughly the same, with a value of 54° and 51°, respectively. This is due to the hydrophobic nature of the peptides that possess the apolar head group that extends from of the monolayer. The hydrophobic character of the peptides prevails even if the monolayer ratio is decreased to 10% with 90% of polar but shorter backfiller. Regarding the dynamic WCA (Advancing and Receding Contact Angle ARCA), the charts

represent the hysteresis cycles over the monolayers. IPS-Fc SAM has a ΔWCA ARCA of 30° which is a relatively high value for a mono-component SAM, indicating the disordered nature of the monolayer. IPS-F SAM has a ΔWCA of 25°, that follows the same trend of poorly packed monolayers. ΔWCA ARCA of IPS-Fc 10% is around 25° as well as IPS-F 10%. The remarkable difference between the two monolayers is the offset that the charts present. Specifically, IPS-Fc 10% has lower advancing and receding angles, ranging from 30° to 55°. Conversely IPS-F 10% has advancing and receding angles from 50° to 75°. This result suggests that IPS-F peptide has a much higher hydrophobic character than IPS-Fc, while both are not able to form a well-packed monolayer.

3.7. Syntheses of photolabile linkers and peptides

The photolabile linkers were designed to be included in our previously optimised solid phase protocols. Specifically, the linker that resides prior to the motogenic sequence had to be bifunctional, with one carboxy moiety and a Fmoc-protected amine. The second one could bear just one functional group that could be used to tether it to the peptide structure. Taking inspiration by the work of Holmes and coworkers[17,18] on nitrobenzyl groups, the design of a bifunctional moiety was tailored to be included into our semi-automatic solid phase peptide synthesis (SPPS). The first photolabile linker prepared was the nitrobenzyl-bearing derivative **3-10** shown below (Scheme 3-8). Since the first step, reactions described in the scheme were performed avoiding light exposure to minimise undesired photocleavage.

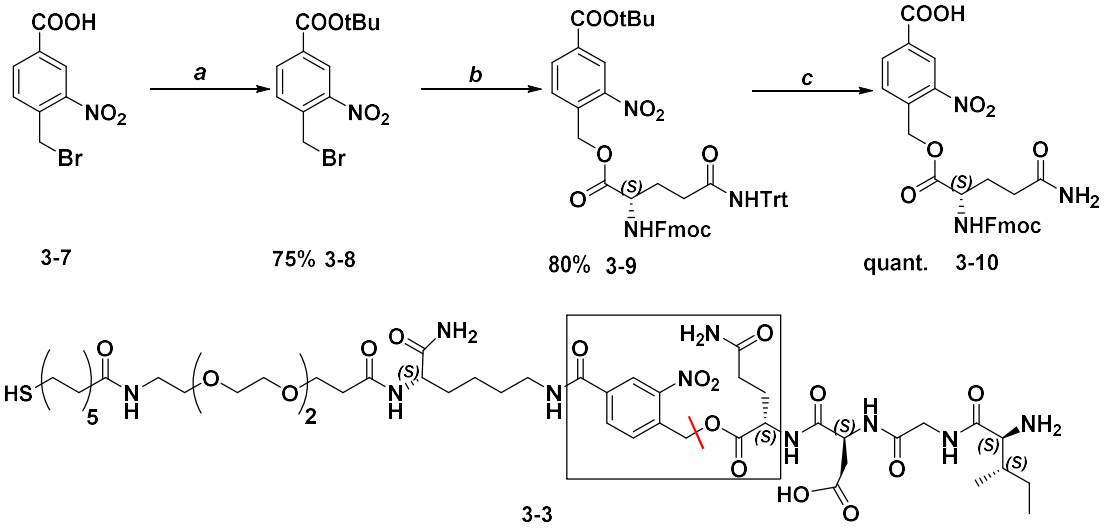

Scheme 3-8 - Synthetic steps for the synthesis of the nitrobenzyl-bearing photolabile linker **3-10** and final photolabile peptide **3-3**. Conditions: *a*: *tert*-BuOH, DCC/DMAP, DMF, 0°C to r.t, overnight; *b*: Fmoc-Gln(Trt)-OH, DIEA, DMF, 0°C to r.t, overnight; *c*: TFA/CH_2Cl_2, 0°C to r.t, 3 h.

Starting from commercially available 3-nitro-4-benzylbenzoic acid **3-7**, the first reaction performed was the carboxylic group protection, affording the *tert*-Butyl protected product **3-8** via a Steglich esterification.[19] The carboxylic acid is deprotonated by the base and the carbodiimide and reacts with the latter forming the corresponding ester. This intermediate is prone to react with the N',N'-dimethylamino pyridine (DMAP) that activates the ester and favours the insertion of weak nucleophiles such as *tert*-Butanol that is present in five equivalent excess, leading to the product.

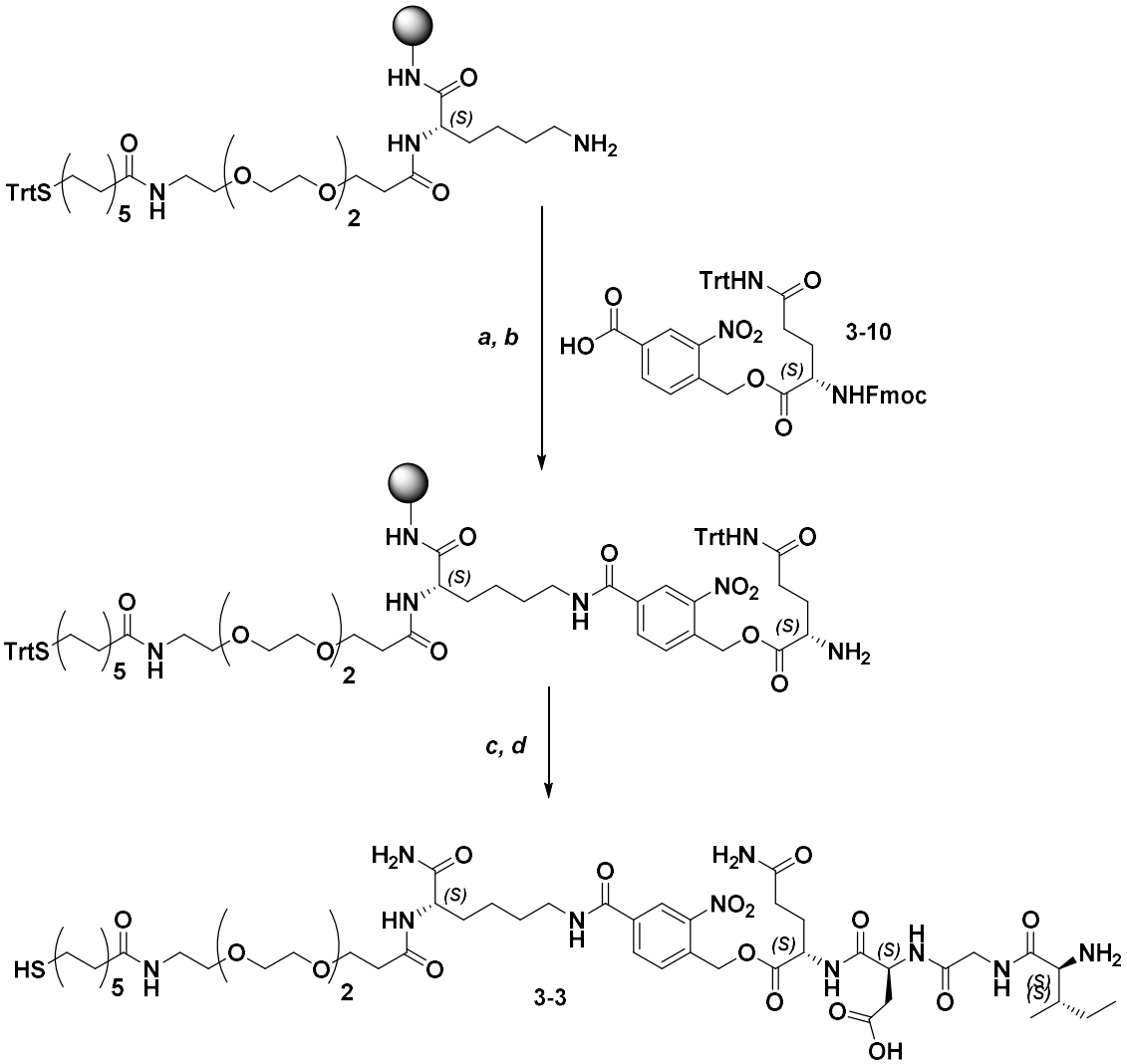

Scheme 3-9 – right-hand side peptide functionalisation: Conditions: *a*: **3-10** (0.2 M in NMP), HATU 0.4 M and DIEA 2 M, NMP, r.t, 1 h; *b*: 20% piperidine/DMF, 6 mL × 4 min x 3, r.t; *c*: D, G, I (0.2 M), HATU (0.4 M) and DIEA (2 M), NMP, r.t, 30 min; *d*: TFA, triisopropylsilane (TIS), 1,2-ethanedithiol (EDT), water, (95: 1: 2.5: 2.5) r.t, 3 h, kept in dark.

The presence of DMAP avoids the formation of side products such as O-acyl ureas therefore enabling product formation in mild conditions. DMAP is indeed a stronger nucleophile (compared to *tert*-Butyl alcohol) that eliminates the dicyclohexyl urea as

unsoluble side product pushing the reaction equilibrium to completion. The second step performed was the S_N2 on the bromobenzyl moiety on **3-8** by the carboxy group of the protected Glutamine, that leads to the concerted elimination of the diethylisopropylammonium bromide salt. Reaction was optimized with a small excess of Glutamine that can be removed easily with an extraction in aqueous conditions. Double substitution on the benzyl carbon does not occur in the chosen mild conditions. The last step of this synthetic pathway is the *tert*-Butyl group removal with TFA in CH_2Cl_2. This last step is quantitative if performed in ice bath or otherwise at room temperature for not more than 2-3 hours. After this step, the photolabile linker was included in the automated peptide synthesis for the synthesis of molecule **3-3**. The common structure shared by all of the peptides included in this thesis was already described as “left-hand side modification” and shown in the following Fig. 3-9 there is only the different right-hand side part. After the Alloc deprotection, photolinker **3-10** was loaded on the structure, with a single coupling reaction of 1 h. After that, iterative cycles of Fmoc deprotection and amide coupling with the three remaining amino acids (Aspartic acid, Glycine and IsoLeucine) were performed.

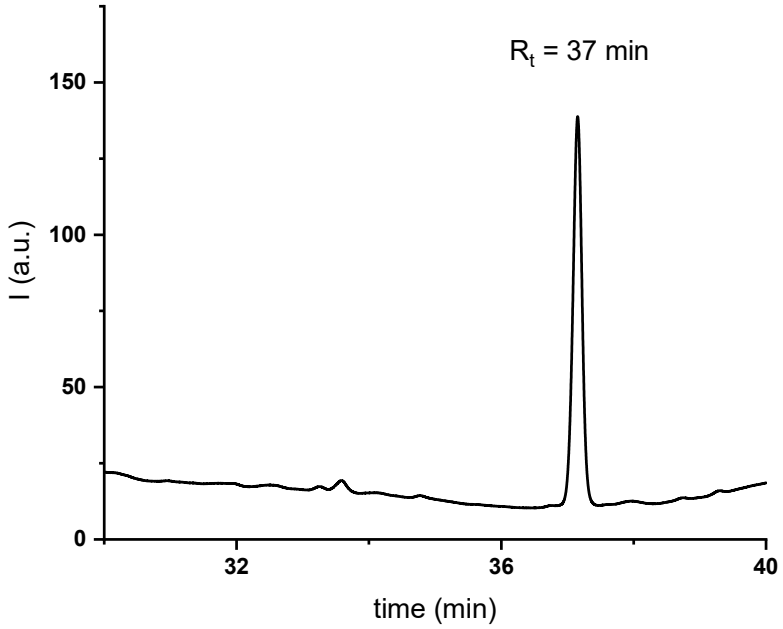

Figure 3-9 - RP-HPLC chromatogram of Nitrobenzyl peptide **3-3**. Processed spectrum.

Peptide **3-3** was analysed and purified by RP-HPLC and show a retention time (R_t) of around 37 minutes. ES-TOF HR-spectrometry was carried out, identifying the protonated molecular peak. The exact mass found for molecule **3-3** is m/z 1185.6113 and 593.3115, which correspond to the $[M+H]^+$ and $[M+H]^{2+}$ peaks of $[C_{53}H_{88}N_{10}O_{18}S]$ having a calculated mass of m/z 1184.5999. The second photolabile linker designed to

mask the IGDQ motogenic sequence was molecule **3-8** taken from the synthetic pathway of **3-10** shown in Scheme 3-8. Reactive benzylbromide group was used directly on solid phase with 2 eq of DIEA as shown in Scheme 3-10.

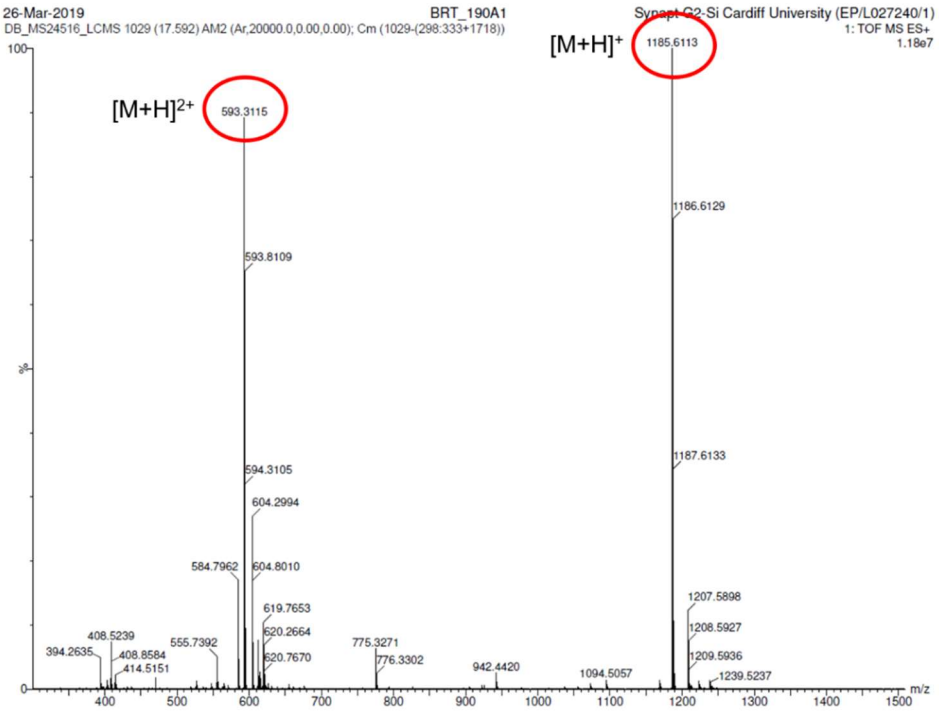

Figure 3-10 - HR-MS of Nitrobenzyl-bearing peptide **3-3**.

Unfortunately, synthesis shown in Scheme 3-10 was attempted several times with different conditions, however not obtaining the desired product **3-4**. In a separate attempt, two equivalents of Hunig's base were used. Triethylamine was also used, while employing 1 eq of nitrobromobenzyl derivative. Since the nitrobenzyl-bearing linker design was partly successful, other and more recent photolabile linkers were explored. The synthesis of two novel photolabile linkers shown below employed a slightly different core, with enhanced photocleavage properties.

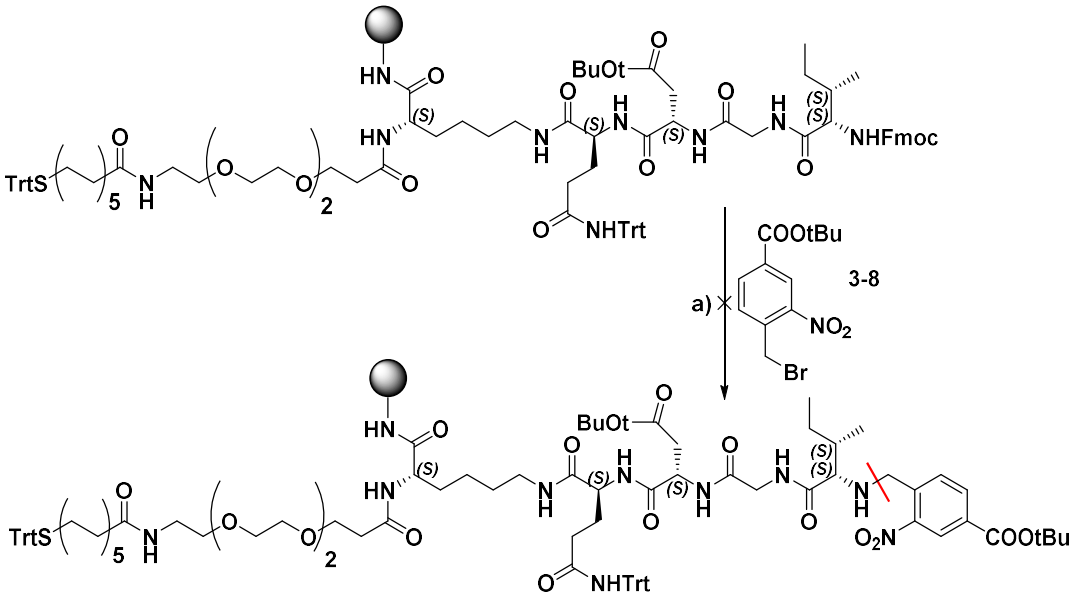

Scheme 3-10 - Synthesis of the second nitrobenzyl peptide - solution and SPPS synthetic steps. Conditions: (a) *tert*-Butyl-3-nitro-4-bromobenzylbenzoate, DIEA, DMF, r.t, 6 h.

3.8. Synthesis of novel photolabile linkers and peptides

In addition to the first nitrobenzyl photolinker, two other caged linkers were successfully synthesized. Longer synthetic pathway was undertaken in return of enhanced photolabile properties, according to literature[18]. Since the first documented use of photolabile nitrobenzyl group by Patchornik[20] in the early 70s, there has been a significant development in the field thanks also to comprehensive reports such the one by Klán[7] and co-workers, describing a wide variety of groups ranging from the nitroaryl groups to the coumarin series, arylmethyl groups and most lately arylsulphonyl moieties and two-photon adsorption techniques. One drawback of the nitrobenzyl linker by Gurawa and Rich was the formation of an aldehyde as photoproduct, prone to react with neighbouring amines and form the correspondent imines. That is why nitrosoaldehydes are potentially toxic to cell cultures. Toxicity is however a relative issue, since the peptide concentration on surface is very low around femtomoles, and surfaces can be gently washed after irradiation, in fact removing the toxic products. That is why the nitrobenzyl strategy was not discarded completely but modified. Novel photolabile core was the nitroveratryloxycarbonyl (NVOC, Holmes 1995 Scheme 3-11) that conversely releases nitrosoketones and lowers the risk of cytotoxicity. The structure of the NVOC is known to be among the most reactive photolabile linkers known for chemical synthesis and solid phase.

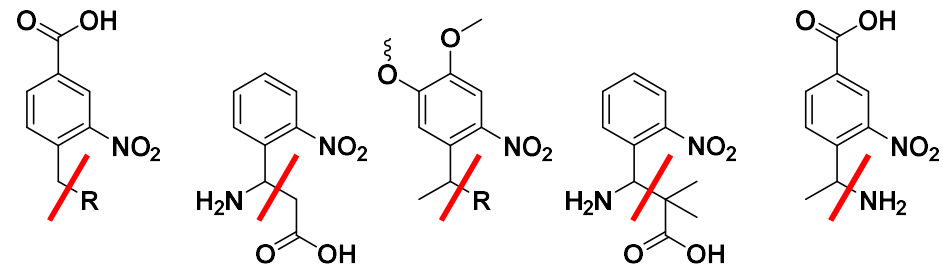

Scheme 3-11 - Different photolabile linkers.

Comparison between the first photolabile linker and the novel cores is shown in Scheme 3-12. The two methoxy groups (pointing arrows on **3-19** and **3-25**) possess an electron-donating character that dramatically influences the photocleavage rate. The NVOC linker **3-19** bears an additional methyl group in place of a hydrogen at the benzylic site. This methyl group has a crucial stabilisation role during the photocleavage mechanism, forming a radical on a secondary carbon. This boosts the cleavage kinetics at least by 10-fold. Specifically, nitrobenzyl's half-life is remarkably higher than its NVOC counterpart in a variety of screened solvents as shown in Table 3-1.

Table 3-1 - Half-life photocleavage (min) rates of two photolinkers according to Holmes.[18] Irradiation with Hg(Xe) Arc lamp, 350-450 nm, 10 mW·cm^{-2}, DTT/PBS is 10 mM DTT in pH 7.4 PBS.

Linker	PBS	DTT/PBS	MeOH	p-dioxane
Nitrobenzyl	**14.1**	47.2	362	36.8
NVOC	**1.74**	1.98	5.81	0.64

The second NVOC photolinker **3-25** holds part of the NVOC **3-19** features but still bearing the nitrobenzyl moiety. Such photolabile group was expected to have intermediate properties between the nitrobenzyl **3-10** and the NVOC **3-19**.

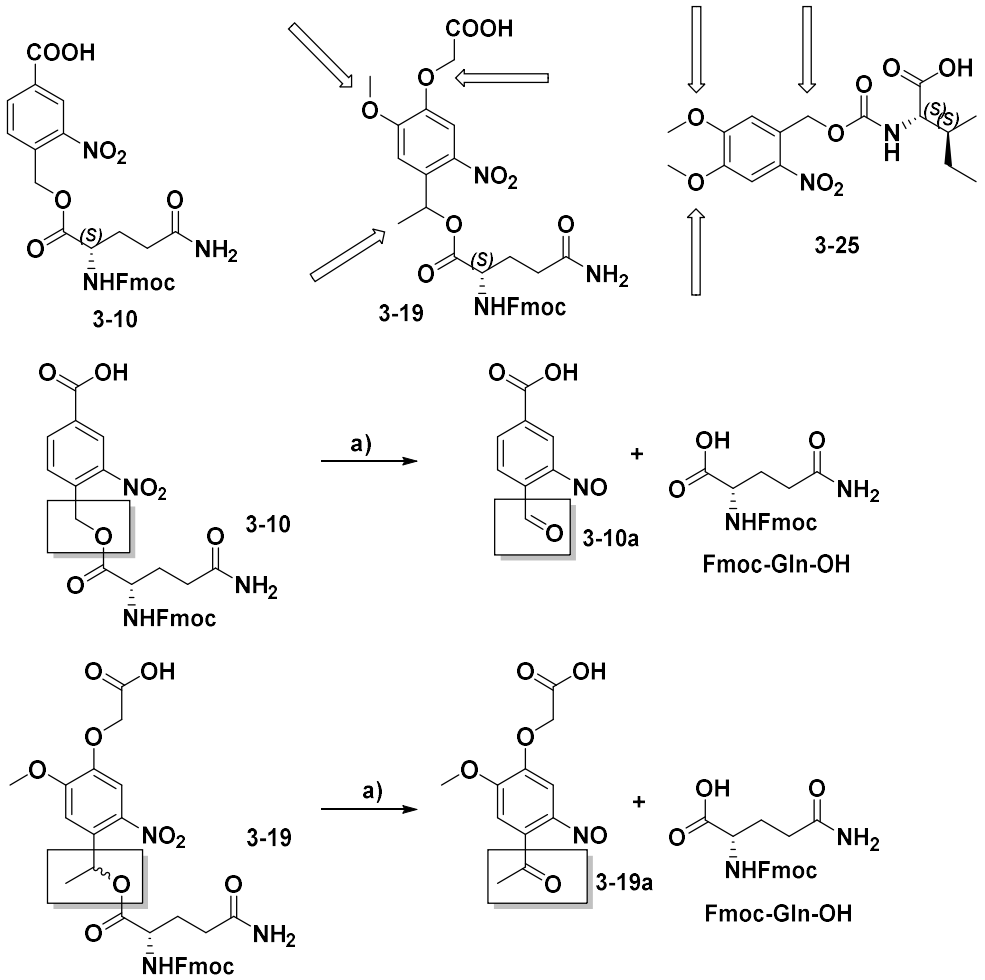

Scheme 3-12 – Nitrobenzyl (left) vs NVOC comparison. General conditions for photocleavage: (a) 350-450 nm, 50 mW·cm^{-2} Hg lamp, polar solvent.

The synthetic pathway of the two novel photolabile linkers is shown in Scheme 3-13) and Scheme 3-14.The synthetic steps to afford the synthesis of the photolabile linkers **3-19** and **3-25** are described above. Because of the reaction scale-up performed up to 20 g, precipitation was the only purification method to afford the desired products in large amounts. For characterisation only, small silica gel flash chromatography separations were occasionally performed. Starting from commercially available Acetovanillone **3-11**, phenol benzylation reaction was performed in refluxing acetonitrile. Recrystallization in MeOH and 1M HCl allowed the formation of pale-yellow crystals. Nitration step was then performed, keeping the mixture at 0°C to minimise nitration of the benzyl protecting group instead of the main ring, leading to a side product that has similar R_f and therefore difficult to separate with silica gel column chromatography. Precipitation in DMF was performed to obtain the desired product. Overnight cleavage of benzyl moiety was performed in neat trifluoroacetic acid (TFA)

and subsequent chain elongation with *tert*-Butylbromoacetate was then completed. Ketone reduction and glutamine esterification were the key steps to obtain the desired precursor that upon *tert*-Butyl group deprotection in TFA afforded molecule **3-19**. Starting from the ketone reduction step, the linker becomes photoactive therefore all the reaction/manipulation steps were carried out in dark. Glutamine esterification was first performed with a Trityl/*tert*-Butyl-bearing substrate.

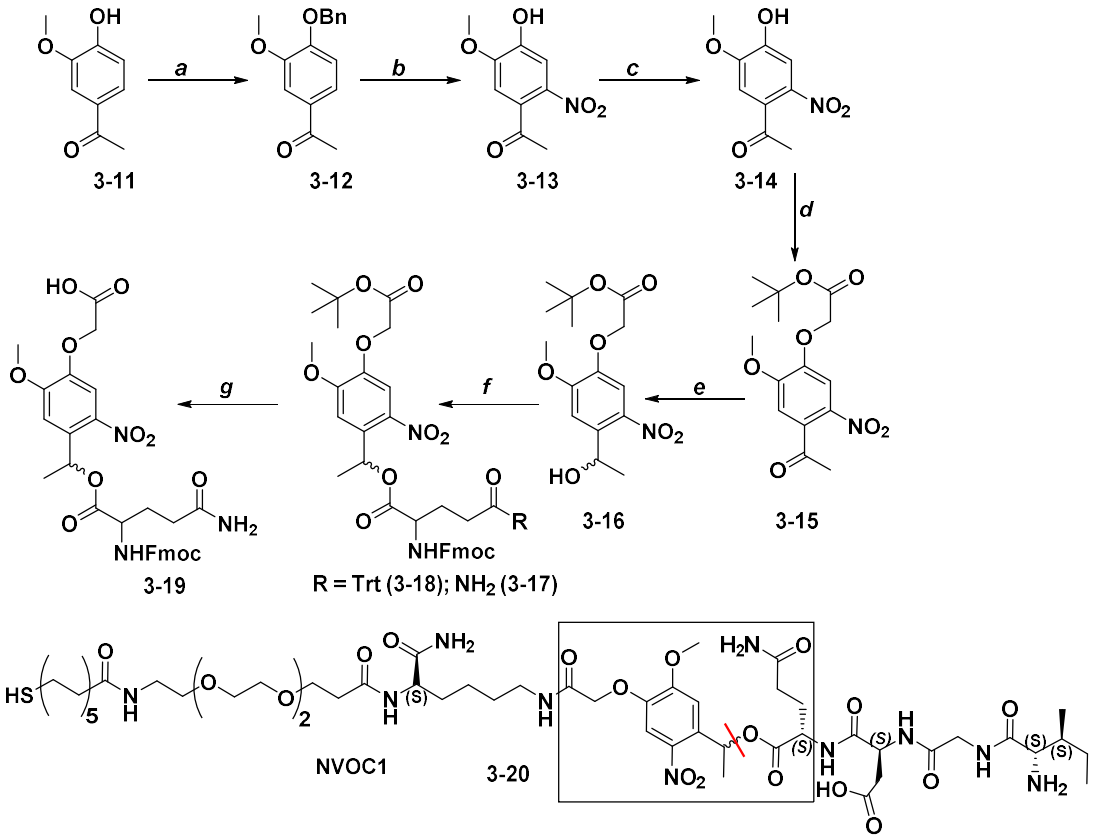

Scheme 3-13 – Synthetic pathway for molecule **3-19** and **3-20**. Conditions: *a*: BnBr, K_2CO_3, DMF, 6 h, reflux, 70%; *b*: HNO_3, 2 h, 0˚C, 50%; *c*: TFA, 16 h, r.t, quant.; *d*: *tert*-Butylbromoacetate, K_2CO_3, DMF, 6 h, r.t, 80%; *e*: $NaBH_4$, THF/MeOH 3:1 ratio, 0˚C, 1 h, quant.; *f*: EDC·HCl, DMAP, Fmoc-Gln-OH, CH_2Cl_2, 16 h, 0˚C->r.t, 90%; *g*: CH_2Cl_2/TFA 1:1 ratio, 0˚C->r.t, quant.; *h*: CDI, CH_2Cl_2, *tert*-Butyl-IsoLeucine, 48 h, r.t.

It was found that Trityl is cleaved faster than *tert*-Butyl on such substrate, giving an intermediate product that if isolated needs to undergo a second TFA cleavage. Longer reaction time was needed to remove both Trityl and *tert*-Butyl, and in some small-scale attempts leading to substrate decomposition. To avoid decomposition, Glutamine without Trityl-protecting group at the -Nγ side chain was chosen. All performed reactions gave moderate to good yields. Switching from DCC to EDC·HCl gave remarkable results on the esterification reaction to obtain the precursor of molecule **3-19**. Reaction is pushed to completion with more than 95% yield in CH_2Cl_2 rather than DMF. As a negative point, nitration reaction gave poor reproducibility with 50% yield at

best, with most of the product in the aqueous phase, presenting double nitration and loss of Benzyl protecting group. Substrate decomposition played a central role in conversion loss and could probably be avoided with milder nitrating agents. Regarding photolabile IsoLeucine **3-25**, synthesis started from commercially available Veratraldehyde **3-15**. Nitration and ketone reduction led to obtain photolabile alcohol **3-23**. This substrate was then activated with carbonyldiimidazole for 1 day at r.t and then *tert*-Butyl protected IsoLeucine was added, without adding any base. Imidazole acting both as base and as leaving group was good enough to afford the intermediate (not characterised) in moderate yields, that upon TFA cleavage led to the desired product **3-26**. After obtaining the photocleavable linkers, solid-phase synthesis was then performed. Nitrobenzyl NVOC was tethered on the resin as the last amino acid, after Glycine Fmoc deprotection reaction (Scheme 3-7).

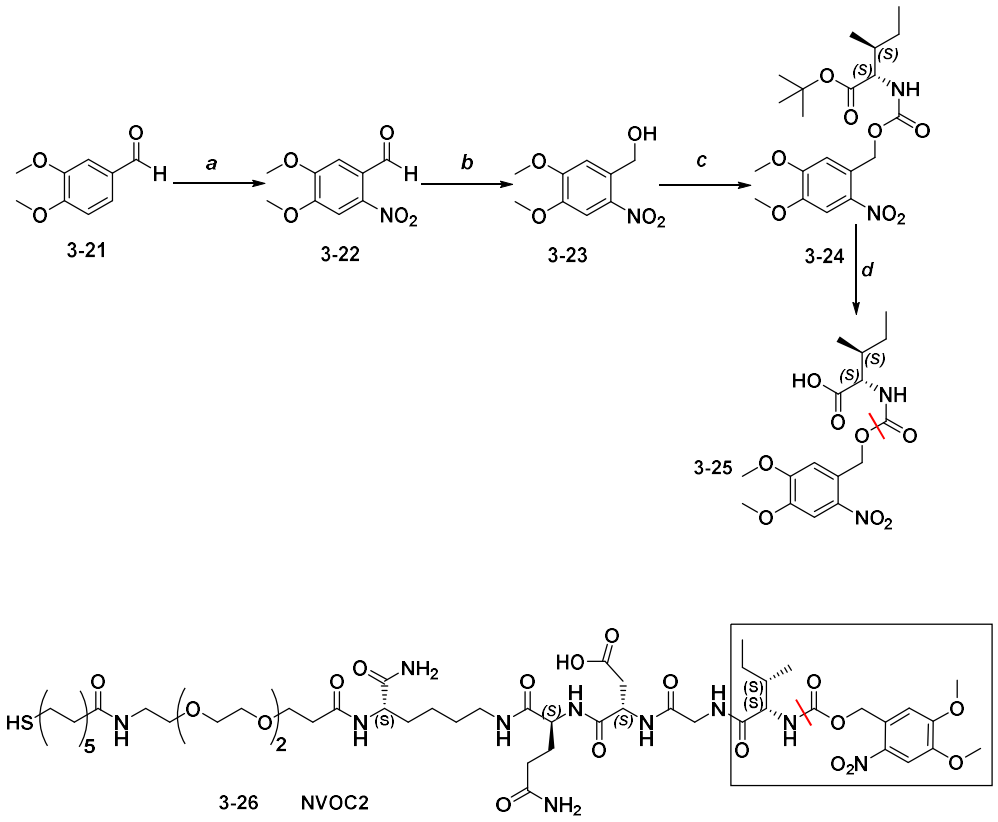

Scheme 3-14 – Synthesis of NVOC2 peptide **3-26**. Conditions: a: HNO_3, 2 h, 0˚C, 50%; b: $NaBH_4$, THF/MeOH 3:1 ratio, 0˚C, 1 h, quant.; c: CDI, CH_2Cl_2, *tert*-Butyl-IsoLeucine, 48 h, r.t.; d: CH_2Cl_2/TFA 1:1 ratio, 0˚C->r.t, quant.

The two peptides shown in Scheme 3-13 and Scheme 3-14 were synthesised in the same way as photolabile peptide **3-3** and **3-6** (Scheme 3-2). Photolinker **3-19** was included in the peptidic scaffold after the Alloc deprotection. Its amide coupling reaction with the peptide was extended for 1 h in the same coupling conditions as standard amino acids. Regarding linker **3-25** for molecule **3-26** (Scheme 3-14) the amide

coupling reaction was performed for 1 h after the last Fmoc deprotection of the IsoLeucine, terminal amino acid of the chain.

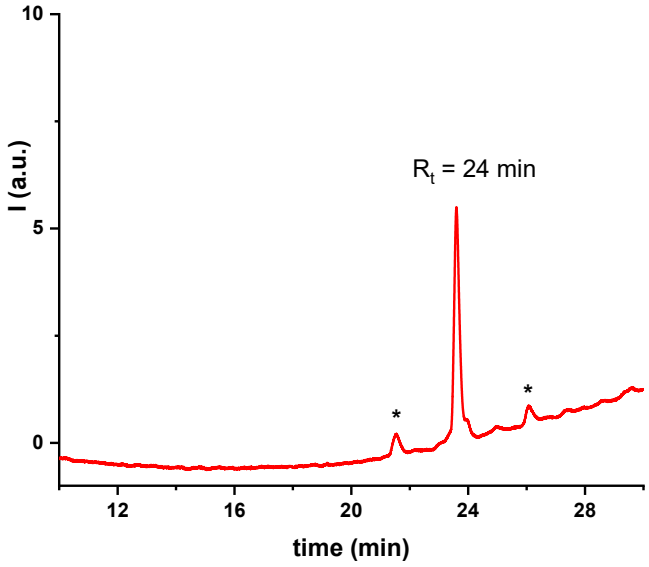

Figure 3-11 - RP-HPLC chromatogram of photolabile peptide **3-20**. Processed spectrum. (*) column contamination.

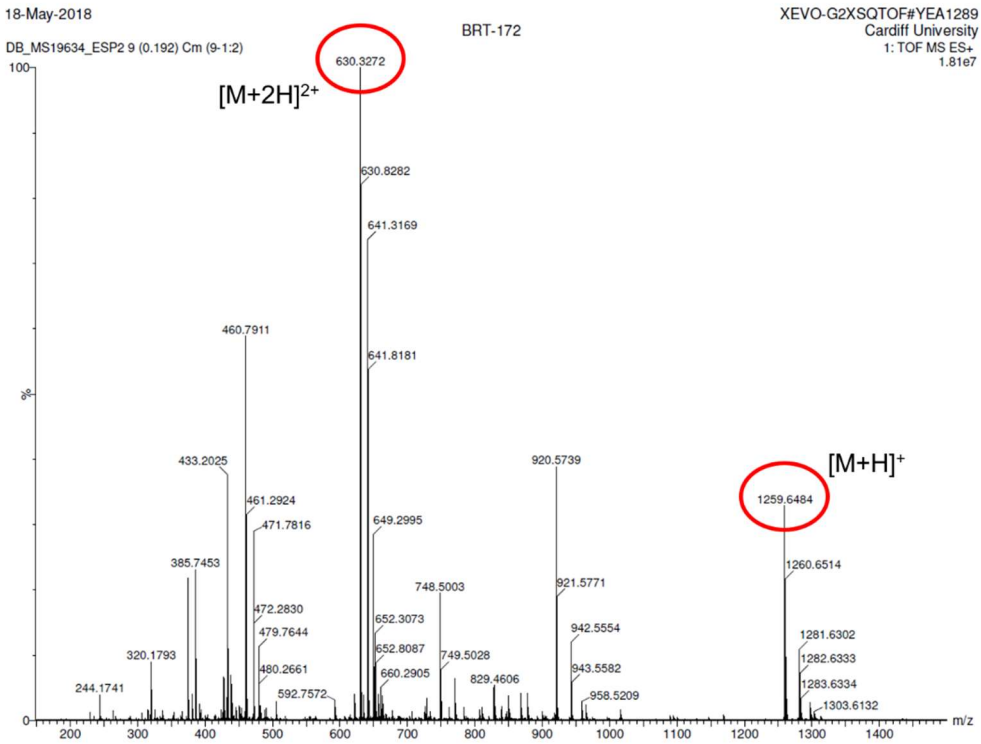

Figure 3-12 - HR-MS of molecule **3-20**

.

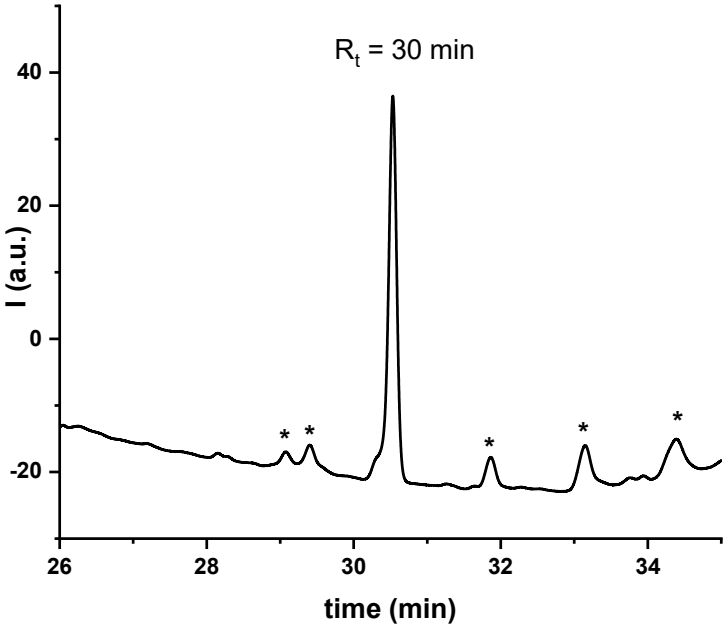

Figure 3-13 - RP-HPLC chromatogram of photolabile peptide **3-26**. Processed spectrum. (*) column contamination.

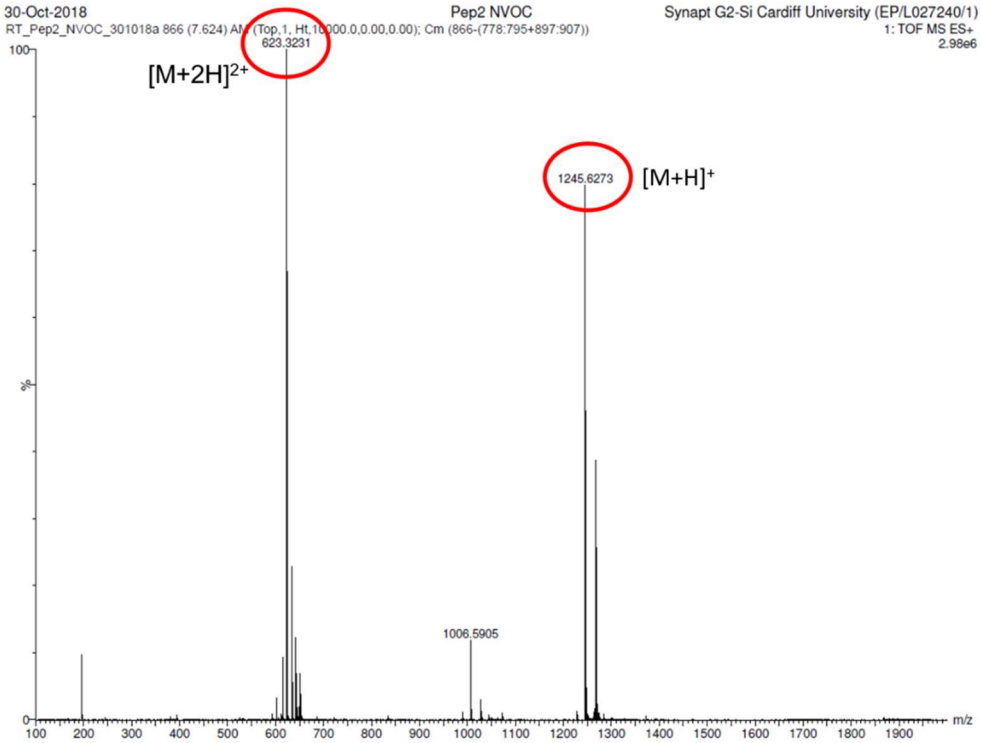

Figure 3-14 - HR-MS chromatogram of molecule **3-26**

Both peptides **3-20** and **3-26** were analysed and purified by RP-HPLC and show retention times (R_t) of 24 and 30 minutes respectively. ES-TOF HR-spectrometry was carried out, identifying in both cases the protonated molecular peak and the doubly-charged disulphide. The exact mass found for molecule **3-20** is m/z 1259.6484 and 630.3272, which correspond to the $[M+H]^+$ peak and $[M+2H]^{2+}$ peaks of $[C_{56}H_{94}N_{10}O_{20}S]$

having a calculated mass of m/z 1258.6367. The exact mass found for molecule **3-26** is m/z 1245.6273 and 623.3231 which correspond to the $[M+H]^+$ peak and $[M+2H]^{2+}$ peaks of $[C_{55}H_{92}N_{10}O_{20}S]$ having a calculated mass of m/z 1244.6210.

3.9. Irradiation of photolabile linkers and peptides

Results of the irradiation experiments performed on the photolabile linkers and peptides are reported in this paragraph. Irradiation experiments in solution were monitored by UV-Vis spectroscopy, RP-HPLC and LC-MS. Irradiation experiments on surface were monitored with WCA and XPS experiments. As a general protocol, the photolabile molecule or surface was analysed before irradiation, and the first spectrum obtained was labelled as tzero. After that, each sample was irradiated and scanned again.

Figure 3-15 - Irradiation lamp with downstream monochromator and shutter-controlled output setup. Output power 50 $mW \cdot cm^{-2}$ with “cold” light.

This procedure was repeated several times and as the repetitions increased, irradiation time was also extended. Photolabile molecules were irradiated at different wavelengths with an irradiation lamp equipped with a monochromator and a shutter (Fig. 3-15). Output lamp power was calibrated around 50 mW and beam radius was adjusted to 2 cm with both monochromator slits fully opened.

3.10. Irradiation of the nitrobenzyl-bearing molecules 3-10 and 3-3

UV-Vis spectra of the 50 μM solution of nitrobenzyl linker **3-10** are shown in Fig. 3-16. Nitrobenzyl linker shows an adsorption band at 264 nm and a smaller one at 300 nm. Although photolinker **3-10** does cleave upon irradiation, a clear UV-Vis endpoint of the experiment was not found, even if irradiation was carried on for several hours. Explorative irradiation experiments on photolinker **3-10** were also performed at 300 nm, 264 nm and 250 nm and are not reported. Nitrobenzyl peptide **3-3** was also irradiated in solution obtaining a similar spectrum (not reported) as the one shown in Fig. 3-16 but with an hypochromic effect in the photocleavage, probably due to inter- and intra-chain interactions influencing chromophore adsorption.

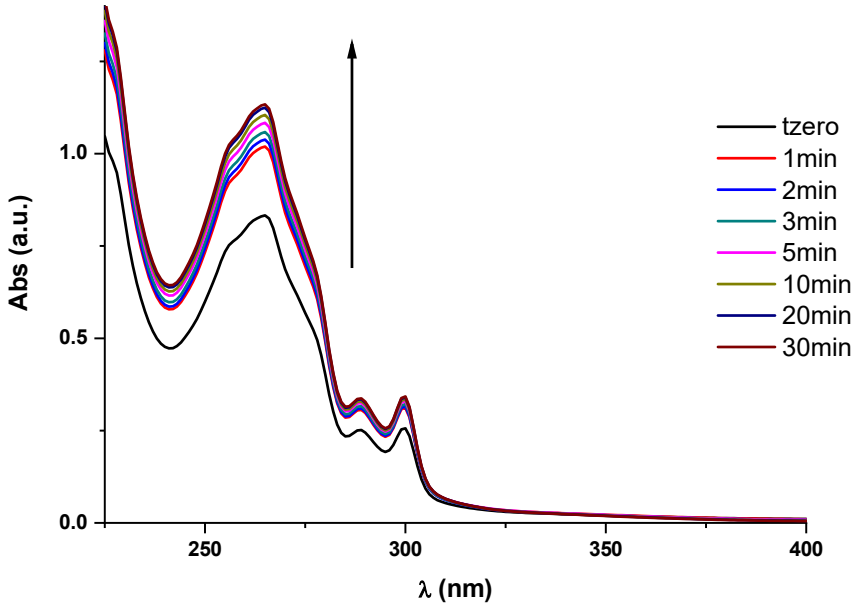

Figure 3-16 - UV-Vis irradiation of nitrobenzyl linker **3-10** solution H_2O/CH_3CN 50μM at 350 nm.

Irradiation of nitrobenzyl linker **3-10** (Fig. 3-16) monitored by RP-HPLC gave more interesting results as a quantitative technique for the determination of the photocleavage kinetics, with the use of an internal standard (IS). Cumulative irradiation time was reported: the same sample was iteratively scanned and irradiated. Irradiation time reported is the sum of the previous irradiation plus the current one. Iso-Leucine-*tert*-Butyl ester·HCl was used as the IS because of its relatively different retention time and its peak shape that was very easy to identify. Other amino acids were screened, but only the selected IS presented such peculiar straight fronting and pronounced tailing effect on RP-HPLC, that makes identification easier. Peak area ratios between molecule **3-10** and IS peak respectively, were plotted (Area linker/Area IS vs. time).

Points were fitted with a decreasing exponential function (see Appendix, Origin 2019 software, default function and settings) and half-life photocleavage was calculated.

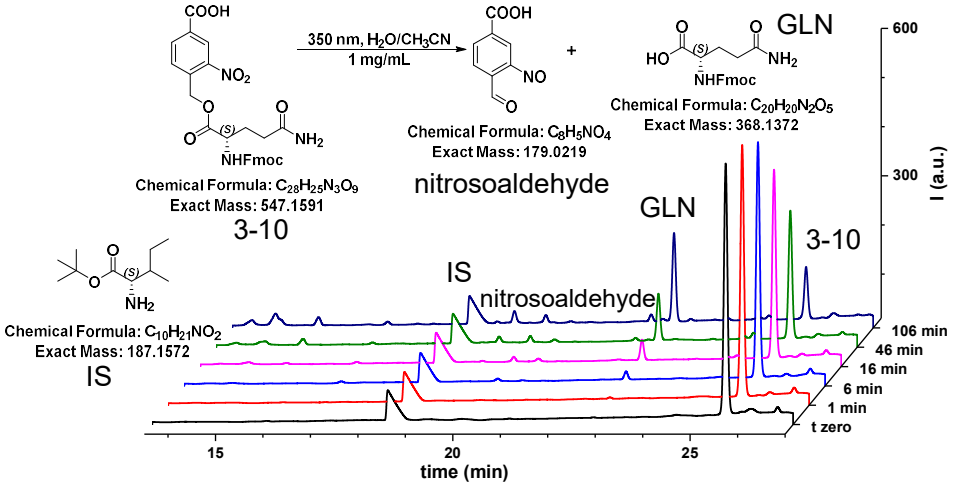

Figure 3-17 - RP-HPLC chromatograms monitoring photocleavage reaction of molecule **3-10**.

Half-life of molecule **3-10** was calculated with a data fitting (see Appendix section 7.20) and appears to be 37.07 minutes (parameter relative to our specific conditions, solvent, lamp power and wavelength). These values were similar to the ones reported by Holmes and co-workers, although determined in different solvents. Chromatogram plot shown in Fig. 3-17 shows that a total time of 106 minutes of irradiation is not enough to photocleave completely the nitrobenzyl linker. Furthermore, Fig. 3-17 shows that only the main photocleavage product Glutamine could be detected with a retention time of 6 minutes, and the possible other side-products were visible in the chromatogram only after 46 minutes, probably due to decomposition. LC-MS results from irradiation of linker **3-10** are shown below (Fig. 3-19). The same samples analysed by RP-HPLC were injected in the LC-MS for peak identification and complete characterisation. Different retention times are due to higher performances of the LC system. IS was identified with a retention time of 8.7 minutes. The second relatively intense peak belonged to the released glutamine from linker **3-10** with a retention time of 16.7 minutes and then the most important peak belonging to the photocleaved product was found with a retention time of 21.1 minutes. Tzero LC-MS chromatogram had some contaminants in the column, but the following runs turned out to have a smoother baseline, indicating that the contaminants (marked with * in Fig. 3-18, and throughout this thesis) were partially removed. LC-MS shows that complete conversion was not reached even after 106 minutes of cumulative irradiation. RP-HPLC monitoring of photocleavage of peptide **3-3** (Fig. 3-18) showed that the photocleavage was almost

complete between 46 and 106 minutes. In this specific case the RP-HPLC chromatograms were plotted individually in Fig. 3-18 due to incoherence in the retention times. The calculated half-life value for peptide **3-3** is 28.2 minutes, indeed smaller than its linker **3-10** irradiated alone. Faster half-life photocleavage for peptide **3-3** compared to molecule **3-10** was not investigated further because both exceeded our standards for safe cell irradiation without decreasing viability. These latest results shifted the choice of the photolabile linkers towards the use of Nitroveratriloxycarbonyl (NVOC) groups, with lower half-lives.

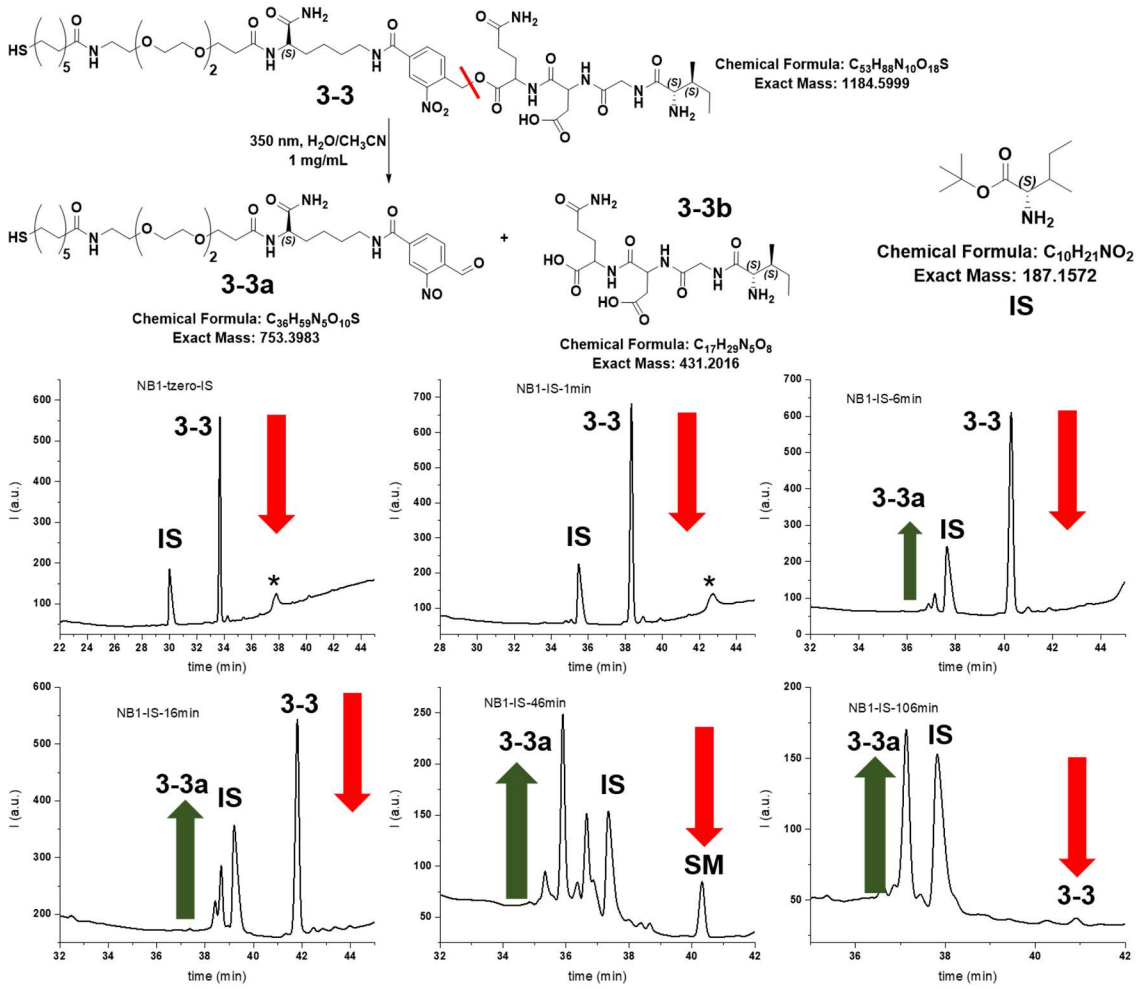

Figure 3-18 - RP-HPLC chromatograms of nitrobenzyl peptide **3-3** irradiation at 350 nm with IS. Green arrows: increasing intensity of photocleaved peak; red arrow: decreasing peak intensity of the starting material.

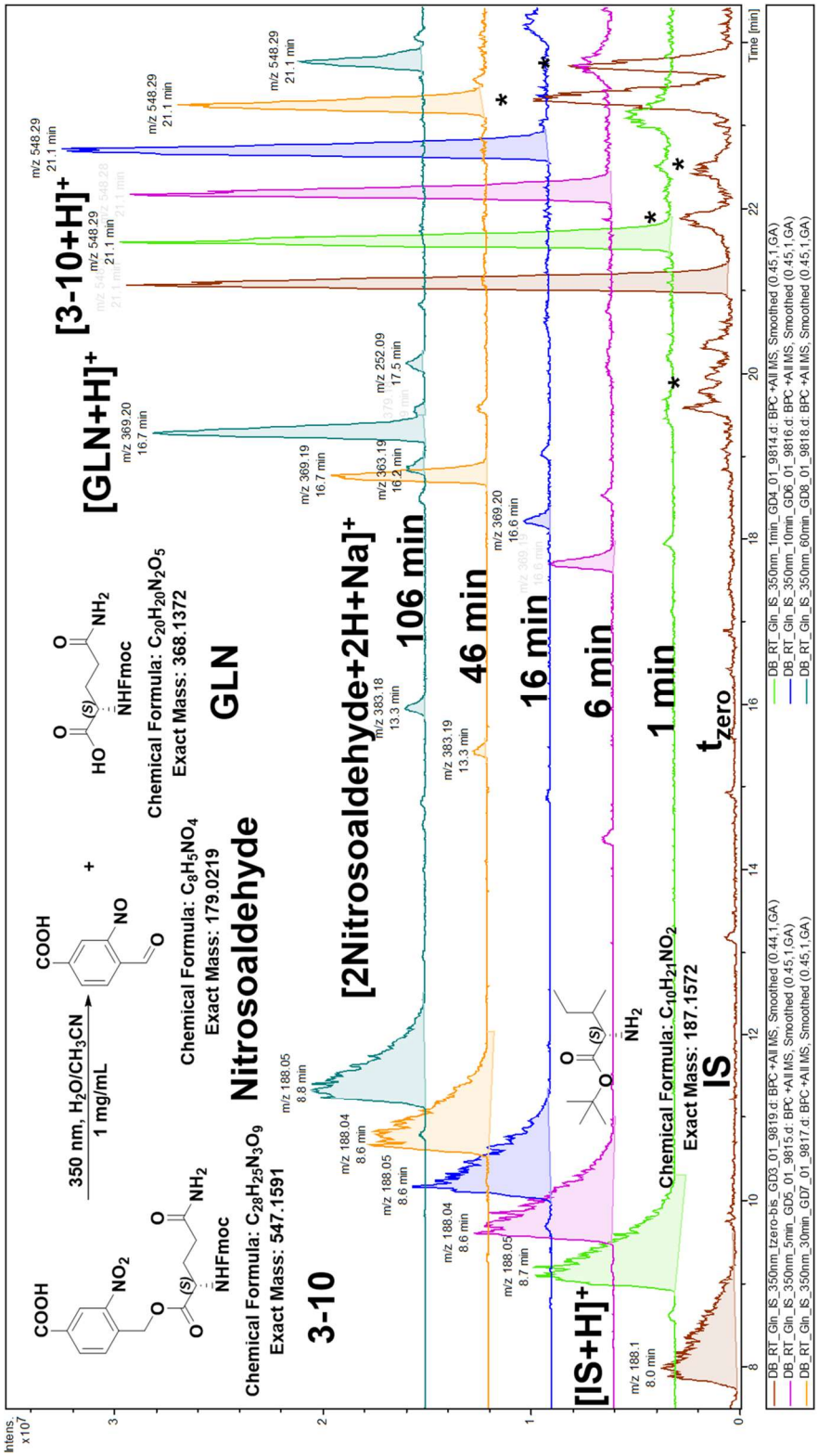

Figure 3-19 – RP-LC-MS chromatograms of Nitrobenzyl linker **3-10** irradiation. (*) impurities.

Different retention times due to a loss of performance by the HPLC column were encountered when monitoring the photocleavage of peptide **3-3** and a consequent different layout was adopted, to track the photocleavage on the chromatograms.

3.11. Irradiation of NVOC-bearing molecules 3-19, 3-20 and 3-26

Linker **3-19** was irradiated with the same conditions for photocleavage in solution (350 nm, 50 $mW \cdot cm^{-2}$; H_2O/CH_3CN; 1 $mg \cdot mL^{-1}$) and RP-HPLC monitoring chromatograms are shown in Fig. 3-20. Remarkably, RP-HPLC chromatograms showed complete photocleavage within 16 minutes. Retention time of starting material **3-19** was around 26 minutes, with two peaks, corresponding to the diastereisomers formed after the esterification with glutamine. IS has a retention time of around 19 minutes. Photocleavage product **3-19a** was not found neither in the LC-MS. Calculated photocleavage half-life for molecule **3-19** was 6.9 and 7.35 minutes for the two diastereoisomers, respectively. This remarkable improvement in the photocleavage rate was due to the methyl group in the benzylic position, that stabilises the radical intermediate, and the electron-donating effect of the methoxy and phenolate groups.

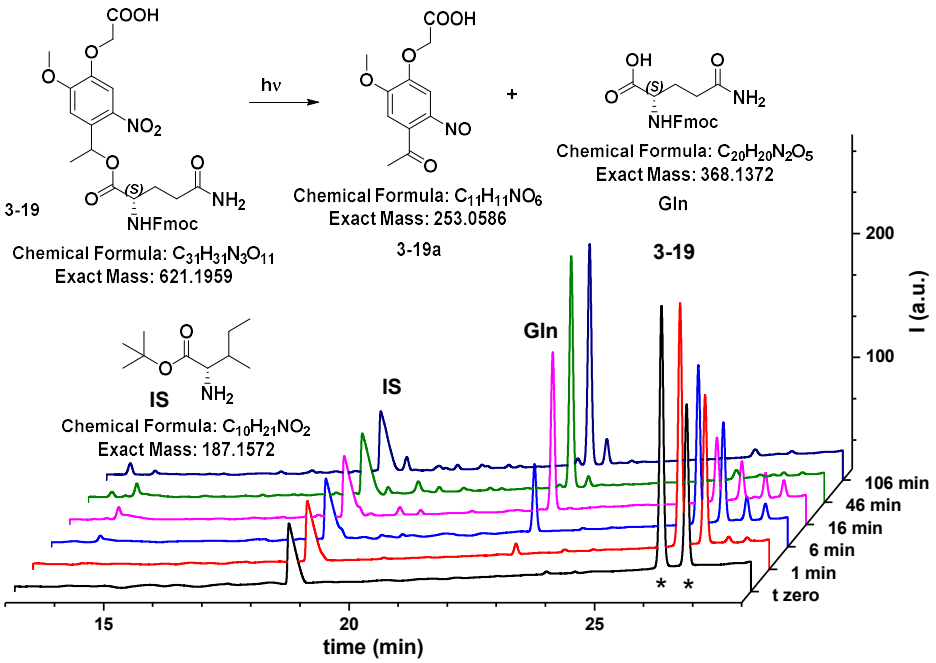

Figure 3-20 - RP-HPLC chromatograms of molecule **3-19** NVOC1 irradiation at 350 nm with IS (IS-Rt = 19 min, **3-19**-Rt = 26 min). (*) diastereoisomers.

Consequent LC-MS irradiation monitoring showed the same trend, confirming the peak assignment given from the RP-HPLC (Fig. 3-21).

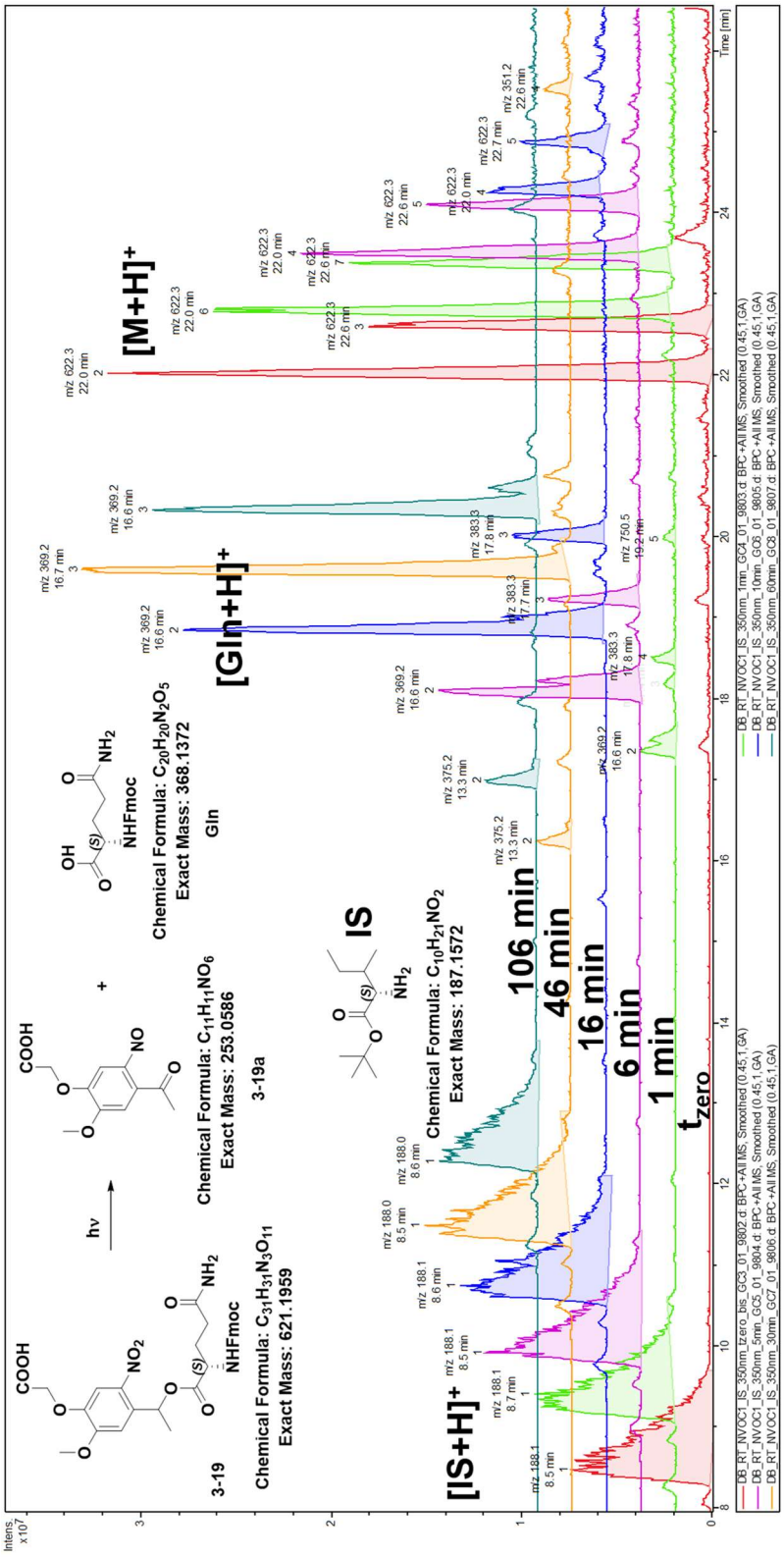

Figure 3-21 – RP-LC-MS chromatograms of molecule **3-19** NVOC1 irradiation at 350 nm with IS (Rt = 22 min).

LC-MS chromatograms (Fig. 3-21) showed a retention time of 8 minutes for IS. Glutamine photoproduct was found to have a retention time of 16.7 minutes, and the starting material was identified with a retention time of 22 minutes. As a last series of experiments, photocleavage properties of peptides **3-20** and **3-26** were screened.

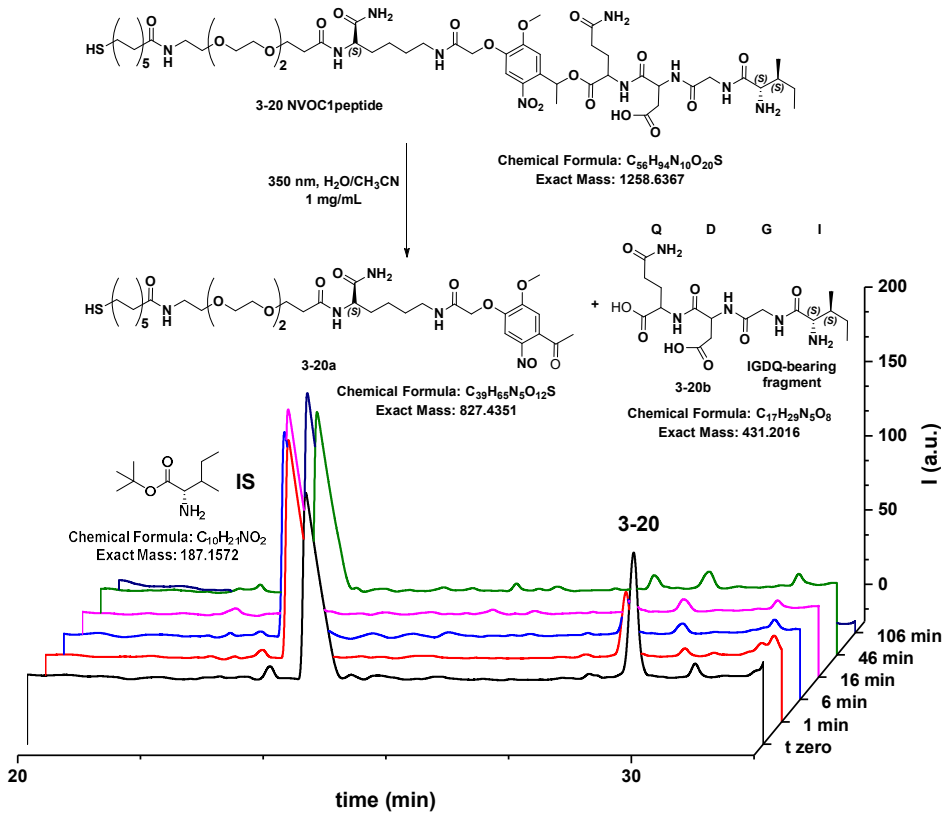

Figure 3-22 - RP-HPLC chromatograms of peptide **3-20** irradiation at 350 nm with IS (Rt = around 30 min).

Peptide **3-20** was irradiated, as shown in Fig. 3-22 and photocleavage was completed within 16 minutes of cumulative irradiation, with a retention time of around 27 minutes. Remarkably, calculated photocleavage half-life for peptide **3-20** was only around 6 minutes (mean value between 3.4 min with a 2nd degree exponential decay fitting and 8.8 min with a 1st degree exponential decay fitting, but discarding the final 3 points; see Appendix section 6.19). Interestingly, from the LC-MS analysis it was possible to detect the two peptide fragments from the photocleavage reaction as shown in Fig. 3-23. The shorter fragment **3-20b** bearing just the tetrapeptide IGDQ was found very early in the chromatogram, at 0.6 minutes. The bigger fragment bearing the mercaptoundecanoic acid and PEG moiety was found at 24 and 26 minutes.

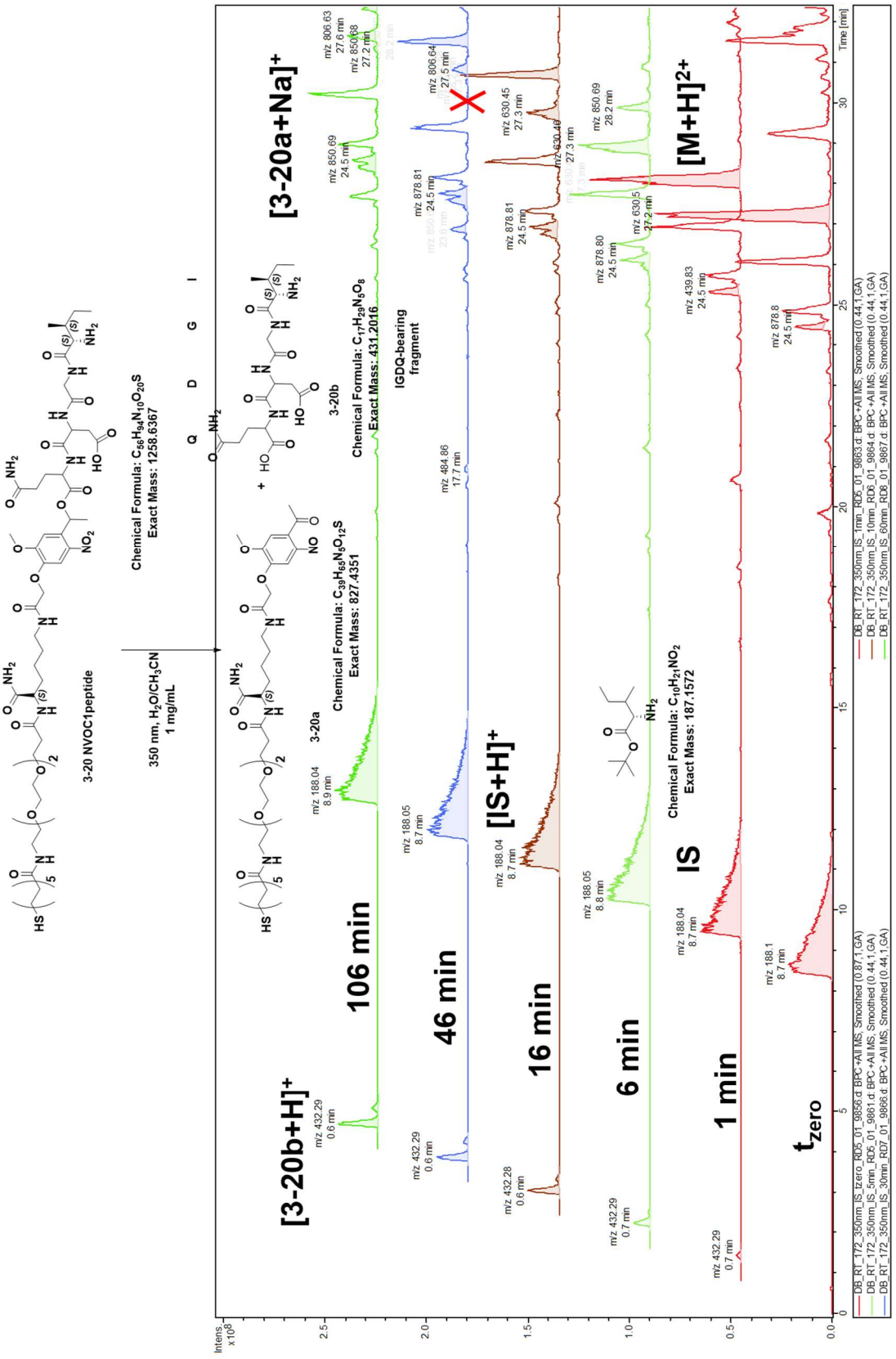

Figure 3-23 - RP-LC-MS chromatogram of **3-20** NVOC1 peptide irradiation at 350 nm with IS (Rt = 8.5 min).

Peptide **3-26** NVOC2 was irradiated and monitored in the same fashion. Photocleavage half-life for peptide **3-26** was 12 minutes. RP-HPLC from NVOC2 peptide irradiation showed a retention time of around 30 minutes. Furthermore, it was possible to identify the photocleavage products for irradiation of peptide **3-20** that can be seen in the LC-MS chromatogram above (Fig. 3-23).

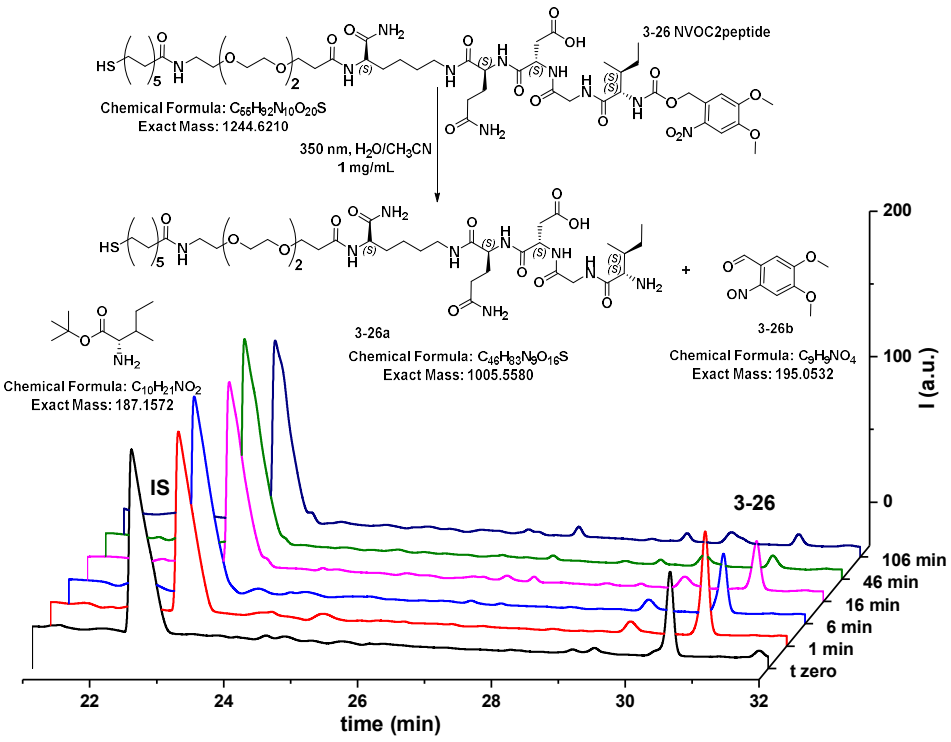

Figure 3-24 - RP-HPLC chromatograms of **3-26** irradiation at 350 nm with IS (Rt = 23 min).

Irradiation of peptide **3-26** monitored via LC-MS enabled the identification of the bigger fragment **3-26a** (retention time 24 minutes, Fig. 3-25) that corresponds to the previously described peptide **3-1** (Scheme 3-1) with a mass peak of $[M+H]^{2+}$ of 503 m/z. Unfortunately, clear detection of the nitrosoaldehyde **3-26b** was not possible. After such promising photocleavage results in solution, model peptides **3-3**, **3-20** and **3-26** were tethered on surface and tested. Results are discussed in the following section.

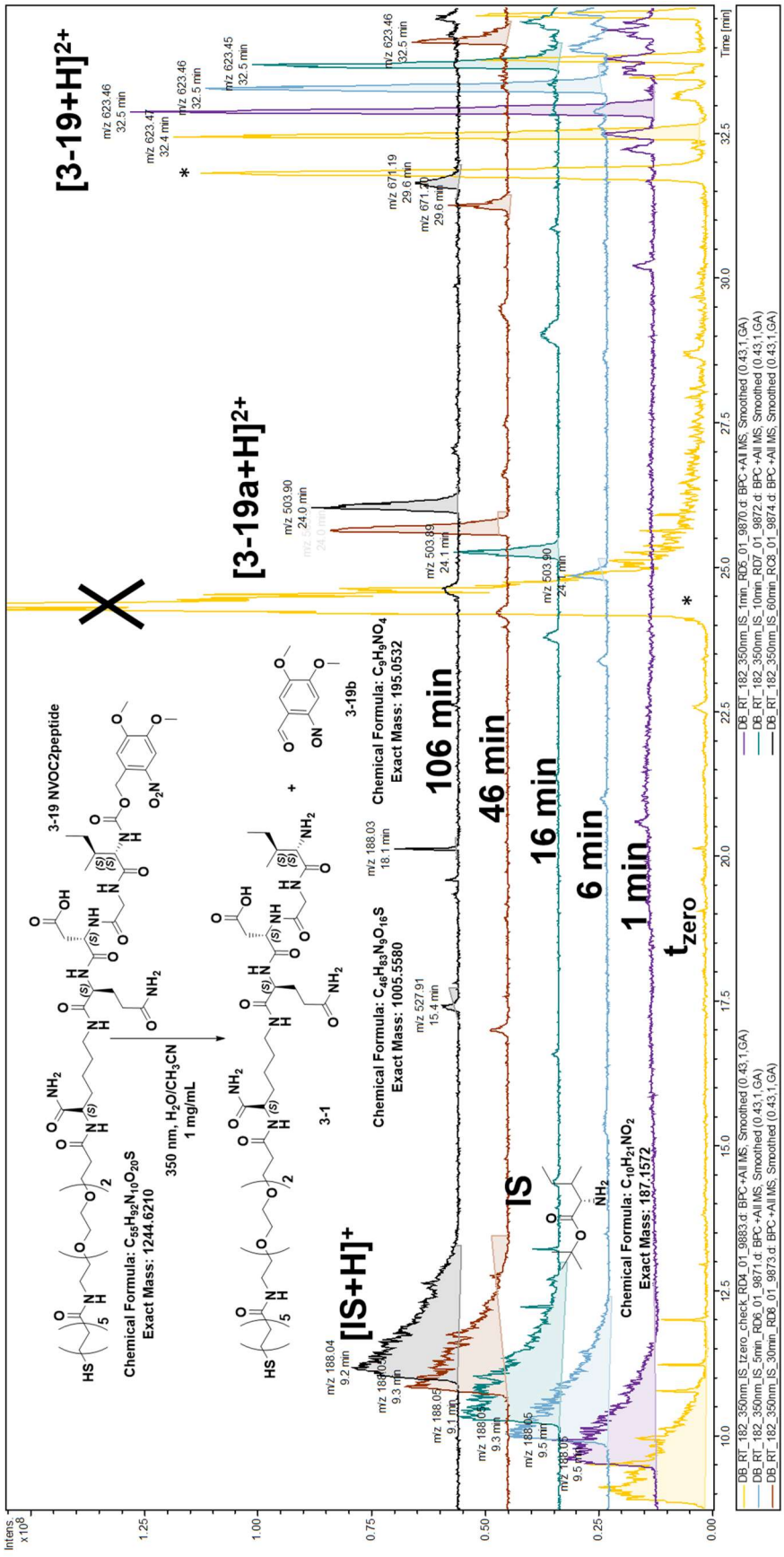

Figure 3-25 - RP-LC-MS chromatogram of peptide **3-26** irradiation at 350 nm with IS (Rt = 8.5 min).

3.12. Irradiation of double gradients of photolabile peptides 3-3, 3-20 and 3-26. WCA characterisation

Results of the irradiation experiments on SAMs of photolabile peptides are reported and discussed in this paragraph. Mixed SAMs of nitrobenzyl-bearing peptide **3-3** were prepared. Static WCA was assessed. Surfaces were then irradiated while submerged in PBS (Gibco), then washed, dried in air and WCA was iteratively performed again. Regarding peptide **3-3** SAM, this procedure was repeated for several hours until WCA values dropped (Fig. 3-27). Wettability and XPS characterisations were performed to monitor photocleavage. Since the shallow nature of the anisotropic peptide gradient, isotropic SAMs were monitored primarily by WCA and anisotropic surfaces were characterised by XPS.

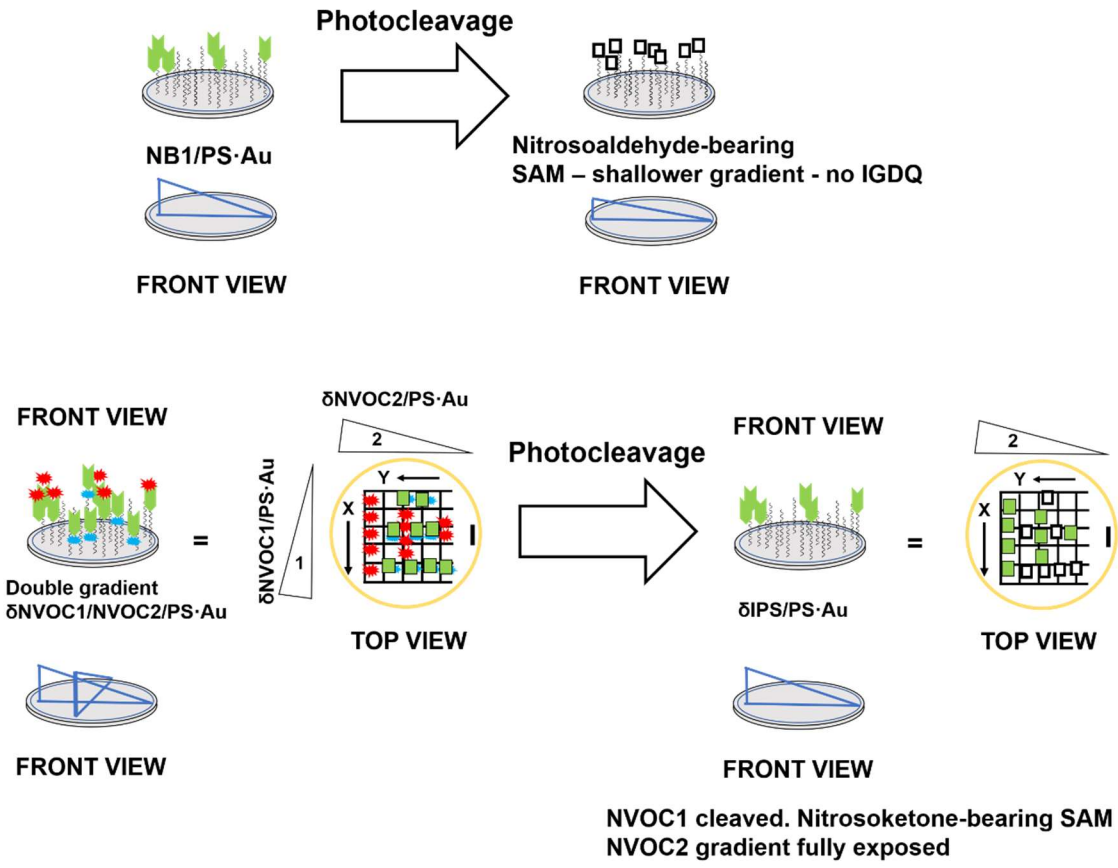

Figure 3-26 - Surface irradiation schemes: TOP Irradiation of the nitrobenzyl-bearing peptide **3-3**. BOTTOM: irradiation scheme of δNVOC1/NVOC2/PS·Au.

As shown from Fig. 3-27, irradiation of peptide **3-3** on an isotropic SAM would have led to the loss of the IGDQ sequence leading to a truncated peptide form with the central Lysine exposed to the cell interface (detail shown below Fig. 3-27). Potentially toxic formation of nitrosoaldehyde that could react with proteins from outer-cell membranes was a possibility that was taken into consideration; however, the large excess of water

medium and nutrients was expected to interact as well, minimising this effect. The first set of surface irradiation experiments were performed on SAMs of nitrobenzyl-bearing peptides **3-3**. The Scheme reported below shows the WCA of an isocratic mixed SAM of nitrobenzyl-bearing peptide and molecule **3-2** (Scheme 3-1) as a backfiller. Backfiller was introduced to have the highest wettability contrast possible, with an extended peptide conformation over the monolayer (see scheme in Scheme 3-15).

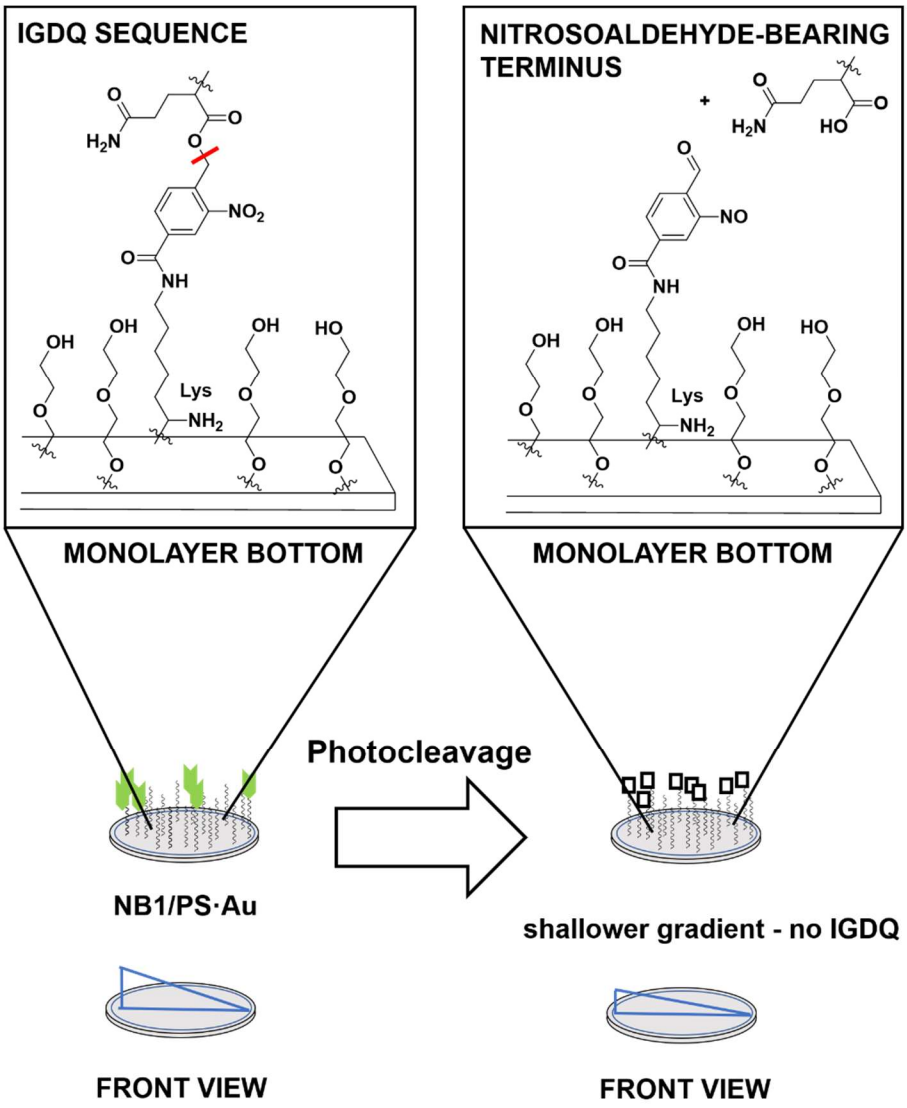

Scheme 3-15 – Detail of a SAM of peptide **3-3** and backfiller **3-2** with a photocleavage reaction cleaving the peptide chain bearing the motogenic sequence IGDQ. Peptide structures are shortened for clarity and only the monolayer top is shown.

Nitrobenzyl-bearing peptide **3-3** was found to have a static WCA of around 50°, as well as peptide **3-1**. Static WCA of the backfiller was 30° in a single-component monolayer. In a mixed SAM with peptide **3-3** and backfiller **3-2** WCA was expected to drop to values near 30°. This change was expected to be detected by successive WCA measurements. This expected result was observed but unfortunately not in the desired

time-frame of 15 to 20 minutes. Specifically, WCA dropped down considerably from around 50° to below 40° and close to 30° in around 2.5 h.

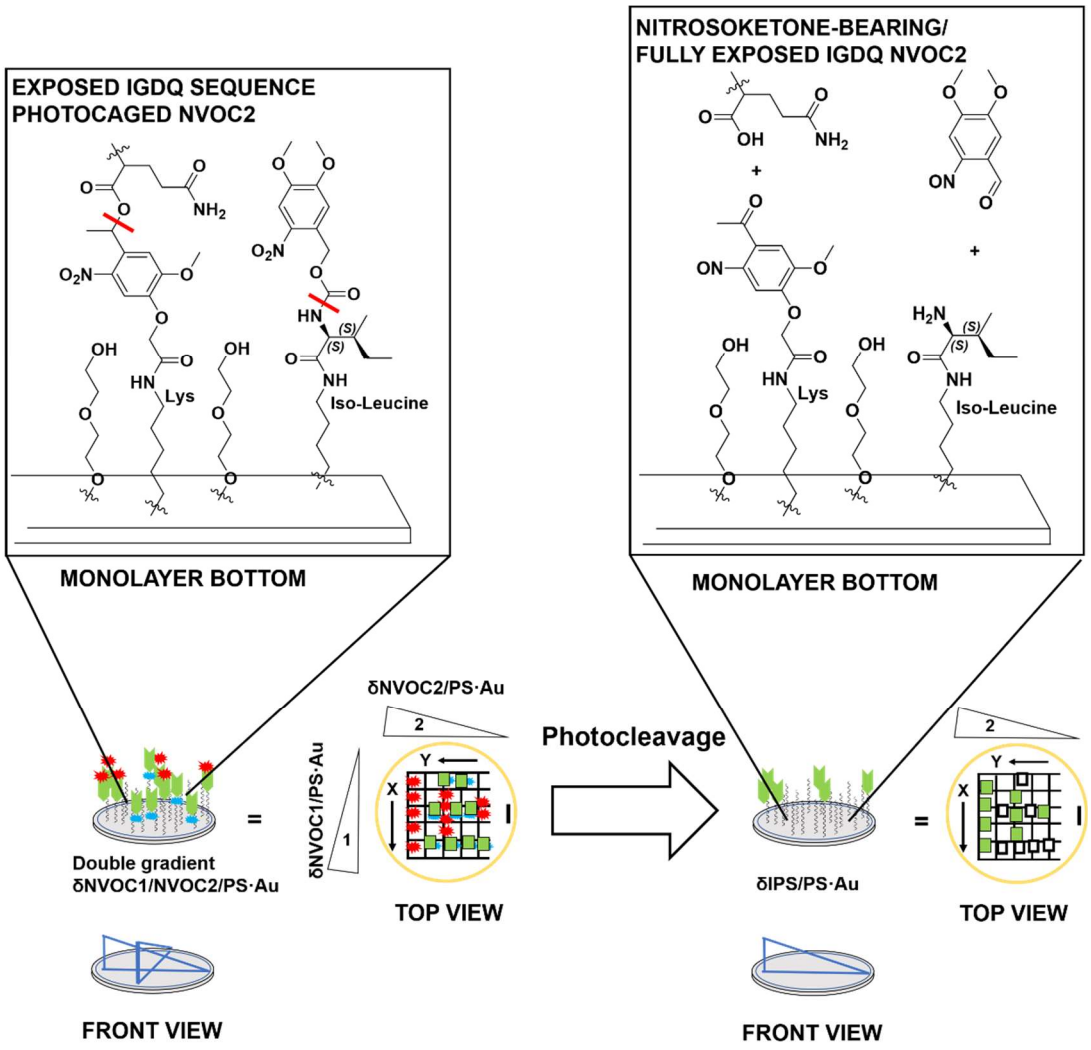

Scheme 3-16 – Detail of a NVOC1/NVOC2 SAM with a photocleavage reaction cleaving the peptide chain bearing the motogenic sequence IGDQ. Peptide structures are shortened for clarity and only the monolayer top is shown.

As shown in Scheme 3-15, peptide **3-3** was expected to cleave forming the corresponding nitrosoaldehyde compound, that in aqueous medium should have reacted and formed the gem-diol derivative (not shown). Because of the poor photocleavage rate of peptide **3-3** shown on surface, the formation of photoproducts upon irradiation was very slow and few hours of irradiation were necessary to cleave the majority of the nitrobenzyl moiety. In conclusion, nitrobenzyl-bearing peptide **3-3** photocleavage half-life obtained from SAM irradiation was not compatible for cell culture irradiation. Isocratic single-component SAMs of peptides **3-20** and **3-26** were also irradiated and their wettability was monitored by static and dynamic WCA. A scheme of SAM irradiation in a monolayer of peptide **3-20** is shown in Scheme 3-16.

Photocleavage of the NVOC group would lead to nitrosoketone group. Ketones are also known to form gem-diol species in water, however a dramatic change in WCA was not observed. Static and dynamic WCA on separate SAMs are reported in a single chart shown below. In Figure 3-28328 3-28, 4 experiments of WCA are summarised: 2 static and 2 dynamic WCA experiments on single-component SAMs of peptides **3-20** and **3-26** are reported. Each trendline shows one experiment.

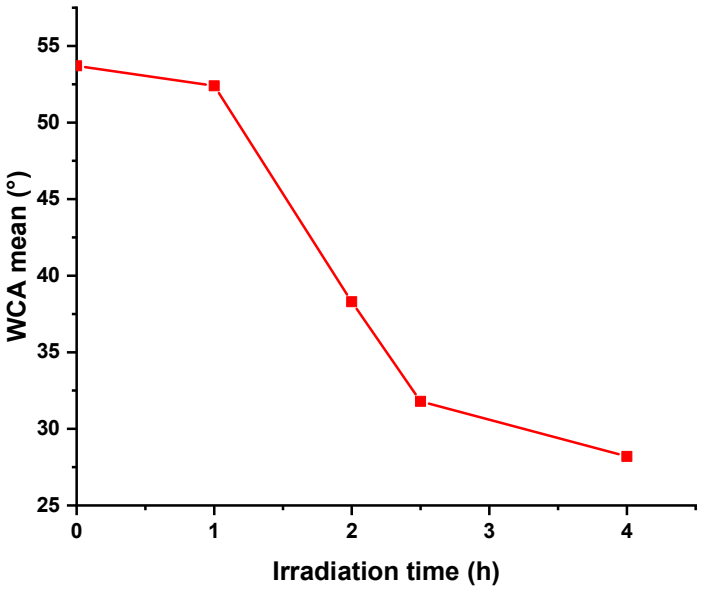

Figure 3-27 – WCA vs time plot of an isocratic mixed SAM of peptide **3-3** and backfiller **3-2** (1:9 molar ratio respectively) irradiated at 350 nm in PBS (surface submerged, 50 $mW \cdot cm^{-2}$, Hg lamp).

Figure 3-28 shows the static and dynamic WCA variation upon irradiation. Peptide **3-26** is very hydrophobic with a static WCA of around 71° and peptide **3-20** is more hydrophilic with an initial WCA value below 50°. As irradiation started, static WCA values shifted up and downwards for NVOC2 and NVOC1 peptides, respectively. As irradiation proceeded, WCA values of peptide **3-26** NVOC2 decreased, since the photocleaved moiety on surface was peptide **3-1** with a known static WCA characterised at around 50°.[1] Static WCA of peptide **3-20** remained constant at around 45°. According to RP-HPLC, LC-MS and XPS data shown in this chapter, it was expected that most of the peptide was photocleaved within 15 minutes of irradiation. Peptide cleavage caused massive disruption in the SAM architecture, showed by the static WCA values shown in the early minutes of irradiation (Fig. 3-28). Concerning the dynamic WCA shown in Fig. 3-28, both peptides presented the same initial value of 10° indicating a rather compact single-component monolayer. As irradiation started, ARCA values diverged respecting the static WCA trend. As irradiation continued, ARCA-WCA of peptide **3-20** was found to be almost as the initial value. This indicates that peptide

irradiation did not change the overall packing of the monolayer. Conversely, peptide **3-26** irradiation trend diverged, increasing the ΔARCA values, showing unexpectedly a weakening of the packing architecture, from 20° to almost 40°. This could be due to the photocleaved nitrosoaldehyde reacting with the peptide, or simply a SAM rearrangement. As a last experiment, isocratic multicomponent SAMs of peptides **3-20** and **3-26** with a molar ratio of 1:1 were fabricated. Figure 3-28b shows the static and ARCA-WCA of the two-component 1:1 isocratic monolayer.

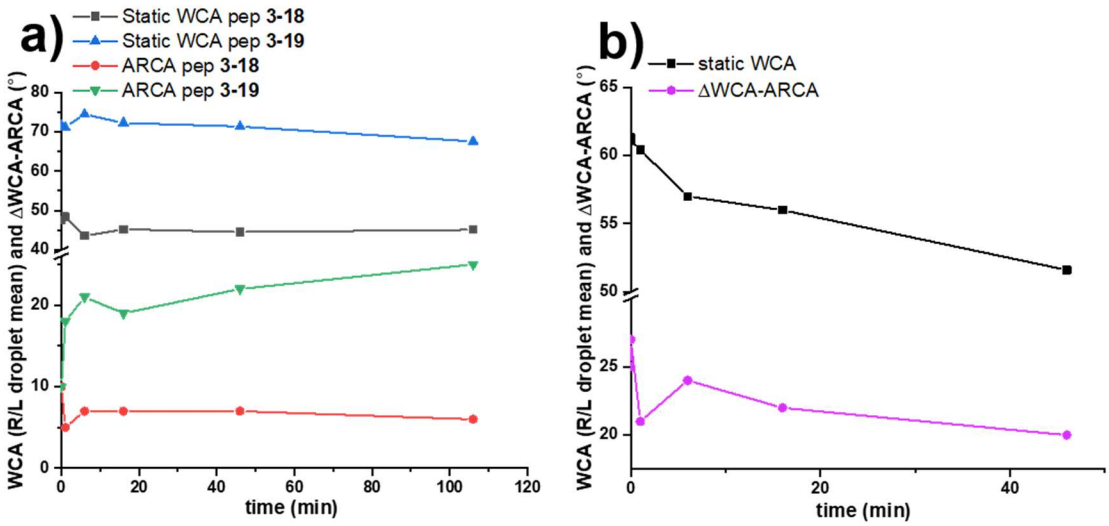

Figure 3-28 – a) WCA and ARCA-WCA vs irradiation time plot of isocratic SAMs of peptides **3-20** and **3-26** (NVOC1 and NVOC2 respectively) irradiated at 350 nm in PBS (surface submerged, 50 mW·cm^{-2}, Hg lamp); b) Isocratic SAM of peptides **3-20** and **3-26** (1:1) with static and ΔWCA-ARCA plots.

This mixed monolayer possessed the characteristics of both peptides. Static WCA value was over 60° but as irradiation continued it dropped down to 50° similarly to static WCA of peptide **3-1**. Dynamic contact angle dropped sharply over 20°, then went midway to the beginning then went again over 20°. The sharp dynamic WCA decrease in the first minutes was speculated to be due to the monolayer cleavage, causing some disorder in its packing. This monolayer disorder effect decreased over time as peptide irradiation was protracted over time, resulting in a lower dynamic WCA value after 40 minutes.

3.13. XPS characterisation of the double gradient of probe peptides 3-5 and 3-6

XPS surface characterisation was performed according to the scheme shown below (Fig. 3-29). Surfaces were patterned according to the previously described procedure and mapped along the shown points b). Model peptides **3-5** and **3-6** were tethered on gold-coated round coverslips following the already optimised procedure (17 μm·s^{-1}

dipping and 10' immersion). Surface flipping between dipping steps was set at 180° as shown in Fig. 3-29 b) and c). Double gradient experiments with probe peptides (colour code peptide **3-5** grey and peptide **3-6** green, throughout this thesis) were the only one performed with 180° dipping orientation.

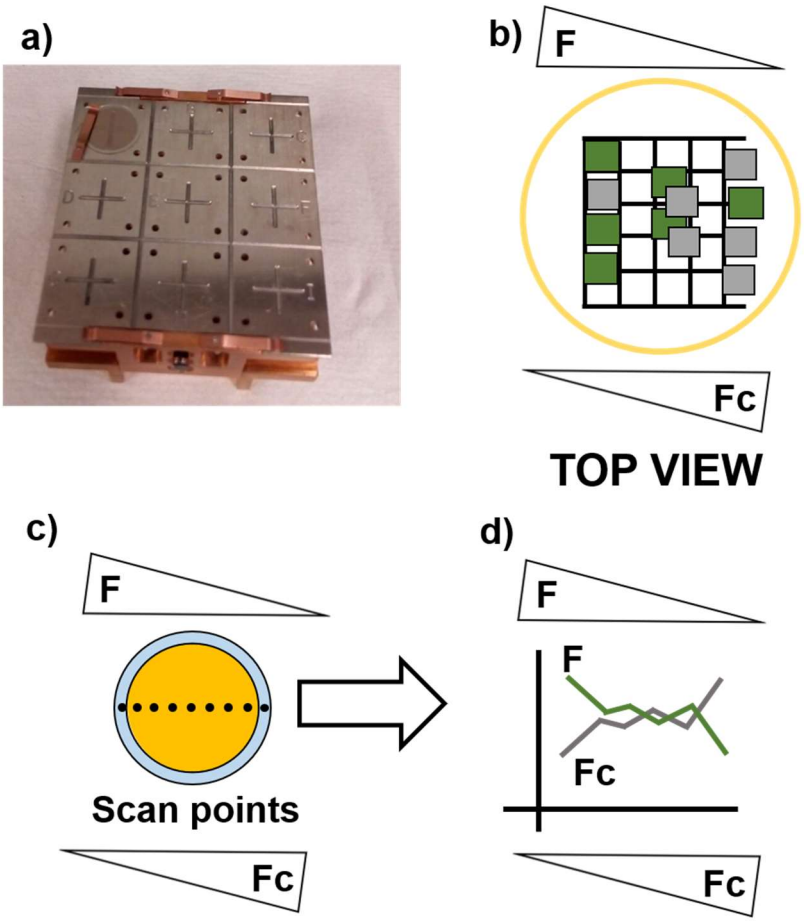

Figure 3-29 – a) XPS sample holder; b) Double peptide gradient pattern for **3-5** and **3-6** (Fc and F respectively). Colour code = Grey for peptide **3-5** and olive green for peptide **3-6**; c) scan points; d) data collection: monitored iron and fluorine are reported in a single plot with two opposite trends.

Double gradients of peptide **3-5** and **3-6** had been fabricated on the same dipping direction, with opposite gradient versus, since the two characteristic elements such as fluorine and iron were present in only one peptide each, not leading to ambiguous gradient characterisation. Targeted elements were F1s for fluorine and $Fe2p^3/_2$ for Iron also because of their relatively high intensity therefore easy assignment. At% detected on the scanned points was plotted in a chart with a standard layout used throughout this thesis for representing the double gradients on surface. Mapping points on the double gradient plots are reported from left to right for peptide **3-5** and from right to left for peptide **3-6**. In all the other double gradient plots the gradient is always set from left to right. Monodirectional gradients were first fabricated and are shown in Fig. 3-30. The

monodirectional gradients are shown in the same plot chart but belong to different surfaces. Patterned Gold surfaces were scanned on 9 points. The first and the last scan points were placed on the bare glass, as reference, while the other were placed along the gradient, from the low concentration to the highest. Dipping speeds were tested, ranging from 10 minutes for each peptide, 7 minutes, with or without the backfilling step. After 6 different conditions screened, the gradient slope was eventually tuned. Since the adsorption kinetics were not assessed, mirror experiments were performed to detect peptide displacement and have a qualitative assessment of the adsorption rate. Two twin experiments were performed, dipping peptide **3-5** first then **3-6** on a surface and then inverting the dipping order on another surface. The first twin experiments were double gradients of peptides **3-5** and **3-6** with 10' dipping each without any backfilling step. These experiments led to asymmetric gradients, with different slopes and poor adsorption.

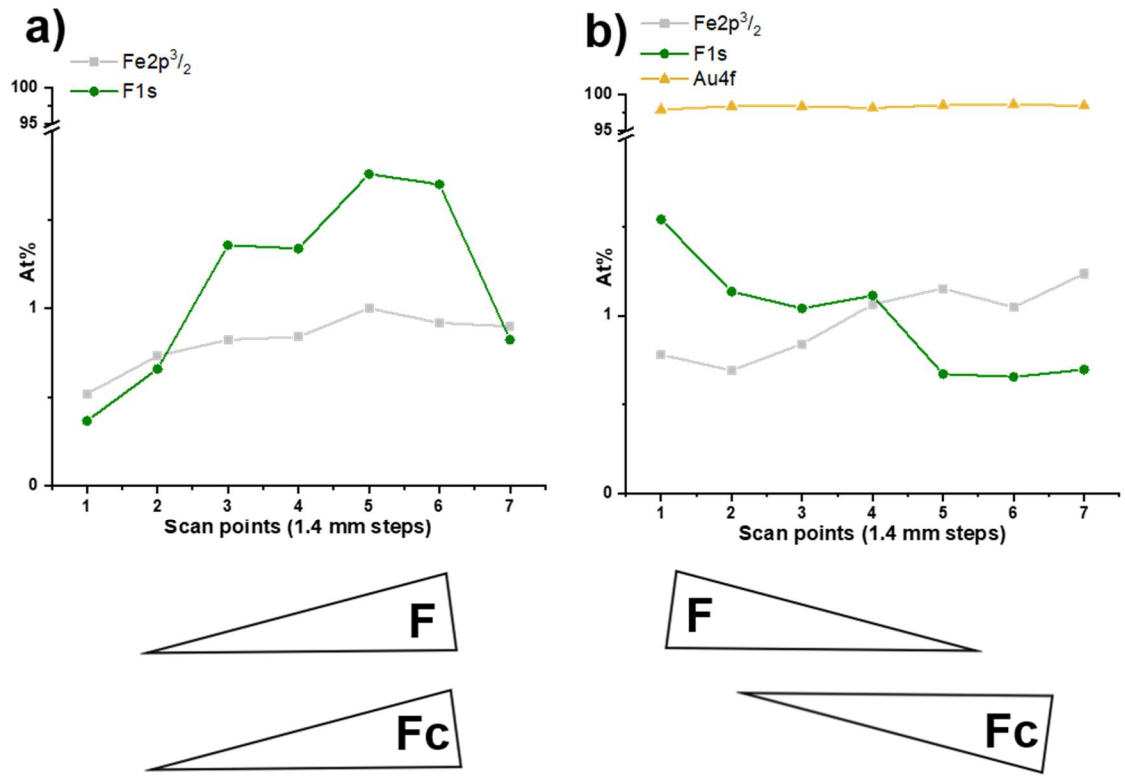

Figure 3-30 – a) separate XPS mappings of single concentration gradients of δF/PS·Au Fluorine (Olive green) and δFc/PS·Au Iron (LT grey) on different surfaces (coverslips); b) δFc/F/PS·Au plotted with the same colour code (golf for dark yellow Au4f At%).

Decreasing the dipping time to 7' led to more homogeneous monolayers with linear trends, minimising the displacement of peptide **3-5** by **3-6**, although no gradient symmetry was recorded. At last, when 7' dipping and a 5' backfilling steps were adopted, the final result displayed was obtained (Fig. 3-30).

Remarkably, peptide **3-6** had a greater adsorption rate in all the experiments and displacement did not seem to occur when increasing the dipping time of its counterpart peptide **3-5**. Since their relatively low abundance in their respective molecules, At% of fluorine and iron did not reach values greater than 1.5%. The dipping speed was increased to 36 $\mu m \cdot s^{-1}$ for a dipping time of 7'. The introduction of the backfiller as a packing step after the anisotropic dipping was very helpful to equilibrate the two different peptide adsorption steps. Having set a protocol for the double gradients on gold-coated coverslips, the next step was the synthesis and characterisation of the photolabile peptides, to be able to characterise the double gradient of photolabile peptides.

3.14. XPS characterisation of double gradient of peptides 3-20 and 3-26

XPS characterisation of double gradient experiments with NVOC series peptides **3-20** and **3-26** have been performed. Single gradients with and without backfilling were fabricated and mapped (experiments reported in the Appendix). Double gradients were fabricated according to the previously described procedure. Twin experiments were performed, using peptide **3-20** as first peptide and then **3-26** as first in the sequence. This procedure led to similar but not identical results, due to the different adsorption kinetics of the two peptides. Surfaces were mapped with grid points shown in Fig. 3-31 below, from low to high concentration. First and last points were placed on the glass surface, and all the other points are scanned on the Gold layer. Double concentration gradients of photolabile peptides were mapped with an XPS technique called "snapshot mapping" that requires shorter acquisition time, compared to the traditional analysis on multiple points. A grid of multiple points is drawn over the surface to be mapped, and the XPS gun scans the sample recording the survey and the selected elements. The survey (not reported but available in the raw data files) is the full spectral collection of signals (typically expressed in $counts \cdot s^{-1}$ or At% vs. Binding Energy BE). Selected elements were carbon C1s, nitrogen N1s, oxygen O1s, Sulphur S2p and gold Au4f. Results are represented by plotting the Atomic percentage of the scanned element (At %) vs. the position on surface, as the general protocol. The scanned points are around 1.4 mm distant from another, along the 13 mm diameter of the Au-coated glass coverslip. Scan points of the entire grid were used as average, plotting the points from the two X and Y axis on two charts shown below (Fig. 3-32). Charts were plotted separately because of the different number of scan points. The number of points

recorded on Y axis is not as much as the X, because of the copper electrode clamped over the metal surface, blocking a part of the surface. Surfaces were placed in the sample holder with the same orientation despite having different dipping sequences. When plotting the double gradient results of XPS mapping the first plot a) corresponded to the X axis and b) to the Y axis (Fig. 3-32). Since the surfaces were positioned in the same way, every X plot mapped δNVOC1 gradient (peptide **3-20**), while Y reported δNVOC2 (peptide **3-26**). This enabled a direct gradient comparison between multiple experiments.

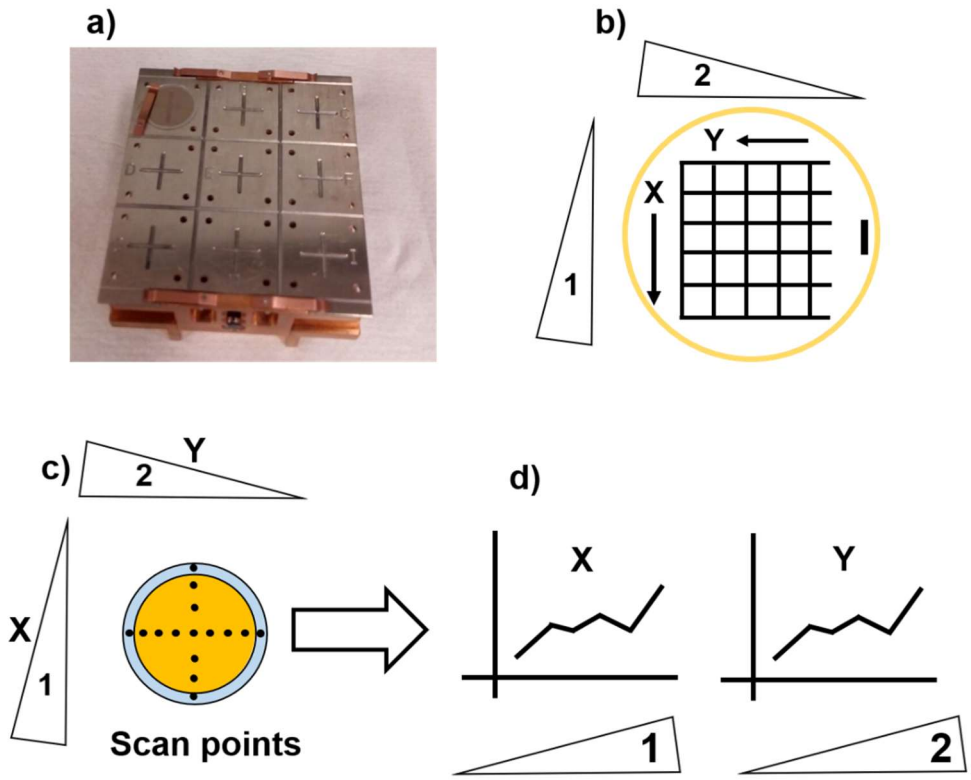

Figure 3-31 – (a) XPS sample holder with a round coverslip; (b) XPS snapshot mapping grid; (c) scan point direction along the two peptide gradients; (d) data processing: gradients from the two axis X and Y are exported in two plots and compared.

The first double gradient plots shown below (Fig. 3-32 a) and b)) have a similar carbon C1s At% trend for δNVOC1 at around 70% and δNVOC2 at around 40%, both being very shallow. Gold content is similar in the two plots, with an opposite trend on the monolayer. Oxygen percentage is much lower in δNVOC2 plot but surprisingly the gradient is much more evident, compared to δNVOC1. Nitrogen gradients can be seen from plots a) and b) even at low At%. Sulphur S2p gradients are very shallow, at the bottom of both charts. From the first gradient, it is possible to conclude that there is preponderant adsorption of peptide 3-20 when used first in the dipping procedure. This

fact led to a higher At% signal of δNVOC1. Carbon and oxygen contents differ in the two plots, indicating that the prevalent gradient established is δNVOC1.

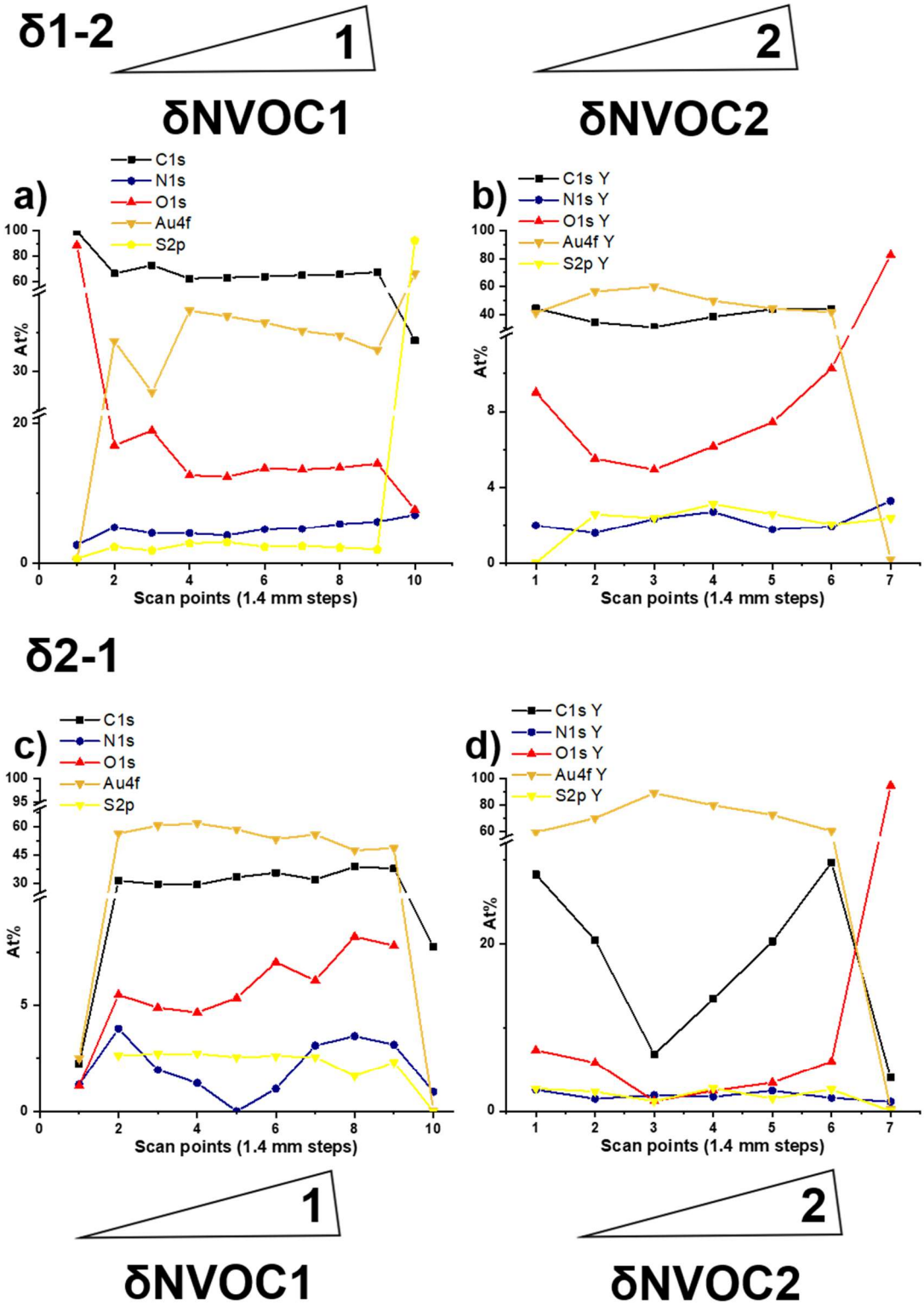

Figure 3-32 – a) δNVOC1/NVOC2/PS·Au X axis (NVOC1 gradient); b) δNVOC1/NVOC2/PS·Au Y axis (NVOC2 gradient); δNVOC2/NVOC1/PS·Au X axis (NVOC1 gradient); b) δNVOC1/NVOC2/PS·Au Y axis (NVOC2 gradient).

Concerning the twin experiment with an opposite dipping procedure (δNVOC2 then δNVOC1) shown in the plots c) and d), carbon C1s At% content is much lower than the previous experiments. δNVOC1 gradients in c) plot are surprisingly much more evident that a), although with lower intensity. Aberrating carbon trend in plot d) could be due to desorption or a damaged surface. Oxygen content was found to be around 5% for δNVOC1 and 10% for δNVOC2, respectively. Similar nitrogen N1s values were found, with poor gradient trends and low At%. Sulphur S2p was found to be roughly constant along the surface. In conclusion, δNVOC2/NVOC1/PS·Au (plots c) and d) Fig. 3-32) gave as outcome a poorly patterned monolayer, with a possible flat adsorption of δNVOC2 as first peptide, probably preventing adsorption of the second one in sequence δNVOC1. This led to lower At% values recorded in the surface mapping. Both experiments showed shallow but evident gradients of nitrogen and oxygen, along with carbon. Inverse trend of gold was always found in the experiments, as indirect proof of anisotropic distribution of peptides along the substrate.

3.15. Irradiation of double gradients of photolabile peptides 3-20 and 3-26 characterised by XPS

After the characterisation of the double gradient, surface irradiations were performed, testing the photocleavage properties of the anisotropic monolayers. Twin experiments were performed also for this section. Different results were obtained for the two dipping sequences but only one is reported below.

Surface irradiation experiments were performed in well-plates were the surfaces were immersed in HBSS (Gibco). Such culture medium is suitable for temporary cell storage outside the incubator, provided with standard nutrients but without the phenol red indicator, that impedes clear imaging. Surface irradiation was performed with UV-C solarium lamps (365 nm, 3 x 40 W) and irradiation power was monitored with a light sensor. A grid of 13 by 8 points was collected and the average of each X and Y axis was plotted in Fig. 3-33 and 3-34. Different elements were scanned such as C1s, N1s, O1s and Au4f, as standard protocol for XPS surface characterisation. Atomic % (At%) of the elements vs. position is reported in the charts. In the first experiment two surfaces were analysed. The first double gradient surface was analysed without any previous irradiation. The second surface was irradiated for 30 minutes and then analysed by

XPS in the same session with the one kept in dark. Figure 3-33 shows two series of charts per element. The first unlabelled chart of a single elements refers to the X axis average signal collected, and the other one reports the Y axis. Surface chemical gradient is traditionally plotted from left to right as standard protocol. Trendlines were added with default Origin fitting and unfortunately do not always shows the actual trend, because of the presence of outliers that were not removed for consistency.

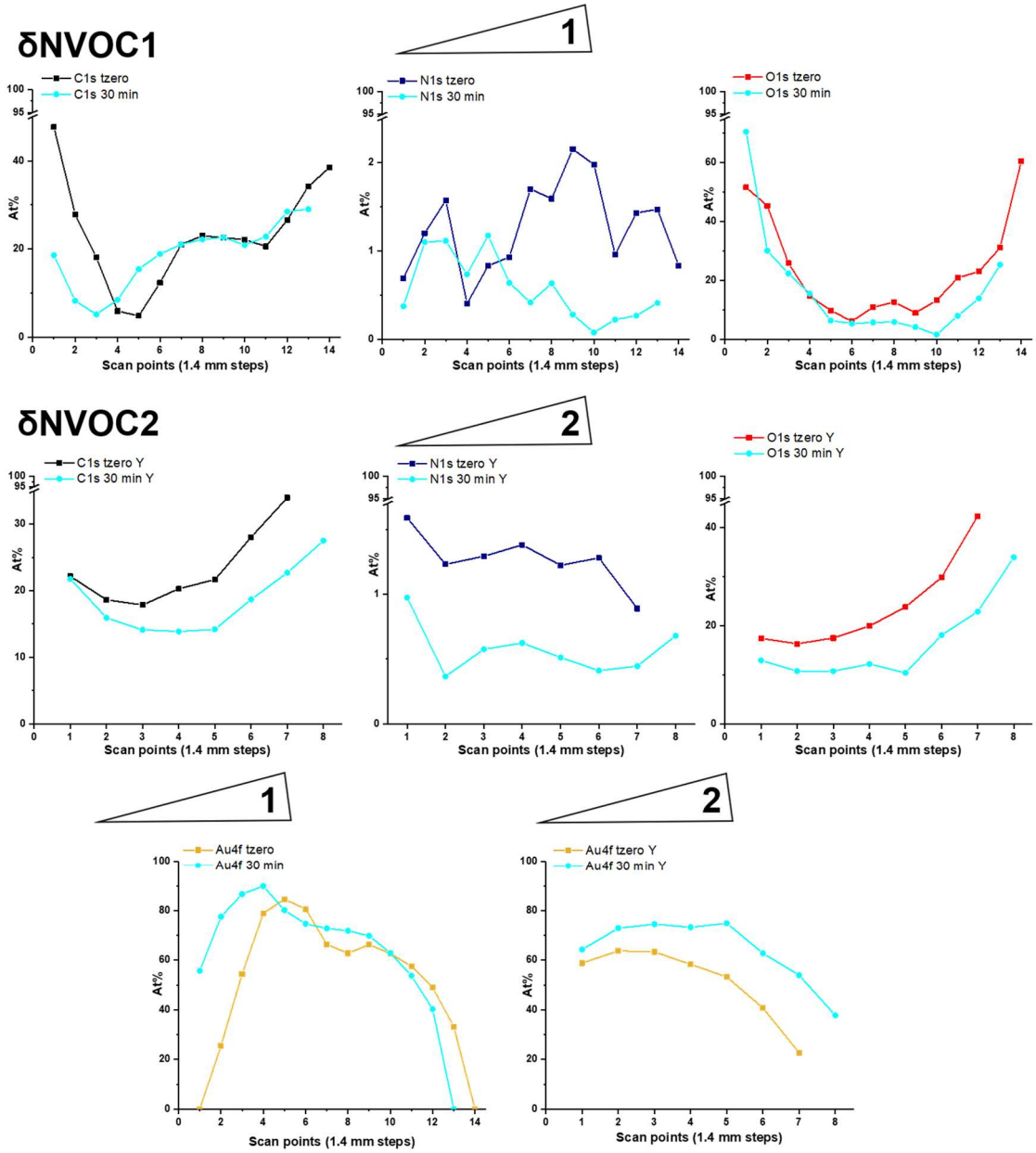

Figure 3-33 – XPS characterisation of double gradient of peptides **3-20** and **3-26**. 30-minute irradiation at 365 nm, 3 x 40 W lamps, full immersion in HBSS cell culture medium.

Colour code was assigned to each element: black for C1s, navy for N1s, red for O1s, gold for Au4f and yellow for S2p. This colour code is maintained throughout the thesis for easier data comparison. Cyan was chosen as universal colour for each element

belonging to the surface irradiated 30 minutes, to be distinguishable from time zero plot. As shown in Fig. 3-33, 30-minute irradiation signal has lower At% due to the photocleavage reaction. Conversely, with less material on surface, Au4f signal increased intensity, as shown at the bottom of the image. Twin experiments were performed, tethering first peptide **3-20** and then **3-26** and vice-versa.

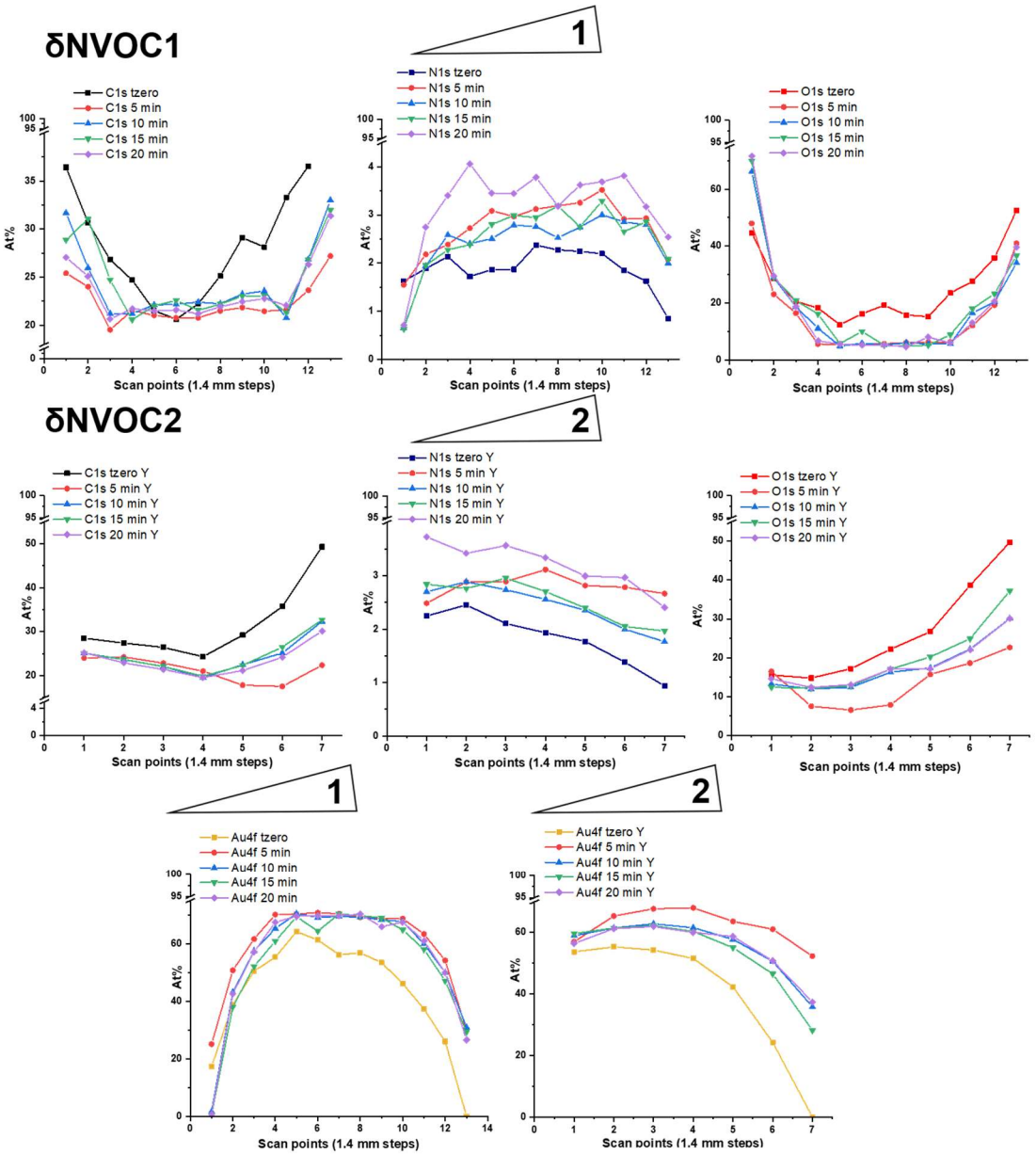

Figure 3-34 - XPS characterisation of δNVOC2/NVOC1/PS; 20-minute irradiation at 365 nm, 3 x 40 W lamps, full immersion in HBSS cell culture medium.

Because of the same sample orientation in the XPS sample holder, peptide **3-20** (NVOC1) gradient is always shown on X axis, meanwhile peptide **3-26** (NVOC2) is shown on Y axis and result comparison is possible. Experiments with NVOC2-NVOC1-

PS double gradient were unfortunately not successful. Specifically, time zero surface signal intensity was lower than the irradiated surface, with the opposite trend for gold. This could be due to incorrect surface manipulation, with accidental light exposure and monolayer photocleavage, leading to unbalanced surface signal of the scanned elements. In this second experiment shown in Fig. 3-34, 5 double gradient substrates were characterised by XPS surface mapping. Dipping sequence for such experiment was δNVOC2 then δNVOC1 and then the final backfilling step. The first surface was not irradiated, and the other 4 were irradiated in progression, one for 5 minutes, one for 10 minutes, another for 15 minutes and the last for 20 minutes. This experiment was repeated multiple times in twin duplicates. The double gradient of photolabile peptides can be seen for almost all the scanned elements. In Fig. 3-34 the At% of different elements were monitored and plotted together. Carbon C1s mapped along the X axis (Fig. 3-31b)) corresponding to δNVOC1 peptide gradient was found to be rather constant among all the irradiated surfaces, confirming that peptide cleavage on our system could be monitored by XPS. This trend was mirrored by all the other elements, except for gold Au4f. Gold trend was the opposite, with increasing intensity as the irradiation proceeded, as an indirect proof that the photocleavage occurred. Regarding the two gradients δNVOC1 and δNVOC2, respectively, although less points were mapped along the Y axis, a better trend was found, with less outlier points. Overall At% values are very low, indicating poor peptide adsorption.

3.16. Conclusions

As shown from sections 3.5 and 3.6, it was possible to design, synthesise and optimise a two-peptide system with a tuneable chemical gradient. Synthesis of the first photolabile peptide was accomplished, however nitrobenzyl-bearing peptide **3-3** did not comply with our irradiation requirements, cleaving in more than 30 minutes both in solution and on surface. Thanks to the novel strategy adopted, NVOC-bearing peptides **3-20** and **3-26** fulfilled our requirements regarding irradiation time and potential toxicity. Furthermore, because of the chosen design of the photolinkers with one carboxy and a Fmoc-protected amino group, solid-phase synthesis tool was used with routine protocols as a dynamic strategy that could host different peptide sequences but also custom monomers, simply extending the coupling time or performing a double-coupling step to ensure maximum conversion.

Irradiation experiments of photolinkers alone and peptides were successful, characterising the photocleavage products for peptide **3-20**. Specifically, peptide **3-20** cleaves very easily within 15 minutes, and even if peptide **3-26** releases a

nitrosoaldehyde molecule, when converting this system to cell irradiation, cell medium will be replaced after irradiation, minimising the exposure to a potentially toxic molecule.

XPS characterisation was successful and enabled a further insight into monolayer formation mechanism. Ferrocene-bearing peptide **3-5** and fluorine-bearing peptide **3-6** revealed to be a very useful tool for the three-step dipping procedure. Protocol optimisation was crucial for understanding peptide adsorption kinetics and behaviour on surface. Peptide dipping sequence was found to be important for the experiment, having the peptides different adsorption kinetics, that influenced the outcome of the experiment. Thanks to the standard analysis settings and representation layout it was possible to compare peptide gradients among the same surface and between experiments.

In conclusion, a novel design for a two-stage migration was produced and its reliability was extensively tested. Such ECM-mimicking system can now be employed for our in vitro imaging experiments with MDA-MB-231 model cells.

3.17. Bibliography

[1] V. Corvaglia, R. Marega, F. De Leo, C. Michiels, D. Bonifazi, *Small* **2015**, 12, 321–329.

[2] F. De Leo, R. Marega, V. Corvaglia, R. Tondo, M. Lo Cicero, S. Silvestrini, D. Bonifazi, *Langmuir* **2017**, 33, 7512–7528.

[3] E. Beurer, N. V. Venkataraman, A. Rossi, F. Bachmann, R. Engeli, N. D. Spencer, *Langmuir* **2010**, 26, 8392–8399.

[4] S. L. Schor, I. Ellis, J. Banyard, A. M. Schor, *J. Cell Sci.* **1999**, 112, 3879–3888.

[5] C. P. Holmes, *J. Org. Chem*. **1997**, 62, 2370–2380.

[6] A. Ajayaghosh, V. N. Rajasekharan Pillai, *Tetrahedron Lett.* **1995**, 36, 777–780.

[7] P. Klán, T. Šolomek, C. G. Bochet, A. Blanc, R. Givens, M. Rubina, V. Popik, A. Kostikov, J. Wirz, *Chem. Rev.* **2013**, 113, 119–191.

[8] E. B. Akerblom, a S. Nygren, K. H. Agback, *Mol. Divers.* **1998**, 3, 137–48.

[9] V. Corvaglia, R. Marega, F. De Leo, C. Michiels, D. Bonifazi, *Small* **2016**, 12, 321–329.

[10] F. Sta, Peptide Synthesis and Applications, Humana Press, Totowa, NJ, **2013**.

[11] H. Rink, *Tetrahedron Lett.* **1987**, 28, 3787–3790.

[12] R. Subiras-Funosas, R. Prohens, R. Barbas, A. El-Faham, F. Albericio, *Chem. - A Eur. J.* **2009**, 15, 9394–9403.

[13] A. El-Faham, F. Albericio, *J. Pept. Sci*. **2010**, 16, 6–9.

[14] N. Thieriet, J. Alsina, E. Giralt, F. Guibé, F. Albericio, *Tetrahedron Lett.* **1997**, 38, 7275–7278.

[15] M. Dessolin, M. G. Guillerez, N. Thieriet, F. Guibé, A. Loffet, *Tetrahedron Lett.* **1995**, 36, 5741–5744.

[16] N. Thieriet, P. Gomez-Martinez, F. Guibé, *Tetrahedron Lett.* **1999**, 40, 2505–2508.

[17] C. P. Holmes, D. G. Jones, *J. Org. Chem.* **1995**, 60, 2318–2319.

[18] C. P. Holmes, *J. Org. Chem*. **1997**, 62, 2370–2380.

[19] B. Neises, W. Steglich*, Angew. Chemie Int. Ed*. **1978**, 17, 522–524.

[20] B. Amit, U. Zehavi, A. Patchornik, Isr. *J. Chem*. **1974**, 12, 103–113.

4. Chapter 4 – Morphological study of MDA-MB-231 cells over ECM-mimicking SAMs

This chapter deals with the formulation of a rationale over the morphological studies performed over the years on MDA-MB-231 cancer cells employed on the ECM-mimicking anisotropic SAMs of gold. The aim of this chapter is to establish a correlation between cell shape influenced by different SAMs on gold. Confocal microscopy was the primary investigation tool of this chapter. The first part of this chapter is focussed on cell shape analyses over the isotropic SAMs and monodirectional gradients of IGDQ-bearing peptides, as shown in paragraph 4.1. Furthermore, comparison between motogenic IGDQ- and RGD-bearing SAMs is made. Cell imaging over 5 days was performed to evaluate proliferation and development of the invasive character over time. Paragraph 4.2 describes the time-lapse cell imaging on monodirectional gradients performed in KULeuven. Cell speed over engineered surfaces was an interesting topic of investigation, comparing different peptides, surfaces for a better control of cancer cells on ECM-mimicking substrates. Paragraph 4.3 discusses the results of the immunostaining of cells over double concentration gradients of photolabile peptides. Comparison between cell shape shift for each different monolayer is rationalised in the conclusion. Confocal imaging was performed thanks to the precious help of Noëlle Ninane but also Miss Sophie Ayama under the supervision of Prof. Carine Michiels at the Unité de Recherche en Biologie Cellulaire (URBC). Transillumination and fluorescence microscopy (not reported) images were recorded at KULeuven with Dr. Annemie Biesemans and Vincent Gielen under the supervision of Prof. Peter Dedecker.

4.1 Immunostaining of cell cultures on gold-coated substrates

Routine analyses of the seeded cells over monodirectional peptide gradients on surface were performed on a phase-contrast microscope. Fig. 4-1 reported below shows a cell-deposition spot with MDA population oriented towards the anisotropic peptide gradient fabricated on surface (left to right). The physical constraints of the PVC self-adhesive mask helped the imaging process introducing reference points. Remarkably, polarised MDA cells orient towards the direction of the gradient, and a smaller sub-population moved. Single-cell migration is therefore observed on ECM-mimicking surfaces. Starting from such experimental result, new imaging techniques were approached, to be able to capture the live-cell movement and characterise in detail the shape evolution to perform the migration.

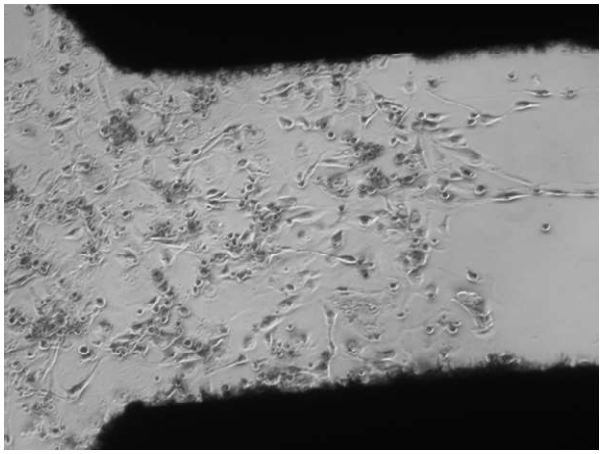

Figure 4-1 - Phase-contrast image of migrating cells over a δIPS/PS·Au SAM; 10x, MDA-MB-231 cells, day 5, Cardiff University.

After taking daily pictures of cells inside the migration channel, our focus went on the morphological aspect of a migrating cell. Our latest findings showed that cells oriented and moved towards the chemical gradient of IGDQ-bearing peptides, as shown in Fig. 4-1. Starting from this empirical observation, the next scientific investigation was therefore on finding a correlation between monolayer architecture, cell shape and migratory behaviour. In this chapter the biological aspects of cell shape and migratory behaviour will be discussed. Confocal microscopy was chosen as primary investigation technique. The general procedure for routine confocal imaging is now described. Before the imaging, surfaces with cells were gently rinsed with PBS, then paraformaldehyde was added to create pores in the membrane. Cell fixation was performed for 30 minutes and then the primary antibodies (Abs) were introduced, according to the different targets. Secondary antibodies binding the primary ones or proteins were also given, tethering a fluorescent chromophore to the biological target that could be imaged. Multiple staining can be performed with different Abs, from different species of with fluorescent protein transfection protocols. Fluorescent dyes bind a biological target, enabling organelle visualisation with laser microscopy. The dyes used for this immunostaining are the Hoechst blue dye for the nucleus and Alexa fluor 488 red for F-Actin (filamentous Actin), mouse anti human FAK (pY397) green for the focal complex and 53BP1. Antigen 53BP1 probe enabled the detection of DNA repair processes caused by cell irradiation. After this routine procedure, imaging process was performed. Confocal microscopy is an investigation technique which uses lasers to excite the specimen at a specific wavelength and collects the fluorescence emission at the detector. This powerful technique has the peculiarity of focussing only on a very small point, excluding all the rest of the sample and light which is not in focus, not belonging to the focal plane. Furthermore, laser penetration power enables the

collection of 2D planes that if stacked together form a 3D image of the specimen. Other fluorescence microscopy instruments such as the wide-field microscope shines light over the whole sample with higher levels of noise and lower resolution.

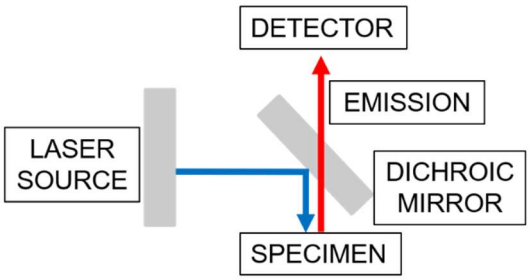

Figure 4-2 - Confocal microscopy structure

As it can be seen from Fig. 4-3, cells have an elongated shape, typical of mesenchymal-type cells, not really overlapping over each other. Bare gold does not stop adhesion nor proliferation, and since the metallic 10 nm layer is semi-transparent, surfaces can be imaged from both bottom and top, according to each microscopy facility requirement.

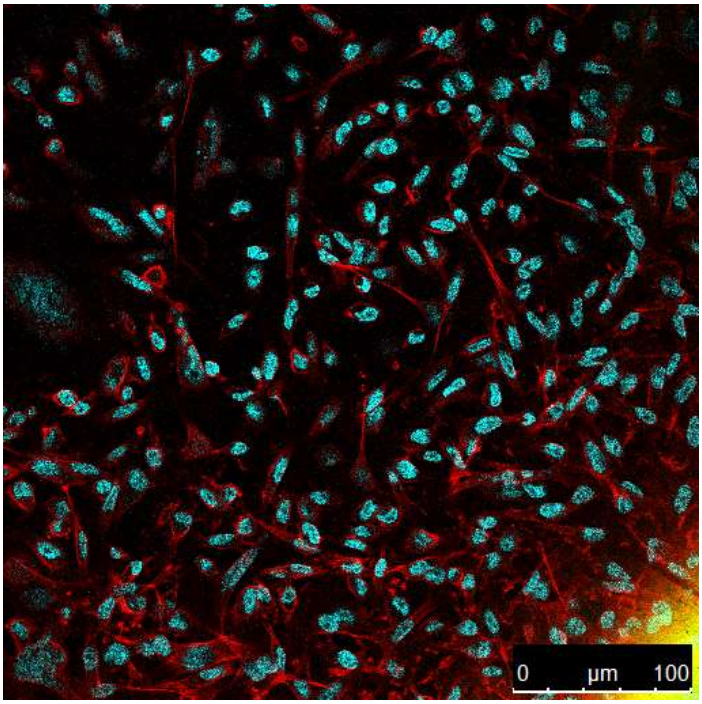

Figure 4-3 - MDA-MB-231 cells on bare gold. Red: Alexa Fluor 488 for F-Actin; Blue: Hoechst for the nucleus.

After the bare gold, systematic proliferation studies were performed over SAMs of different peptides, such as IPS100%, its backfiller PS100%, or RGD-bearing reference peptide GPS100%. The nomenclature is the same for the other chapters, indicating either an isotropic SAM (overnight dipping) with the correlated percentage or the

anisotropic gradient (two-step immersion protocol) with the δ symbol. Since the cell fixing solution and our Ab staining protocols are not compatible with cell survival, used monolayers could not be recycled.

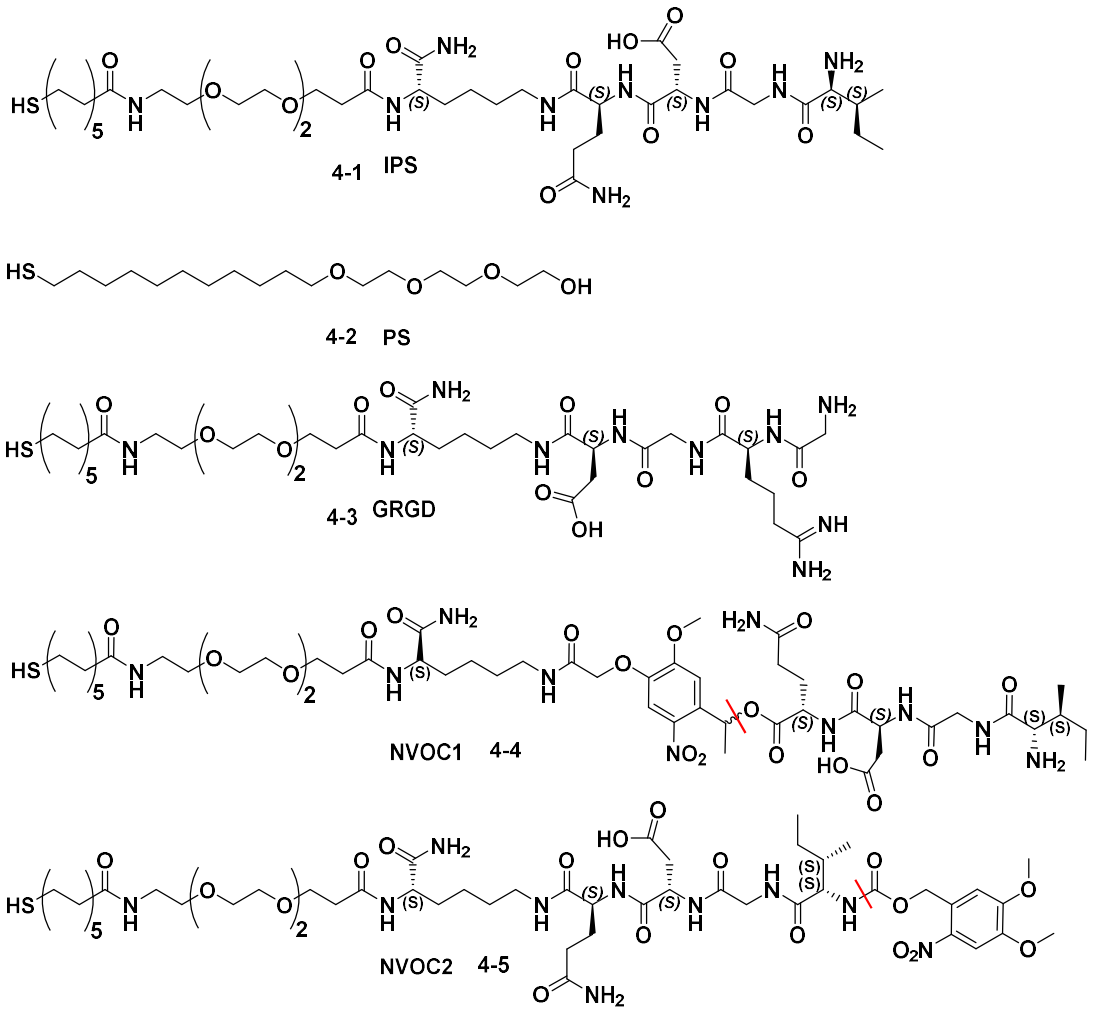

Figure 4-4 - Peptides used for cell imaging. Nomenclature: IPS was the motogenic IGDQ-bearing peptide **4-1**, GRGD was the control peptide **4-3**[1], PS was our chosen backfiller **4-2**, NVOC1 and NVOC2 were the two photolabile peptides **4-4** and **4-5**, respectively.

Because of this reason, a large number of surfaces had to be coated and seeded with cells, to image on different days, in biological triplicates (3 independent cell passages, 3 replicates). Among the representative samples, only the most interesting ones are presented and discussed in this chapter.

Isocratic SAMs of PS100% were imaged and the results are shown in Fig. 4-5 below. Images taken from day 2 of the isocratic PS SAM were similar to those taken on day 5. On day 2, cells were relatively small in size, with fairly elongated shapes along the edges of the proliferation spot. Picture #2 and picture #3 from Fig. 4-5 showed the

elongated shape with protruded sensing fronts of lamellipodia. On day 5, it was observed that cells recovered from the detachment and re-deposition shock, and expressed again their invasive character, with an increased percentage of elongated cells also in the peripheral zones of the culture. An image of a recovered invasive cell could be picture #5 with a wide lamellipodia front, protruded to the left, and a pointy rear end on the opposite side.

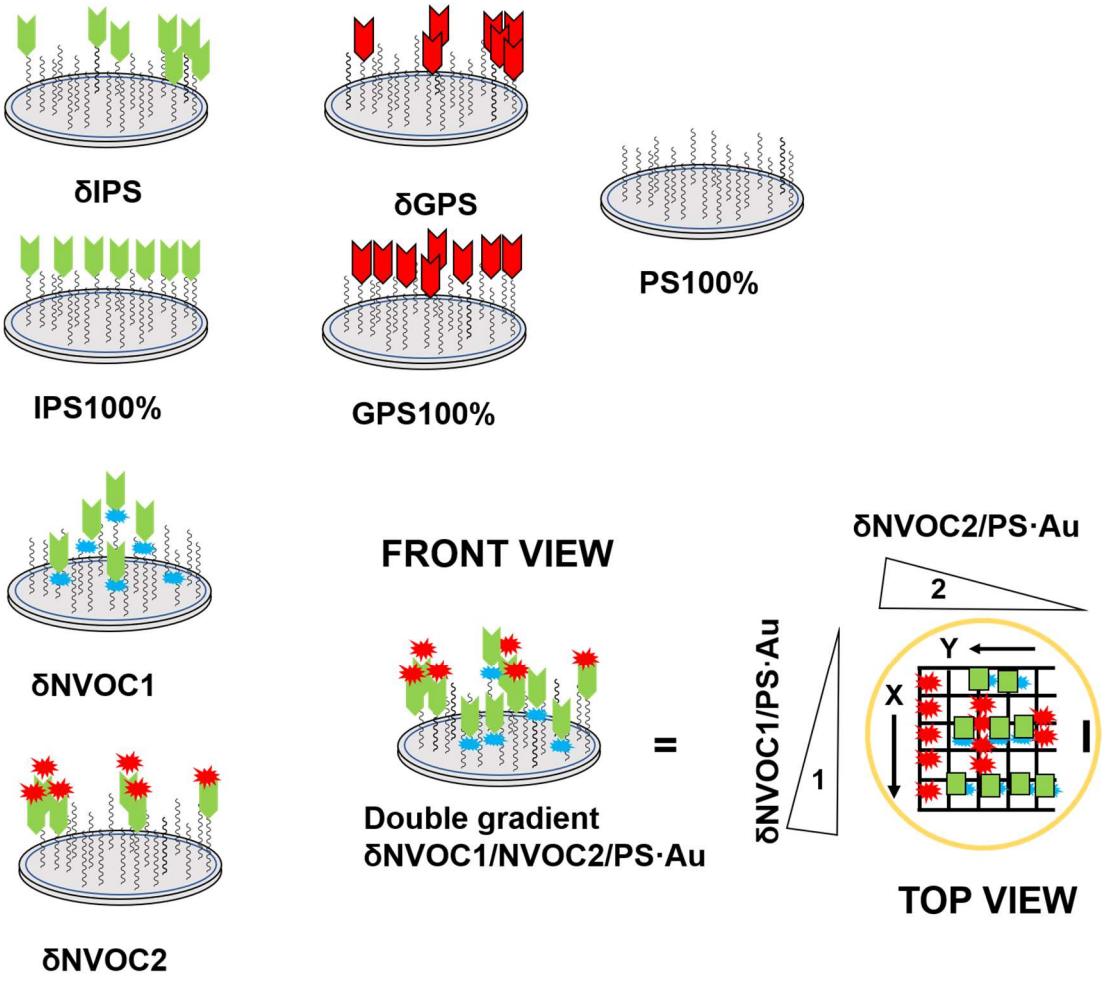

Scheme 4-1 – SAMs of IPS, GPS, PS and the photolabile derivatives NVOC1 and NVOC2.

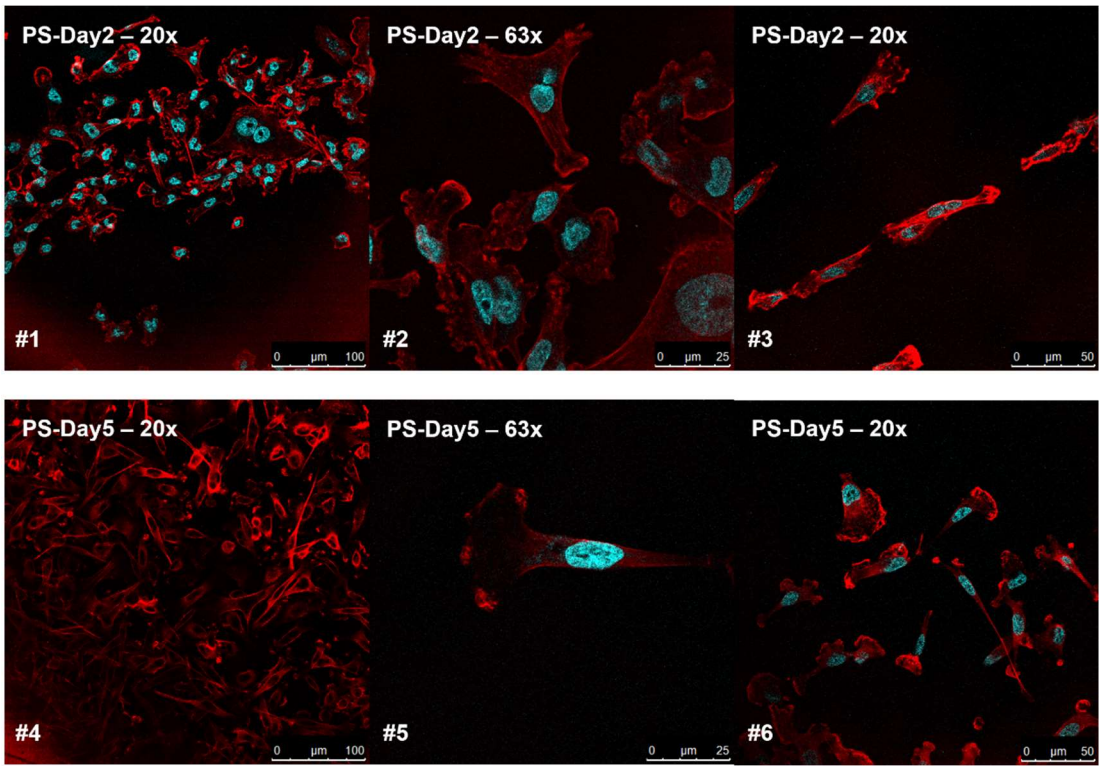

Figure 4-5 - Confocal microscopy of MDA cells on isocratic SAMs of PS. Red: Alexa Fluor 488 for F-Actin; Blue: Hoechst for the nucleus.

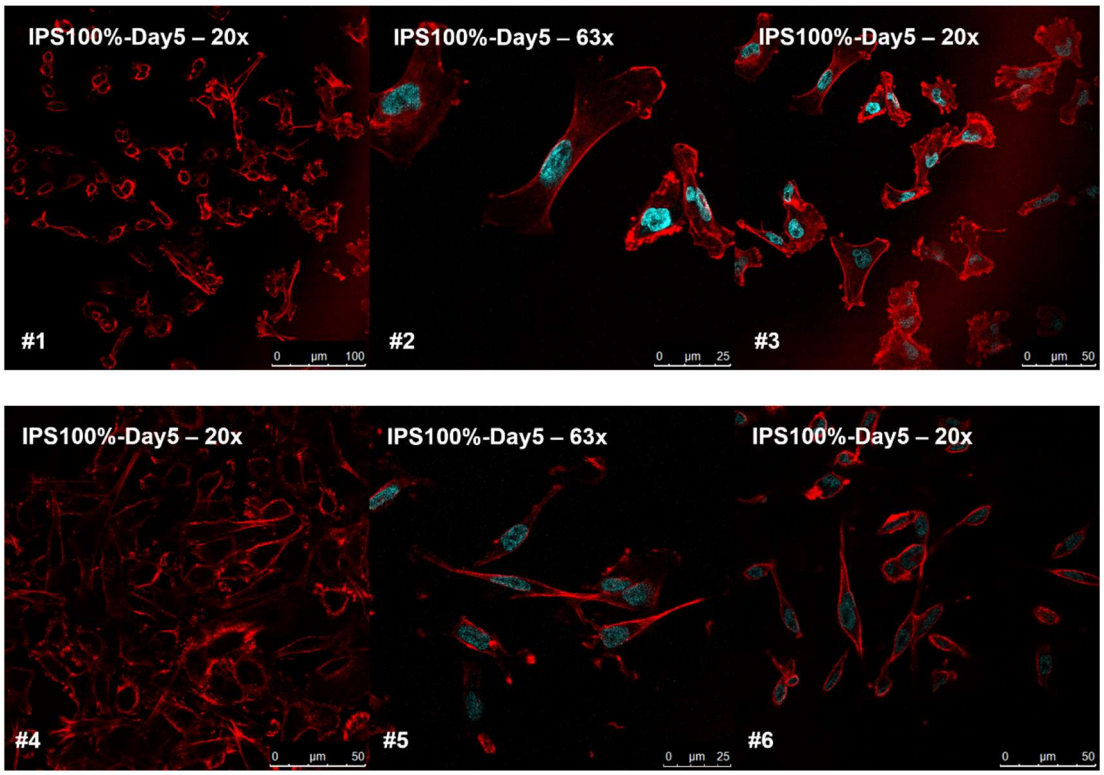

Figure 4-6 - Confocal microscopy of MDA cells on isocratic SAMs of IPS.

As a second series of monolayers imaged, IPS100% pictures are shown in Fig. 4-6 above. Interestingly, spread lamellipodia seen from day 2 were replaced by pointy

edges and ovoidal cell shape of the majority of isolated cells and from the bulk. After the isocratic single-component SAMs, the systematic study was extended to anisotropic δIPS/PS·Au SAMs. A 5-day monitoring campaign was performed. Since day 1, MDA cell population started to re-shape from round to polarised, with some cells already elongated. Different shapes of MDA cell population already present from day 1 could be due to an intrinsic different phenotype, with a higher integrin β3 expression, that could be the cause of the pronounced invasiveness of this cell line.[2–4] Widespread cells, with large lamellipodia seemed to be prone to proliferate. Polarised cells, with palette-like front edge and narrow rear seemed to be prone to migrate.

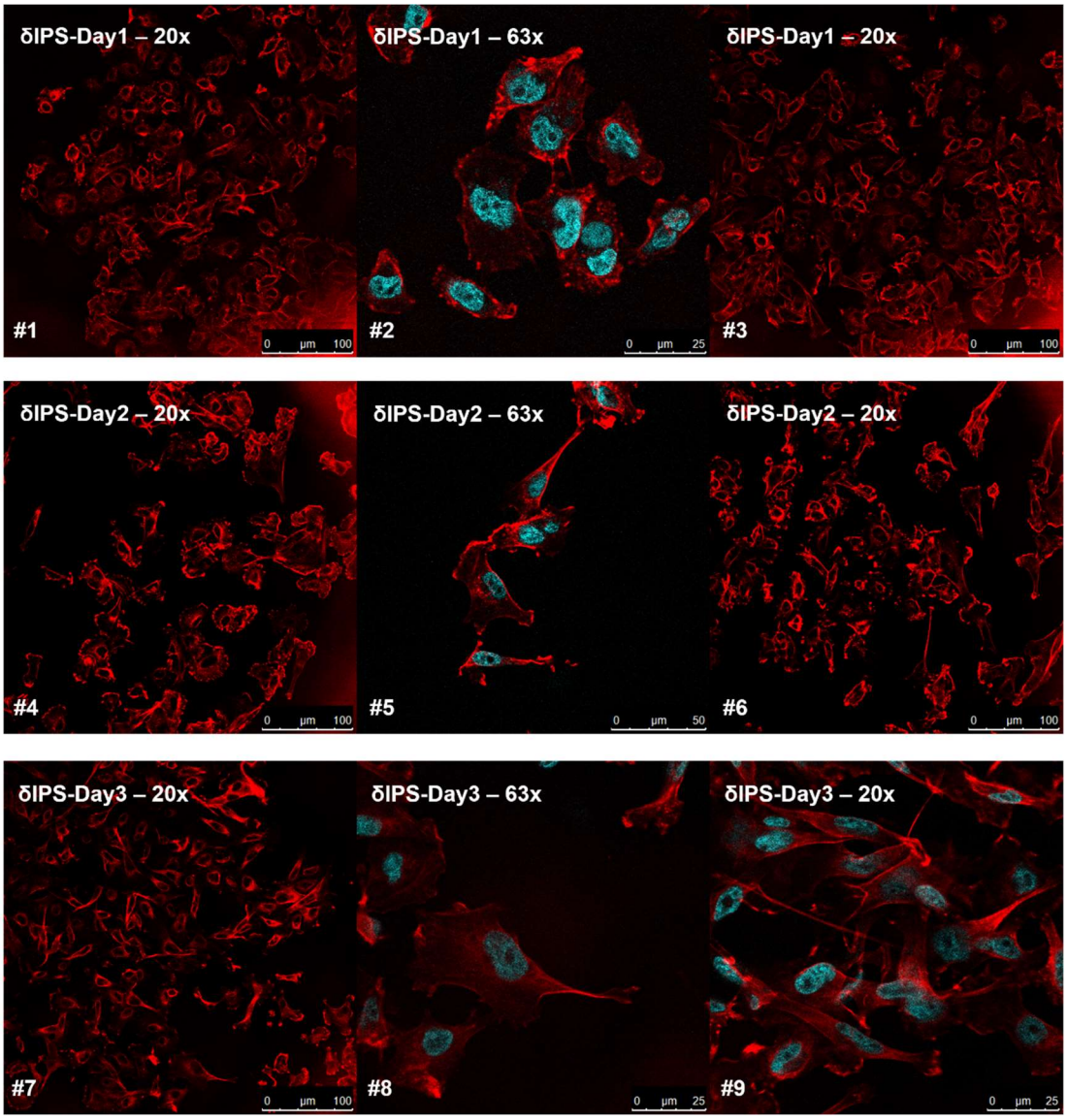

Figure 4-7 - Immunostaining of MDA cells over δIPS gradient. Day 1 to day 3.

From day 2 in monitoring shown above (Fig. 4-7), cell population seemed to change shape and rearrange. After the stress of trypsin detachment, seeding and re-growth, conditions are restored to normal and cell population is re-settling/adjust according to

space, nutrient levels and substrate. There are already spiked cells, but the general trend seems to have large lamellipodia edges, sensing the ECM. From day 3 the cell population seems to shift in favour of the migratory phenotype: cells in contact with each other retrieve faster their “migration” shape, and conversely those at the periphery are still spread out with wide lamellipodia and pointy rear ends.

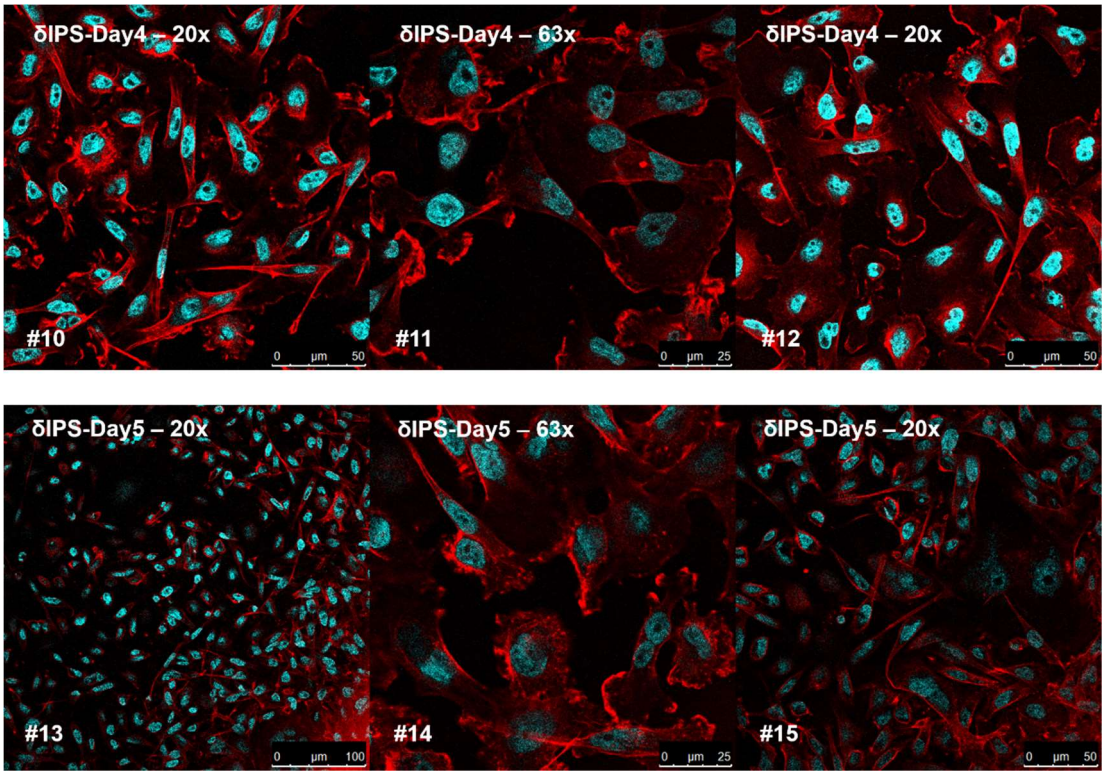

Figure 4-8 - Immunostaining of MDA cells over δIPS gradient. Day 4 to day 5.

This could be due to a space-seeking factor. When reaching confluence, cells could enhance their migratory behaviour to reach further space and growth. From day 4, cells increased remarkably in length. It seemed that the population took all the space, heading to full polarisation and confluence on the substrate. On day 5 most of the cell population had an elongated shape. Proliferation seemed to be slower, due to space consumption but most importantly because of the integrin β3 activation, due to the IGDQ-bearing peptide coating.[5,6] After 5 days the invasive character has been restored, since detachment and adhesion upon a new substrate with a concentration gradient. In conclusion, from day 0 to day 2 the activity could be addressed as “sensing time” in which cells need to adapt to the new substrate. From day 3 the transition was clearly visible, with more elongated cells, that increased in size over the following days.

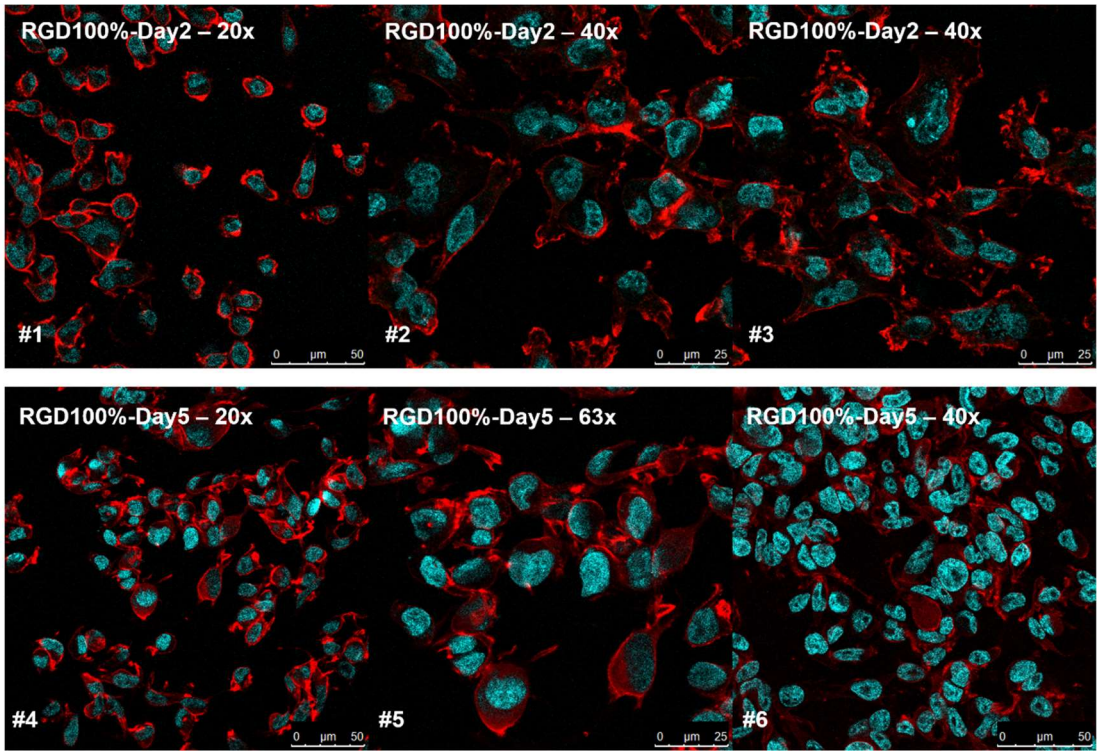

Figure 4-9 - Immunostaining of MDA cells over isotropic SAMs of RGD100%.

Concerning the RGD100% SAMs shown above (Fig. 4-9), cells at day 2 and day 5 possessed a remarkable and very distinctive round shape, clearly different from the other experiments. This shape was maintained throughout all 5 days of the experiment and is probably due to the RGD-bearing peptide that activates the integrin α5β1, that deals primarily with cell proliferation, rather than migration.[1,7] RGD peptide mimicking the ECM seemed to maximise cell volume through spherical shape shifting. Population seemed to grow in close proximity without the partial overlapping that could be seen in the experiments with the IGDQ peptide.

4.2 Morphological study of MDA-MB-231 cells over engineered surfaces

As a conclusion of this systematic morphological study on MDA cells on SAMs, two comprehensive “shape/behaviour correlation tables” were filled (Fig. 4-10 and Fig. 4-11). The images shown below in Fig. 4-10 framed the 2D single-cell migration movement cycle, along δIPS/PS·Au ECM-mimicking SAMs. Images from fluorescence microscopy (trans-illumination mode) and confocal microscopy experiments were adapted to fit the table, therefore cells do not have exactly the same scale. From row #1 in the first two images, cells adhered to the gold surface and started to protrude lamellipodia from one edge (Fig. 4-10, picture #1 to #3). Pointy edges at the rear and

wide fronts are the most common cell shapes that are found when culturing MDA cells on patterned Au surfaces.

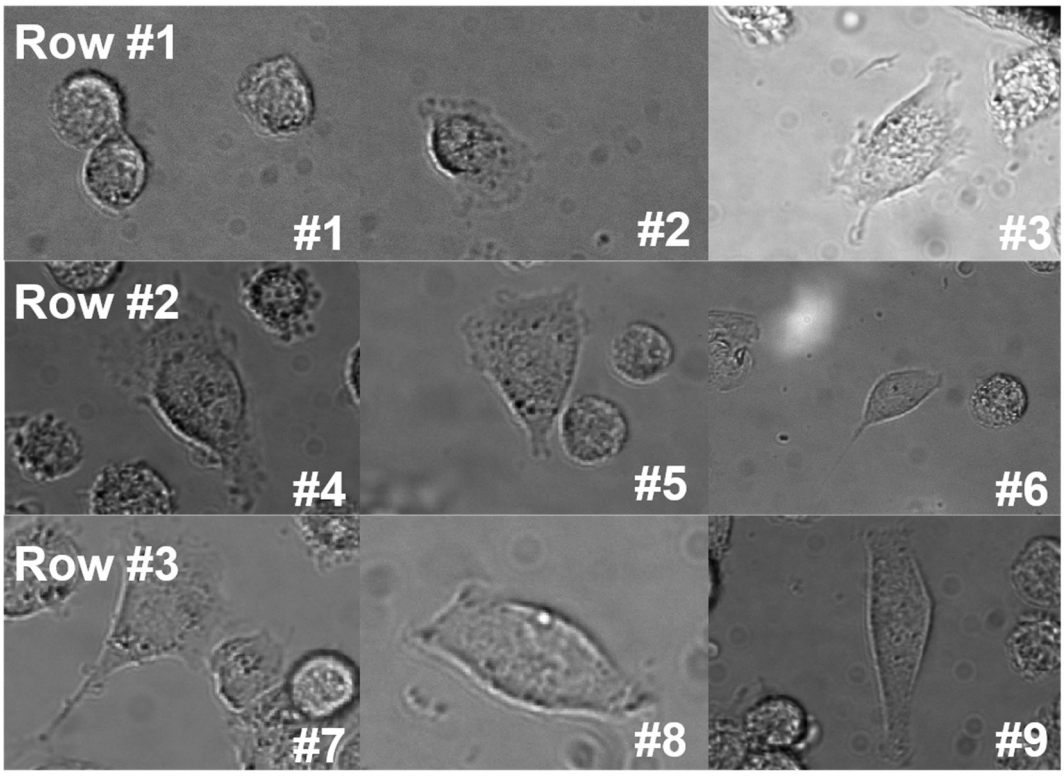

Figure 4-10 – Optical imaging of MDA-MB-231 cells on δIPS/PS coverslips: shape characterisation. 3 Rows for three different cell behaviours: Row #1 (pictures #1 to #3) adhesion and proliferation; Row #2 (pictures #4 to #6) sensing and sub-μm migration; Row #3 (pictures #7 to #9) cm-scale migratory behaviour.

After sensing the ECM with a wider front (Fig. 4-10 pictures #1 to #3), cell population started to narrow down the front lamellipodia, having a more compact and polarised cytoplasm. Row #2 (Fig. 4-10 pictures #4 to #6) have a relatively pointier rear end, thanks to the ongoing polarisation process. In the last row #3 (pictures #7 to #9) the cell shape observed was the one seen for the migrated cells on surface. As a second shape vs. behaviour correlation table, confocal microscopy images were reported below (Fig. 4-11). Confocal images have more contrast and resolution than the transillumination images shown in Fig. 4-10. Confocal images (Fig. 4-11) are divided in three rows, according to the observed invasive behaviour on surface. It was observed that the first row (pictures #1 to #4, Fig. 4-11) could be ascribable to stationary or primarily proliferative behaviour. The second row (pictures #5 to #8) was dedicated to sensing and micro-movements, while the third row to migration at the cm-scale (Row #3, pictures #9 to #12, Fig. 4-11). Although picture #10 from Fig. 4-11 was found on a PS100% isocratic SAM (Fig. 4-5), that specific cell shape was chosen as representative of migratory behaviour, found in IGDQ-bearing SAMs.

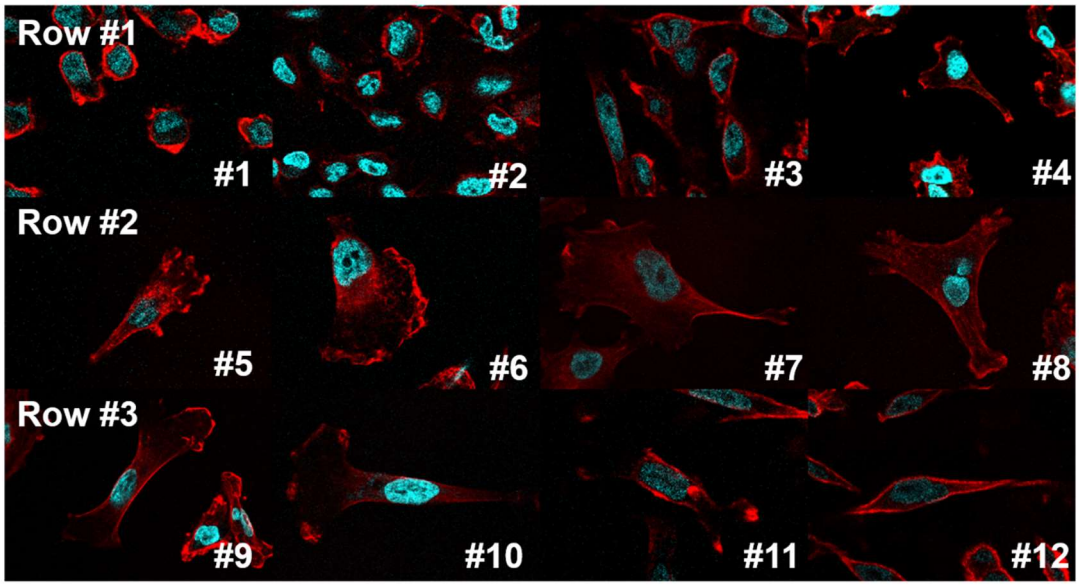

Figure 4-11 – Confocal imaging of MDA cells: shape characterisation. 3 Rows for three different cell behaviours: Row #1 (pictures #1 to #4) adhesion and proliferation; Row #2 (pictures #5 to #8) sensing and sub-μm migration; Row #3 (pictures #9 to #12) cm-scale migratory behaviour.

4.3 Imaging on δIPS/PS·Au SAMs

Fluorescence microscopy technique (Fig. 4-10) was unfortunately not able to give high-resolution pictures as good as the confocal microscope (Fig. 4-11), because of the lens operating at a higher distance that could not focus higher magnifications. Another unexpected issue encountered was surface floating while moving the stage to different sites causing the loss of saved reference points during overnight imaging. Furthermore, it was found that MDA cells took more than 12 hours to migrate consistently over a cm-scale pathway. Unfortunately, prolonged imaging was not possible, therefore transillumination images were only taken after several attempts because of the surface drift in the medium. Results from this type of imaging are now reported and discussed. A time-lapse video reconstruction of a moving MDA-MB-231 cell on an δIPS/PS·Au is shown below (Fig. 4-12). Images were recorded at KULeuven with a fluorescence microscope in transillumination mode, every 30 minutes at 20x magnification. Pre-set positions along the functionalised Au surface made the migration detection possible, with a Peltier chamber keeping the temperature at 37° and CO_2-independent medium to support cell viability outside the incubator (5% CO_2). Results from the time-lapse experiments monitoring cell migration showed that a very small sub-population of the polarised/elongated cell moved coherently on the cm-scale. Smaller movements were surface adjustments and protrusion towards other cells for communication. As shown in Fig. 4-12 reconstruction below, cell movement started with lamellipodia sensing, being protruded to the right-hand side of the picture. Two branches protruded while the

rear end was retracted. Another cell came in contact from above the picture frame, as can be seen from 120 minutes. To better capture MDA cell movement within the correct time-frame, confocal imaging for at least 48 hours should be performed. In such large time-frame, the whole-population could be studied, and micro-movements can be distinguished from the actual migration chasing a chemical gradient of motogenic peptides. Optional immunostaining of multiple targets such as integrins and components of the focal complex would in principle help the full characterisation of single cell migration on surface.

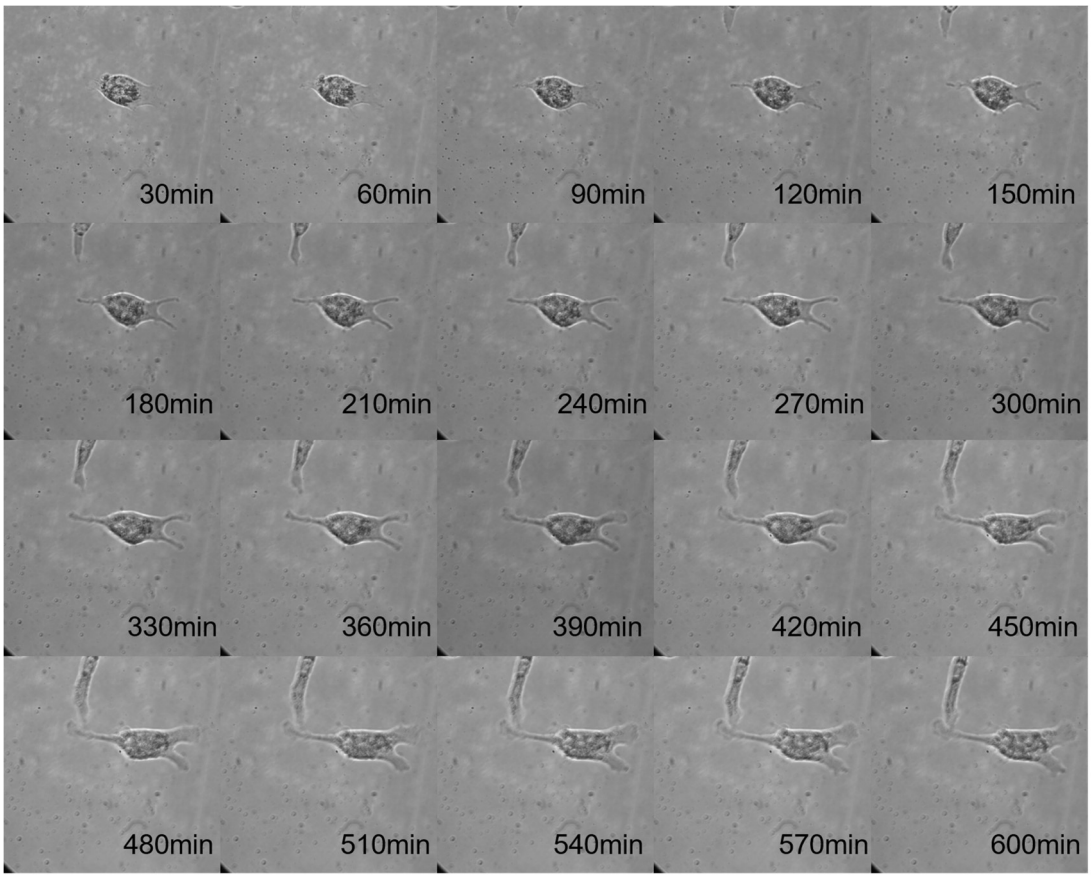

Figure 4-12 – Time-lapse pictures: MDA cell migrating along δIPS/PS·Au.

4.4 Immunostaining of MDA-MB-231 cells over double gradients of photolabile peptides

Morphological studies of MDA cells proliferating on photolabile peptides were performed. Cells were deposited either over the red dots (Fig. 4-13), without any PVC masking.

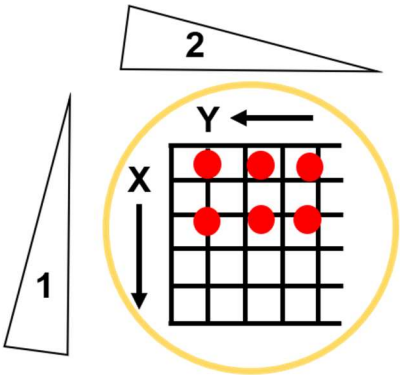

Figure 4-13 – Cell deposition spots (red dots) on a gold surface with a double peptide gradient.

As a first explorative experiment, double gradients were fabricated, and cells were seeded over the substrates (see red dots in Fig. 4-13). Standard immunostaining procedure was performed[8], targeting the nucleus (blue) and F-Actin (red) and the results are shown in Fig. 4-14. Green staining was due to anti FAK Ab for Fig. 4-14. Conversely, green staining for experiments shown in Fig. 4-15 and Fig. 4-16 were due to 53bP1 staining, monitoring ongoing DNA repair processes. Surfaces were placed in the confocal microscope with the same orientation, so the axis shown in Fig. 4-13 are mirrored in the microscopy images. Since in this project cells were never deposited over a double gradient of motogenic peptides, this first immunostaining experiment was performed to observe MDA cell population proliferate. As expected, immunostaining was successful, and no peculiar cell shapes or apoptotic cells were observed. Interestingly, MDA cells on double gradients were oriented in every direction, with a notable number of cells with very large lamellipodia sensing the environment, as seen in picture #5, Fig. 4-14. It was noticed that many cells at the edges were not elongated having a shape attributed to sensing, rather than migration. This could be caused by the small amount of IGDQ-exposing peptide present, due to the double gradient. Reported below are the results of the main experiments on photolabile peptides on surface. Twin experiments were performed, seeding the cells δNVOC1/NVOC2/PS·Au and its counterpart δNVOC2/NVOC1/PS·Au. Two surfaces per day were used for imaging. Cell proliferation and migration were monitored for 8 days. On day 5, surfaces were irradiated as described in Chapter 3. Surfaces were stained with 53bP1 protein, checking for ongoing DNA-repair processes. Phalloidin red was used to tag F-Actin and Hoechst blue for the nucleus. No green intracellular regions can be seen in both images below, indicating that no significant DNA repair was found. As shown by the Fig. 4-15, at day 4 the cell population is small, and a few polarised cells reside at the edges, where the majority has a spread lamellipodia sensing from 180° to 270° around. In the image, the monitored zone was the middle, where cell population was growing and the

possibility to find migrated cells was higher. A few migrated cells were found. After that, surfaces were irradiated, and stained with the same procedure. As it can be seen from Fig. 4-16 cells did not polarise along one peptide gradient neither the other, but there is a small cohort of population that oriented at 45° from the two axis. Interestingly, this situation can be explained with the parallelogram law, imagining the two gradients as two vectors pulling the cells on surface.

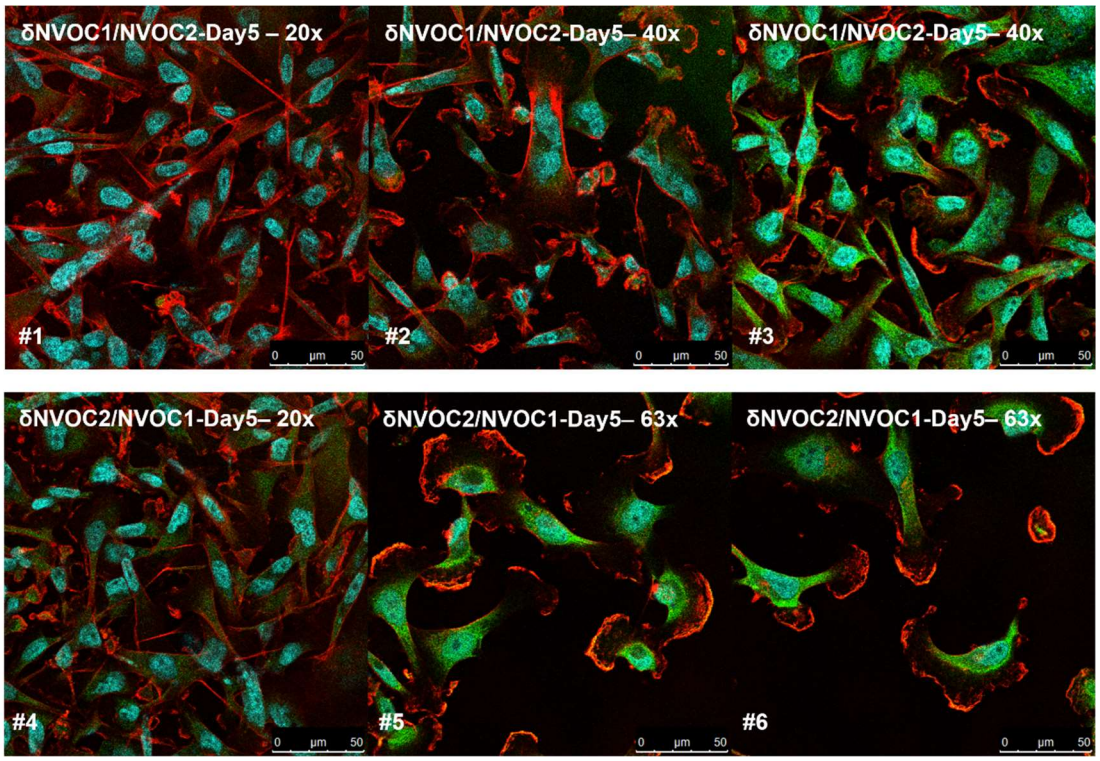

Figure 4-14 – Confocal imaging of MDA cells on δNVOC1/NVOC2/PS·Au and δNVOC2/NVOC1/PS·Au.

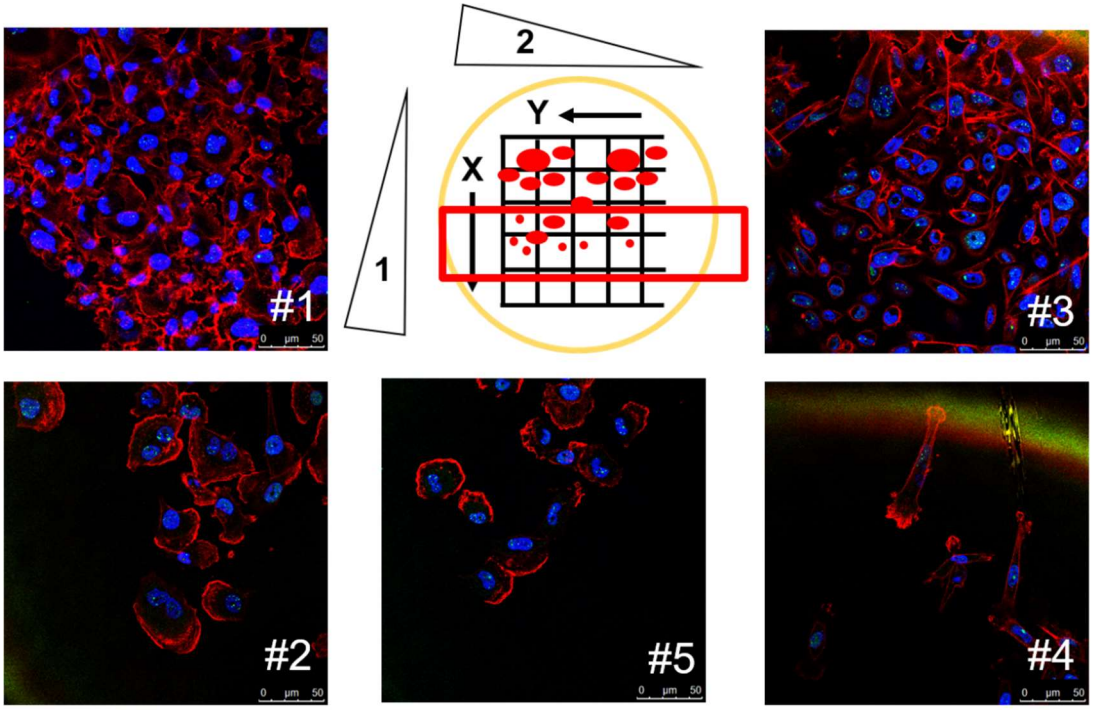

Figure 4-15 – Cells over a double concentration gradient of photolabile peptides (Day 4). Pictures #1 to #5 taken at 20x and 40x in the highlighted region of the surface (red rectangle). No cell confluence reported. Pictures were taken after 4 days but before irradiation.

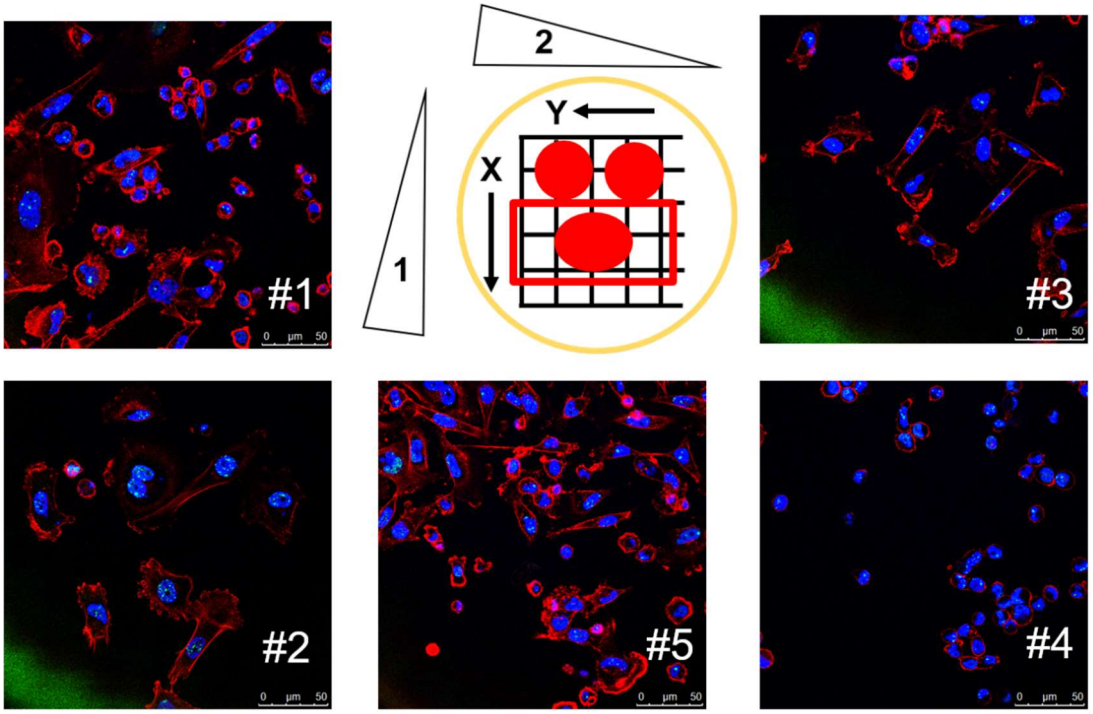

Figure 4-16 - Cells over a double concentration gradient of photolabile peptides (Day 8). Irradiation (day 4) was performed for 15 minutes at 365 nm (3 x 40 W UV-C solarium lamps in HBSS). Pictures #1 to #5 taken at 20x and 40x at the edges of the highlighted region of the surface (red rectangle).

4.5 Conclusions

Section 4.1 showed the remarkable effects of IGDQ-bearing SAMs influencing cell shape to a more elongated form, as well as triggering and guiding cell migration along the chemical gradient on the substrate. RGD-bearing substrates are conversely prone to influence MDA model cells to a more spherical shape, for a distinct cell response. Section 4.2 is a gathering of a large array of pictures of MDA cells that were collected and sorted to represent cell behaviour, specifically adhesion and migration over ECM-mimicking SAMs. Results showed that polarised cells are more prone to migrate, but this is not a constant, since resting-state cells can convert into invasive and move as well. Three main behavioural features were found, stated as proliferative type, typical of round-shaped cells, sensing cell type with sub-cm movements, and invasive with the typical elongated shape. Each category can be found in a specific point of the substrates: at the edges but close to the bulk reside the highly invasive type, proliferative type can be found both isolated and in bulk while the sensing one are often found following the trail of the invasive type. Section 4.3 reported a de-stacked time-lapse imaging of a MDA cell, showing the podosome ensemble polarising the cell, protruding lamellipodia while retracting the rear end. Such type of imaging was very difficult to set up because of intrinsic flaws of the substrate, being too light and floating in the cell medium. Different substrates such as coated glass slides can be used as a heavier replacement that would stay in place without any drift. As a last part of the investigation, immunostaining of MDA cells over photolabile SAMs are reported in section 4.4.

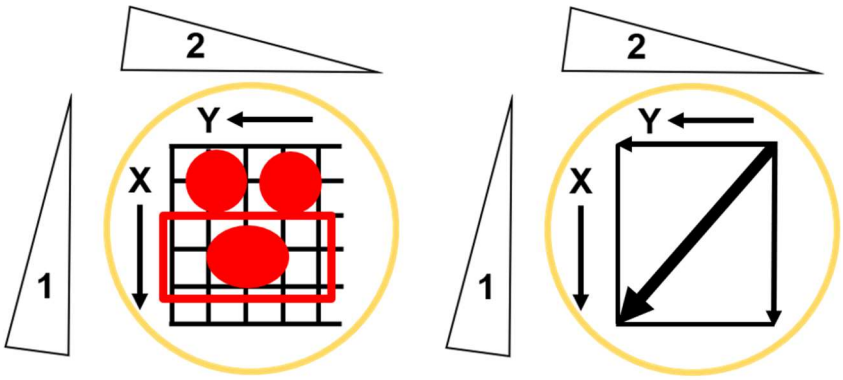

Figure 4-17 - double gradients on surface. Influence on migratory directions.

After this extensive investigation over structural properties of SAMs, two novel photolabile peptides were designed, synthesised and tested for the fabrication of a novel photolabile substrate with a double chemical gradient system. Such setup was designed to resemble to a greater extent the complex nature of a biological tissue, that

has multiple chemical messengers both in solution and on surface. After having improved such design with a simple approach, peptides were tested as a light-controlled substrate for MDA cells. Double gradients of photolabile peptides showed that the first peptide with the exposed motogenic sequence triggers the first movement while the second peptide is masked with a photolabile linker prior to the same IGDQ sequence that is tethered in both peptides. After 4 days irradiation occurred, and the second gradient was then revealed on the monolayer, while cleaving the first. Because of an unexpected delayed cell response, experimental data showed a 45° movement. The first chemical gradient (see X axis in Fig. 4-17) influences the orientation of a small sub-population at the edges of the cell deposition spot. Interestingly, after the irradiation event occurred on day 4, the second gradient (fabricated along the Y axis) seemed to play a role, influencing both the sensing- and the invasive-type MDA cells. Because of the slow cell movement, the intermediate direction (45°) is taken by a small sub-group of cells. The inability to sharply change the migration course by 90° seems to be due to the shallow peptide gradient but also caused by intrinsic “inertial” cell movement, that is delayed in respect to the anisotropic switch. Longer surfaces with a steeper gradient could improve the system, but SAM stability issues would start to raise, since the 2D movements should be monitored for at least 15 days therefore a switch to μ-Contact printing or PDMS microfluidic molds could be considered as an alternative.[9,10]

4.6 Bibliography

[1] E. Ruoslahti, *Annu. Rev. Cell Dev. Biol* **1996**, *12*, 697–715.

[2] F. Rechenmacher, S. Neubauer, J. Polleux, C. Mas-Moruno, M. De Simone, E. A. Cavalcanti-Adam, J. P. Spatz, R. Fässler, H. Kessler, S. M. De, et al., *Angew. Chem. Int. Ed.* **2013**, *52*, 1572–1575.

[3] R. E. Seftor, E. A. Seftor, K. R. Gehlsen, W. G. Stetler-Stevenson, P. D. Brown, E. Ruoslahti, M. J. Hendrix, *Proc. Natl. Acad. Sci. U. S. A.* **1992**, *89*, 1557–61.

[4] P. Friedl, Y. Hegerfeldt, M. Tusch, *Int. J. Dev. Biol.* **2004**, *48*, 441–449.

[5] S. L. Schor, I. R. Ellis, S. J. Jones, R. Baillie, K. Seneviratne, J. Clausen, K. Motegi, B. Vojtesek, K. Kankova, E. Furrie, et al., *Cancer Res.* **2003**, *63*, 8827–8836.

[6] I. R. Ellis, S. J. Jones, D. Staunton, I. Vakonakis, D. G. Norman, J. R. Potts, C. M. Milner, N. A. G. Meenan, S. Raibaud, G. Ohea, et al., *Exp. Cell Res.* **2010**, *316*, 2465–2476.

[7] E. A. Cavalcanti-Adam, T. Volberg, A. Micoulet, H. Kessler, B. Geiger, J. P. Spatz, *Biophys. J.* **2007**, *92*, 2964–74.

[8] V. Corvaglia, R. Marega, F. De Leo, C. Michiels, D. Bonifazi, *Small* **2016**, *12*, 321–329.

[9] B. M. Lamb, D. G. Barrett, N. P. Westcott, M. N. Yousaf, *Langmuir* **2008**, *24*, 8885–8889.

[10] G. M. Whitesides, E. Ostuni, X. Jiang, D. E. Ingber, *Annu. Rev. Biomed. Eng.* **2001**, *3*, 335–73.

5. General Conclusions

In conclusion, ECM-mimicking peptides were successfully employed to trigger integrin receptors that promote and sustain cell movement over 2D SAM substrates. SAM morphology studies were carried out in this PhD thesis, fulfilling the knowledge demand that was created after obtaining the remarkable results on surface. This PhD Thesis contributed with an in-depth study of the biomimicking SAM architectures responsible of triggering a biological signalling cascade in MDA cells, sustaining cell migration over custom substrates. Further studies on SAM architectures were carried out in this PhD Thesis thanks to wettability experiments and AFM analyses on the novel ultra-flat chip substrates. In-silico studies performed by Dr. De Leo explained and corroborated the key interaction of inter and intra-chain hydrogen bonding on the peptide scaffold that ensures sequence readability especially in low concentration regions of the gradients. The shallow nature of chemical gradients of IGDQ-bearing peptides was also confirmed by XPS mapping experiments.

After this comprehensive study, the scope was moved to the fabrication of a substrate being able to switch from one chemical gradient to another in the orthogonal direction, ensuring selective peptide readability for complete spatio-temporal control of MDA-MB-231 cancer cells. Important literature works investigated on SAM micropatterning to control cell adhesion and migration with electrical stimuli and with photoactivatable triggering.[1,2] Such innovative procedures require μ-Contact printing and laser technology to pattern the surfaces.[3] Conversely, the goal of this second part of the project was to develop a large-scale migration substrate that would require no more than a two-stage dipping and timed thiol immersion to be fabricated. While other fine chemists privilege the engineering aspects of a substrate fabrication, our design and development were centred on the chemical aspects influencing the SAM architectures since these aspects were not investigated so far. To fill this gap, photolabile linkers were employed to selectively cleave parts of the peptide backbones with no reagents used, avoiding toxicity drawbacks to the cell culture. The use of photolabile linkers bound prior and after the motogenic sequences IGDQ allowed the spatiotemporal control of a small sub-population of cells that responded to a double chemical gradient switch on surface. The 45° orientation acquired by the small sub-population of MDA cells over a double gradient of photolabile peptides was an important result that shed some light over the dynamics of cell movement on ECM-mimicking substrates. Gaining

spatio-temporal control on a highly invasive cancer cell line represents the starting point for the development of further studies and has the potential to attract for future therapeutics in metastasis treatment.

5.1. Future outlook improving the photolabile linker design

As shown from Scheme 4-2, the synthesis of the NVOC photolabile linker **3-19** is the same, while the second photolabile linker for peptide **4-9** is different from peptide **4-5**. Peptide **5-4** would present the photolabile linker head group derived from NVOC1 synthesis but exerting the same caging function as the previous design. Molecule **5-1** would be obtained by the optimised $NaBH_4$ ketone reduction of **3-12** in MeOH/THF. Precipitation in water can be performed in place of flash chromatography purification. Carbonyldiimidazole coupling in CH_2Cl_2 could be performed for 48 h affording the *tert*-Butyl protected photolabile linker. TFA deprotection step could then be performed to obtain the desired molecule **5-3**. This novel photolinker could be used for solid phase synthesis in place of the previous one, since no modifications to the amino acid scaffold would be performed. This simplification is not only synthetically cheaper in terms of atom economy, but allows higher scale synthesis, since the first synthetic steps are performed on a 20 g scale. A further advantage of this modified synthesis would be that the photocleavage rates would be expected identical and no possible toxic metabolites could form, since the photoproducts would be nitrosoketones, then washed away with PBS.

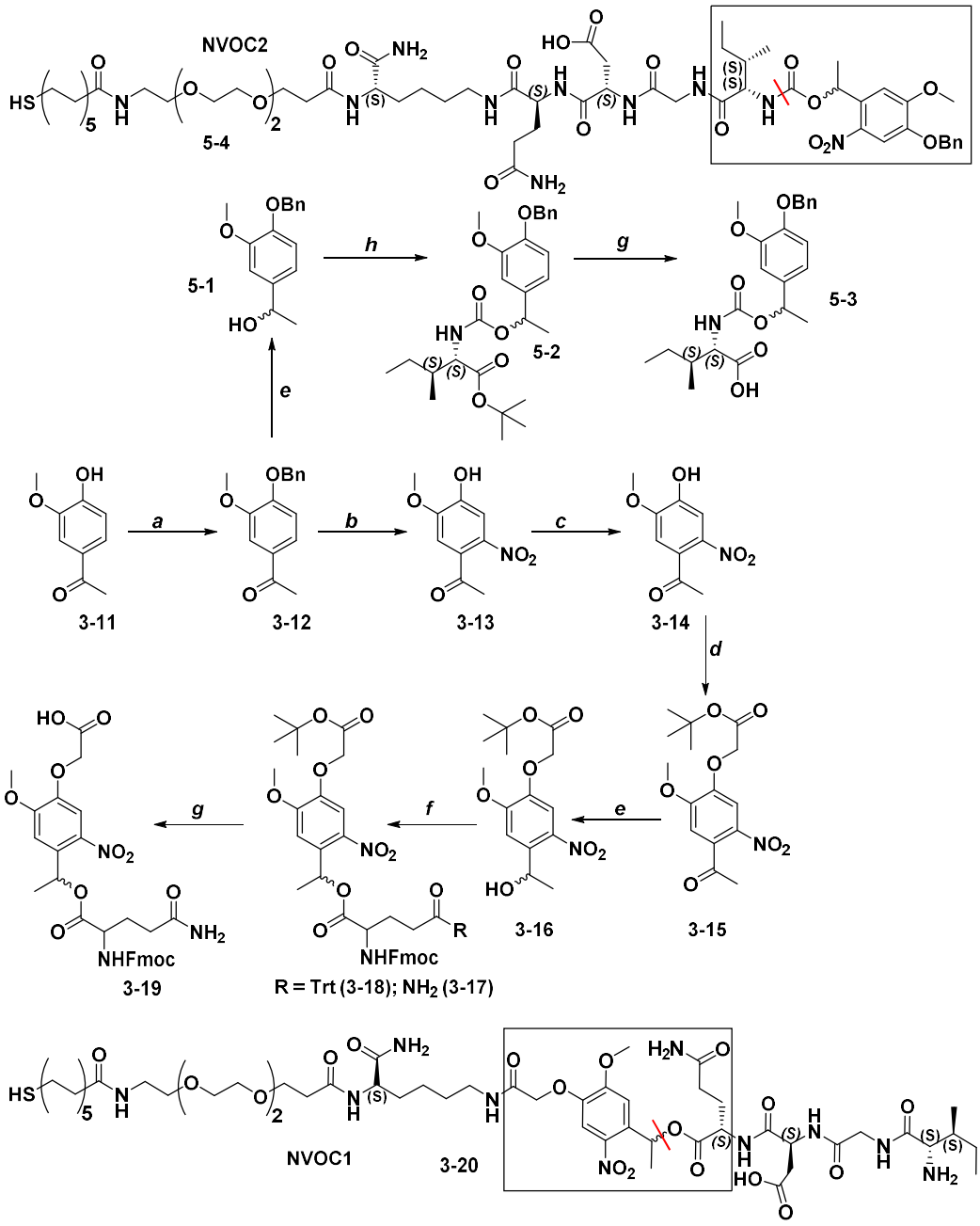

Scheme 5-1 - Synthesis of the two NVOC photolinkers **3-20** and **5-4**. Conditions: a: BnBr, K_2CO_3, DMF, 6 h, reflux, 70%; b: HNO_3, 2 h, 0˚C, 50%; c: TFA, 16 h, r.t, quant.; d: tert-Butylbromoacetate, K_2CO_3, DMF, 6 h, r.t, 80%; e: $NaBH_4$, THF/MeOH 3:1 ratio, 0˚C, 1 h, quant.; f: EDC·HCl, DMAP, Fmoc-Gln-OH, CH_2Cl_2, 16 h, 0˚C->r.t, 90%; g: CH_2Cl_2/TFA 1:1 ratio, 0˚C->r.t, quant.; h: CDI, CH_2Cl_2, tert-Butyl-IsoLeucine, 48 h, r.t.

5.2. Engineering SAMs – Click chemistry to expand our substrate portfolio

Switching towards a more high-throughput and engineering approach could help the fabrication of a higher number of different surfaces for future biological testing.

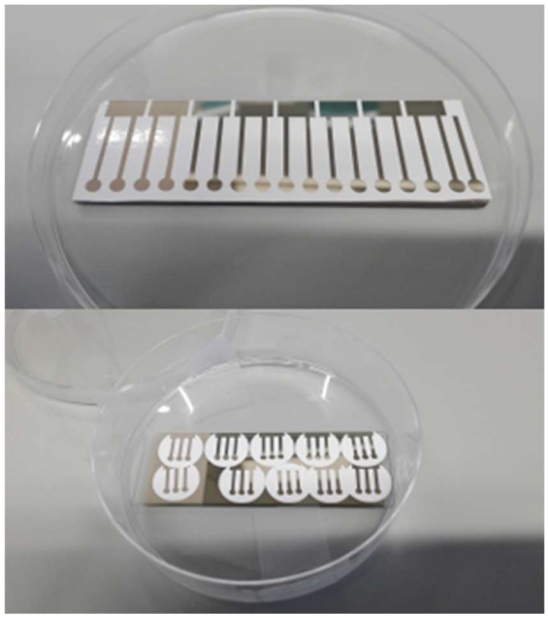

Figure 5-1 - PVC masks (new design) adhered on a glass slide for high throughput (top picture) compared to round coverslips (bottom picture). Both surface types were coated at Université de Namur, 10 nm Au layer, 2 nm Ti adhesive layer, LARN physics dept. Courtesy of Prof. Stefan Lucas. Masks were reprinted by Dr. Andrea Faresin, University of Padua.

As shown in Fig. 5-1, action was taken towards high throughput with coated glass slides that could host more migration experiments per surface. Glass slides were patterned by the short side. Chemical gradient steepness can be the same with the same dipping speed or be slower, for a denser monolayer that could last up to two weeks, prior to oxidation and desorption. As a last perspective on the work, a different approach could be applied, using the knowledge gathered so far on SAM-architecture control and having a more chemically flexible peptide head that could be functionalised at will. Click chemistry represents a versatile tool for surface functionalisation as shown by the work of Luo and Pauloehrl.[3-5] Copper-catalysed azide-alkyne cycloaddition (CuAAC) and Diels-Alder reactions are routinely performed on surface substrates for the fabrication of devices. Employing removable masks, the desired pattern on surface can be fabricated. By combining such expertise with the reaction tool palette developed in our research group by Dr. Rocard a set of surface functionalisation reactions can be performed and optimised.[6]

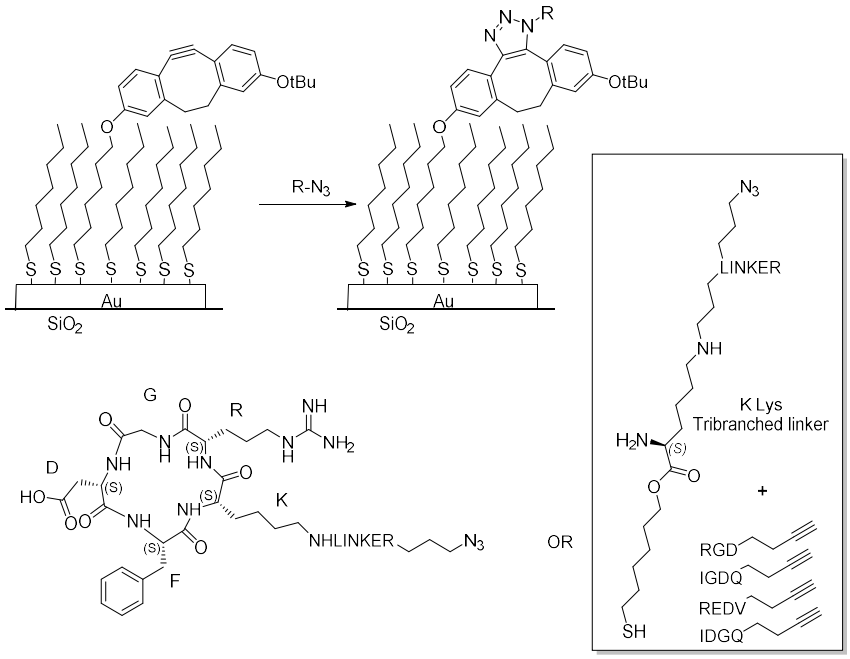

Scheme 5-2 - Surface functionalisation with Click Chemistry. Scheme adapted from Ref.[7]

Taking inspiration from the work of Hudalla and Heinrich a set of thiols could be prepared.[7] Monocomponent or mixed SAMs with oligo-ethylene glycol chains and alkanethiols can be employed since there are crucial for monolayer packing and preventing unspecific protein adsorption. A suitable head group amino acid could be Lysine, because of its 2 amino groups that can be protected and functionalised orthogonally. The approach of Orski is shown in Scheme 5-2.[8,9] Having activated a cyclooctyne moiety and by adding the matching azide, surface functionalisation can be performed easily. By this method, cyclic RGD can be tethered on surface, to be able to study cell adhesion in different conditions. The opposite approach would employ having the azide moiety tethered on surface and preparing a different variety of alkynes such as an IGDQ-analog, its scrambled equivalent IDGQ and other motogenic peptides to test their activity on MDA-MB-231 cells. By doing so, a library of integrin-binding molecules can be synthesised and used to modulate cell response and study cancer cell migration.

5.3. Azobenzene for the light-triggered dynamic control of cell migration

Another important use of the expertise gathered in our research group would be using azobenzene to modulate peptide readability through light stimulation.[10,11] The approach by Liu and co-workers had an oligo-PEG moiety with an azobenzene prior to the integrin-binding RGD.[12] This approach is very appealing because of its reversible

nature, that could be employed in our system. As shown in the Scheme 5-3, alkane-oligo-PEG chains can be functionalised to create a library of screening compounds for suitable adhesion and migration tests.[13] Such dynamic surfaces can be switched reversibly from a maximised-readability state to a "buried" conformation and *vice-versa* to study the corresponding cell response. Migration speed can be finely tuned exposing different peptides and molecules, having a simple screening tool that could be used for multiple cell lines.

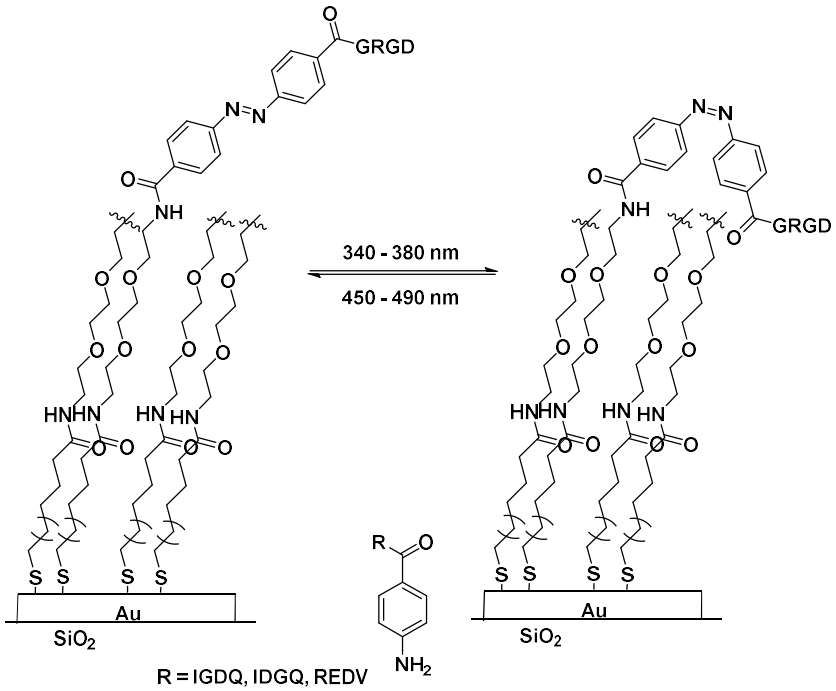

Scheme 5-3 - Azobenzene switch mechanism on surface. Scheme adapted from Ref.[12]

5.4. Future work and perspectives on the biological side of cancer cell migration

The improvements and potential future developments and implications of this PhD Thesis are several and will be discussed in the following section. It is useful to split the issue in two subjects, such as surface chemistry and on the other hand the biochemical response triggered by integrin-binding peptides at the cell-substrate interface.

5.5. Targeting the integrins

Concerning the biological part, future perspectives could imply full characterisation of the integrins involved in the interaction with the IGDQ-bearing substrate which is still a rather unexplored field of research. Integrin family is numerous with 18α and 8β subunits that could form at least 24 heterodimers, for cell adhesion, tissue regeneration and cancer metastasis.[13] It is therefore easy to understand that since the biological targets can be hundreds, it is necessary to focus first on the most biologically relevant, such as αvβ3 and α5β1 since it is well known that they are the most important integrin subtypes involved in cell adhesion and angiogenesis. Zhao and co-workers showed evidence of a prominent role of αvβ3 integrin heterodimer in cancer metastasis, with a primary role as adhesion receptor.[14] Taherian and co-workers showed that αvβ5 is expressed exclusively in MDA-MD-231 breast cancer cells, compared to other cell lines.[15] The heterogenic distribution of integrin subtypes along different cell lines suggests a phenotypical intrinsic difference that could be exploited for future therapeutics. Concerning this matter, our group is currently working on the full characterisation of αvβ3 and α5β1 integrin receptor activation by IGDQ-bearing peptides via confocal microscopy and live-cell imaging, for the identification of a possible different phenotype of MDA-MB-231 breast cancer cells that could explain the highly invasive character of a small sub-population that could move up to a cm-scale distance over patterned substrates developed in this research group, as previously reported.

5.6. Developing FRET sensors to characterise integrin activity in cancer cells

A further promising topic with MDA cells in cancer research could be employing Förster Resonance Energy Transfer (FRET) sensors to characterise integrins and their conformation upon surface stimulation with specific integrin-binding peptides. Chigaev and co-workers developed a FRET sensor with an α4-integrin binding peptide ligand (donor) that upon interaction with the matching integrin and a membrane-tethered Rhodamine (acceptor) could generate a signal to study receptor activation and conformation (Scheme 5-4).[15] An adaptation to such design is shown in Scheme 5-4 with modified features that could be employed in this project. Different setups can be used, changing the position of both donor and acceptor. This design could be useful to co-localize different integrins and monitor their activation state over different substrates,

being able to discover the unknown overlapping functions of these transmembrane receptors.Different integrin-binding molecules can be tested too. An extensive review by Mas-Moruno and co-workers described a wide library of integrin-binding molecules that could be employed to trigger selectively integrin subtypes.[13] Taking inspiration from such remarkable studies, targeted design, synthesis and testing of peptide ligands for αvβ3 and α5β1 receptors could pave the way to receptor characterisation over our ECM-mimicking substrates with confocal microscopy and fluorescence live-cell microscopy.

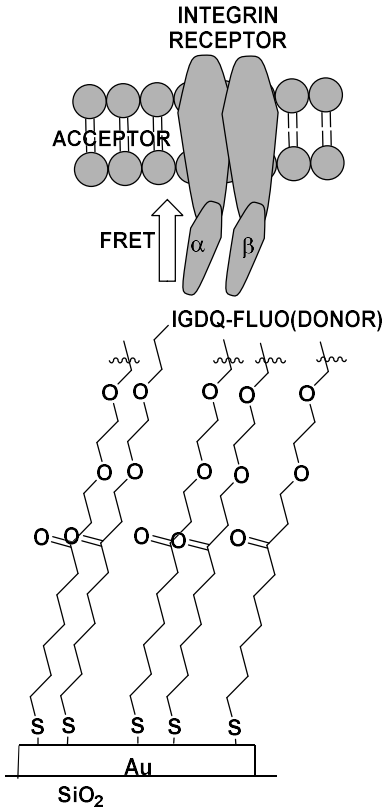

Scheme 5-4 - Scheme concept of FRET sensor for integrins. Scheme adapted from Ref.[16]

5.7. SAM gradients for enhanced fluorescence imaging

A different approach to improve the current imaging techniques could be the use of a SAM gradient with a mixture of thiols in the backfilling step, one of them being tethered with a fluorescent head group. Such strategy could allow the same peptide readability that was previously achieved, but the introduction of the fluorescent group could enhance the imaging results, thanks to fluorophores interacting with the membrane and enhancing co-localisation. The aim of such approach would be to fully characterise integrin-peptide binding mechanism and unravel an interesting aspect of a rather

complex topic such as cell-substrate interaction. Confocal microscopy could be used as a faster and easier method to image migrating cells over ECM-mimicking substrates with time-lapse videos recorded on live-cell microscopy that could be performed with a simple hardware upgrade namely a Peltier chamber setup for a temperature-controlled stage.

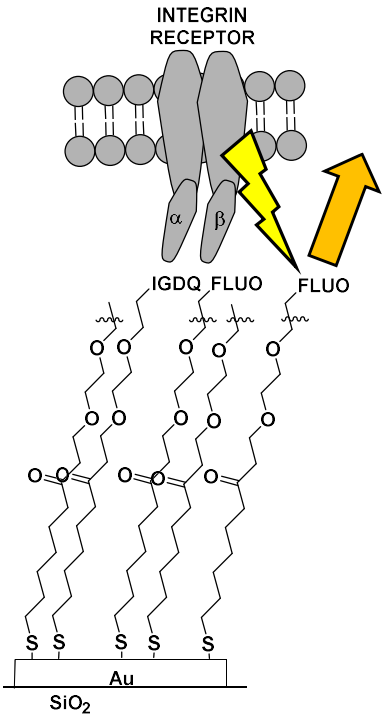

Scheme 5-5 - Concept for confocal microscopy at cell-monolayer interface. Scheme adapted from Ref.[16]

5.8. Targeting the focal complexes

When facing the challenge of metastasis research, a potential therapeutic target could be the disruption of the focal complex assembly for cell movement. To study such aspect, a multi-colour imaging tool palette for the complete characterisation of integrin-to-cytoplasm interactions is needed. Confocal microscopy could be employed to monitor cell interactions over ECM-mimicking substrates, coated with integrin-binding peptides with RGD and most importantly IGDQ sequences. Preliminary transfection experiments (Fig. 5-2) in collaboration with Prof. Dedecker from KULeuven with the objective of optimisation of transfection protocols of constructs for the overexpression of GFP-fused proteins such as Vinculin, Paxillin, Actin and integrin receptor β3 on MDA cells were started.

Unfortunately, low transfection rates resulted in weak signal when imaging with fluorescence microscopy. As shown from Fig. 5-2, the first image on the left is the transillumination picture taken with white light. After switching each laser on and applying the complementary dichroic filter, fluorescence microscopy was performed for the detection of fluorescent proteins (FPs) transfected to overexpress actin (mRuby3-RED), Vinculin (mVenus-YELLOW) and integrin β3 receptor (greenGFP). Parameters in the picture such exposure time ET and EM brightness gain are also shown for each picture. An improved and more reliable transfection protocol is needed for multiple transfection experiments that could produce different GFP-fused organelles with different fluorescence emissions. A further investigation step is also needed to fully characterise the focal complex organelle assembly for the different cell behaviours encountered in this chapter, namely the resting state, the sensing and the highly invasive cell type.

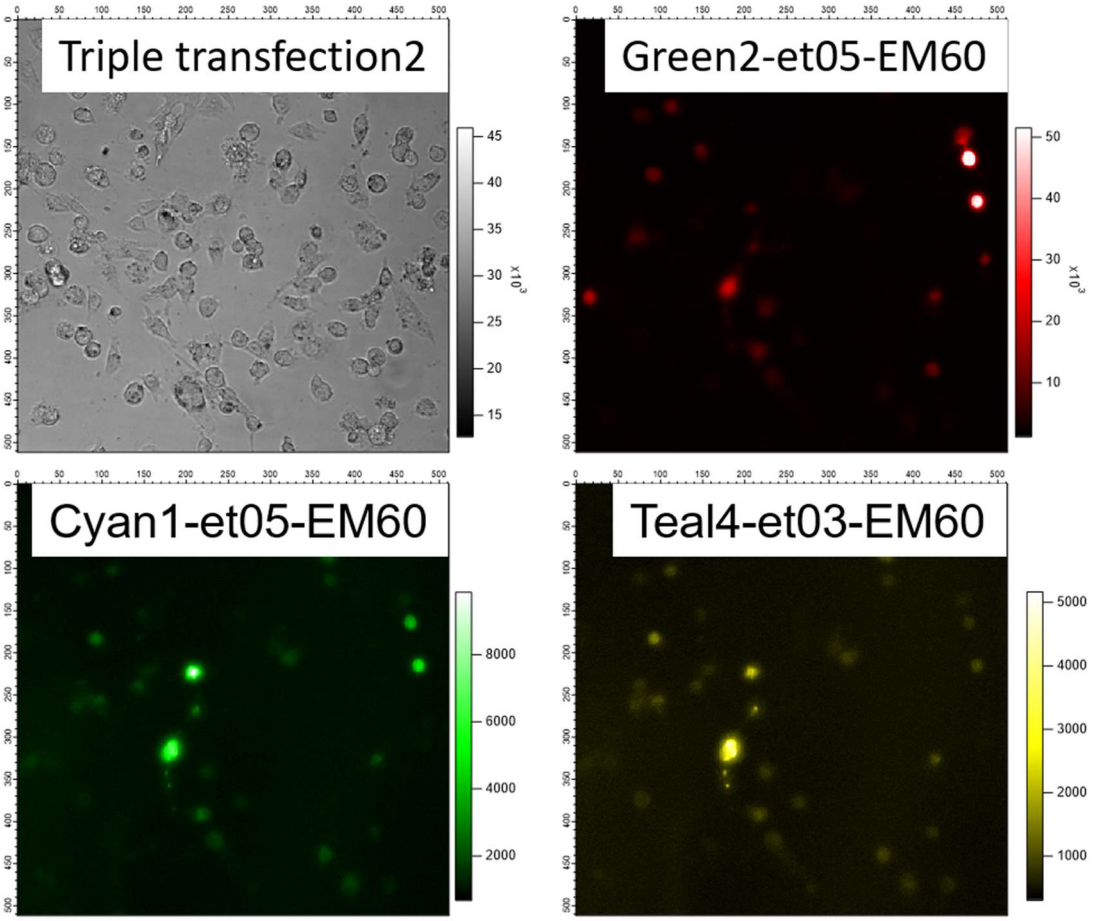

Figure 5-2 – Fluorescence microscopy imaging of transfected MDA cells. Top left: Transillumination image; Top right: Green dichroic filter, mRuby3 Actin RED emission; Bottom right: mVenus Vinculin Yellow dichroic: Bottom left: integrin b3 GFP green dichroic.

5.9. Bibliography

[1] V. Sriraghavan, R. A. Desai, Y. Kwon, M. Mrksich, C. S. Chen, *Langmuir* **2010**, *26*, 17733–17738.

[2] M. J. Salierno, A. J. García, A. Del Campo, *Adv. Funct. Mater.* **2013**, *23*, 5974–5980.

[3] N. H. Abdullah, W. A. W. Abu Bakar, R. Hussain, M. B. Bakar, M. Mohamed, M. K. A. A. Razab, J. H. van Esch, *ARPN J. Eng. Appl. Sci.* **2015**, *10*, 9538–9543.

[4] W. Luo, S. M. Legge, J. Luo, F. Lagugné-Labarthet, M. S. Workentin, *Langmuir* **2020**, *36*, 1014–1022.

[5] T. Pauloehrl, G. Delaittre, V. Winkler, A. Welle, M. Bruns, H. G. Börner, A. M. Greiner, M. Bastmeyer, C. Barner-Kowollik, *Angew. Chem. Int. Ed.* **2012**, *51*, 1071–1074.

[6] L. Rocard, A. Berezin, F. De Leo, D. Bonifazi, *Angew. Chem. Int. Ed.* **2015**, *54*, 15739–15743.

[7] G. A. Hudalla, W. L. Murphy, *Langmuir* **2009**, *22*, 5737–5746.

[8] T. Heinrich, C. H. H. Traulsen, E. Darlatt, S. Richter, J. Poppenberg, N. L. Traulsen, I. Linder, A. Lippitz, P. M. Dietrich, B. Dib, et al., *RSC Adv.* **2014**, *4*, 17694–17702.

[9] S. V. Orski, A. A. Poloukhtine, S. Arumugam, L. Mao, V. V. Popik, J. Locklin, *J. Am. Chem. Soc.* **2010**, *132*, 11024–11026.

[10] R. J. Mart, R. K. Allemann, *Chem. Commun.* **2016**, *52*, 12262–12277.

[11] R. Vulcano, P. Pengo, S. Velari, J. Wouters, A. De Vita, P. Tecilla, D. Bonifazi, *J. Am. Chem. Soc.* **2017**, 18271–18280.

[12] D. Liu, Y. Xie, H. Shao, X. Jiang, *Angew. Chem. Int. Ed.* **2009**, *48*, 4406–4408.

[13] C. Mas-Moruno, R. Fraioli, F. Rechenmacher, S. Neubauer, T. G. Kapp, H. Kessler, *Angew. Chem. Int. Ed.* **2016**, 7048–7068.

[14] Y. Zhao, R. Bachelier, I. Treilleux, P. Pujuguet, O. Peyruchaud, R. Baron, P. Clément-Lacroix, P. Clézardin, *Cancer Res.* **2007**, *67*, 5821–5830.

[15] A. Taherian, X. Li, Y. Liu, T. A. Haas, *BMC Cancer* **2011**, *11*, 293.

[16] A. Chigaev, T. Buranda, D. C. Dwyer, E. R. Prossnitz, L. A. Sklar, *Biophys. J.* **2003**, *85*, 3951–3962.

6. Experimental Part

6.1. Instrumentation

Experimental procedures were adapted from Carloni PhD Thesis (2015), Corvaglia PhD Thesis (2016), Rocard PhD Thesis (2018) from Bonifazi Research Group. Further experimental procedures adopted in this thesis are reported at the end of this Chapter.[1,2]

Thin layer chromatography (TLC) was conducted on pre-coated aluminium sheets with 0.20 mm Machevery-Nagel Alugram SIL G/UV254 with fluorescent indicator UV254. **Column chromatography** purification was carried out using Merck Gerduran silica gel 60 (particle size 63-200 µm).

Solid Phase Peptide Syntheses were carried out on a semi-automatic FOCUS XC peptide synthesizer from aapptec with a control system.

Lyophilisation was performed on a Christ Freeze Dryer ALPHA 2-4 LDplus, connected to a Vacuubrand Chemistry-HYBRID-pump. The ice condenser was approx. -80 °C and the vacuum around $4 \cdot 10^{-3}$ mbar.

UV-Vis absorptions were recorded on a Varian Cary 5000 Bio or Agilent Cary 5000 UV-Vis spectrophotometer using quartz cell (pathlength of 1 cm).

Melting points (Mp.) were measured on i) a Büchi Melting Point B-545 or on ii) a Gallenkamp apparatus in open capillary tubes.

Nuclear magnetic resonance (NMR) 1H, 13C and 19F spectra were obtained on a 270 MHz (Jeol JNM EX-270), 300 MHz (Brüker), 400 MHz (Jeol JNM EX- 400 or Brüker AVANCE III HD), 500 MHz (Jeol JNM EX-500 or Brüker) or 600 MHz (Brüker) NMR at rt otherwise stated. Chemical shifts were reported in ppm according to tetramethylsilane using the solvent residual signal as an internal reference ($CDCl_3$: δ^1H = 7.26 ppm, $\delta^{13}C$ = 77.16 ppm; DMSO-d6: δ^1H = 2.50 ppm, $\delta^{13}C$ = 39.52 ppm; MeOH-d4: δ^1H = 3.31 ppm, $\delta^{13}C$ = 49 ppm; Acetone-d6: δ^1H = 2.05 ppm, $\delta^{13}C$ = 29.84 ppm; DMF-d7: δ^1H = 8.03 ppm, $\delta^{13}C$ = 163.15 ppm). Coupling constant values (J) were given in Hz as average. Resonance multiplicity was described as s (singlet), d (doublet), t (triplet), dd (doublet of doublets), dt (doublet of triplets), td (triplet of doublets), q (quartet), m (multiplet) and br (broad signal). Carbon spectra were acquired with a complete decoupling for the proton. **Infrared spectra** (IR) were recorded on a Shimadzu IR Affinity 1S FTIR spectrometer in ATR mode with a diamond mono-crystal.

Mass spectrometry experiments were performed Cardiff University, United Kingdom. High-resolution ESI mass spectra (HRMS) were performed on a Waters LCT HR TOF mass spectrometer in the positive or negative ion mode.

Ultraviolet-Visible absorption spectra (UV-Vis) were recorded in quartz cuvettes using a Cary-Agilent UV-Vis-NIR spectrophotometer.

HPLC analyses and purifications were performed on a Varian 940-LC liquid chromatograph system and Agilent 1260 series. The analytical HPLC column used was a Varian Pursuit C18, 5µ, 4.6 × 250 mm column. The preparative HPLC column used was a Varian Pursuit C18, 5µ, 21.2 × 250 mm column. HPLC analytical and preparative eluents were 0.1% TFA in H_2O and 0.1% TFA in CH_3CN in all cases. The flow rates for analytical and preparative HPLC were 1 $mL \cdot min^{-1}$ and 10 $mL \cdot min^{-1}$, respectively. Gradient elution was applied from 5 % to 60 % CH_3CN in 20 min; 65 % to 95 % CH_3CN in 5 min then 95 % for 1 min and 95 % to 5 % in 3 min (Solvent A: H_2O; Solvent B: CH_3CN) with a flow of 1 $mL \cdot min^{-1}$ for the analytical and 10 $mL \cdot min^{-1}$ for the preparative. UV-HPLC detector was set at 220 nm and 260 nm for the analytical while the preparative was set at 220 nm. Liquid chromatography mass spectrometry (**LC-MS**) was performed on a Bruker Amazon ion trap system, operated in positive ion mode, coupled to a Thermo Ultimate 3000 system equipped with a C18 column. High-resolution mass spectrometry (**HR-MS**) was performed on a Waters Synapt quadrupole time of flight mass spectrometer coupled to a Waters Acquity H-class UPLC system equipped with a C18 column.

6.2. Materials and methods

Chemicals were purchased from Sigma Aldrich, Acros Organics, TCI, ABCR, Apollo Scientific, Alfa Aesar and Fluorochem and were used as received. Solvents were purchased from Sigma Aldrich, Fluorochem or Fischer Scientific while deuterated solvents from Sigma Aldrich. Diethyl ether (Et_2O), tetrahydrofuran (THF), dichloromethane (CH_2Cl_2) and toluene were spilled from Braun MB SPS-800 solvent purification system, dried and stored over molecular sieves. Anhydrous DMF was purchased from Acros Organics. Hydrochloridic acid (HCl 32%) was purchased from Fischer Scientific. MeOH, $CHCl_3$ and acetone were purchased as reagent-grade and used without further purification. Anhydrous conditions were achieved by drying Schlenk tubes or 2-neck flasks by flaming with a heat gun under vacuum and then purging with Ar or N_2. The inert atmosphere was maintained using Argon or N_2-filled balloons equipped with a syringe and needle for the rubber stoppers. Additions of liquid reagents were performed using dried plastic syringes or cannulas. After extraction and

washing, the organic phase containing the target compound was dried using $MgSO_4$ or Na_2SO_4 as drying agent. All other materials were obtained from commercial suppliers: HPLC grade acetonitrile (CH_3CN) and water (H_2O), piperidine (pip.), ethanedithiol (EDT), trifluoroacetic acid (TFA), triisopropylsilane (TIS), N-methylpyrrolidone (NMP), dimethylformamide (DMF), glass wool (Sigma Aldrich), diisopropylethylamine (DIEA), Nα-Fmoc amino acids, HATU from Fisher Scientific, Sigma Aldrich, Carbosynth., Fluorochem, Acros or AGTC Bioproducts, and Rink-amide MBHA resin from Aapptec.

6.3. General procedure for gold surface patterning

All the glassware used for the Au functionalisation was pre-treated and cleaned with piranha solution (1:1 $^{v}/_{v}$ of H_2SO_4/H_2O_2(30% soln.)). Before the SAMs production, Au surfaces were thoroughly cleaned by first heating at 450 °C for 30 min (model HT40L, France Etures), and after UV/Ozone treatment at r.t for 15 min (model PSD-UV3, Novascan technologies). In order to monitor and direct the cellular migration Au surfaces were patterned with a self-adhesive polymeric PVC mask purchased from Intercoat. The desired PVC masks were fabricated by Xurography technique which employed the use of a cutting plotter for cutting graphics in adhesive vinyl films. Xurography was performed by Dr. Simone Silvestrini and Dr. Andrea Farison whom I thank for the precious help and effort. Before chemical and biological evaluations, all functionalised Au surfaces were stored in aqueous media at 4 °C. This procedure allowed the storage of chemical gradients for up to five days.

6.4. Chemical gradients preparation

The SAM gradients were generated by varying the immersion time in alkanethiol-containing solutions along the longitudinal axis of the Au-coated cover slips. The immersion of the substrates was controlled by a computer-driven linear-motion drive (model T-NA08A50, Zaber technologies), with a variable speed in the range between 0.22 μ s^{-1} and 8 mm s^{-1}. Before chemical characterisations, surfaces were rinsed with absolute EtOH and dried with a gentle stream of N_2.

6.5. Water contact angle (WCA) measurements

The hydrophobicity variation due to the chemical gradients was determined by WCA measurements as a function of position along the longitudinal axis of the Au surfaces. Static contact angle analyses were performed with 1 μL droplets for water and carried out on a TBU90E Dataphysics contact angle goniometer. Dynamic WCA protocol with advancing and receding contact angle measurements (ARCA) was performed dispensing 5 μL of HPLC grade H_2O onto the functionalised SAMs. The droplet was

automatically tracked and measured by the SCA20 software (Dataphysics) dispensing 5 µL at a rate of 0.1 µL·s^{-1} for 50 s with a delay between the steps of 5 s. ARCA measurements of each surface were repeated several times (5 to 10).

6.6. HPLC analytical and preparative protocols

All analytical samples both crudes and purified were analysed with the same RP-HPLC solvent gradient shown below (Fig. 5-1, black line). Preparative RP-HPLC gradients were first set as standard and then adjusted for every crude (Fig. 5-1, red and blue lines), to be able to isolate the desired peptide product. Preparative RP-HPLC methods were modified in flow (10 mL to 20 mL), length (45 min to 50 min) and gradient steepness (see Fig. 5-1, red and blue lines respectively).

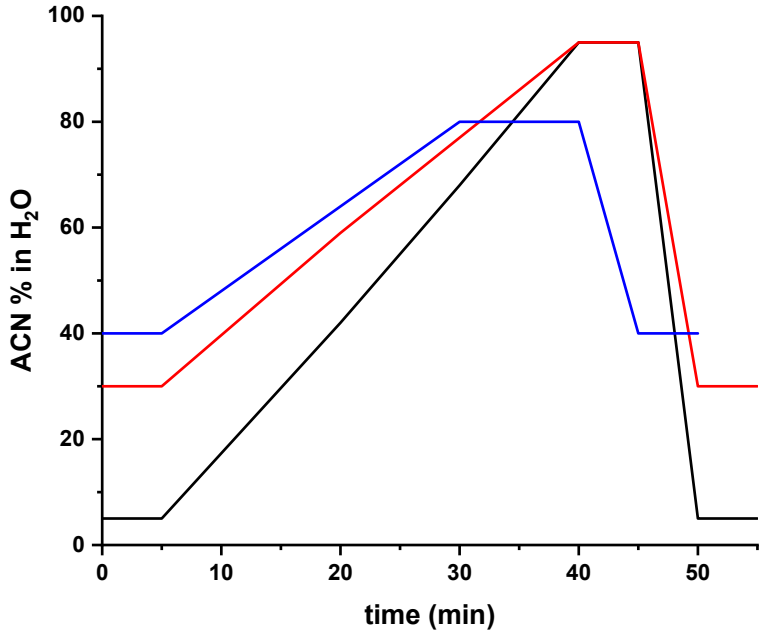

Figure 6-1 - RP-HPLC analytical and preparative gradient methods: standard analytical and preparative (black), shallower (red) and shorter (blue) preparative methods.

HPLC UV lamp was set to 220 nm and 260 nm.

Table 6-1 - Standard RP-HPLC analytical gradient method (shown also in Fig. 5-1, black line) used for every irradiation experiment, purity analysis and crude analysis. pH correction with TFA must be considered standard unless specified otherwise.

Time (min)	ACN % in H_2O 0.1% TFA
0	5
5	5
40	95
45	95
50	5

6.8. Tapping mode atomic force microscopy analyses (TM-AFM)

TM-AFM measurements on the Au substrates were carried out on air at 298 K by using a Nanoscope V (model MMAFMLN, Digital Instrument Metrology Group). The tips used in all measurements were antimony-doped silicon cantilevers (T = 3.5–4.5 μm, L = 115–135 μm, fo = 271–305 kHz, k = 20–80 N m^{-1}, Bruker) at a resonant frequency of ca. 280 kHz. The collected images were then analysed with WsxM 5.0 software (Nanotec Electronica S. L.) to acquire the cross-sectional values and profiles of SAMs and processed images.[3]

6.9. X-ray photoelectron spectroscopy (XPS) analysis

All the analyses were performed on a Thermo Scientific Kα XPS system (Thermo Fisher Scientific, UK). Spectra were collected using a monochromatic Al-Kα radiation (1486.6 eV). The surface-emitted photoelectrons were analysed in a double-focussing hemispherical analyser and recorded on a multi-channel detector. All spectra were acquired in “constant analyser” energy mode. The Thermo Scientific Avantage software (Thermo-Fisher Scientific) was used for digital acquisition and data processing. XPS studies were performed to investigate the chemical composition of the functionalised Au surfaces and monitor the IGDQK-SH nitrogen increase along the chemical gradient. For each sample, the analyses were initially performed on twenty-one different spots using an ESCA SPECTROMETER where the photon source is a monochromatic Al-Kα line (1486.6 eV) applied with a take-off angle of 35°. The survey spectra are the result of the accumulation of 5 scans where the EV Step-1 is 0.08. The C1s core level peak was taken as reference at 284.7 eV.

6.10. Photocleavage irradiation protocol

Photocleavage irradiation experiments were performed on a Lot system with a 50 mW Hg lamp with a MSH 300 monochromator (for “cold” light, timer and electronically-controlled shutter). Irradiation experiments were performed at 300 nm and 350 nm. Explorative irradiations were performed also at 250 nm and 420 nm and are not reported. The chosen wavelength for surface irradiation and peptide irradiation in solution was 350 nm, compatible with biological environment, preventing any cell damage produced by intense UV. Gold surface irradiation experiments were performed on dry surfaces and in HBSS medium, to simulate the biological conditions. Regarding the surface irradiation experiments performed at the Université de Namur URBC, UV-A Philips solarium lamps (3 x 40 W) set at 365 nm were used. Experiments were performed using a photon-counter to monitor the total energy delivered to the samples.

Functionalised surfaces with single and double gradients of photolabile peptides (no cells deposited) were irradiated for 5 min, 10 min, 15 min, 20 min and 30 min both dry and into HBSS medium. After irradiation, surfaces were rinsed gently with MilliQ H_2O, Absolute EtOH and dried in air. Samples were then analysed with a Themo-Fisher X-Ray Photoelectron Spectroscopy (XPS) by the Physics department at the Université de Namur by Dr. Alexander Felten. Irradiation on biological samples made of bare glass (13 mm Ø glass coverslip) and functionalised Au surfaces with MDA-MB-231 cells deposited was performed in HBSS medium (Sigma Aldrich). Cells cultured in a 24-well plate at a known concentration of 80 kCells·well^{-}1 were taken out of the incubator (5 % CO_2, 37 °C), washed gently with sterile PBS (1 mL x 3 x 1 mL well) and HBSS was added.

Figure 6-2 - Lot irradiation lamp setup

6.10.1 General procedure for photolinker a peptide irradiation

4-((((((9H-fluoren-9-yl)methoxy)carbonyl)-L-glutaminyl)oxy)methyl)-3-nitrobenzoic acid **3-10** (1 mg) was dissolved in ACN/H_2O + 0.1% TFA (HPLC grade, 14 mL; 1:1). Sonication was performed to achieve complete dissolution. LOT irradiation lamp () was turned on and warmed-up for 30 minutes and then set via monochromator software control to 350 nm. Quartz cuvette was primed with ACN/H_2O + 0.1% TFA (1:1; HPLC grade) and then filled with the photolinker solution. A small magnetic stirrer was used, set on gentle but constant stirring. Solution of photolabile linker was kept in dark and injected in the analytical RP-HPLC with the standard gradient method described in Table 5-1 to obtain a t_{zero} chromatogram. After that, L-Isoleucine *tert*-Butyl ester hydrochloride (10 mg; Fluorochem) were dissolved in 3 mL of ACN/H_2O + 0.1% TFA -HPLC grade-). Solution of Isoleucine internal standard (IS) was kept in dark and separate from the photolinker solution. Many internal standards were screened but only IsoLeucine was selected because of its characteristic RP-HPLC fronting peak shape that made the identification unambiguous even in complex matrices. Aliquots of both solutions were only combined after each irradiation. A first aliquot of 200 µL of photolinker solution was withdrawn from the cuvette solution and combined with 200 µL of internal standard. The combined solution was injected into the RP-HPLC to obtain the t_{zero} chromatogram with the IS. After that, the cuvette solution of photolinker was irradiated for 1 minute at 350 nm. Another aliquote of 200 µL was taken from the irradiated solution and combined with the same volume of IS. The combined solution labelled (1 min) was then injected at the RP-HPLC following the same procedure. These steps were repeated iteratively. The photolinker cuvette solution was sequentially irradiated and analysed for t_{zero}, 1 min, 5 min, 10 min, 30 min and 60 min. The total irradiation time that the cuvette solution was stated as the sum of single irradiation events, such as t_{zero}, 1 min, 6 min, 16 min, 46min and 106 min.

6.11. Experimental part from Chapter 2

WCA experiments were performed at Université de Namur and Cardiff University. Atomic Force Microscopy (AFM) experiments were performed on functionalised gold chips and coverslip surfaces, with the aim of unravelling the SAM architectures responsible for cell migration on engineered substrates. The first part of this investigation was carried out by Dr. Marega and Dr. Corvaglia on the round coverslips.[2] Round coverslips were analysed again *via* AFM then attention was moved to ultra-flat gold chips analysed by Dr. Matteo Lo Cicero. These novel substrates are smoother

than the coverslips therefore ideal to study anisotropic SAM architectures at the nm level. AFM studies were performed in Cardiff University. AFM instrument was also switched to Scanning Tunnelling Microscopy (STM) mode (low resolution, in air), unfortunately such method did not yield any results, because of the insulating nature of the glass substrate. Every plot in each AFM figure was extracted from WSxM[3] analysis software and re-plotted with *Origin 2019* with the same Y scale to be able to compare between images and monolayers. X-Ray Photoelectron Spectroscopy (XPS) experiments were also performed to visualise the anisotropic functionalisation over gold surfaces. XPS experiments were performed at Université de Namur by Dr. Marega and Dr. Alexandre Felten then in Cardiff University by Dr. Dave Morgan and Dr. Matteo Lo Cicero respectively. As a final part of the characterisation, *in silico* classical Molecular Dynamics' (MD) results are presented as a further support for the morphological study. Calculations were set by Dr. Federica De Leo, and will only be summarised as conclusions, as her topic of investigation is not part of this thesis. The work reported in this chapter was published as "Unfolding IGDQ Peptides for Engineering Motogenic Interfaces" in Langmuir in 2017, thanks to the collective effort of Dr. Federica De Leo, Dr. Riccardo Marega, Dr. Valentina Corvaglia, Dr. Matteo Lo Cicero, Dr. Simone Silvestrini and Prof. Davide Bonifazi.

6.11.1. XPS plot of δIPS/PS·Au

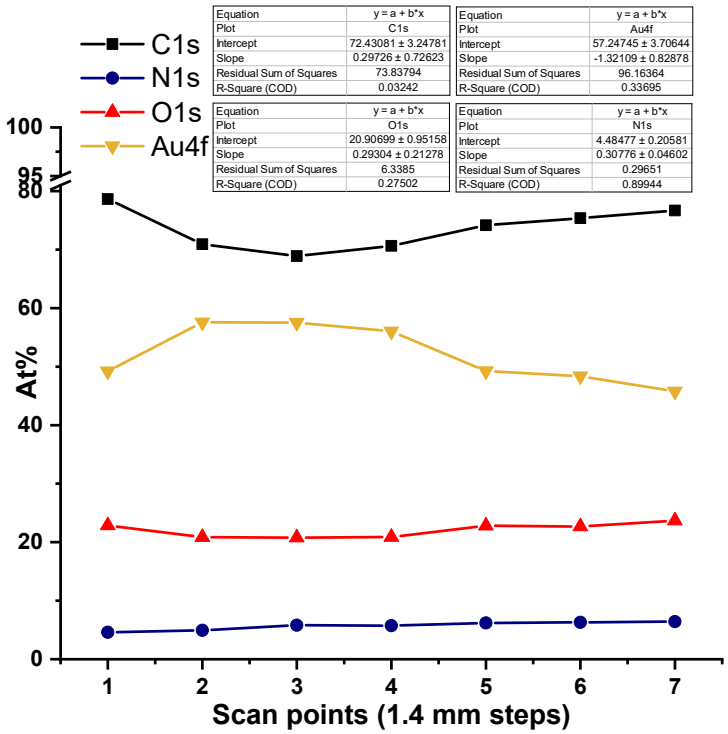

Figure 6-3 - Position-dependent chemical composition of δIPS/PS·Au. Colour code: O1s (red triangles), N1s (blue dots), Au4f (gold inverted triangles) and C1s (black squares).

6.11.2. XPS plot of δIPS/PS·Au on an ultra-flat gold chip

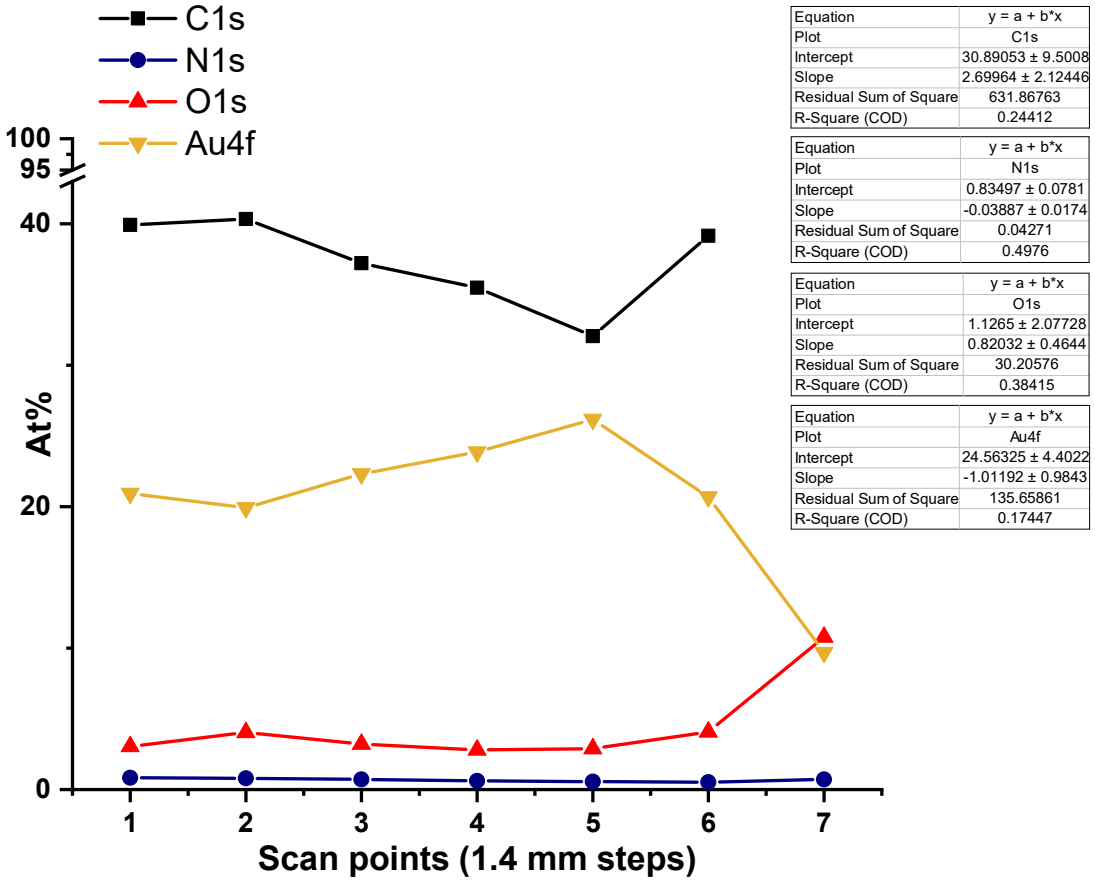

Equation	y = a + b*x
Plot	C1s
Intercept	30.89053 ± 9.5008
Slope	2.69964 ± 2.12446
Residual Sum of Square	631.86763
R-Square (COD)	0.24412

Equation	y = a + b*x
Plot	N1s
Intercept	0.83497 ± 0.0781
Slope	-0.03887 ± 0.0174
Residual Sum of Square	0.04271
R-Square (COD)	0.4976

Equation	y = a + b*x
Plot	O1s
Intercept	1.1265 ± 2.07728
Slope	0.82032 ± 0.4644
Residual Sum of Square	30.20576
R-Square (COD)	0.38415

Equation	y = a + b*x
Plot	Au4f
Intercept	24.56325 ± 4.4022
Slope	-1.01192 ± 0.9843
Residual Sum of Square	135.65861
R-Square (COD)	0.17447

Figure 6-4 - Position-dependent chemical composition of δIPS/PS·Au of ultra-flat chips. Colour code: O1s (red triangles), N1s (blue dots), Au4f (gold inverted triangles) and C1s (black squares).

6.11.3. Molecular Dynamics (MD) studies

Experimental part reported from reference.[2] Classical MD simulations of model systems were run in explicit Methanol (MeOH) in time of 10 ns to evaluate the peptide conformations during the experimental conditions as employed for the formation of the SAMs. In order to compare such results with the conditions in which SAMs are exposed to the cells, 10 ns MD simulations in explicit H_2O were also performed on the last snapshot of the MD in MeOH. Hence, inspired by the fabricated surfaces and the experimental conditions, fourteen different systems were identified to systematically study the behavior of IPSH and ISH in both H_2O and MeOH solvents. The time scale is limited (20 ns in total for each system), but it was deemed sufficient to simulate the

initial stages of adsorption. Specifically, 10 ns classical MD simulations were performed for all the systems first in MeOH. The last snapshot of each simulation was then solvated in water and additional 10 ns of MD simulations were carried out. For all the systems, the Root-Mean Square Deviation (RMSD) on the Cα, C, and N atoms of the IPSH and ISH backbones, and the Radius of Gyration (Rg) were calculated over the MD trajectories. The radial distribution functions (RDFs), the Solvent Accessible Surface Area (SASA) and the Electrostatic surface potentials were further determined.

Decision was taken to simulate the first layer where the alkanethiols are adsorbed to, approximating the Au (111) substrate to one-slab surface counting 480 atoms. Although aware that the multilayer underneath are the ones involved in charge transfer processes, their presence was neglected as our focus was set on the organization of the SAM and the secondary non-covalent interpeptide interactions. Au (111) is characterized by an atomic arrangement of six-fold hexagonal symmetry which corresponds to the most efficient way of packing atoms within a single layer ("closed packed"). Thanks to the strong interaction between thiol molecules and Au (111) substrate, the sulfur chemisorbs on specific site of the surface, forming densely packed monolayer with a chain tilt of about 30° respect to the surface normal. This arrangement allows the maximum packing driven by VdW interactions between the alkyl chains and a structure with a (√3x√3)R30° overlayer (R=rotated) lattice. The one-slab Au surface designed for our simulations can fit 130 thiol molecules.

6.11.3.1. Parameterization

ISH and IPSH starting structure were parameterized with protonated Isoleucine (NH_3^+), deprotonated Aspartate (COO^-) and one neutral sulfur atom, resulting in a neutral molecule. Charges were computed using the restrained electrostatic potential (RESP) approach, applying the antechamber module available in AMBER14, and the force field (ff) parameters were assigned to the peptide according to the AMBER parm99SB ff. Only for the MD simulation of ISH and IPSH in MeOH, the terminal thiol group was explicitly parameterized as a thiolated species SH. Similarly, CSH and PSH were parameterized using the general Amber ff (gaff). The Au-S bond between self-assembled molecules and Au atoms was placed at the distance of 2.682 Å and treated with a Lennard-Jones potential of 9.033 kcal mol^{-1} , as reported in the Dreiding ff. The gold-thiol interaction described with a non-bonded potential provides a more realistic representation of the organothiols, demonstrated experimentally to be able to hop from one site to another allover the Au surface. The Au-Au bond distance was set at 2.884 Å and Au atoms were restrained by setting the force imposed by organic molecules to

zero. Freezing the Au atoms is justified by reported evidences that demonstrate their relaxation has a negligible effect on the conformation of the SAMs. The Au-Au interactions were neglected by excluding them from the neighbor list.

6.11.3.2. Force field based MD simulations

10 ns classical MD simulations were performed for all the systems first in MeOH. The last snapshot of each simulation was then solvated in water and additional 10 ns of MD simulations were carried out. The AMBER 14 package was employed, and in all the cases the initial structures were relaxed by short minimization runs of 2000 steps, using the conjugate gradient energy minimization algorithm (convergence criterion $1.0E^{-4}$ kcal $\cdot mol^{-1}$ Å). The MD simulations were performed at constant volume (NVT) and temperature (298 K) using Langevin thermostat with a 2 fs time step. Periodic boundary conditions were applied. Non-bonded cut-off of 8 Å was set and Particle Mesh Ewald (PME) summation was used to calculate the long-range electrostatic interactions. The bonds involving hydrogen atoms were kept fixed using the SHAKE algorithm, and the Au atoms were held fixed along all the simulations. MEOHBOX model was used to simulate methanol molecules, while TIP3P model was used to represent the water molecules.

6.12. General procedures for Chapter 3

6.12.1. Solid Phase Peptide Synthesis (SPPS)

The following general protocol for semi-automated peptide synthesis performed on Aapptec Focus XC under N_2 atmosphere, equipped with two reactors, one mixing vessel and 25 amino acid vessels. The reported procedure was adapted from Dr. Carloni's PhD Thesis, Dr. Corvaglia's PhD Thesis and Dr. Rocard's PhD Thesis.

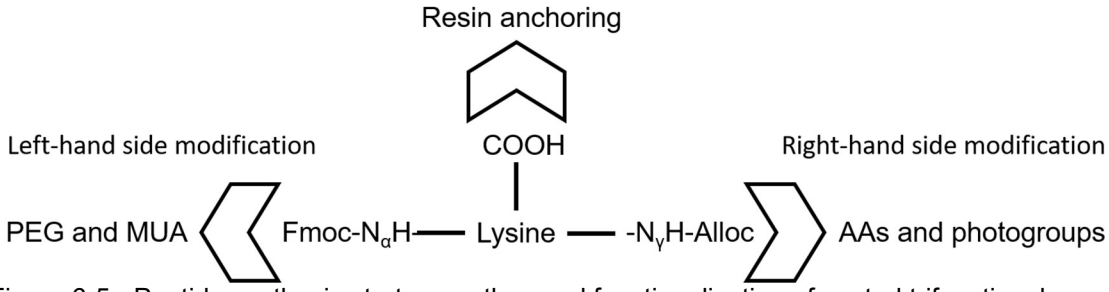

Figure 6-5 - Peptide synthesis strategy: orthogonal functionalisation of central trifunctional Lysine.

This solid phase synthesis protocol was designed for Fmoc-protected amino acids performing amide coupling reactions on piperidine-deprotected resin beads. Fig. 5-5 represents the general protocol used in this thesis for peptide chain elongation on solid phase. Lysine is used as tri-branched amino acid, enabling resin tethering with two other orthogonal chain functionalisation possibilities such as the Fmoc-protected α-amino group and the ε-amino group that bears the allyloxycarbonyl (Alloc) moiety. Synthetic strategy after Lysine anchoring to the resin proceeds with α-amino group deprotection and functionalisation (left-hand side modification). After mercaptoundecanoic acid (trityl protected) is tethered, alloc deprotection is performed. After deprotection of the ε-amino group, chain elongation can be performed on the B branch of the molecule. The right-hand side modification consists of the coupling of all the motogenic amino acids starting from Glutamine, Aspartic acid, Glycine and Iso-Leucine (IGDQ). This order follows the synthetic strategy, having Glutamine as the internal residue of the chain, bound to the central Lysine and Iso-Leucine as the exposed moiety, towards the top of the monolayer when considering the peptide on surface.

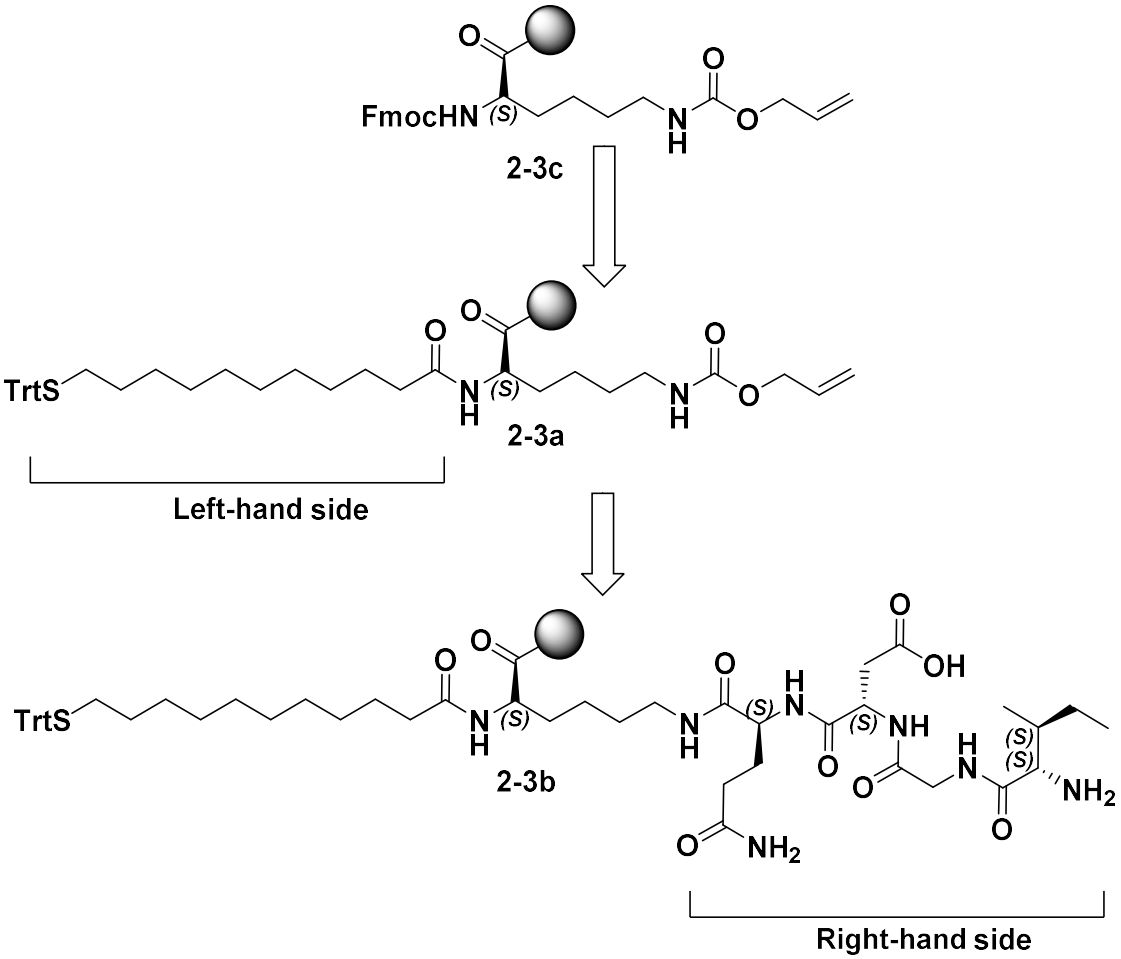

Scheme 6-1 - Solid phase synthesis design applied for this PhD thesis

6.12.2. General protocol for resin swelling, deprotection and functionalisation

Rink methyl-Benz-Hydril Amide (MBHA) Resin swelling was routinely performed at r.t for 30 minutes in NMP (15 mL) under N_2/mechanical stirring in the reaction vessel (RV). Fmoc deprotection was performed routinely using always the same protocol with 20% piperidine in DMF solution, three times for 4 minutes each step (6 mL x 4 min, x 3). Carboxylic acid was pre-activated separately via ester formation with HATU (0.4 M in DMF) in the presence of the non-nucleophilic base DIEA (2.5 M in NMP) in the mixing vessel (MV). After pre-activation, MV content was mixed with the deprotected beads in RV. Coupling reaction took place with mechanical/N_2 stirring/mixing. Kaiser tests were performed during the optimisation process to determine a general coupling time.[4] Three standard coupling conditions differing only by the time were used during every solid-phase synthesis: 30-minute coupling, 60-minute and 3-hour coupling, depending on the different substrate. The 30-minute coupling was used for every commercially available amino acid such as Iso-Leucine, Aspartic acid or Glycine and a second

"double-coupling" was also performed to ensure the highest resin functionalisation. Glutamine coupling after the Alloc deprotection was kept for 60 minutes with a "double-coupling" only for the commercially available amino acids, not for custom amino acids. Fmoc-triethyleneglycol carboxylic acid (Iris biotech) and Trityl-mercaptoundecanoic acid (Iris biotech) couplings were always performed once and for three hours each. Alloc deprotection was performed twice in manual mode, with 9 washings in between the two cleavage reactions (15 mL CH_2Cl_2 x 3, 10 mL DMF x 3, 15 mL CH_2Cl_2 x 3).

Table 6-2 - Summary of SPPS quantities for a generic peptide synthesis

Reagent/ solvent	**mmol**	**eq**	**MW ($g \cdot mol^{-1}$)**	**Molarity**	**m (g)**	**V (mL NMP)**	**d ($g \cdot mL^{-1}$)**	**Resin loading $mol \cdot g^{-1}$**
MBHA Rink resin	0.125	1	See loading	//	0.189	//	//	0.66
Fmoc-Lys-(Alloc)-OH	0.625	5	452.50	0.26 M in NMP	0.283	2.4	//	//
Trityl-mercapto undecanoic acid	0.625	5	460.67	0.26 M in NMP	0.288	2.4	//	//
Fmoc-NH-PEG(4)-COOH	0.625	5	487.54	0.26 M in NMP	0.305	2.4	//	//
HATU	0.562	4.5	380.23	0.3 M in DMF	11.4	100 mL DMF	//	//
DIEA	1.5	12	129.24	2 M in NMP	0.194	60 mL in 120 mL NMP	0.742	//
Every AA	0.625	5	//	0.26 M in NMP	//	2.4	//	//

Resin cleavage was performed with freshly prepared cleavage cocktail (TFA-EDT-H_2O-TIPS; 95:2.5:2.5:1). The resin was filtered and TFA was evaporated under fume cupboard with a gentle stream of N_2. The pellet was precipitated with Et_2O at 0 °C, dried and purified by RP-HPLC. As displayed in the table above, automated peptide synthesis on solid phase is performed with fixed reagent quantities, dispensing precise volumes into the reaction vessel. Thanks to this technique, it was possible to routinely prepare many peptides even in parallel, using both Aapptec reactors at the same time. Washing and swelling cycles can be tailored at will, for different purposes and synthetic requirements.

6.12.3. Synthesis of (3S,6S,13S)-3-(2-((2S,3S)-2-amino-3-methylpentanamido) acetamido)-6-(3-amino-3-oxopropyl)-13-carbamoyl-41-mercapto-4,7,15,31-tetraoxo-18,21,24,27-tetraoxa-5,8,14,30-tetraazahentetracontanoic acid (3-1)

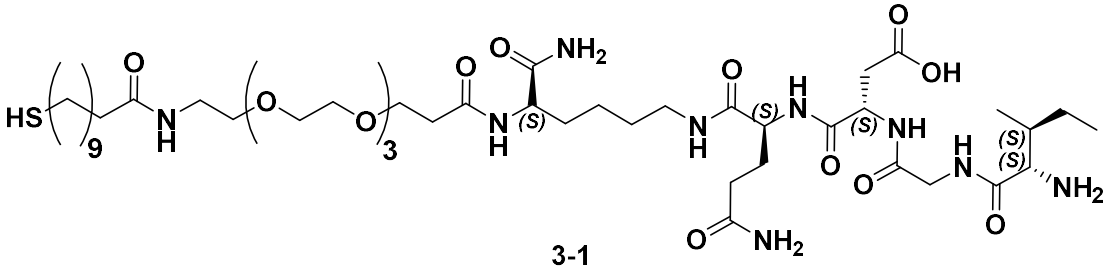

3-1

Chemical Formula: $C_{33}H_{59}N_9O_{12}S$
Exact Mass: 1005.5304

Molecule **3-1** was synthesised in a 0.125 mmol scale using a five-fold excess of Fmoc-protected Amino acids (AA, 0.625 mmol) relative to the Rink-amide MBHA resin (189 mg, 0.66 mmol·g^{-1}). Prior to the synthesis, all the AAs, Fmoc-triethylene-Glycol-COOH (Fmoc-TEG-COOH) and the Trityl-mercaptoundecanoic acid (Trityl-MUA) were dissolved in NMP (2.4 mL, 0.2 M). HATU (0.4 M in DMF), DIEA (2.5 M in NMP) and 20% piperidine in DMF solutions were freshly prepared. Rink resin was transferred in the synthesiser (reaction vessel RV) and swollen in NMP (15 mL) at r.t for 30 minutes. Fmoc deprotection was performed routinely using fixed protocol. The resin was stirred with 20% Piperidine in DMF solution for 4 minutes. This procedure was repeated 2 more times (6 mL x 4 min, x 3). After the Fmoc-deprotection stage, the carboxylic moiety needed for chain elongation was separately activated with HATU and DIEA as a routine activation step in the mixing vessel (MV). In this case Fmoc-Lys-(Alloc)-OH (2.4 mL, 0.2 mM) was separately activated with HATU (2 mL, 0.4 M) and DIEA (1 mL, 2.5 M) for 1 min at r.t under N_2 atmosphere. After the mixing, the activated carboxylic ester was mixed with the free-amine bearing resin. The coupling reaction was mixed at r.t for 30 minutes under N_2. After that, the resin was washed with NMP (10 mL x 2) and

DMF (15 mL x 2). A double coupling was performed after the washing, to ensure maximum resin loading. Afterwards, Fmoc-Lys deprotection was achieved with the afore-mentioned Fmoc-deprotection protocol. The resin was then coupled with Fmoc-TEG-COOH (2.4 mL 0,2 M) at the free α-amino (α-NH_2) group of the Lysine following the same pre-activation step. In this specific case, the amide coupling reaction was mixed at r.t for 3 hours under N_2 atmosphere. The resin was then washed with NMP (6 mL x 2) and DMF (15 mL x 2). Fmoc-TEG-amide was deprotected with Fmoc-deprotection protocol. 11-Tritylmercapto-undecanoic (2.4 mL 0.2 M) acid was linked to the Lys-TEG moiety by the free α-amino (α-NH_2) group of the TEG. The reaction was mixed at r.t. for 3 hours and after that the resin was washed with NMP (6 mL x 2) and DMF (15 mL x 2).

6.12.4. General protocol for Alloc deprotection on solid phase[5],[6]

Alloc deprotection was performed in manual mode on Focus XC peptide synthesizer by Aapptec. Rink resin was washed and then swollen in CH_2Cl_2 (wash: 5 x 15 mL, 15 mL swelling) for 30 minutes under N_2 atmosphere. After the swelling step, the Alloc deprotection reaction was performed as described in the following section.

To a solution of suspended Rink resin and Phenylsilane (1.15 mmol in 2 mL, 24 eq, 284 µL) in dry degassed CH_2Cl_2, [$Pd(P(Ph_3)_3$] (0.0336 mmol in 4 mL dry degassed CH_2Cl_2, 0.35 eq, 38 mg) was added at r.t and the mixture was stirred for 30 minutes under N_2 atmosphere. The resin colour shifted from pale yellow to dark brown/black. The resin was washed (15 mL CH_2Cl_2 x 3, 15 mL DMF x 3, 15 mL CH_2Cl_2 x 3). The Alloc deprotection was repeated. The deprotected resin was washed and then swollen again in NMP (15 mL) for 30 minutes and then was coupled with Fmoc-protected Glutamine (Fmoc-Gln-(Trt)-COOH). After being separately pre-activated, the ester was mixed to the deprotected resin. Amide coupling reaction was carried out for 1 h and a double coupling was performed afterwards to ensure the highest resin functionalisation. Reaction vessel was washed with NMP (6 mL x 2) and DMF (15 mL x 2). Glutamine Fmoc deprotection was achieved using the standard Fmoc-deprotection protocol. Subsequently the coupling reaction between the resin and the AA sequence (Fmoc-Aspartic Acid-OH, Fmoc-Glycine-OH and Fmoc-IsoLeucine-OH 2.4 mL of 0.2 mM each) was performed using the same conditions described before, cyclically. All reagents were pre-activated separately as previously described. Each coupling reaction was carried out for 30 min under N_2 atmosphere.

6.12.5. General procedure for resin cleavage and thiol deprotection

Final Fmoc deprotection CH_2Cl_2 washing were performed after the last amino acid coupling reaction. The dry resin was transferred in a vial and cooled to 0 °C. A freshly prepared cleavage cocktail solution of TFA, TIPS, water and EDT (10 mL, 94:1:2.5:2.5 respectively) was cooled to 0 °C and then added to the resin (3 mL). The reaction was stirred at r.t for 3 hours while protected from light. The reaction mixture was filtered on glass wool. The filtered solution was evaporated with a gentle stream of N_2 and precipitated with Et_2O (20 mL at 0 °C) and centrifugated (5 min @ 5000 rpm x 3) in a Falcon tube (non-sterile, 50 mL PP, Corning). The pellet was washed twice with Et_2O (20 mL at 0 °C). The organic layers were decanted and the solid was dried under a gentle stream of N_2, then in vacuo (freeze-dryer, overnight).

6.12.6. General procedure for HPLC analytical and preparative purifications

Crude and purified samples were dissolved in H_2O/CH_3CN + 0.1% TFA (8:2 ratio) to 0.5 $mg \cdot mL^{-1}$ to 1 $mg \cdot mL^{-1}$ concentration range, filtered on cotton wool and transferred into screw-cap vials for HPLC autosampler injection. The standard method to test the purity of the peptides and molecules is shown below in Fig. 5-5 and on Table 5-3. This procedure was applied for every peptide in this thesis. Crude and purified batches were compared using exclusively the method shown below.

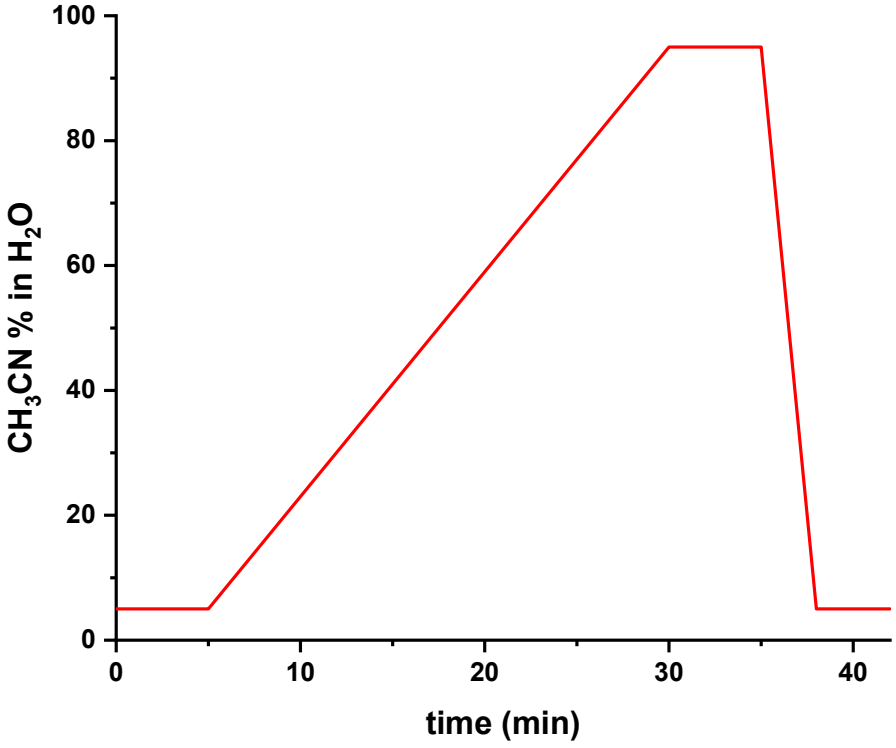

Figure 6-6 - Analytical RP-HPLC standard gradient

Table 6-3 - HPLC solvent gradient and flow chart

time	Solvent A (H_2O + 0.1% TFA)	Solvent B (CH_3CN + 0.1% TFA)
0	**95**	**5**
5	**95**	**5**
30	**5**	**95**
35	**5**	**95**
38	**95**	**5**
42	**95**	**5**

After purity evaluation from the analytical chromatogram, RP-HPLC preparative purification were performed. Preparative purifications were initially performed mirroring the analytical solvent gradient, and then lowering the slope to increase separation and peak resolution. This iterative procedure allowed greater peptide purity at the expense of the yield. An example of iterative purification method is shown below. Multiple solvent gradients are shown in Fig. 5-7: the explorative one has the highest slope, while the others differ in gradient and also in duration.

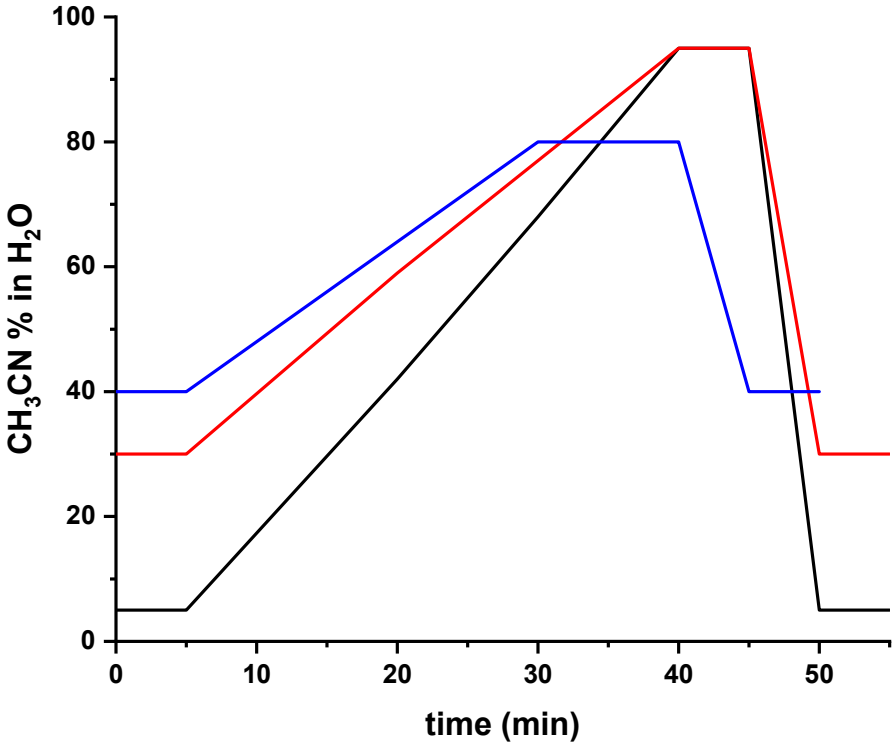

Figure 6-7 - RP-HPLC preparative gradients for iterative purification: first run (black), second run (red) and third run (blue).

After RP-HPLC purification, the selected fractions were analysed by LC-MS (Bruker), to confirm the correct peak isolation. Analytical RP-HPLC chromatogram of the purified molecule **3-1** is shown below in red (Fig. 5-8). Retention time is around 25 minutes. Following the RP-HPLC chromatogram, the HR-MS (Synapt, Cardiff School of Chemistry) is reported (Fig. 5-9). ESI+MS showed peaks of 503.7970 and 1006.5848 corresponding to $[M+H]^{2+}$ and $[M+H]^{2+}$, respectively. The following peptides reported in this experimental part were synthesised with the same described procedure.

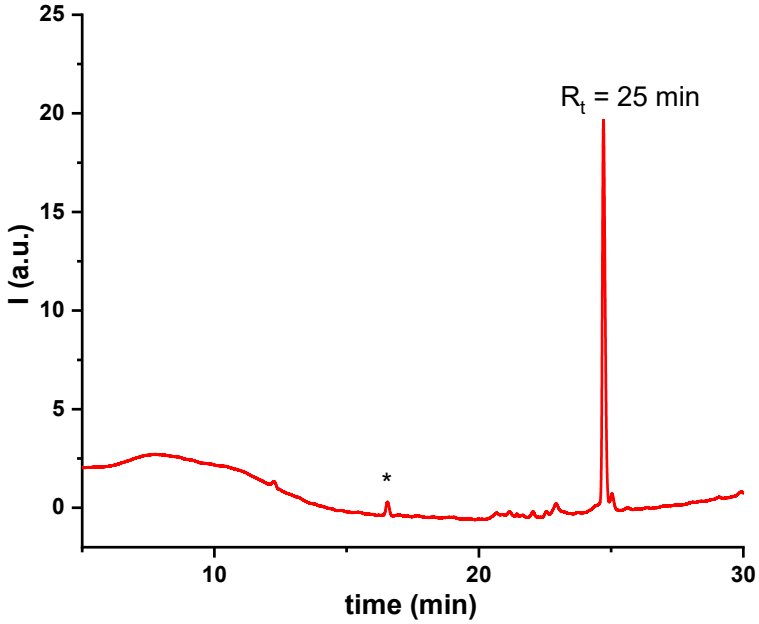

Figure 6-8 - RP-HPLC chromatogram of molecule **3-1**.

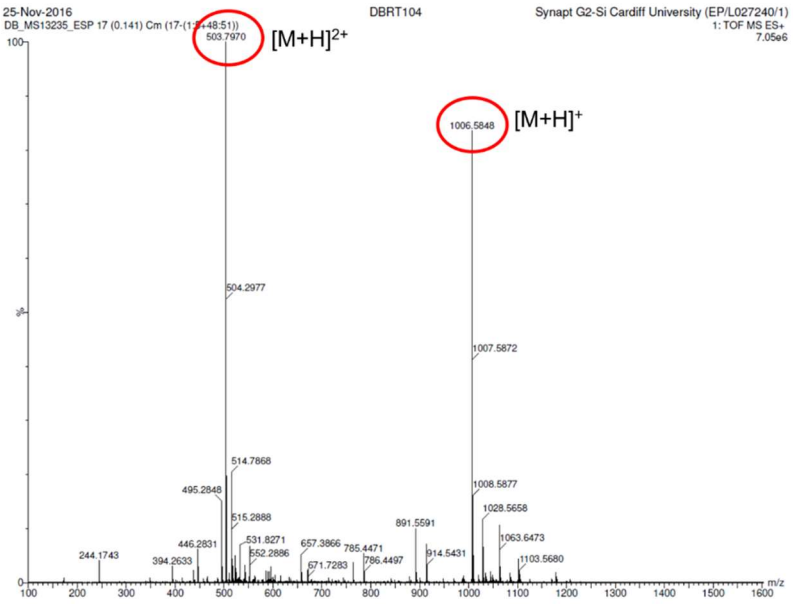

Figure 6-9 - HR-MS of molecule **3-1** with the molecular peak and the doubly-charged fragment highlighted.

6.12.7. Synthesis of (3S,6S,13S)-6-(3-amino-3-oxopropyl)-13-carbamoyl-3-(2-((2S,3S)-2-(cyclopenta-1,3-diene-1-carboxamido)-3-methylpentanamido)acetamido)-41-mercapto-4,7,15,31-tetraoxo-18,21,24,27-tetraoxa-5,8,14,30-tetraazaferrocenecarboxylic acid (3-5)

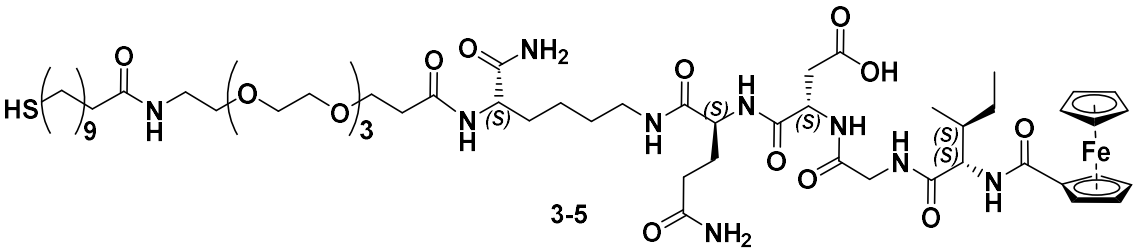

Chemical Formula: $C_{56}H_{91}FeN_9O_{15}S$
Exact Mass: 1217.5705

This the same procedure followed for **3-1** was employed for the synthesis of peptide **3-5** and Ferrocene-carboxylic acid was coupled as the last amino acid. RP-HPLC showed a peak with 26 minutes of retention time, while TOF-ESI+MS showed two major peaks of 631.7741 and 1240.5601 corresponding to $[M+Na]^{2+}$ and $[M+Na]^{+}$, respectively. Furthermore, two minor peaks of 609 and 1218.5867 corresponding to $[M+H]^{2+}$ and $[M+H]^{+}$ respectively, were recorded.

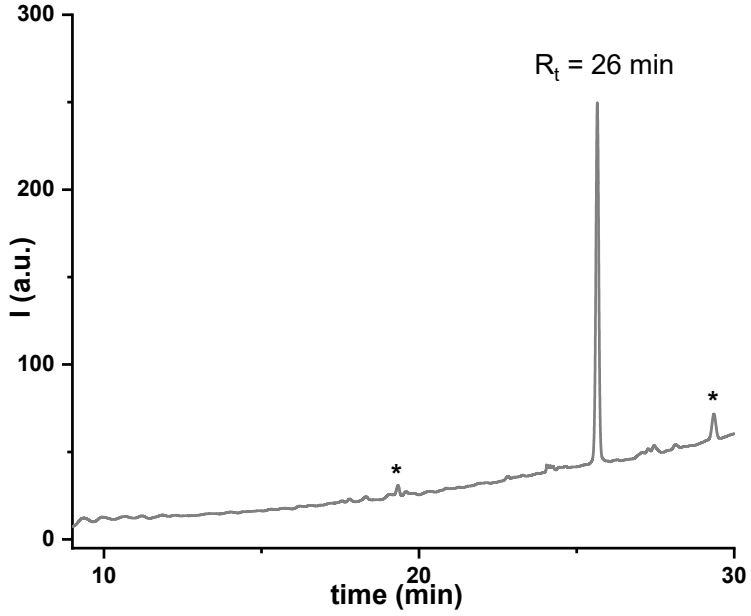

Figure 6-10 - RP-HPLC chromatogram of peptide **3-5** (R_t = 26 min). Processed spectrum. (*) column contamination. Colour code: LT grey for Ferrocene-bearing peptide **3-5**.

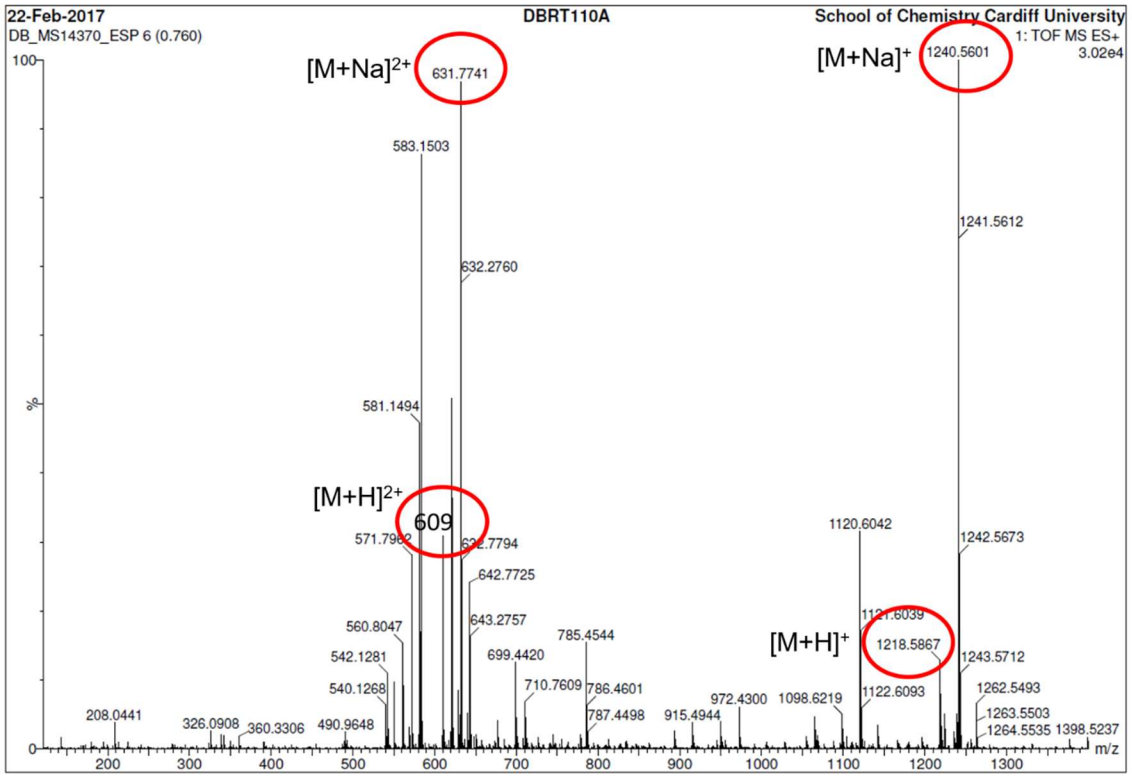

Figure 6-11 - HR-MS of molecule **3-5** or IPS-Fc

6.12.8. Synthesis of (3S,6S,13S)-6-(3-amino-3-oxopropyl)-13-carbamoyl-41-mercapto-3-(2-((2S,3S)-3-methyl-2-(4-(perfluoroethyl)-benzamido)-pentanamido)acetamido)-4,7,15,31-tetraoxo-18,21,24,27-tetraoxa-5,8,14,30-tetraazahentetracontanoic acid (3-6)

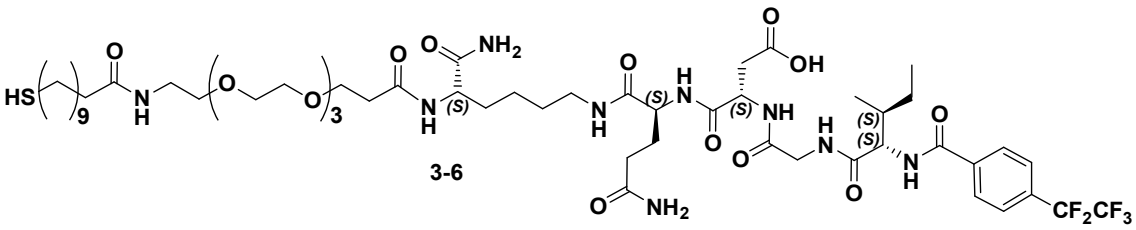

Chemical Formula: $C_{54}H_{86}F_5N_9O_{15}S$
Exact Mass: 1227.5884

The same procedure followed for peptide **3-5** was performed for peptide **3-6**. RP-HPLC chromatogram of **3-6** shows a retention time peak of around 27 minutes, with a TOF-ESI+MS showing two major peaks at 1250.5763 and 636.7802, corresponding to the $[M+Na]^+$ peak and $[M+Na]^{2+}$, respectively. Furthermore, two minor peaks of 614.7994 and 1228.6014 corresponding to $[M+H]^{2+}$ and $[M+H]^+$ respectively, were recorded.

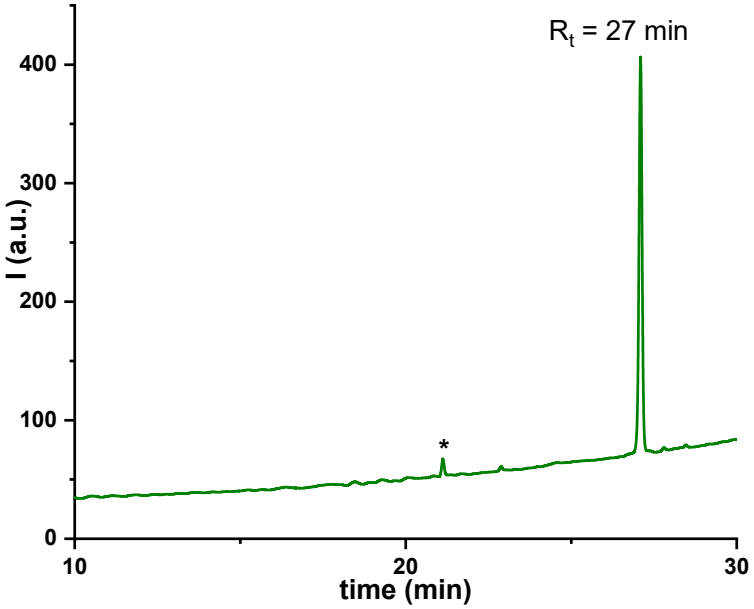

Figure 6-12 - RP-HPLC chromatogram of peptide **3-6** (R_t = 27 min). Processed spectrum. (*) column contamination. Colour code: Olive green for Fluorinated peptide **3-6**.

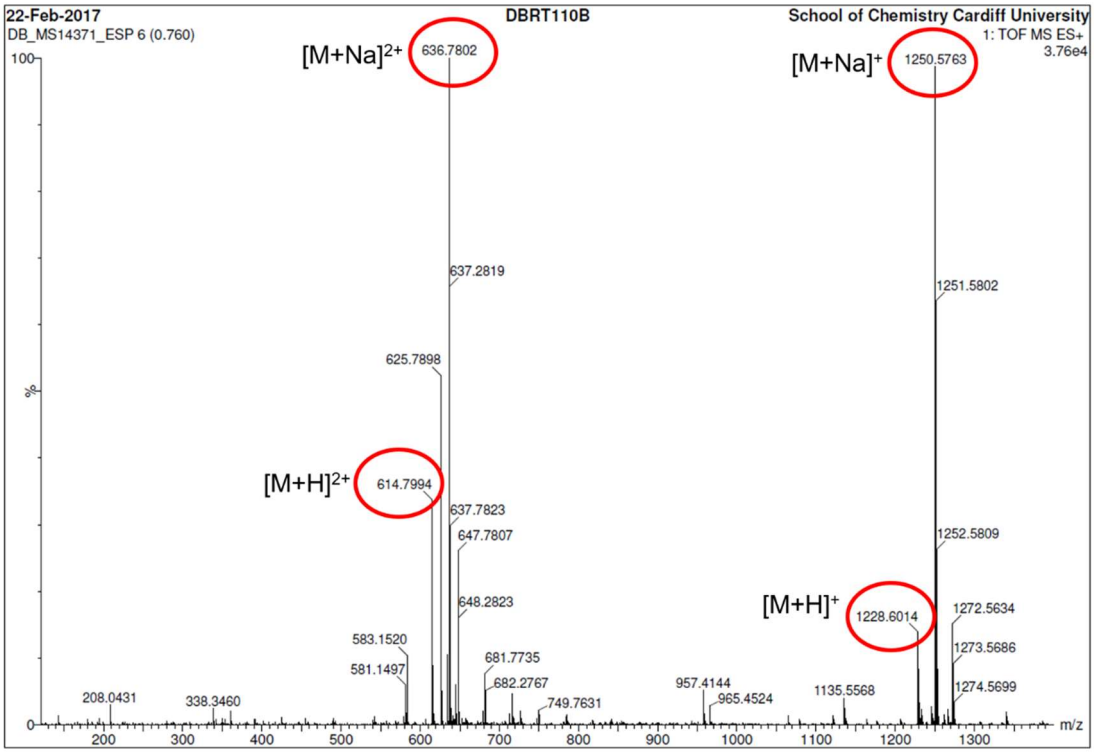

Figure 6-13 - HR-MS of molecule **3-6** or IPS-F

6.12.9. XPS characterisation of δF/PS·Au and δFc/PS·Au SAMs on gold coverslips

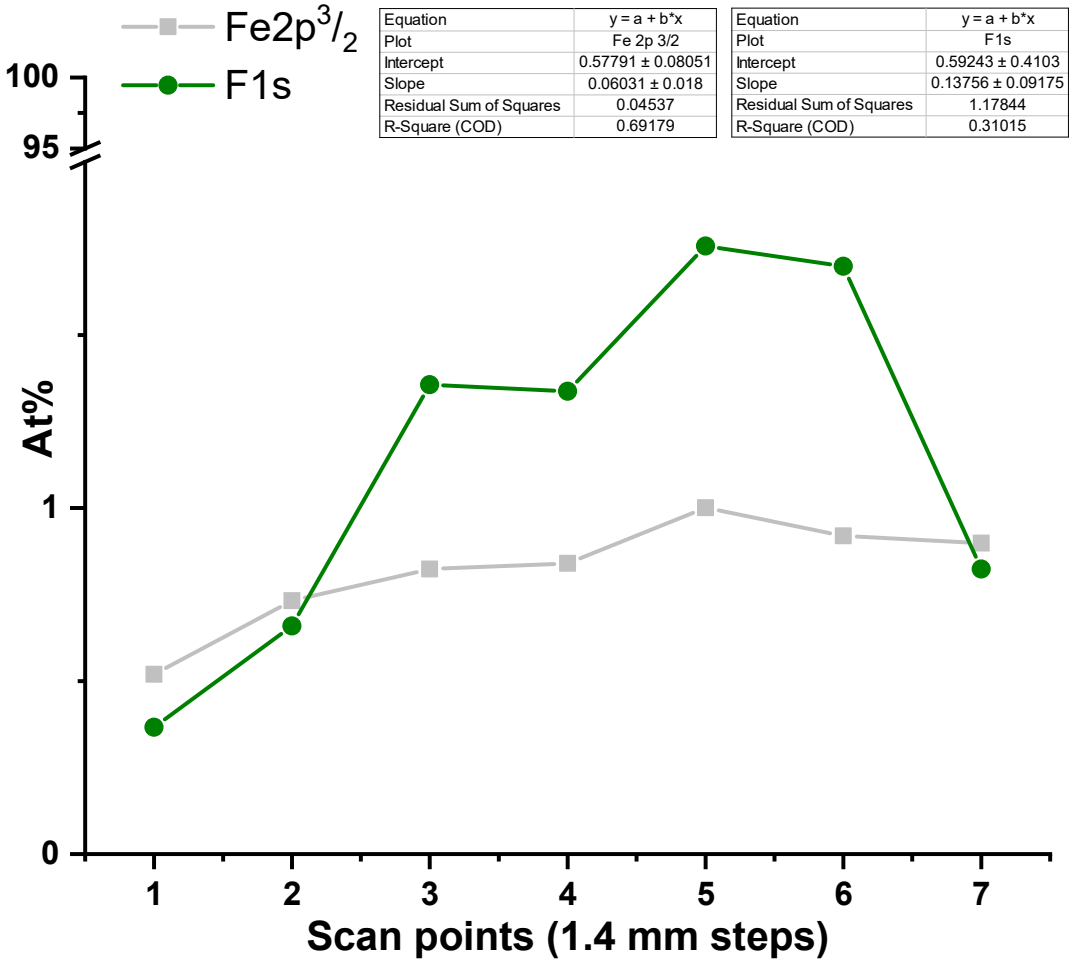

Figure 6-14 - Separate XPS mappings of single concentration gradients of **3-6** (Olive green) and **3-5** (LT grey) on different surfaces (coverslips).

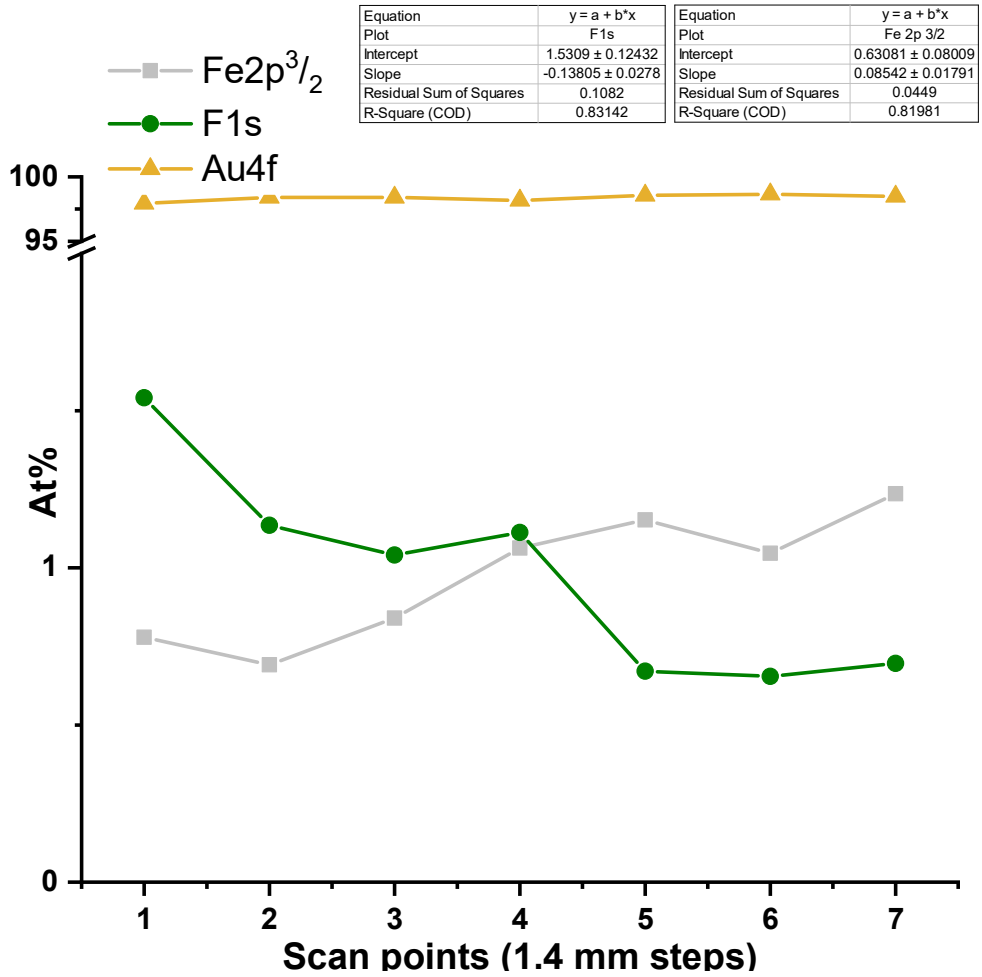

Figure 6-15 - XPS mapping of a double gradient of peptides **3-6** (LT grey) and **3-5** (Olive green) respectively.

6.12.10. Synthesis of nitrobenzyl photolabile linker

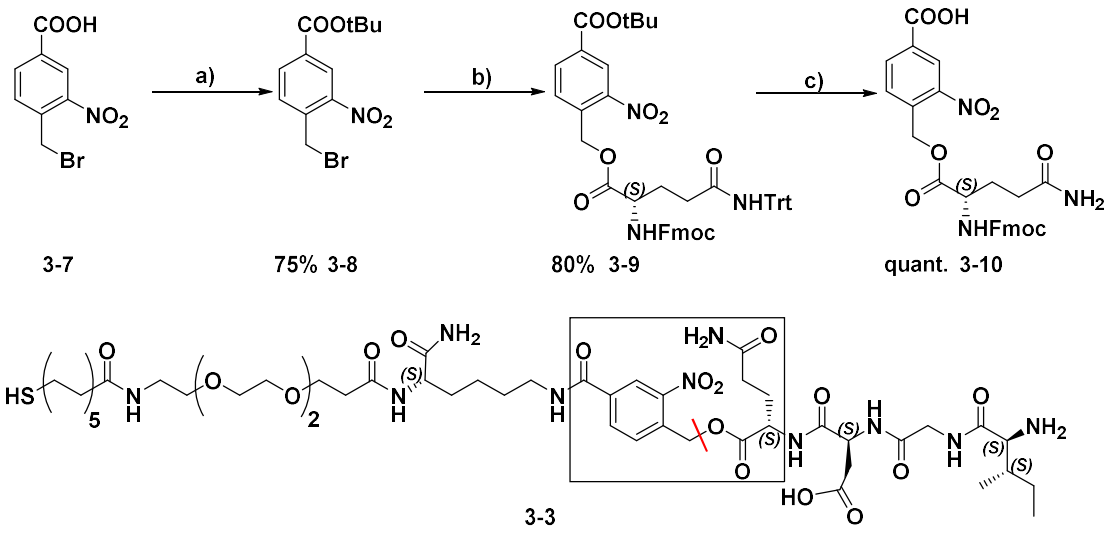

Scheme 6-2 - Synthetic route for the synthesis of the nitrobenzyl-glutamine photolabile linker. Conditions: a): DMAP, DCC, *tert*-BuOH, CH_2Cl_2, 0°C -> r.t., overnight; b): Fmoc-Gln(Trt)-COOH, DIEA, DMF, 0°C -> r.t, overnight; c): TFA/ CH_2Cl_2 1:1 $^{v}/_{v}$, 0°C -> r.t, 2h.

6.12.11. Synthesis of *tert*-Butyl 4-(bromomethyl)-3-nitrobenzoate (3-8)

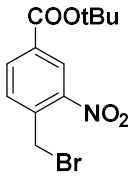

3-8

Procedure adapted and combined from literature protocols.[7,8] To a solution of **3-7** (1 g, 3,85 mmol, 1 eq) in dry degassed CH_2Cl_2 (20mL) at 0°C under Ar, DMAP (47 mg, 0,385 mmol, 0,1 eq) was added. After 5 minutes DCC (874 mg, 4,24 mmol, 1,1 eq) and *tert*-BuOH (previously stored overnight over 3Å molecular sieves; 1,83 mL, 19,2 mmol, 5 eq) were added. The mixture was stirred overnight at r.t in the dark under Ar atmosphere. The crude was filtered, and the solid filtrate was washed with CH_2Cl_2 (50 mL). The organic layers were washed with water and brine (3 x 50 mL CH_2Cl_2 washings), dried over anhydrous $MgSO_4$, filtered and the solvent was removed in vacuo. The crude was purified by silica gel column chromatography (pet/EtOAc). The desired product **3-8** (0,655 g, 53% yield) was obtained as a light-yellow solid (R_f = ca. 0.75 pet/EtOAc 2:1). M.p.: 50°C±2°C. ^{1}H NMR (400 MHz, $CDCl_3$) δ 8.58 (d, J = 1.7 Hz, 1H), 8.18 (dd, J = 8.0, 1.7 Hz, 1H), 7.63 (d, J = 8.0 Hz, 1H), 4.83 (s, 2H), 1.60 (s, 9H). ^{13}C NMR (101 MHz, $CDCl_3$) δ 171.43 (s), 163.09 (s), 147.98 (s), 136.54 (s), 134.23 (s), 133.75 (s), 132.70 (s), 126.45 (s), 82.87 (s), 28.20 (s). IR: v_{MAX} (cm^{-1}): 3282, 2927, 2854,

1643 (C=O), 1533 (N=O), 1336, 1236. EI-HRMS $[M+H]^+$ calc for $[C_{12}H_{14}BrNO_4]^+$: 315.0106, found: $[M+Na+2H]^+$ = 341.0501.

6.12.12. Synthesis of *tert*-Butyl 4-(((N2-(((9H-fluoren-9-yl)methoxy)carbonyl)-N5-trityl-L-glutaminyl)oxy)methyl)-3-nitrobenzoate (3-9)

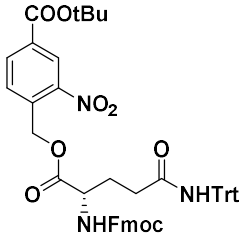

3-9

Procedure adapted from literature protocol.[9] To a solution of Fmoc-Gln(Trt)-OH (100 mg, 1 eq, 0,164 mmol) in dry DMF (2 mL) under Ar atmosphere at 0°C, Hunig's base (57 µL 0,328 mmol, 2 eq) and **3-8** (104 mg, 0,328 mmol, 2 eq) were added. The mixture was stirred overnight at r.t in dark. The mixture was diluted with EtOAc (50 mL) and extracted with water and brine (1:1; 3 x 50 mL). The organic layers were dried over anhydrous Na_2SO_4, filtered and the solvent was removed in vacuo. The crude mixture (127 mg) was purified on a silica gel column (pet/EtOAc 4/1). The desired product **3-9** (102 mg, 89% yield, R_f = ca. 0.5 pet/EtOAc 1:1) was obtained as a white solid. M.p.: 174-175°C±2°C. ^{1}H NMR (400 MHz, DMSO-d6) δ 8.61 (s, 1H), 8.44 (d, J = 1.3 Hz, 1H), 8.10 – 8.05 (m, 1H), 7.90 (d, J = 7.6 Hz, 1H), 7.85 (d, J = 7.6 Hz, 2H), 7.76 (d, J = 8.2 Hz, 1H), 7.68 (t, J = 6.6 Hz, 2H), 7.37 (t, J = 7.5 Hz, 2H), 7.30 – 7.09 (m, 18H), 5.50 (s, 2H), 4.39 – 4.05 (m, 4H), 2.43 – 2.29 (m, 2H), 2.02 – 1.68 (m, 2H), 1.51 (d, J = 8.6 Hz, 9H). ^{13}C NMR (75 MHz, DMSO-d6) δ 172.36, 171.48, 163.26, 156.74, 147.51, 145.34, 144.22, 144.20, 141.20, 136.60, 134.22, 132.36, 129.85, 129.01, 128.12, 127.94, 127.56, 126.80, 125.68, 125.59, 120.62, 83.46, 82.71, 80.96, 79.68, 76.54, 69.71, 66.28, 66.16, 65.46, 63.22, 54.06, 47.12, 33.98, 32.67, 28.74, 28.13, 27.01, 24.60, 21.52, 21.20, 20.88, 17.93, 17.26, 15.65, 15.12, 8.37. Quaternary Carbons and *tert*-Butyl Carbons not observed. IR: ν_{MAX} (cm^{-1}): 3263, 1751, 1716, 1676, 1651, 1533, 1298, 1153, 738, 698. EI-HRMS $[M+H]^+$ calc for $[C_{51}H_{48}N_3O_9]^+$: 846.3312, found: 846.3372.

6.12.13. Synthesis of 4-((((((9H-fluoren-9-yl)methoxy)carbonyl)-L-glutaminyl)oxy)methyl)-3-nitrobenzoic acid (3-10)

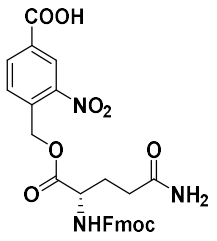

3-10

Procedure adapted from literature.[6] Molecule **3-9** (845 mg, 1 eq, 0,12 mmol) was dissolved in CH_2Cl_2 (1 mL) at 0°C under Ar atmosphere. TFA (1 mL, 100 eq, 13 mmol) was added portion-wise to the mixture. The solution turned yellow after the TFA addition. The reaction mixture was stirred for 2 hours at 0 °C. TFA was removed by a gentle stream of N_2 which was cannulated into the solution kept open to facilitate vapour removal. The crude product was precipitated in Et_2O (25 mL) at 0°C, filtered and dried in vacuo. The desired product **3-10** was obtained as a white solid (515 mg, 94% yield, R_f ca. = 0.2 in EtOH). M.p.: 238-239±2°C. ^{1}H NMR (400 MHz, DMSO-d6) δ 8.50 (d, J = 2.0 Hz, 1H), 8.16 (dd, J = 8.3, 2.0 Hz, 1H), 7.93 (d, J = 8.6 Hz, 1H), 7.85 (d, J = 8.1 Hz, 2H), 7.79 (d, J = 8.3 Hz, 1H), 7.68 (dd, J = 8.8, 2.6 Hz, 2H), 7.37 (t, J = 8.0 Hz, 2H), 7.31 – 7.21 (m, 3H), 6.80 (s, 1H), 5.51 (s, 3H), 4.43 – 4.00 (m, 3H), 2.23 – 1.68 (m, 3H). Amide protons not observed. ^{13}C NMR (101 MHz, DMSO-d6) δ 173.28, 171.94, 165.29, 156.26, 147.04, 143.80, 143.77, 140.75, 136.10, 134.13, 131.60, 129.35, 127.68, 127.11, 127.10, 125.46, 125.26, 125.23, 120.18, 65.81, 64.97, 62.84, 53.66, 46.62, 31.05, 26.21, 15.21. Quaternary Carbon not observed. IR: ν_{MAX} (cm^{-1}): 3309, 1681, 1533, 1263, 734. EI-HRMS $[M+H]^+$ calc for $[C_{28}H_{26}N_3O_9]^+$: 548.1591, found: 548.1657.

6.12.14. Synthesis of (3S)-4-((5-amino-1-((4-(((S)-5-carbamoyl-33-mercapto-7,23-dioxo-10,13,16,19-tetraoxa-6,22-diazatritriacontyl)carbamoyl)-2-nitrobenzyl)oxy)-1,5-dioxopentan-2-yl)amino)-3-(2-((2S,3S)-2-amino-3-methylpentanamido)acetamido)-4-oxobutanoic acid (3-3)

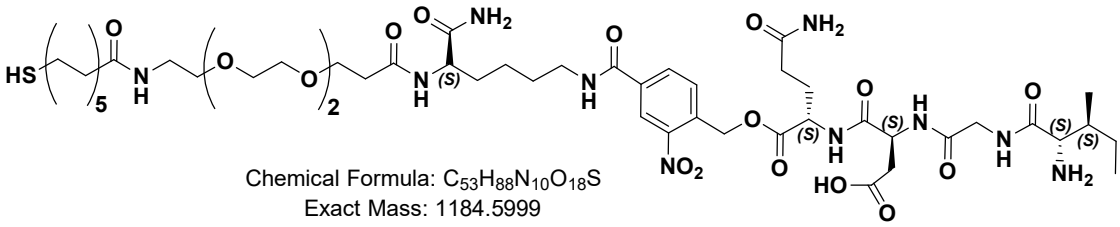

Chemical Formula: $C_{53}H_{88}N_{10}O_{18}S$
Exact Mass: 1184.5999

3-3

This photolabile peptide was synthesised with the same procedure reported above. Specifically, this peptide presents almost the same structure as the ones showed before, but there is a photolabile core in addition to the Glutamine, in the middle of the sequence. This custom amino acid was specifically designed to be included in the peptide synthesis, bearing a Fmoc-protected amine and a Trityl-protected amide on the side chain. Molecule **3-10** was employed in place of standard Fmoc-Gln(Trt)-OH. The custom amino acid **3-10** was dissolved in 2.4 mL of NMP (342 mg, 5 eq, 0.26 M, 0.625 mmol) and loaded to the peptide chain with the same protocols previously described. Coupling time was set for 1 hour. All the other amino acids were loaded mirroring the same structure described for the IGDQ-bearing peptide. RP-HPLC chromatogram showed a retention time peak of about 33 minutes and HR-MS EI-HRMS showed to major peaks of 593.3115 and 1185.6113 corresponding to $[M+H]^{2+}$ and $[M+H]^{+}$, respectively.

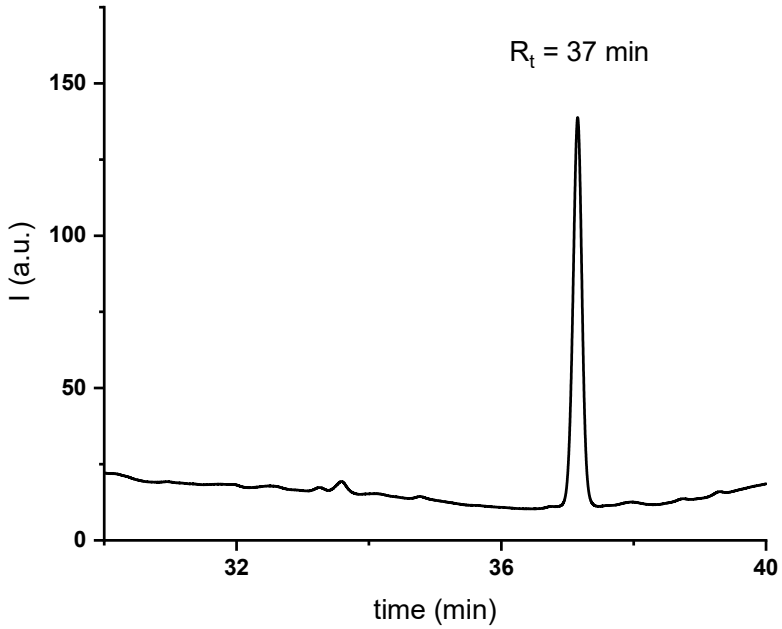

Figure 6-16 - RP-HPLC chromatogram of Nitrobenzyl-bearing peptide **3-3**.

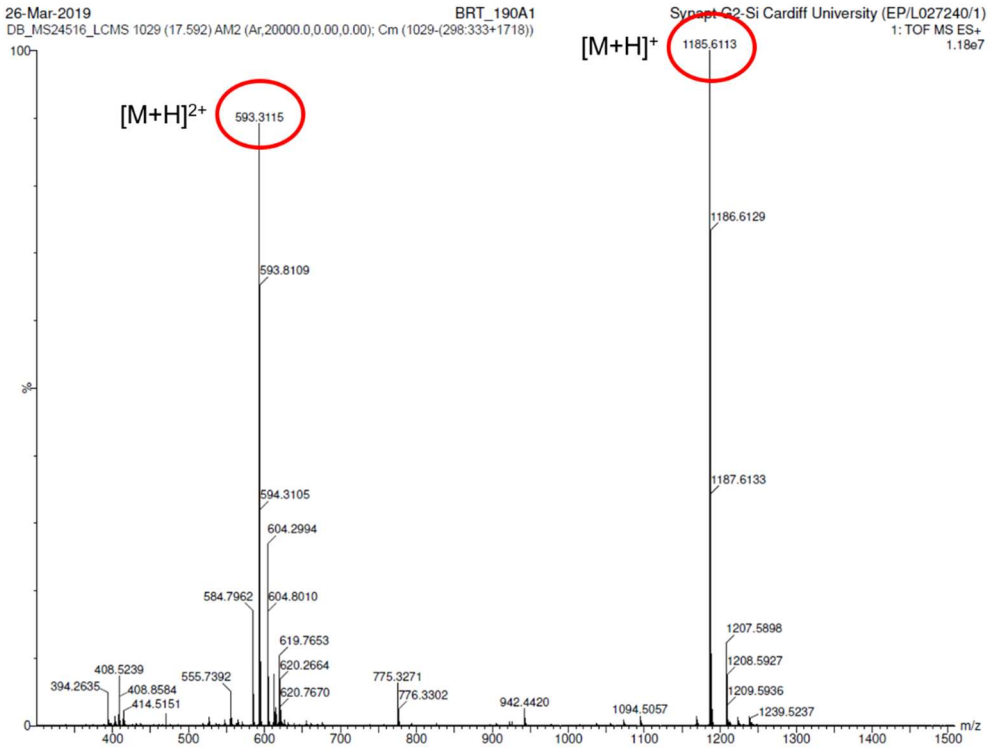

Figure 6-17 - HR-MS of Nitrobenzyl-bearing peptide **3-3**

6.12.15. Synthesis of a novel photolabile linker

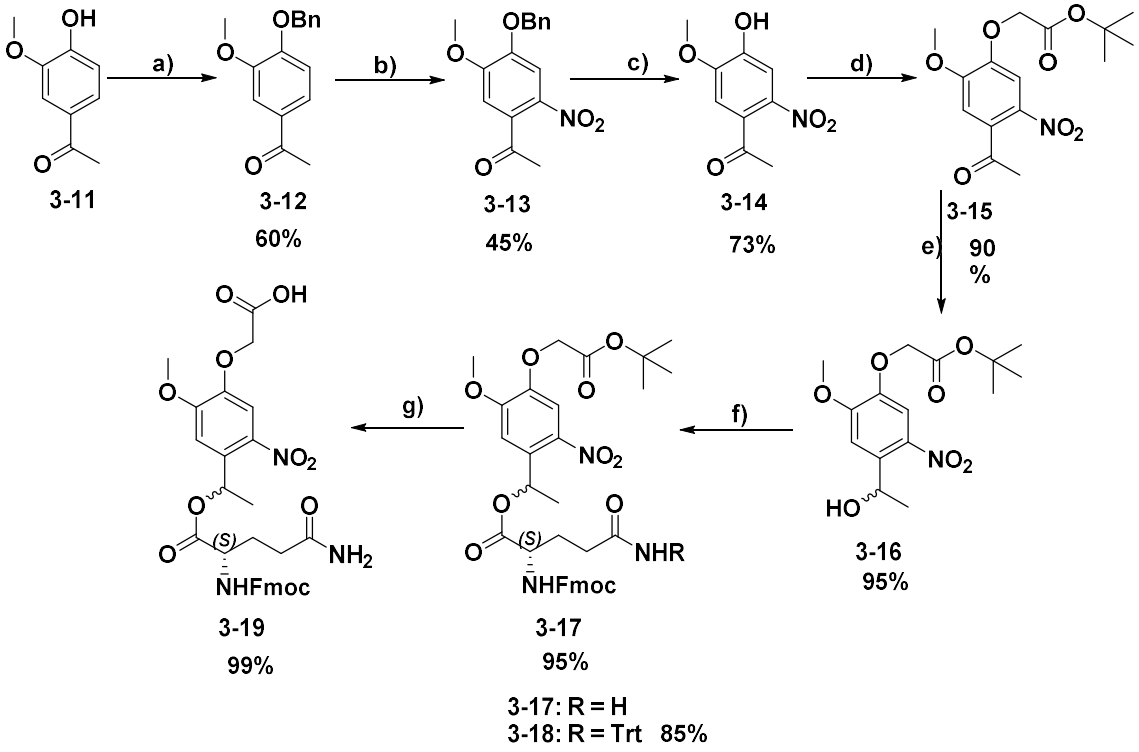

Scheme 6-3 - Synthetic pathway for the synthesis of photolabile molecule **3-19**. Conditions: *a*: BnBr, KI, CH_3CN reflux, overnight; *b*: HNO_3, 0 °C, 2 h; *c*: TFA, r.t, overnight; *d*: *tert*-Butylbromoacetate, K_2CO_3, DMF, r.t, overnight; *e*: $NaBH_4$, 0 °C, THF/MeOH, 2 h.; *f*: EDC·HCl, DMAP, r.t, CH_2Cl_2, overnight; *g*: TFA/CH_2Cl_2 (1:1), 0 °C, 2 h.

The synthetic pathway chosen to obtain molecule **3-19** employed 7 steps that started from commercially available acetovanillone. Synthesis of the intermediates is shown below.

6.12.16. Synthesis of 1-(4-(benzyloxy)-3-methoxyphenyl)ethan-1-one (3-12)

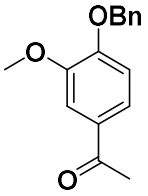

3-12

Procedure adapted from published procedure.[10] To a suspension of **3-11** (10 g; 1 eq; 60.2 mmol), K_2CO_3 (9.98 g; 1.2 eq; 72.2 mmol), KI (12 g; 1.2 eq; 72.2 mmol) and 18-crown-6 (0.525 mg; 0.033 eq; 1.99 mmol) in Acetonitrile (200 mL), Benzyl Chloride (8.3 mL; 1.2 eq; 72.2 mmol) was added. The reaction was refluxed for 12 h. Reaction conversion was monitored via TLC (pet/EtOAc 1:1; Starting material R_f = 0.5). Reaction mixture was filtered, and the solvent was removed in vacuo obtaining a black oil. The crude mixture dissolved in EtOAc (300 mL) and washed with H_2O/brine (3 x 250 mL).

The organic layers were dried over anhydrous Na_2SO_4, filtered and the solvent was removed in vacuo. The crude mixture was purified by silica gel column chromatography with pet/EtOAc (95:5, respectively) and then recrystallised in two batches, one in Hexane and one in MeOH/HCl 1M. The desired compound **3-12** was obtained as light-yellow crystals (9 g; 60% yield, R_f = ca. 0.75, pet/EtOAc 2:1). M.p.: 78-80°C±2°C. ^{1}H NMR (300 MHz, $CDCl_3$) δ 7.54 (d, J = 2.0 Hz, 1H), 7.50 (dd, J = 8.3, 2.0 Hz, 1H), 7.47 – 7.28 (m, 5H), 6.89 (d, J = 8.3 Hz, 1H), 5.24 (s, 2H), 3.95 (s, 3H), 2.55 (s, 3H). ^{13}C NMR (75 MHz, $CDCl_3$) δ 197.02, 152.47, 149.55, 136.36, 130.78, 128.83, 128.25, 127.30, 123.23, 112.13, 110.52, 70.89, 56.19, 26.39. IR: ν_{MAX} (cm^{-1}): 1666, 1579, 1508, 1411, 1143, 1028, 989. EI-HRMS $[M]^+$ calc for $[C_{16}H_{16}O_3]^+$: 256.1099, found: 256.1098.

6.12.17. Synthesis of 1-(4-(benzyloxy)-5-methoxy-2-nitrophenyl)ethan-1-one (3-13)

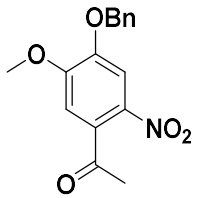

3-13

Procedure adapted from literature.[10] Molecule **3-12** (2.8 g; 1 eq; 10.9 mmol) was added portion-wise to pre-cooled HNO_3 (50 mL, 0°C in ice bath). The reaction was stirred for 1 h at 0 °C and monitored by TLC (pet/EtOAc 2:1). After 45 minutes the mixture solidified and was temporarily taken out of the ice bath to melt. After 2 hours the mixture was poured over ice. A yellow precipitate which formed instantly was filtered and washed with water (1 L). The crude filter cake was purified by precipitation from DMF (4 mL for 2 g of crude). The mixture was heated until complete dissolution of the suspension. MeOH (100 mL) was added and a yellow precipitate formed. The product was filtered, and the procedure was repeated to afford the desired product **3-13** as a light-yellow solid (6 g; 45% yield, Rf ca. = 0.55 in 2:1 pet:EtOAc). M.p.: 106-110°C±2°C. ^{1}H NMR (300 MHz, $CDCl_3$) δ 7.67 (s, 1H), 7.51 – 7.29 (m, 5H), 6.77 (s, 1H), 5.22 (s, 2H), 3.97 (s, 3H), 2.49 (s, 3H). ^{13}C NMR (75 MHz, $CDCl_3$) δ 200.21, 154.66, 148.68, 138.36, 135.33, 133.21, 128.96, 128.69, 127.69, 108.96, 108.92, 71.54, 56.80, 30.53. IR: ν_{MAX} (cm^{-1}): 1695, 1521, 1506, 1330, 1288, 1215, 1041. EI-HRMS $[M]^+$ calc for $[C_{16}H_{15}NO_5]^+$: 301.0950, found: 301.0948.

6.12.18. Synthesis of 1-(4-hydroxy-5-methoxy-2-nitrophenyl)ethan-1-one (3-14)

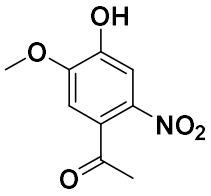

3-14

Procedure adapted from literature.[10] Molecule **3-13** (1.9 g; 1 eq; 6.34 mmol) was dissolved in TFA (20 mL) at r.t and stirred overnight. The reaction mixture turned green. TFA was removed by a gentle stream of N_2 bubbled in the flask. The crude oil was precipitated with Et_2O at 0 °C, filtered and dried in vacuo. The desired product **3-14** was obtained as a white solid (1.1 g; 73% yield, R_f ca = 0.4 pet/EtOAc 1:1). M.p.: 108-112°C±2°C. ^{1}H NMR (300 MHz, $CDCl_3$) δ 7.65 (s, 1H), 6.79 (s, 1H), 6.01 (s, 1H), 4.01 (s, 3H), 2.48 (s, 3H). ^{13}C NMR (75 MHz, $CDCl_3$) δ 200.01, 151.14, 146.75, 146.66, 132.01, 110.86, 108.72, 56.90, 30.45. IR: ν_{MAX} (cm^{-1}): 3126, 1654, 1577, 1527, 1294, 1213, 1033, 871, 802. EI-HRMS $[M]^+$ calc for $[C_9H_9NO_5]^+$: 211.0481, found: 211.0479.

6.12.19. Synthesis of *tert*-Butyl 2-(4-acetyl-2-methoxy-5-nitrophenoxy) acetate (3-15)

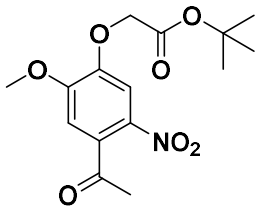

3-15

Procedure adapted from literature.[11,12] To a suspension of **3-14** (1.1 g; 1 eq; 5.2 mmol) and K_2CO_3 (2.5 g; 2 eq; 10.4 mmol) in DMF (10 mL), *tert*-Butyl Bromoacetate (0.78 mL; 1.1 eq; 5.7 mmol) was added. Reaction mixture was stirred at r.t for 4 h while being monitored by TLC (pet/EtOAc 2:1). After 4 hours full conversion was observed. Reaction mixture was filtered, and the organic layers were poured directly in H_2O (150 mL). A white precipitate formed. The precipitate was filtered off and dried in vacuo. The desired product **3-15** (1.56 g; 95% yield, R_f ca. = 0.8 pet/EtOAc 1:1) was obtained as a white solid. M.p.: 140-144°C±2°C. ^{1}H NMR (300 MHz, $CDCl_3$) δ 7.52 (s, 1H), 6.77 (s, 1H), 4.67 (s, 2H), 3.98 (s, 3H), 2.49 (s, 3H), 1.50 (s, 9H). ^{13}C NMR (75 MHz, $CDCl_3$) δ 199.97, 166.57, 154.36, 147.72, 138.01, 133.81, 109.13, 108.62, 83.40, 66.30, 56.78, 30.46, 28.07. IR: ν_{MAX} (cm^{-1}): 2985, 2358, 1741, 1707, 1506, 1336, 1290, 1238, 1207, 1151, 1070, 875, 788. EI-HRMS $[M]^+$ calc for $[C_{15}H_{19}NO_7]^+$: 325.1162, found: 325.1162.

6.12.20. Synthesis of *tert*-Butyl 2-(4-(1-hydroxy-1λ^3-ethyl)-2-methoxy-5-nitrophenoxy)acetate (3-16)

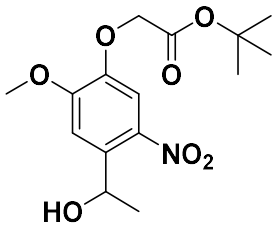

3-16

Procedure adapted from literature.[13] To a suspension of **3-15** (1.5 g; 1.1 eq; 4.6 mmol) in THF/MeOH (10 mL; 7:3) at 0 °C, $NaBH_4$ (0.174 g; 1 eq; 4.6 mmol) was added portion-wise. Reaction mixture turned red and everything dissolved. Reaction mixture was stirred for 30 min at 0 °C. Reaction was monitored by TLC (pet/EtOAc 1:1). Full conversion was reached after 20 minutes. After 30 minutes HCl 1M (12 mL) was slowly poured into the mixture then H_2O (100 mL) was poured into the mixture. The reaction turned yellow and a light-yellow precipitate formed. The precipitate was filtered, washed with H_2O (100 mL) and dried in vacuo. The desired product **3-16** (1.45 g; 95% yield; R_f ca. = 0.5 pet/EtOAc 1:1) was obtained as a light-yellow solid. M.p.: 110-114°C±2°C. ^{1}H NMR (300 MHz, $CDCl_3$) δ 7.48 (s, 1H), 7.33 (s, 1H), 5.56 (q, J = 6.3 Hz, 1H), 4.62 (s, 2H), 3.99 (s, 3H), 2.35 (bs, 1H), 1.53 (d, J = 6.3 Hz, 3H), 1.49 (s, 9H). ^{13}C NMR (75 MHz, $CDCl_3$) δ 167.01, 154.08, 145.80, 139.21, 138.10, 109.62, 109.14, 83.09, 66.31, 65.76, 56.45, 28.03, 24.33. IR: ν_{MAX} (cm^{-1}): 2980, 2358, 1728, 1506, 1456, 1246, 1151, 1105. EI-HRMS $[M]^+$ calc for $[C_{15}H_{25}NO_7]^+$: 345.1662, found: 345.1664.

6.12.21. Synthesis of 1-(4-(2-(*tert*-Butoxy)-2-oxoethoxy)-5-methoxy-2-nitrophenyl)-1λ^3-ethyl(((9H-fluoren-9-yl)methoxy)carbonyl)-L-glutaminate (3-18)

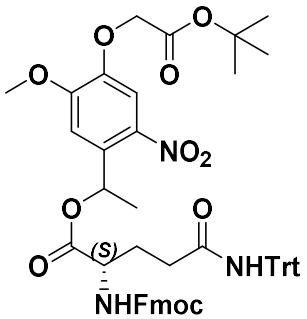

3-18

Procedure adapted from literature.[14] To a suspension of **3-16** (0.6 g; 1.1 eq; 1.8 mmol) in CH_2Cl_2 (20 mL) at 0 °C under N_2 atmosphere Fmoc-Gln(Trt)-OH (1 g; 1 eq; 1.66

mmol), EDC·HCl (0.3 g; 1.2 eq; 1.9 mmol) and DMAP (0.02 g; 0.1 eq; 0.17 mmol) were added. The mixture was stirred overnight at 0 °C to r.t under N_2 atmosphere. Solvent was removed in vacuo and the yellow solid obtained was purified by silica gel column chromatography (pet/EtOAc 90:10). The desired product **3-18** (1.3 g, 85% yield, R_f ca. = 0.7 pet/EtOAc 2:1) was obtained as a light-yellow foamy solid. M.p.: 80-86°C±2°C. ^{1}H NMR (300 MHz, CD_2Cl_2) δ 7.88 – 7.75 (m, 2H), 7.71 – 7.48 (m, 3H), 7.48 – 7.16 (m, 18H), 7.10 - 7.03 (m, 1H), 6.91 (s, 1H), 6.50 (m, 1H), 5.66 (m, 1H), 4.61 (m, 2H), 4.42 (m, 2H), 4.26 (m, 1H), 3.9 (m, 2H), 2.55 – 2.18 (m, 2H), 1.84 (m, 1H), 1.60 (m, 6H), 1.52 (s, 9H). ^{13}C NMR (75 MHz, CD_2Cl_2), two rotamers visible in carbon spectra δ 171.79, 171.32, 171.26, 167.44, 156.73, 154.90, 146.83, 146.78, 145.20, 144.33, 141.80, 129.22, 128.42, 128.22, 127.59, 127.53, 125.62, 120.47, 110.22, 109.32, 95.19, 83.27, 71.04, 70.30, 70.04, 67.42, 66.91, 57.13, 57.02, 47.72, 33.57, 28.29, 22.21. IR: ν_{MAX} (cm^{-1}): 3734, 2978, 2358, 1716, 1508, 1338, 1280, 1209, 1151, 698. EI-HRMS $[M]^+$ calc for $[C_{54}H_{54}N_3O_{11}]^+$: 920.3758, found: 920.3763.

6.12.22. Synthesis of 1-(4-(2-(*tert*-Butoxy)-2-oxoethoxy)-5-methoxy-2-nitrophenyl)ethyl (((9H-fluoren-9-yl)methoxy)carbonyl)-L-glutaminate (3-17)

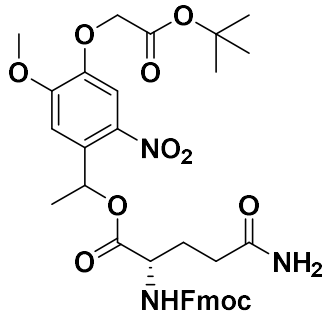

3-17

Molecule **3-17** was synthesised with the same conditions used for **3-18**. To a solution of molecule **3-17** (0.6 g; 1.1 eq; 1.8 mmol) in CH_2Cl_2 (20 mL) at 0 °C under N_2 atmosphere, Fmoc-Gln-OH (0.6 g; 1 eq; 1.66 mmol), EDC·HCl (0.3 g; 1.2 eq; 1.9 mmol) and DMAP (0.02 g; 0.1 eq; 0.17 mmol) were added. The mixture was stirred overnight from 0 °C to r.t under N_2 atmosphere. The mixture was evaporated in vacuo to yield a yellow solid and purified by silica gel column chromatography (pet/EtOAc 90:10). The desired product **3-17** (1.15 g, 95% yield; R_f ca. = 0.25 pet/EtOAc 1:1) was obtained as a light-yellow foamy solid. M.p.: 96-108°C±2°C. ^{1}H NMR (300 MHz, CD_2Cl_2) δ 7.77 (dd, J = 7.3, 3.7 Hz, 2H), 7.67 – 7.53 (m, 2H), 7.48 (d, J = 5.4 Hz, 1H), 7.44 – 7.35 (m, 2H), 7.35 – 7.23 (m, 2H), 7.08 (d, J = 3.2 Hz, 1H), 6.47 (dq, J = 9.3, 6.4 Hz, 1H), 5.98 – 5.91 (m, 1H), 5.77 (s, 1H), 5.64 (m, 1H), 4.58 (d, J = 5.9 Hz, 2H), 4.45 – 4.28 (m, 2H), 4.23 – 4.17 (m, 1H), 3.96 (d, J = 7.5 Hz, 3H), 2.34 – 2.14 (m, 2H), 2.09 – 1.77 (m, 1H), 1.70

– 1.55 (m, 3H), 1.48 (m, 9H). ^{13}C NMR (75 MHz, CD_2Cl_2) δ 174.89, 174.82, 171.91, 171.55, 167.49, 167.45, 156.79, 156.66, 154.82, 154.72, 146.79, 146.71, 144.46, 144.36, 144.30, 141.73, 139.99, 139.61, 134.18, 133.83, 128.22, 128.19, 127.58, 127.55, 125.57, 120.46, 120.44, 110.13, 110.00, 109.32, 109.24, 83.37, 83.28, 70.24, 69.99, 67.42, 67.36, 66.83, 66.79, 58.62, 57.08, 56.98, 47.67, 47.63, 31.78, 31.70, 28.51, 28.26, 28.00, 27.74, 22.13, 22.06, 18.78. IR: v_{MAX} (cm^{-1}): 3309, 1735, 1687, 1517, 1209, 1151, 1082, 726. EI-HRMS $[M]^+$ calc for $[C_{54}H_{54}N_3O_{11}]^+$: 920.3758, found: 920.3763.

6.12.23. Synthesis of 2-(4-(1-(((((9H-fluoren-9-yl)methoxy)carbonyl)-L-glutaminyl)oxy)-1λ^3-ethyl)-2-methoxy-5-nitrophenoxy)acetic acid (3-19)

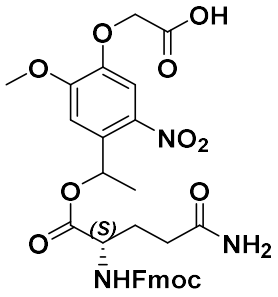

3-19

To a solution of molecule **3-17** (0.2 g; 1 eq; 0.3 mmol) and TIPS (0.3 mL; 3 eq; 1 mmol) in CH_2Cl_2 (5 mL) at 0 °C under N_2 atmosphere, TFA (4 mL; 43 eq; 13 mmol) was added dropwise at 0 °C. Reaction was monitored by TLC (EtOAc 100%). The reaction was stirred for 3 h at 0 °C. The solvent was then removed from the mixture with a gentle stream of N_2 bubbled into the flask. The resulting oil was dried in vacuo and then precipitated with Et_2O (25 mL at 0 °C), centrifugated (10 min @ 5000 rpm) and re-precipitated again after supernatant removal. The desired product **3-19** was obtained as a white solid (180 mg; 99% yield; R_f ca. = 0.25 in EtOAc). M.p.: 200-210°C±2°C. ^{1}H NMR (300 MHz, DMSO) δ 7.94 – 7.78 (m, 3H), 7.72 – 7,67 (m, 2H), 7.49 – 7.37 (m, 3H), 7.38 – 7.29 (m, 3H), 7.11 (s, 1H), 6.80 (s, 1H), 6.22 (m, 1H), 4.59 (s, 2H), 4.31 – 4.00 (m, 4H), 3.91 (m, 3H), 2.22 – 1.63 (m, 4H), 1.56 (m, 3H). Proton from Carboxylic acid not observed. ^{13}C NMR (75 MHz, DMSO) δ 173.72, 172.12, 171.85, 170.64, 170.44, 156.76, 156.58, 154.11, 153.99, 147.07, 144.24, 144.15, 141.19, 139.71, 139.18, 132.71, 128.13, 127.55, 125.68, 120.60, 109.20, 108.86, 104.09, 68.93, 68.66, 66.24, 66.17, 56.60, 56.51, 55.40, 54.13, 47.07, 31.59, 31.49, 26.68, 22.07, 21.89.IR: v_{MAX} (cm^{-1}): 3321, 1718, 1517, 1278, 1201, 1082, 740. ES-HRMS $[M]^+$ calc for $[C_{31}H_{30}N_3O_{11}]^+$: 620.1880, found: 620.1882.

6.12.24. Synthesis of (3S)-4-(((2S)-5-amino-1-(1-(4-(((S)-8-carbamoyl-36-mercapto-2,10,26-trioxo-13,16,19,22-tetraoxa-3,9,25-triazahexatriacontyl)oxy)-5-methoxy-2-nitrophenyl)ethoxy)-1,5-dioxopentan-2-yl)amino)-3-(2-((2S,3S)-2-amino-3-methylpentan-amido)acetamido)-4-oxobutanoic acid (3-20)

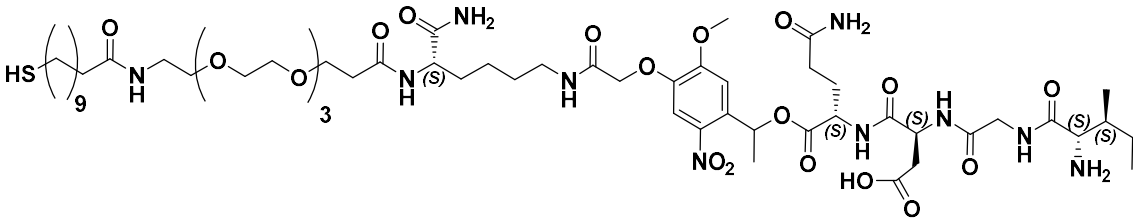

Chemical Formula: $C_{56}H_{94}N_{10}O_{20}S$
Exact Mass: 1258.6367

3-20

Peptide **3-20** was synthesised according to the procedure used for peptide **3-3**. Molecule **3-19** was used in place of Fmoc-Gln(Trt)-OH. Coupling time was extended to 3 h. ES-HRMS $[M+H]^+$ calc for $[C_{56}H_{95}N_{10}O_{20}]^+$: 1259.6445, found: 1259.6484; $[M+H]^{2+}$: 630.3272. RP-HPLC presents a chromatogram with a retention time of around 24 minutes, and a HR-MS showing two peaks of 630.3272 and 1259.6484 corresponding to $[M+H]^{2+}$ and $[M+H]^+$.

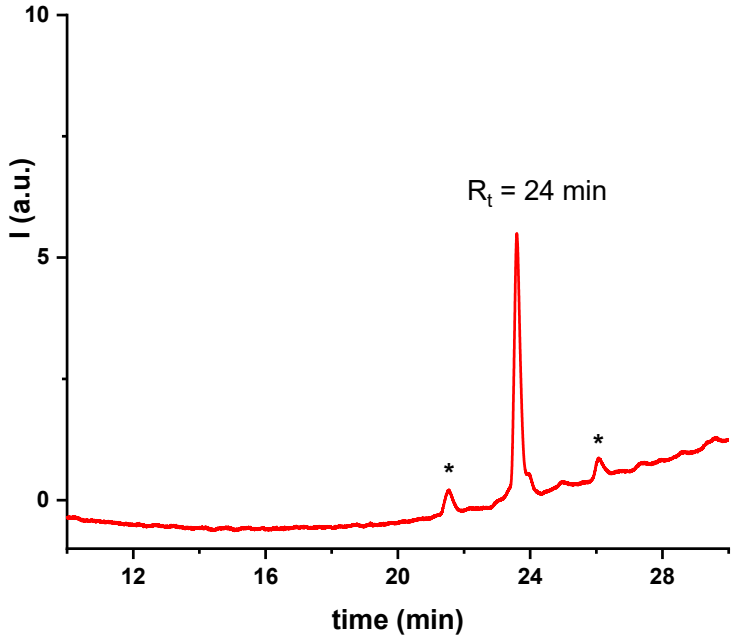

Figure 6-18 - RP-HPLC chromatogram of photolabile peptide **3-20**. (*) column contamination.

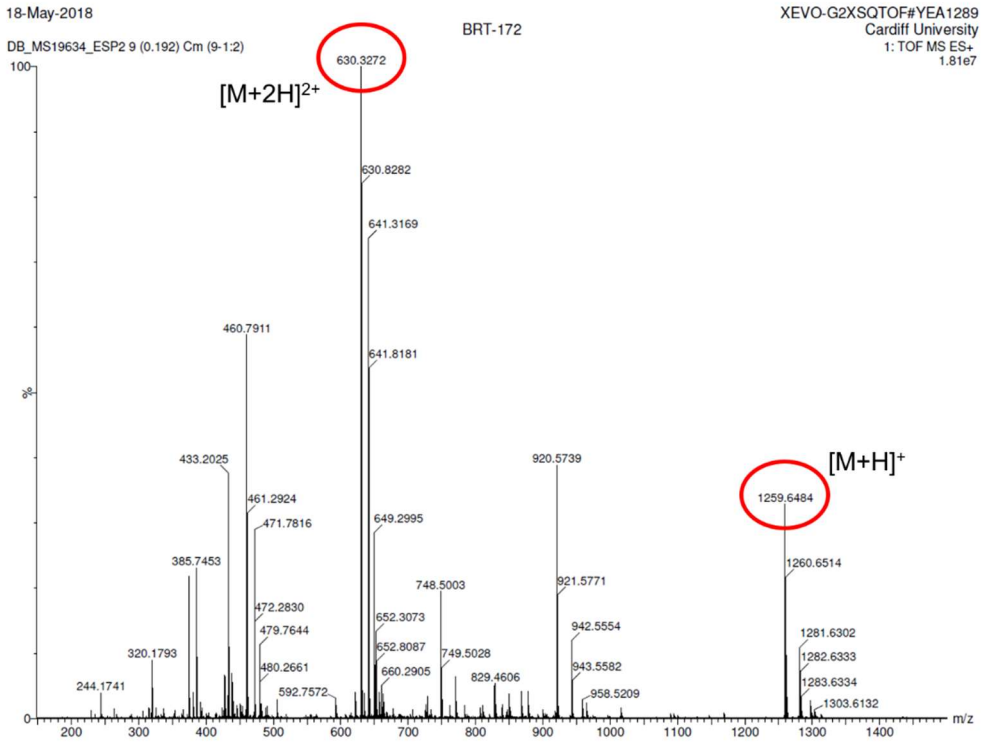

Figure 6-19 - HR-MS of molecule **3-20**.

6.12.25. Synthesis of the NVOC2 photolinker

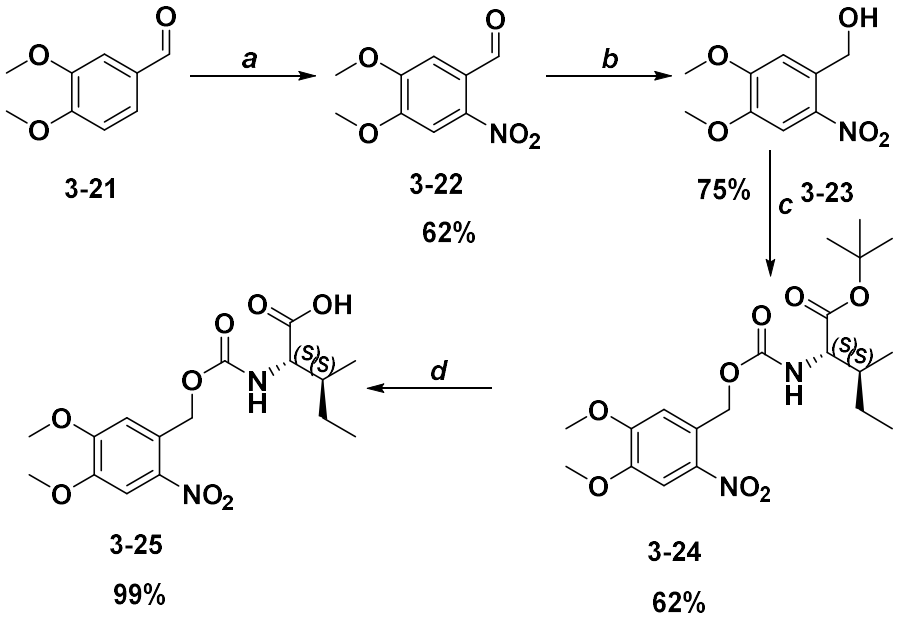

Scheme 6-4 - Synthetic pathway for the synthesis of photolabile molecule **3-26**. Conditions: *a*: HNO_3, 0 °C, 2 h; *b*: $NaBH_4$, 0 °C, THF/MeOH (7:3), 2 h; *c*: CDI, CH_2Cl_2, Iso-Leu-*tert*-Butylester·HCl, r.t, 48 h; *d*: TFA/CH_2Cl_2 (1:1), 0 °C, 2 h.

Concerning this synthetic route shares some reaction conditions that were applied for the previous pathway. First nitration step has the same conditions as previously described, as well as the aldehyde reduction. Alcohol activation via carbonyldiimidazole afforded high conversion and enabled the one-pot synthesis by simple addition of the amino acid for the preparation of the photocaged target molecule **3-26**.

6.12.26. Synthesis of 4,5-dimethoxy-2-nitrobenzaldehyde (3-22)

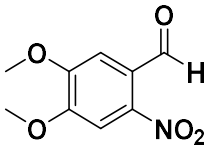

3-22

Procedure adapted from literature.[14] Commercially available Veratraldehyde **3-21** (7.3 g; 1 eq; 43.9 mmol) was dissolved in HNO_3 (25 mL; 12.6 eq; 0.56 mol) at 0 °C. The reaction mixture was stirred at 0˚C for 2 h, then it solidified forming a yellow solid which was dissolved and extracted with chloroform/water/brine (3 x 500 mL of $CHCl_3$ with 500 mL H_2O/brine 8:2). The organic layers were dried over anhydrous $MgSO_4$, filtered and evaporated in vacuo. The desired product **3-22** was obtained as a light-yellow solid (6 g; 65% yield; R_f ca. = 0.65 in pet/EtOAc 1:1). M.p.: 116-120°C±2°C. ^{1}H NMR (300 MHz, $CDCl_3$) δ 10.44 (s, 1H), 7.61 (s, 1H), 7.41 (s, 1H), 4.03 (s, 3H), 4.02 (s, 3H). ^{13}C NMR (75 MHz, $CDCl_3$) δ 187.81, 153.27, 152.45, 143.95, 125.62, 109.79, 107.24, 56.90,

56.84. IR: ν_{MAX} (cm^{-1}): 1685, 1571, 1508, 1282, 1224, 1060, 794. EI$^+$-HRMS $[M]^+$ calc for $[C_9H_9NO_5]^+$: 211.0481, found: 211.0480.

6.12.27. Synthesis of (4,5-dimethoxy-2-nitrophenyl)methanol (3-23)

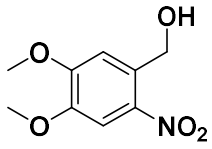

3-23

Procedure adapted from literature.[14] To a suspension of **3-22** (2 g; 1 eq; 9.47 mmol) in THF/MeOH (20 mL; 7:3) at 0 °C, $NaBH_4$ (359 mg; 1 eq 9.47 mmol) was added portion-wise. Reaction turned red from yellow and all the material dissolved completely. The reaction was stirred at 0°C for 2 h and monitored by TLC (pet/EtOAc 2:1). The reaction was quenched with HCl 1M (30 mL) carefully added in at 0 °C. H_2O (200 mL) was added and a yellow precipitate formed. The product was filtered off and dried in vacuo. The desired product **3-23** was obtained as a yellow solid (1.5 g; 75% yield; R_f ca. = 0.40 in pet/EtOAc 1:1). M.p: 128-134°C±2°C. ^{1}H NMR (300 MHz, $CDCl_3$) δ 7.69 (s, 1H), 7.17 (s, 1H), 4.95 (s, 2H), 3.99 (s, 3H), 3.95 (s, 3H), 2.75 (m, 1H). ^{13}C NMR (75 MHz, $CDCl_3$) δ 153.91, 147.97, 139.76, 132.32, 111.01, 108.12, 62.88, 56.53, 56.44. IR: ν_{MAX} (cm^{-1}): 3493, 1496, 1325, 1265, 1209, 1155, 1068, 871, 754. EI$^+$-HRMS $[M]^+$ calc for $[C_9H_{11}NO_5]^+$: 213.0637, found: 213.0635.

6.12.28. Synthesis of *tert*-Butyl (((4,5-dimethoxy-2-nitrobenzyl) oxy) carbonyl)-L-isoleucinate (3-24)

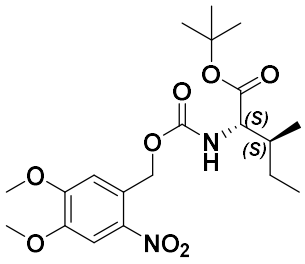

3-24

Procedure adapted from literature.[8] To a solution of molecule **3-23** (0.1 g; 1 eq; 0.46 mmol) in dry CH_2Cl_2 (5 mL) under N_2 atmosphere, CDI (0.084 g; 1.1 eq; 0.52 mmol) was added. The mixture was stirred until full conversion at r.t under N_2 atmosphere for 24 h. Reaction was monitored by TLC (pet/EtOAc 1:1). L-Isoleucine *tert*-Butyl ester hydrochloride (0.095 g; 1.3 eq; 0.42 mmol) was added to the mixture. The reaction was stirred for further 48 h at r.t under N_2 atmosphere. The solvent was then removed under reduced pressure and the obtained crude was purified by silica gel column

chromatography (pet/EtOAc 95/5). The desired product **3-24** was obtained as a light-yellow solid (0.11 g; 62% yield; R_f ca. = 0.9 pet/EtOAc 1:1). M.p.: 75°C±2°C. ^{1}H NMR (300 MHz, $CDCl_3$) δ 7.71 (s, 1H), 7.01 (s, 1H), 5.53 (m, 2H), 4.24 (dd, J = 9.0, 4.4 Hz, 1H), 3.99 (s, 3H), 3.95 (s, 3H), 1.90 (s, 2H), 1.46 (s, 9H), 1.18 (m, 2H), 0.93 (t, J = 7.3 Hz, 6H). ^{13}C NMR (75 MHz, $CDCl_3$) δ 171.14, 155.67, 153.71, 147.95, 139.48, 128.65, 109.43, 108.11, 82.21, 63.70, 58.71, 56.48, 56.43, 38.15, 28.09, 25.13, 15.52, 11.82. IR: ν_{MAX} (cm^{-1}): 2970, 2500, 1724, 1506, 1276, 1222, 1153, 1068. ES$^-$-HRMS $[M]^+$ calc for $[C_{21}H_{31}N_2O_{10}]^+$: 471.1979, found: 471.1982.

6.12.29. Synthesis of (((4,5-dimethoxy-2-nitrobenzyl)oxy)carbonyl)-L-isoleucine (3-25)

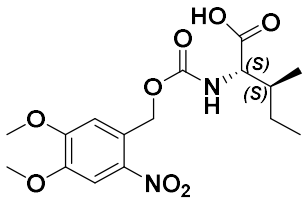

3-25

Molecule **3-24** (0.2 g; 1 eq; 0.47 mmol) was dissolved in CH_2Cl_2 (3 mL) at 0 °C. TIPS (0.5 mL; 4.5 eq; 2.1 mmol) and TFA (3 mL; 180 eq; 85 mmol) were added at 0 °C. The reaction mixture was stirred at 0 °C for 3 h. TFA was evaporated with a stream of N_2 and the crude product was precipitated with Et_2O (20 mL at 0 °C), filtered and dried in vacuo. The desired product **3-25** was obtained as a white solid in quantitative yield (0.17 g; 99% yield; R_f = 0.1 in EtOAc 100%). M.p.: 222-226°C±2°C. ^{1}H NMR (300 MHz, $CDCl_3$) δ 7.69 (s, 1H), 6.98 (s, 1H), 6.54 (s, 1H), 5.52 (m, 2H), 4.37 (dd, J = 8.9, 4.6 Hz, 1H), 3.96 (s, 3H), 3.94 (s, 3H), 1.97 (s, 1H), 1.58 – 1.37 (m, 1H), 1.22 (m, 1H), 1.09 – 0.87 (m, 6H). ^{13}C NMR (75 MHz, $CDCl_3$) δ 176.46, 155.95, 153.73, 148.17, 139.70, 128.16, 109.86, 108.25, 58.48, 56.51, 37.69, 28.15, 24.96, 17.76, 12.34, 11.73. IR: ν_{MAX} (cm^{-1}): 3334, 2962, 1705, 1517, 1273, 1217, 1064. ES$^-$-HRMS $[M]^+$ calc for $[C_{16}H_{21}N_2O_8]^+$: 369.1298, found: 369.1303.

6.12.30. Synthesis of (3S,6S,13S)-6-(3-amino-3-oxopropyl)-13-carbamoyl-3-(2-((2S,3S)-2-((((4,5-dimethoxy-2-nitrobenzyl)oxy)carbonyl)amino)-3-methylpentanamido)acetamido)-41-mercapto-4,7,15,31-tetraoxo-18,21,24,27-tetraoxa-5,8,14,30-tetraazahentetracontanoic acid (3-26)

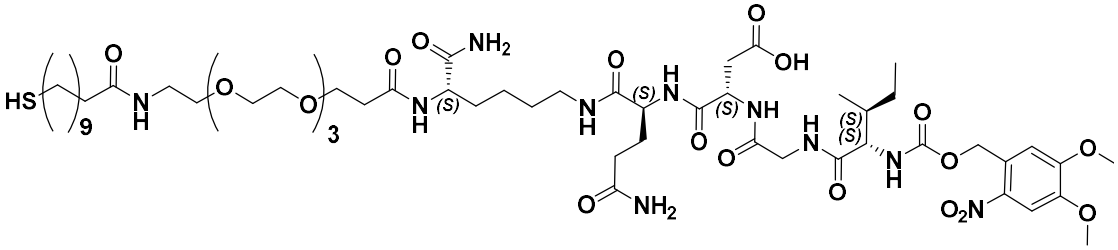

Chemical Formula: $C_{55}H_{93}N_{10}O_{10}S$
Exact Mass: 1045.6288

3-26

This peptide was synthesised according to the previously described procedure (see peptide **3-5**). Molecule **3-25** was used as last amino acid, instead of Fmoc-Ile-OH. The coupling time was extended to 3 h instead of standard 30 min. RP-HPLC presents a chromatogram with a retention time of around 30 minutes. ES^+-HRMS $[M]^+$ calc for $[C_{55}H_{93}N_{10}O_{20}S]^+$: 1245.6288, found: 1245,6273; ES^{2+}-HRMS $[M]^{2+}$ calc for $[C_{55}H_{93}N_{10}O_{20}S]^{2+}$: 623.8144, found: 623.3231.

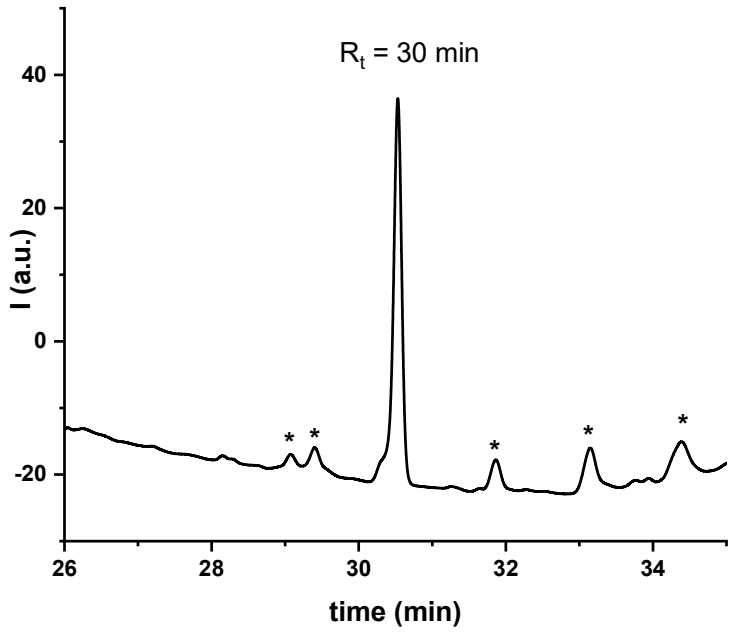

Figure 6-20 - RP-HPLC chromatogram of photolabile peptide **3-26**. (*) column contamination.

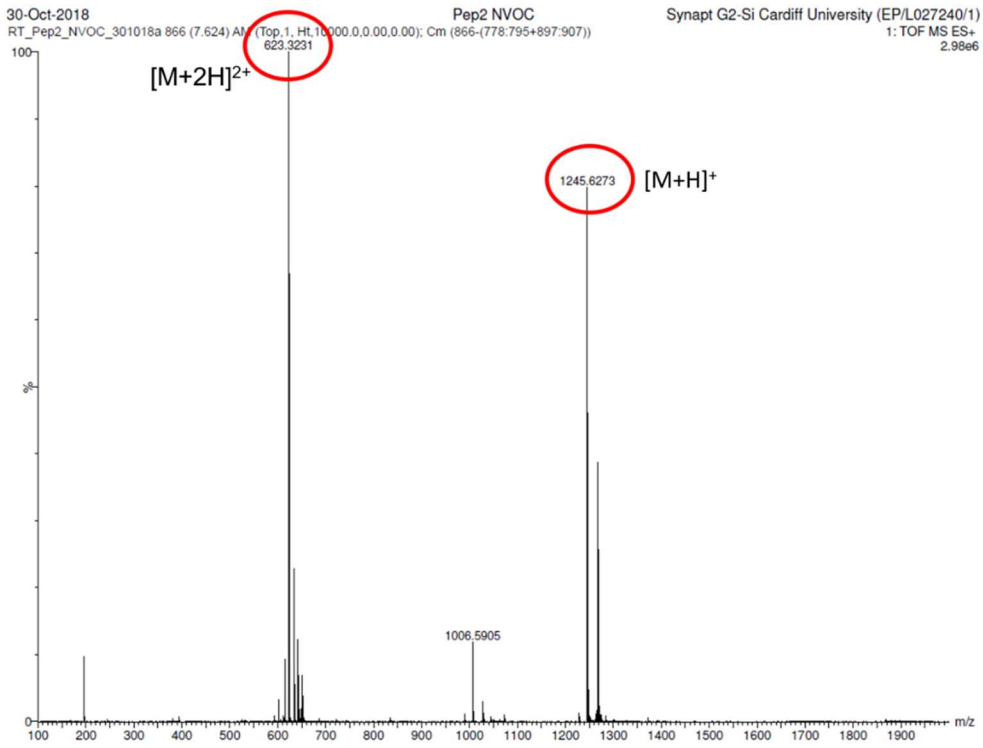

Figure 6-21 - HR-MS chromatogram of molecule **3-26**.

6.13. Experimental part for chapter 4

Human epithelial cells from metastatic breast adenocarcinoma (MDA-MB-231 cells, ATCC® HTB-26™), human melanoma cells from metastatic breast (MDA-MB-435S cells,ATCC® HTB-129™), and human dermal fibroblasts (HDFs), isolated from fetal skin (AG04431, Corriel Institute for Medical Research, USA) were maintained in culture in 75 cm2 polystyrene flasks (Corning) with 15 - 20 mL of Roswell Park Memorial Institute medium (RPMI 1640, Invitrogen) for MDA-MB-231 cells and MDA-MB-435S cells or Basal Medium Eagle (BME, 7 Invitrogen), supplemented with L-glutamine (2 mM, supplied by Sigma-Aldrich), for HDFs. HDF and MDA-435 cultures are not reported in this Thesis. All cell media were supplemented with 10% of fetal calf serum (Invitrogen) and cells were grown under an atmosphere containing 5% CO2. Phosphate buffer saline (PBS) was purchased from Lonza, while trypsin, trypsin-EDTA and CO2 independent medium (lacking L-Glutamine) and HBSS were obtained from Gibco. Hoechst 33258 pentahydrate and IP lysis buffer, Goat anti-Mouse IgG Secondary Antibody, Alexa Fluor® 633 conjugate (#A-21052), α-Tubulin Antibody, and Alexa Fluor® 488 conjugate (B-5-1-2, #322588) were obtained from Life Technologies, while Rabbit mAb anti-GM130 (#12480) was purchased from Cell signalling.[1]

6.13.1. Cell culture

Human epithelial cells from breast adenocarcinoma (MDA-MB-231, ATCC® HTB-26™), isolated from foetal skin (AG04431, Corriel Institute for Medical Research, USA) were maintained in culture in 75 cm^2 polystyrene flasks (Corning) with 15 - 20 mL of Roswell Park Memorial Institute medium (RPMI 1640, Invitrogen) or Basal Medium Eagle (Invitrogen UK), respectively. All cells media were supplemented with 10% of foetal-calf serum (Invitrogen) and cells were grown under an atmosphere containing 5 % CO_2.

6.13.2. General procedure for cell deposition onto the Au surfaces

After their fabrication, gold surfaces were left for 10 min inside pure MeOH, before being slowly dried inside an incubator (no CO_2 supply) for about 20 min. In the meantime, MDA-MB-231 cells or HDF, at about 80% confluence, were independently detached with Trypsin (Invitrogen) for 3 min and 7 min, respectively, and then centrifuged twice and resuspended in their own medium (RPMI + 10% fetal serum for MDA-MB-231 and BME + 10% foetal serum supplemented with 2 mM L-Glutamine for the fibroblasts). Cells suspension were adjusted to an average amount of 1.1 - 1.3 MCells mL^{-1} for MDA-MB-231 and 250-350 kCells·mL^{-1} for the HDF; after that 0.6 µL of such suspensions were deposited on to each deposition spot on the Au surfaces. After an average time

of 3 ± 0.5 min, the respective growth mediums were slowly added to the wells containing the functional surfaces (average speed of 2 - 2.2 mL min^{-1}), and the cells were kept under an atmosphere containing 5 % CO_2 for 120 h. Every 48 hours medium renewal was performed, and optical microscopy images were taken respectively at t = 0, 48, 96 and 120 h after the cell deposition.

6.13.3. Optical microscopy imaging

Once cells were deposited onto the Au surfaces, they were monitored through an inverted transmitted- light microscope (model Leitz Labovert FS, Alliance Analytical Inc.), recording the images as a function of the position along the Au substrates on a time lapse of five days (t = 0, 48, 96 and 120 h after cell deposition).

6.13.4. Cell staining for confocal imaging

Cell staining on individual modified functional Au surfaces was carried out 120 h after initial cell deposition and required three washings of 2 min each with 1 mL of warm PBS. After that, cells were fixed 10 min with PBS containing 4% paraformaldehyde solution. Again, three cycles of washing with warm PBS (2 min) were performed. In order to ensure membrane permeabilization, a warm PBS solution of BSA (2%) and Triton-X (0.2 %) was added for each substrate-containing well and the whole system was kept at r.t for 3 h protected from light. After that, three cycles of washing with warm PBS (2 min) were performed, and then the substrates were interfaced with 60 µL of rhodamine-phalloidin solution (7 µL) in PBS/BSA/Triton-X (200 µL) for 10 min at r.t and protected from light. Again, three cycles of washing with warm PBS (2 min) were carried out. Finally, the substrates were interfaced with 60 µL of DAPI solution (12 µL) in PBS/BSA/Triton-X (200 µL) for 20 min at r.t. and protected from light. Eventually three cycles of washing with warm PBS (2 min) were then performed. Substrates were dried and mounted on glass slides with Muviol for confocal microscopy imaging.

6.14. Bibliography

[1] V. Corvaglia, R. Marega, F. De Leo, C. Michiels, D. Bonifazi, Small **2016**, 12, 321–329.

[2] F. De Leo, R. Marega, V. Corvaglia, R. Tondo, M. Lo Cicero, S. Silvestrini, D. Bonifazi, Langmuir **2017**, 33, 7512–7528.

[3] I. Horcas, R. Fernández, J. M. Gómez-Rodríguez, J. Colchero, J. Gómez-Herrero, A. M. Baro, Rev. Sci. Instrum. **2007**, 78, 013705.

[4] E. Kaiser, R. L. Colescott, C. D. Bossinger, P. I. Cook, Anal. Biochem. **1970**, 34, 595–598.

[5] M. Dessolin, M. G. Guillerez, N. Thieriet, F. Guibé, A. Loffet, Tetrahedron Lett. **1995**, 36, 5741–5744.

[6] F. Albericio, A. Isidro-Llobet, A. Mercedes, M. Álvarez, F. Albericio, Chem. Rev. **2009**, 109, 2455–2504.

[7] S. W. Wright, D. L. Hageman, A. S. Wright, L. D. Mcclure, **1997**, 38, 7345–7348.

[8] R. Shelkov, M. Nahmany, A. Melman, **2004**, 397–401.

[9] S. Strategies, S. Ficht, R. J. Payne, R. T. Guy, C. Wong, **2008**, 3620–3629.

[10] M. A. Azagarsamy, D. L. Alge, S. J. Radhakrishnan, M. W. Tibbitt, K. S. Anseth, Biomacromolecules **2012**, 13, 2219–2224.

[11] E. B. Akerblom, Mol. Divers. **1999**, 4, 53–69.

[12] E. B. Akerblom, a S. Nygren, K. H. Agback, Mol. Divers. **1998**, 3, 137–48.

[13] C. P. Salerno, H. J. Cleaves, Synth. Commun. **2004**, 34, 2379–2386.

[14] T. Konishi, T. Hashimoto, N. Sato, K. Nakajima, K. Yamaguchi, Bull. Chem. Soc. Jpn. **2016**, 89, 125–134.

7. Appendix

Here shown below the HPLC analytical blank runs of photolabile molecules **3-10**, **3-19** and **3-20**. Parasite peaks due to column contamination can be seen.

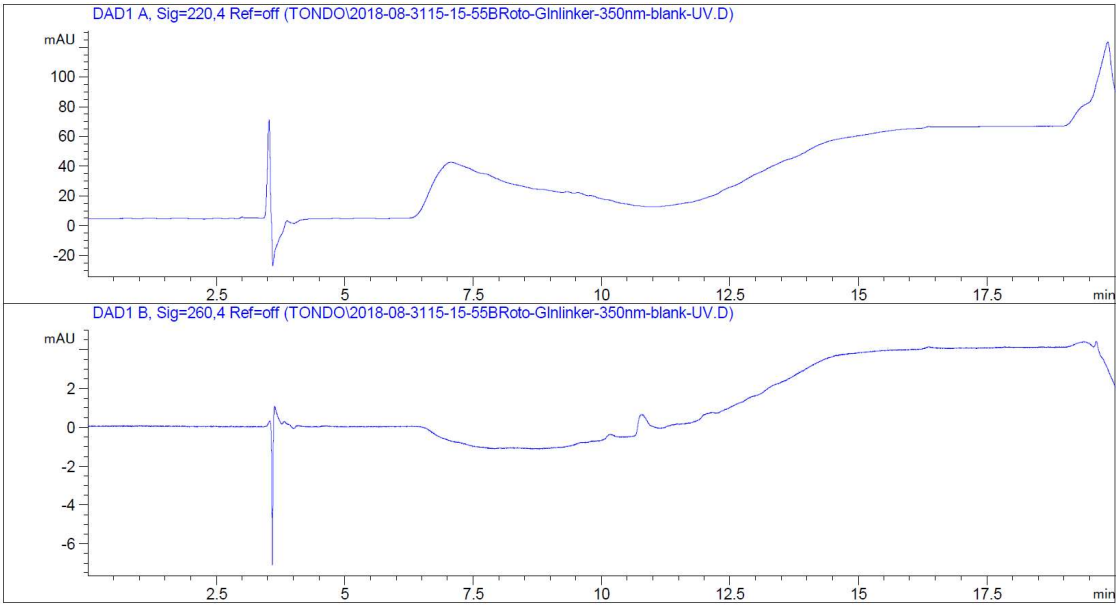

Figure 7-1 - Linker **3-10** HPLC analytical blank run.

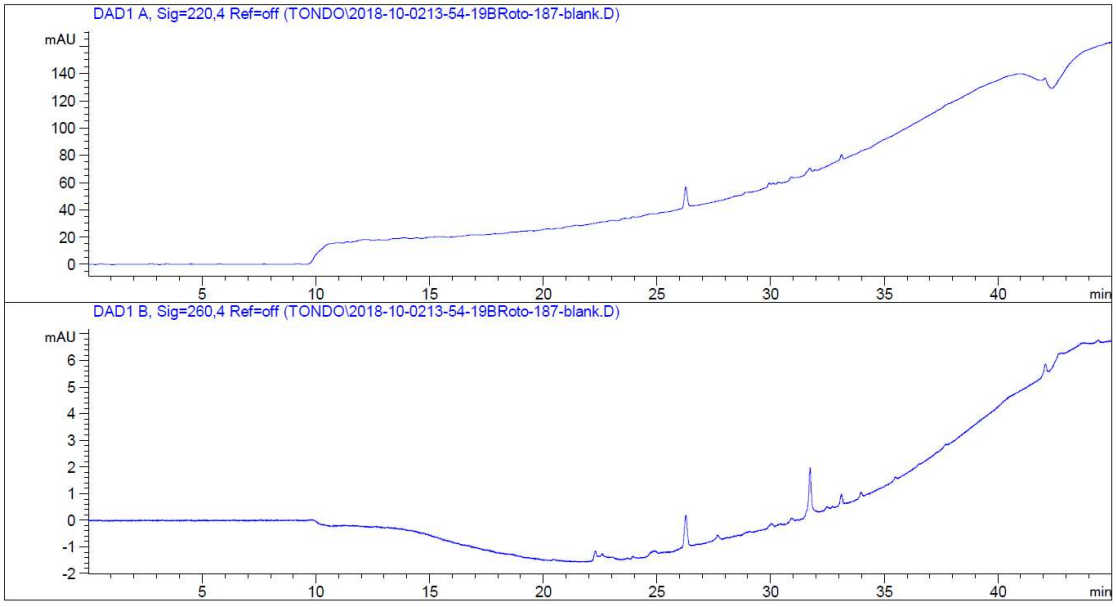

Figure 7-2 - Linker **3-19** NVOC1 linker HPLC analytical blank run.

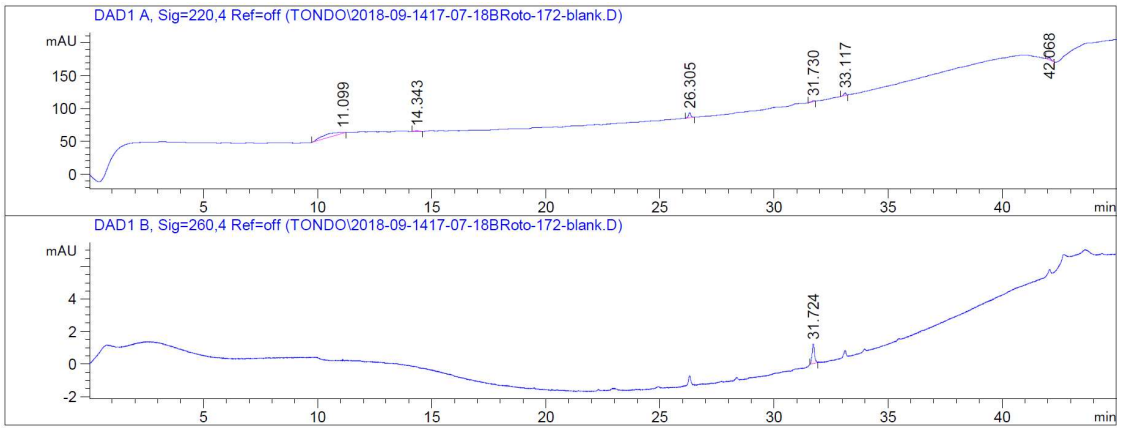

Figure 7-3 - NVOC1 peptide **3-20** HPLC analytical blank run.

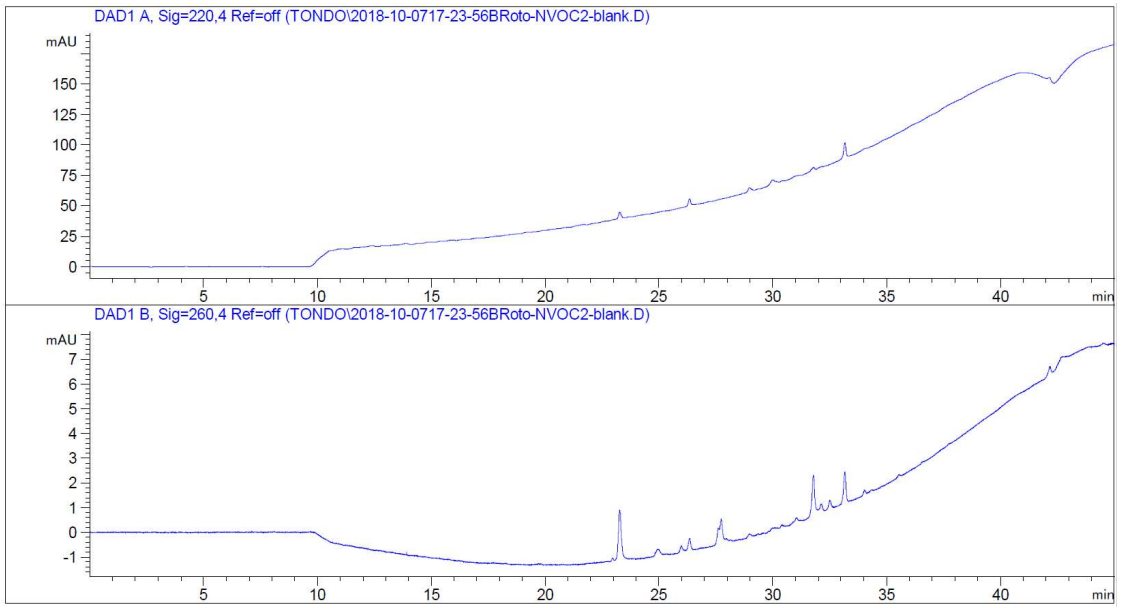

Figure 7-4 - NVOC2 linker **3-25** HPLC blank run.

7.1. *tert*-Butyl 4-(bromomethyl)-3-nitrobenzoate (3-8)

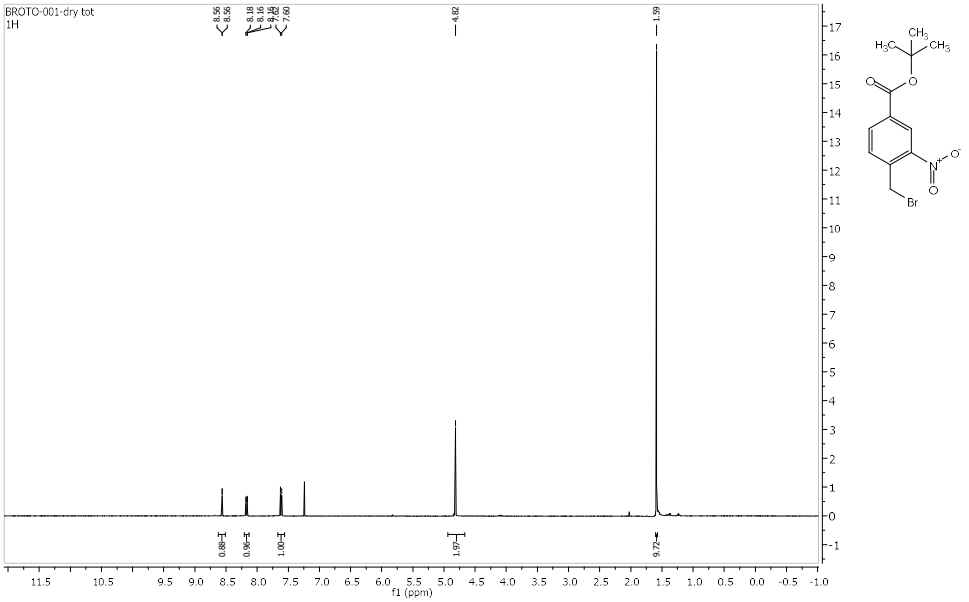

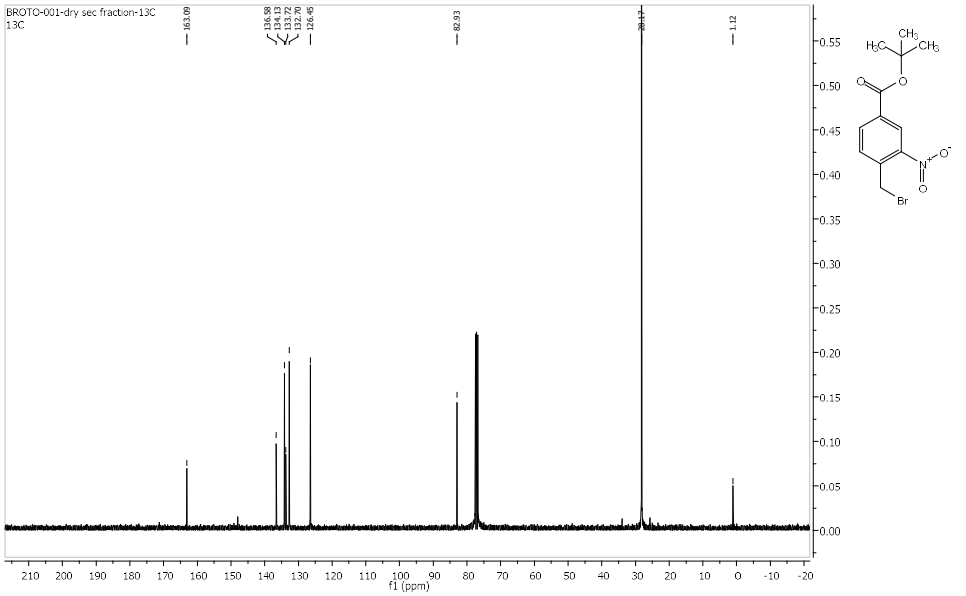

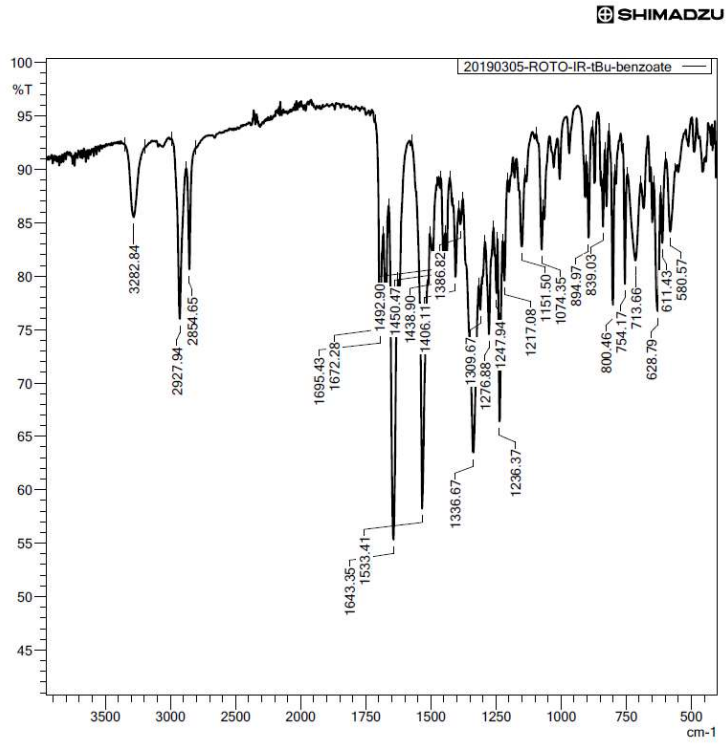
SHIMADZU
20190305-ROTO-IR-tBu-benzoate
%T
3282.84
2927.94
2854.65
1695.43
1672.28
1643.35
1533.41
1492.90
1450.47
1438.90
1406.11
1386.82
1336.67
1309.67
1276.88
1247.94
1236.37
1217.08
1151.50
1074.35
894.97
839.03
800.46
754.17
713.66
628.79
611.43
580.57
cm-1

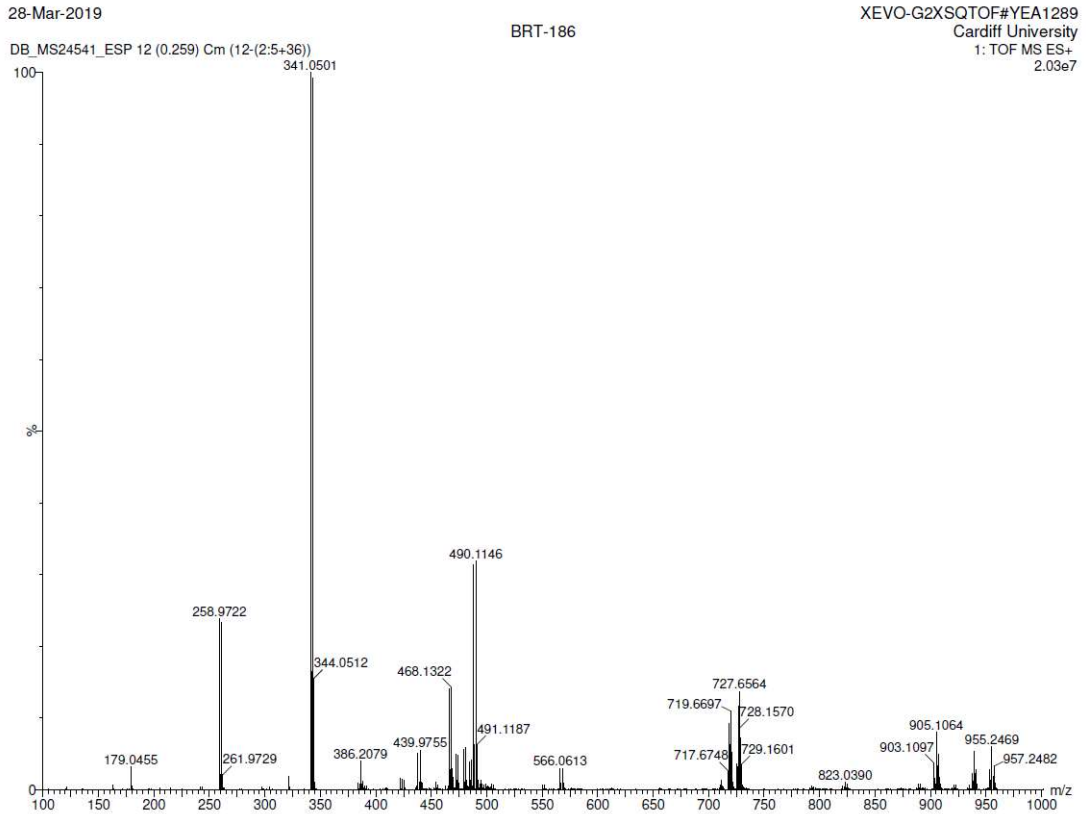
28-Mar-2019
BRT-186
XEVO-G2XSQTOF#YEA1289
Cardiff University
1: TOF MS ES+
2.03e7
DB_MS24541_ESP 12 (0.259) Cm (12-(2:5+36))
%
341.0501
490.1146
258.9722
344.0512
468.1322
727.6564
719.6697
728.1570
491.1187
905.1064
955.2469
903.1097
957.2482
439.9755
729.1601
179.0455
261.9729
386.2079
566.0613
717.6748
823.0390
m/z

7.2. *tert*-Butyl 4-(((N2-(((9H-fluoren-9-yl)methoxy)carbonyl)-N5-trityl-L-glutaminyl)oxy)methyl)-3-nitrobenzoate (3-9)

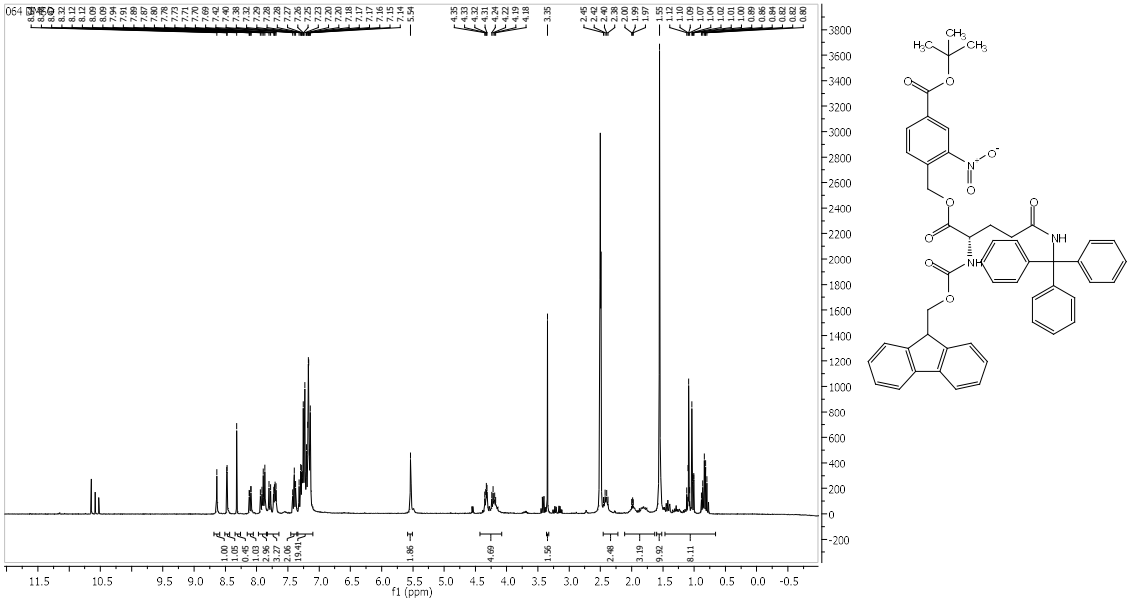

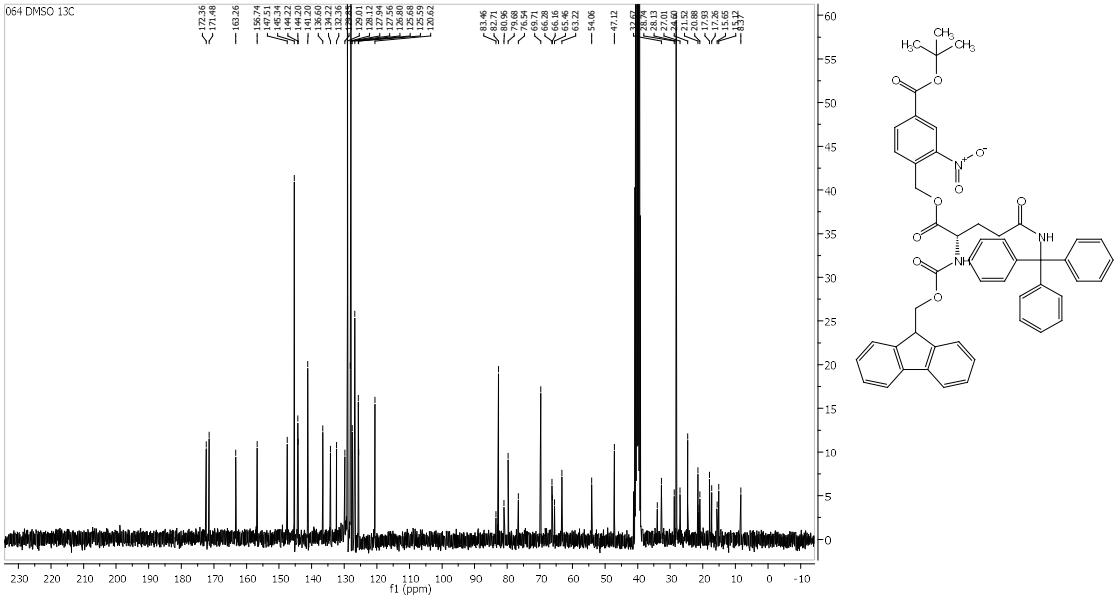

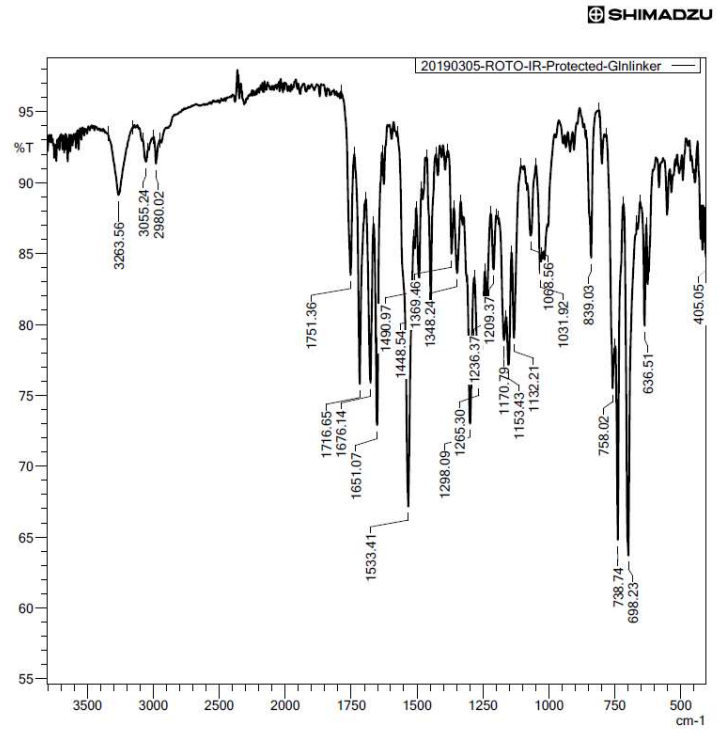

Analysis Info

Sample Name	**BRoTo 008**	Acquisition Date	11/02/2015 17:29:15
Analysis Name	X018116CYC.d	Instrument / Ser#	maXis 255552.00086
		Method	Positif.m

Acquisition Parameter

Source Type	ESI	Ion Polarity	Positive	Set Nebulizer	0.6 Bar
Scan Begin	50 m/z	Set Capillary	4500 V	Set Dry Heater	200 °C
Scan End	3000 m/z	Set Collision Cell RF	500.0 Vpp	Set Dry Gas	7.0 l/min

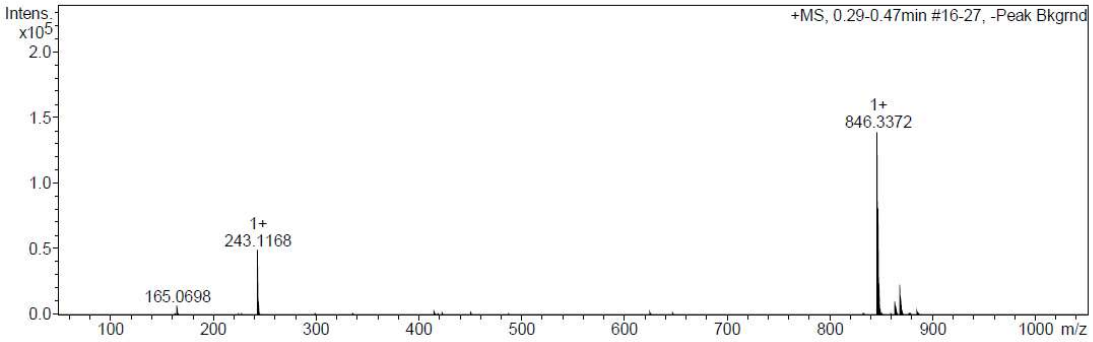

7.3. 4-(((((9H-fluoren-9-yl)methoxy)carbonyl)-L-glutaminyl)oxy)methyl)-3-nitrobenzoic acid (3-10)

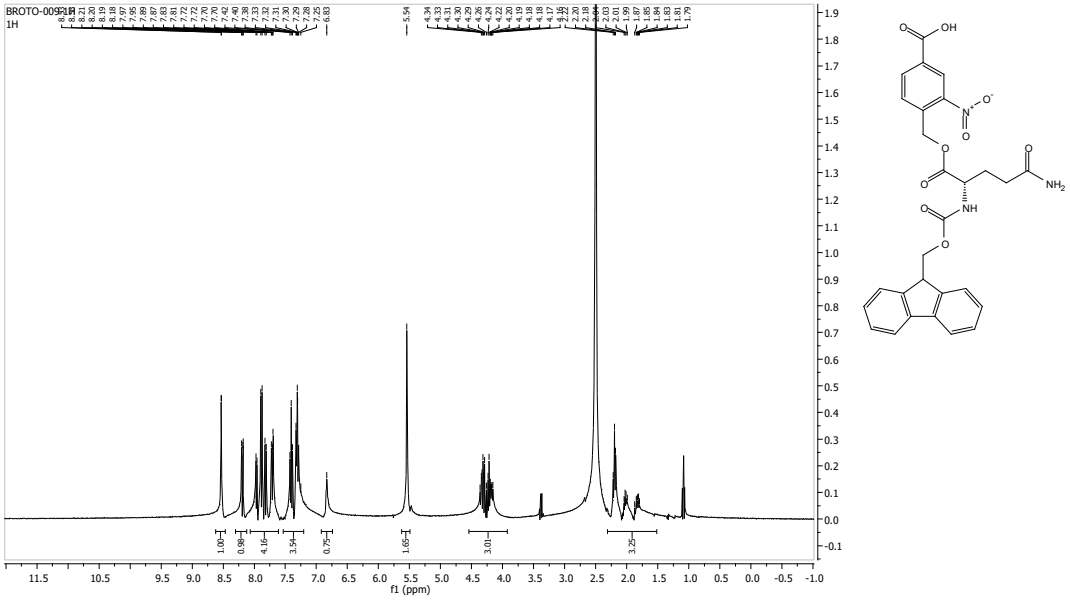

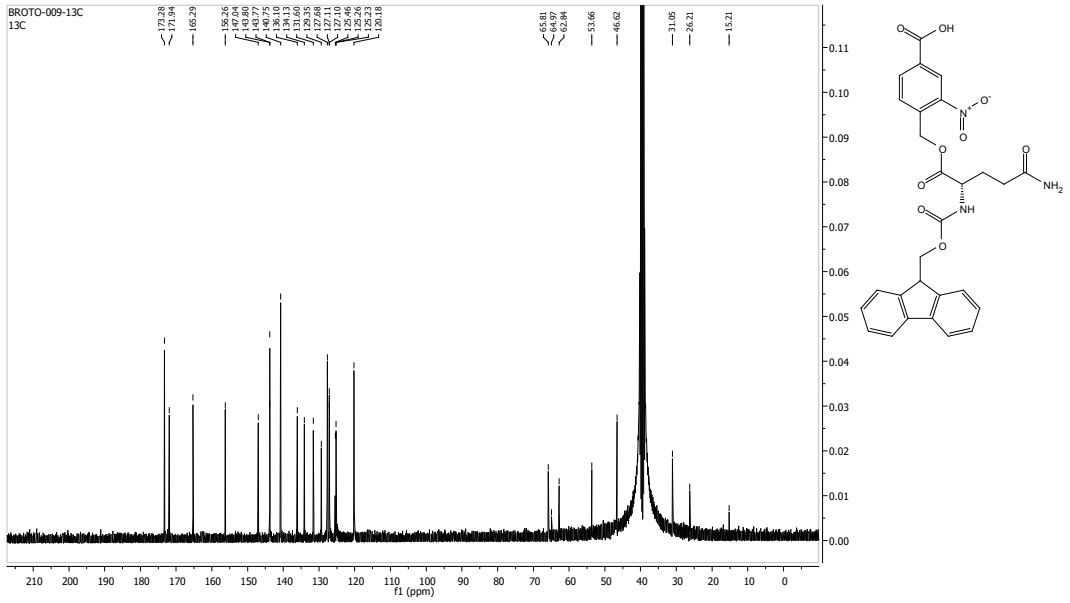

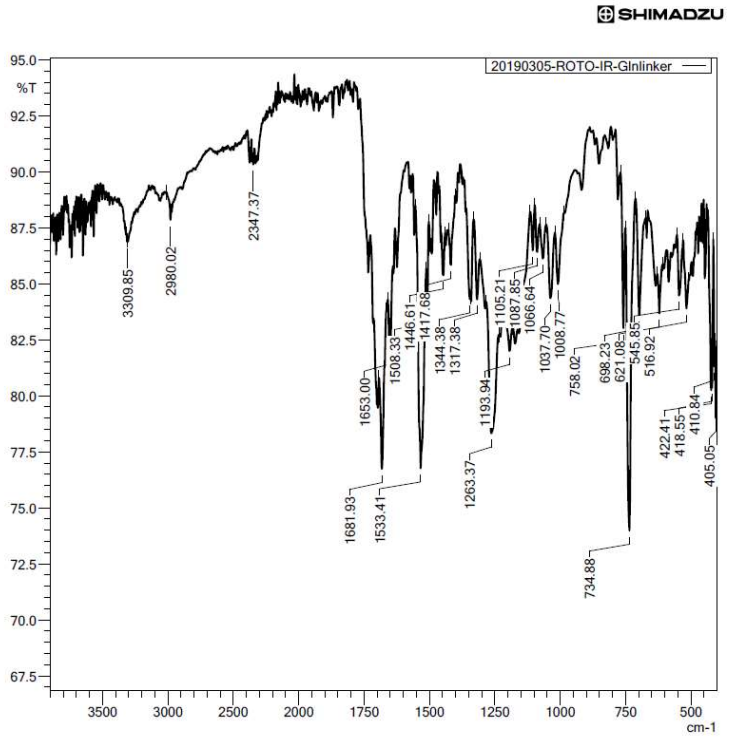

Sample Name	**BRoTo 009**			Instrument / Ser#	maXis 255552.00086
Analysis Name	X018117CYC.d			Method	Positif.m

Acquisition Parameter

Source Type	ESI	Ion Polarity	Positive	Set Nebulizer	0.6 Bar
Scan Begin	50 m/z	Set Capillary	4500 V	Set Dry Heater	200 °C
Scan End	3000 m/z	Set Collision Cell RF	500.0 Vpp	Set Dry Gas	7.0 l/min

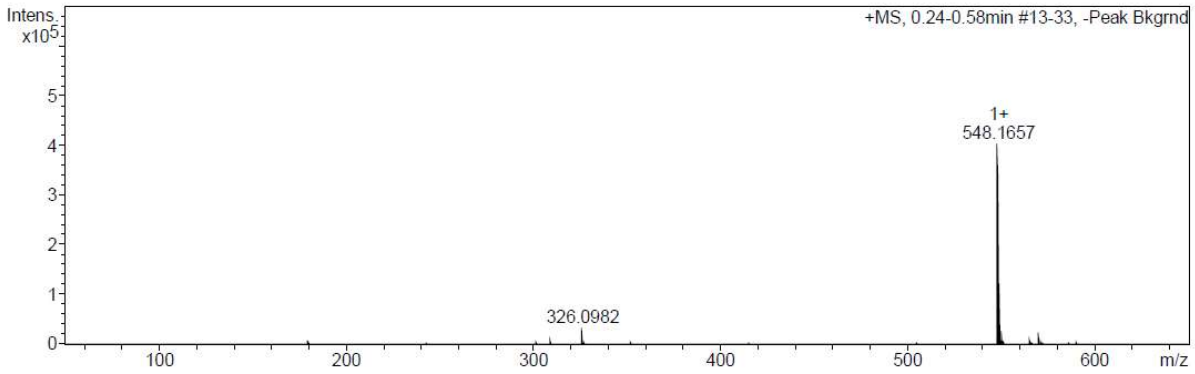

7.4. (3S)-4-((5-amino-1-((4-(((S)-5-carbamoyl-33-mercapto-7,23-dioxo-10,13,16,19-tetraoxa-6,22-diazatritriacontyl)carbamoyl)-2-nitrobenzyl)oxy)-1,5-dioxopentan-2-yl)amino)-3-(2-((2S,3S)-2-amino-3-methylpentanamido)acetamido)-4-oxobutanoic acid (3-3)

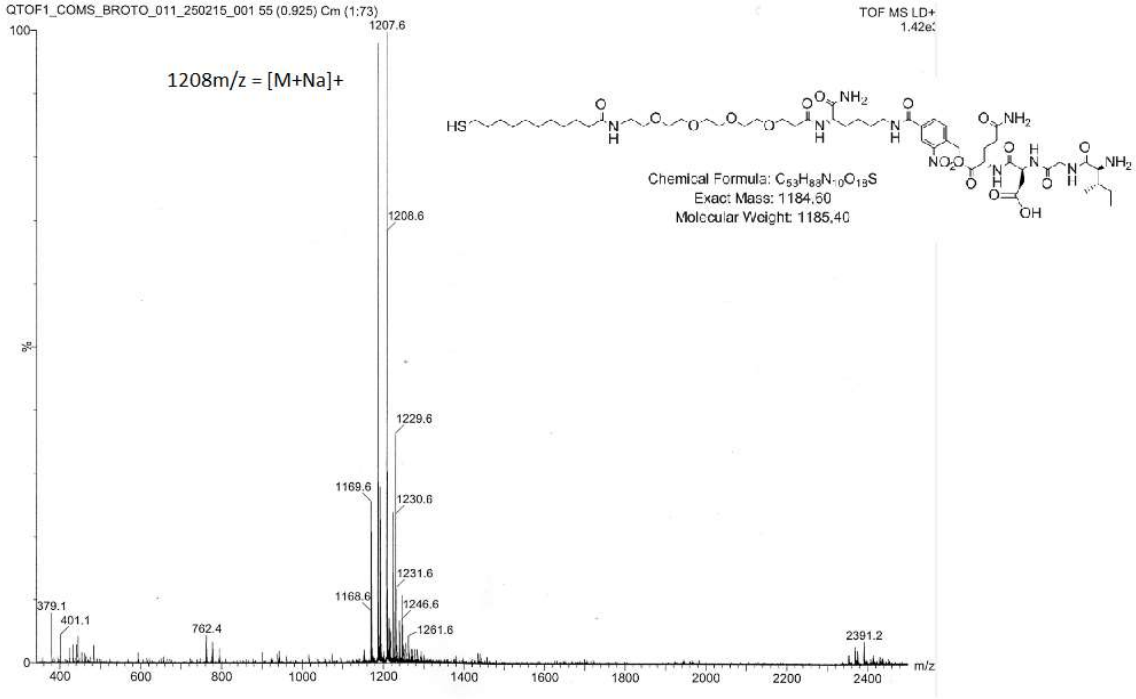

RUN_BROTO-011-ANALYT-FR1-B1_channel2

System : 940LC
Method : ROTO-ptotopep IGDQK-analytical-METH
User : varian

Acquired : 12/02/2015 12:02:27
Processed : 12/02/2015 12:46:24
Printed : 12/02/2015 14:38:49

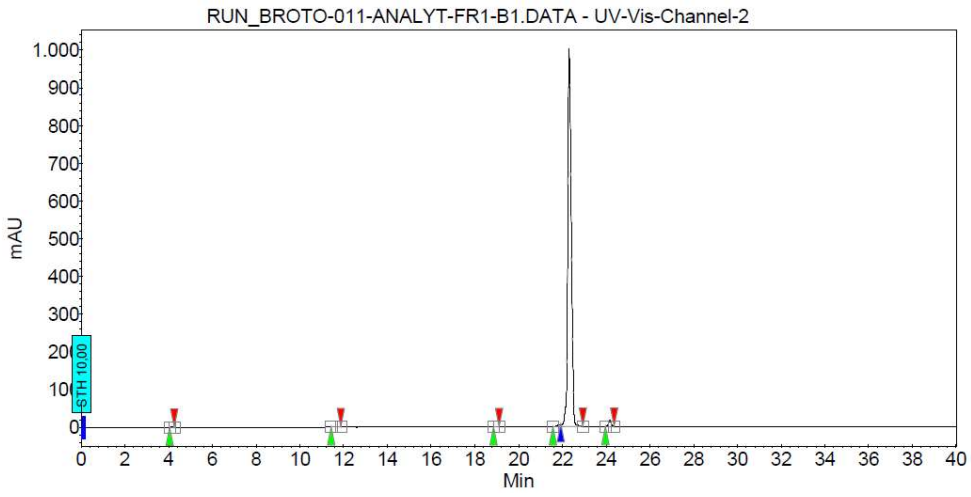

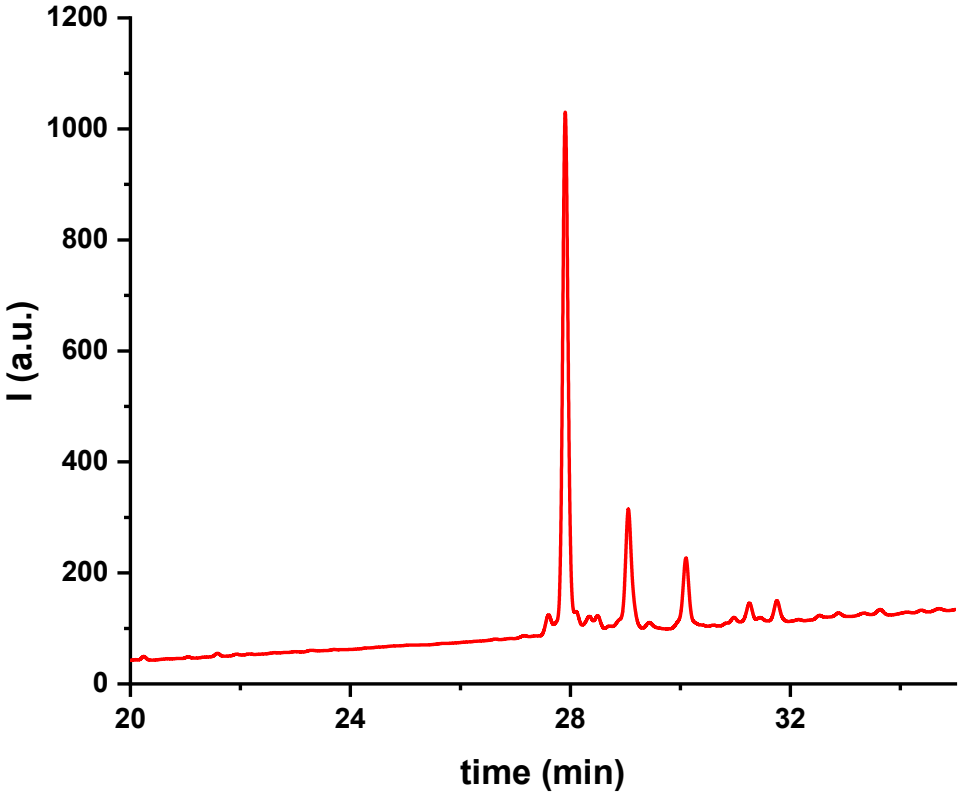

RP-HPLC chromatogram of nitrobenzyl peptide (crude)

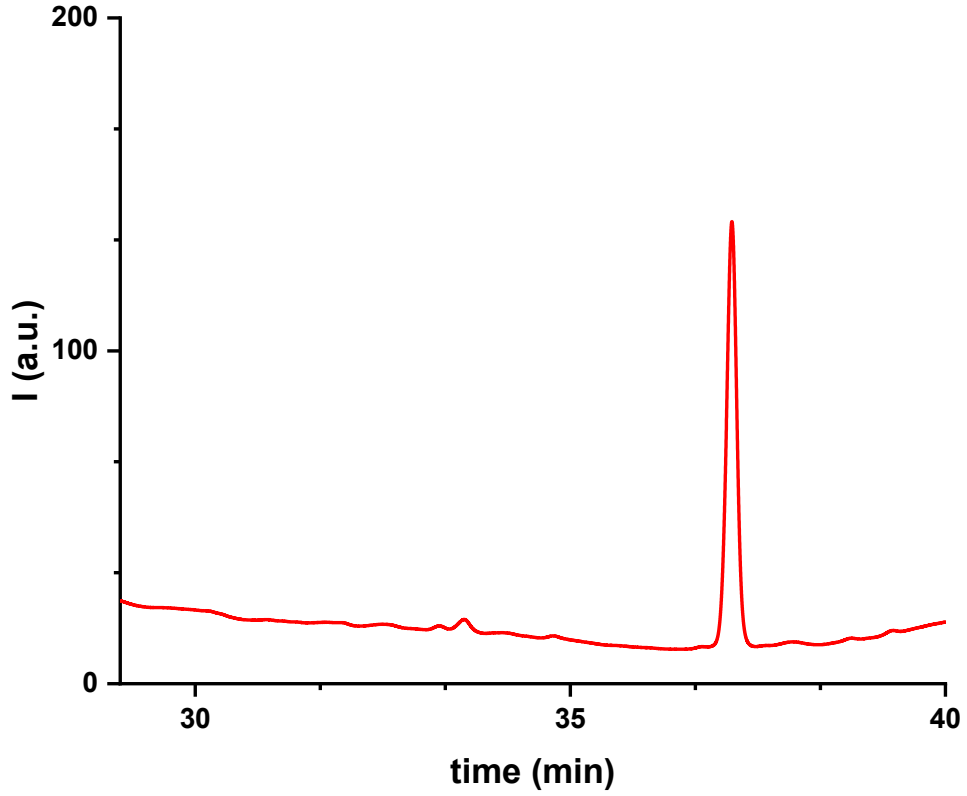

RP-HPLC chromatogram of purified nitrobenzyl peptide

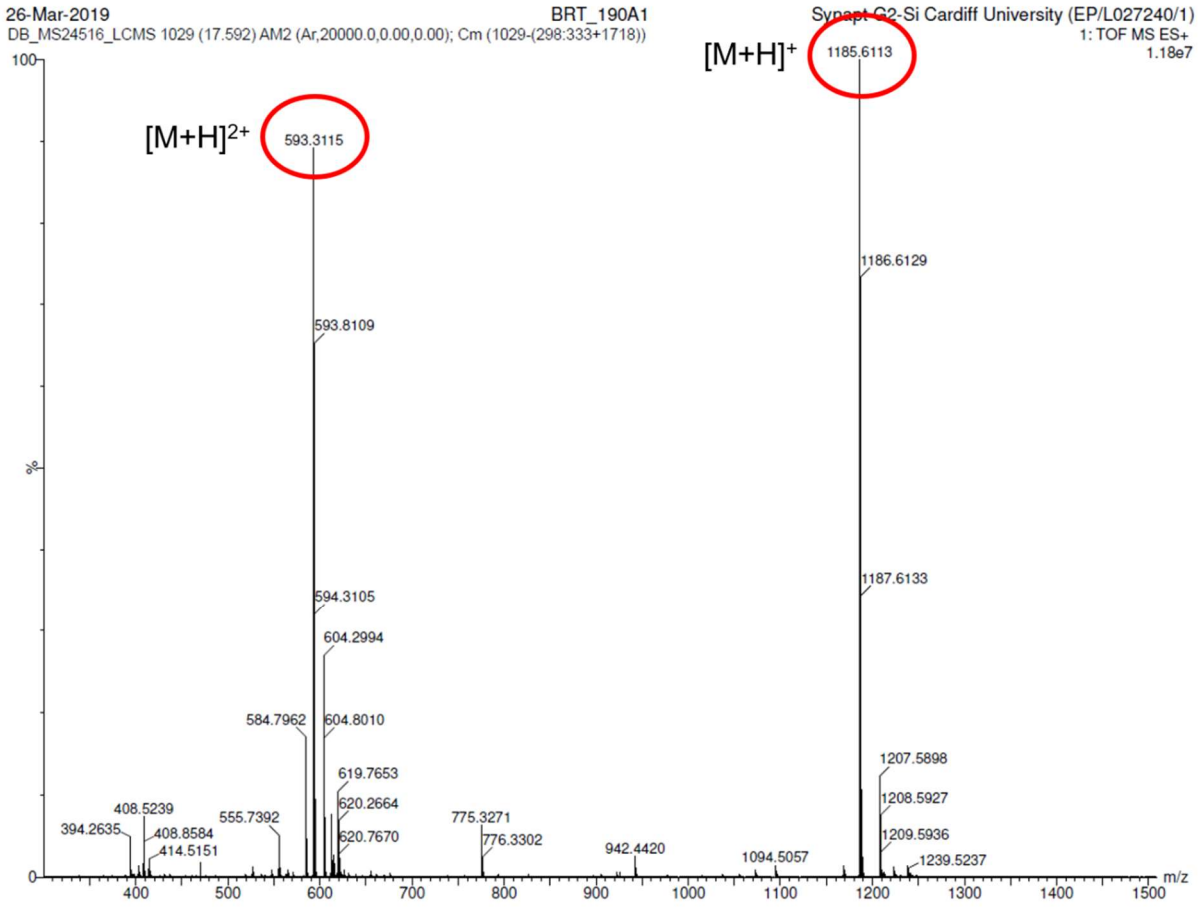
26-Mar-2019
BRT_190A1
DB_MS24516_LCMS 1029 (17.592) AM2 (Ar,20000.0,0.00,0.00); Cm (1029-(298:333+1718))
Synapt G2-Si Cardiff University (EP/L027240/1)
1: TOF MS ES+
1.18e7
[M+H]2+
593.3115
[M+H]+
1185.6113
1186.6129
593.8109
1187.6133
594.3105
604.2994
584.7962
604.8010
619.7653
620.2664
620.7670
408.5239
394.2635
408.8584
414.5151
555.7392
775.3271
776.3302
942.4420
1094.5057
1207.5898
1208.5927
1209.5936
1239.5237
%
m/z

7.5. 1-(4-(benzyloxy)-3-methoxyphenyl)ethan-1-one (3-12)

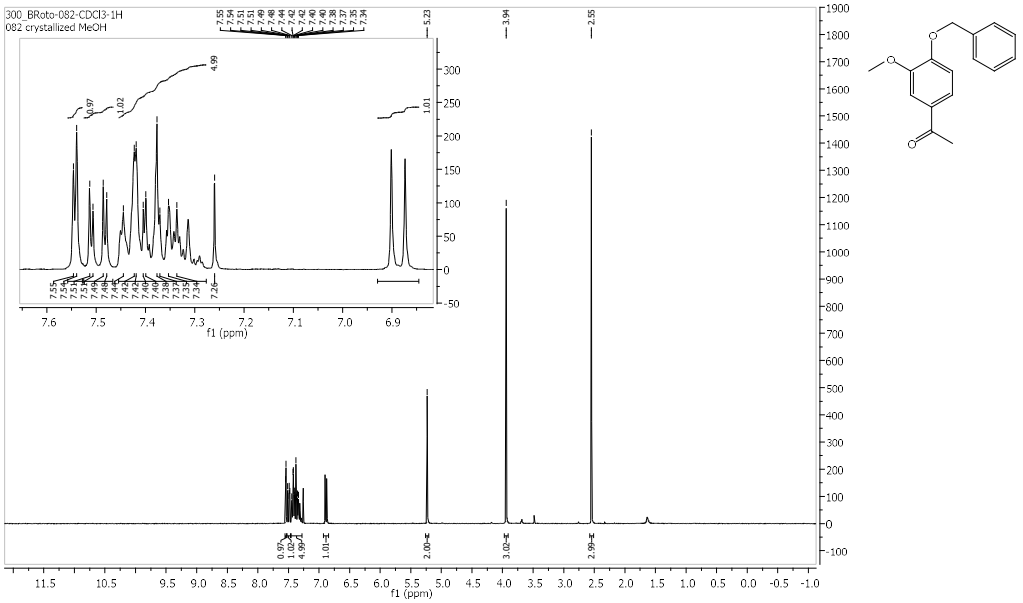

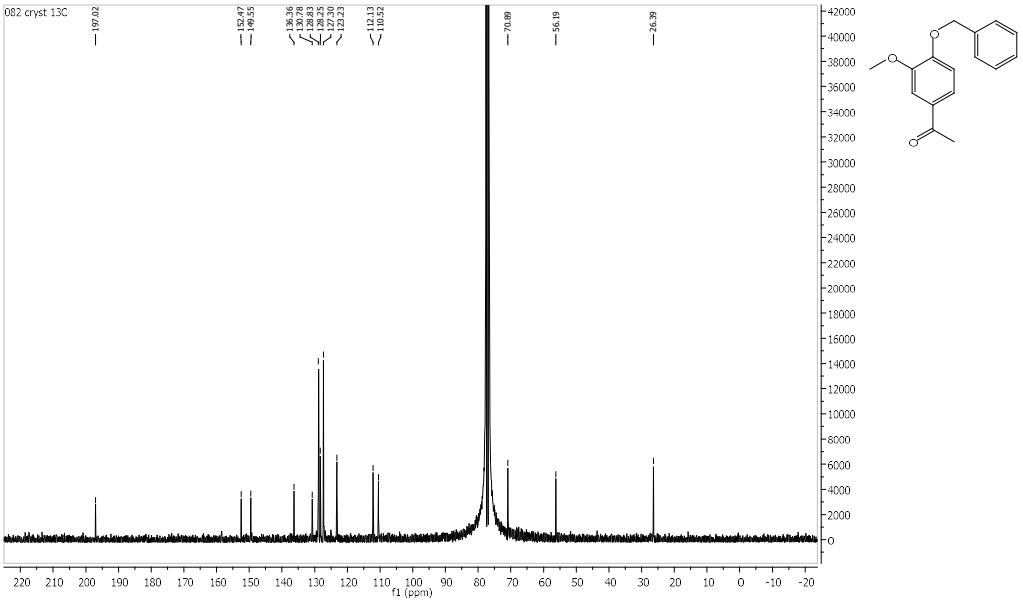

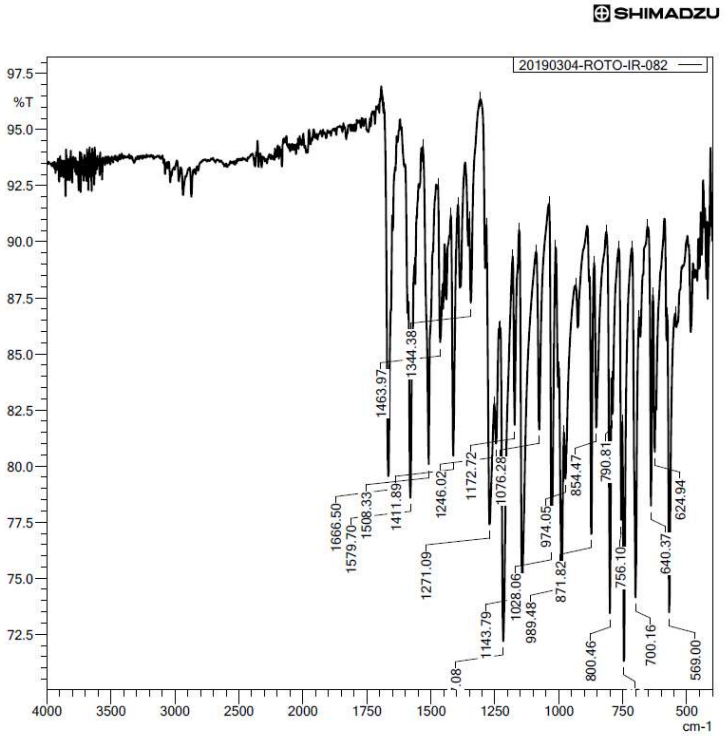
SHIMADZU
20190304-ROTO-IR-082
%T
97.5
95.0
92.5
90.0
87.5
85.0
82.5
80.0
77.5
75.0
72.5
1463.97
1344.38
1666.50
1579.70
1508.33
1411.89
1246.02
1172.72
1076.28
974.05
854.47
790.81
624.94
1271.09
1028.06
989.48
871.82
756.10
640.37
1143.79
800.46
700.16
569.00
4000
3500
3000
2500
2000
1750
1500
1250
1000
750
500
cm-1

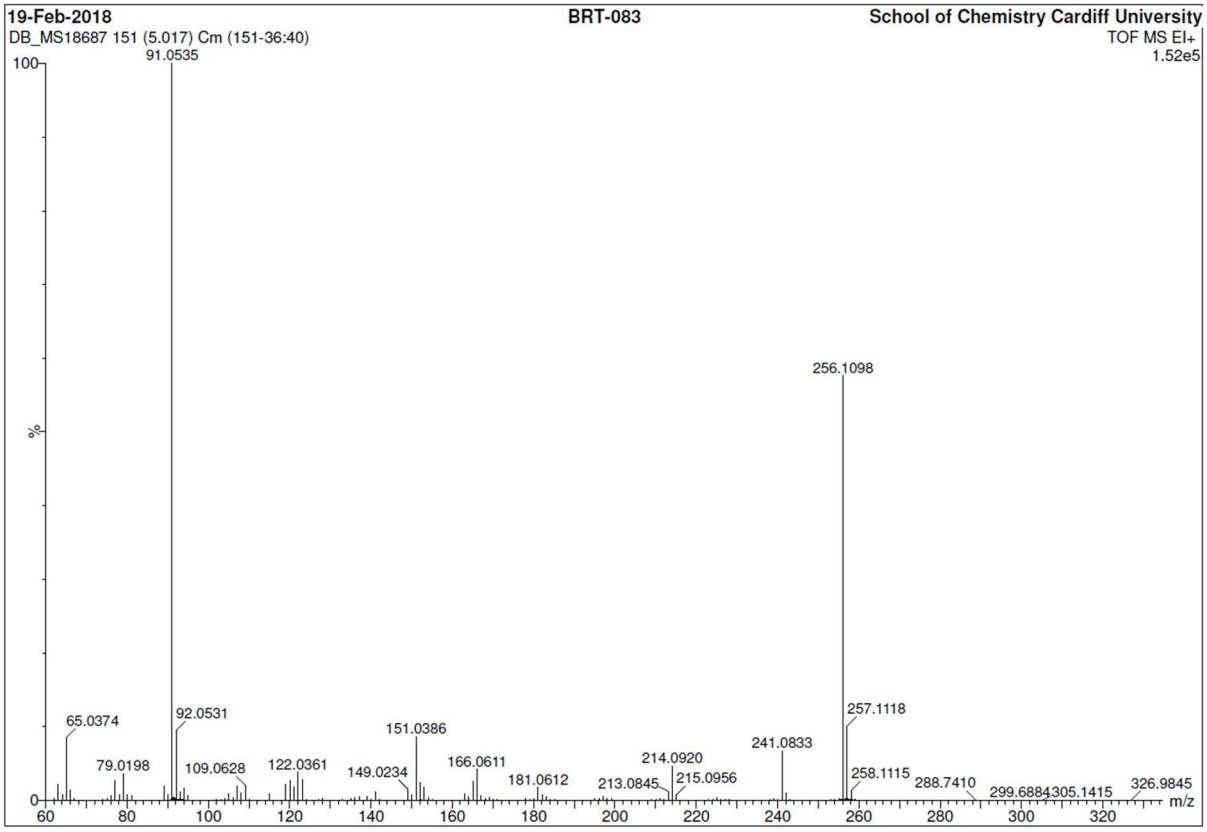
19-Feb-2018
BRT-083
School of Chemistry Cardiff University
DB_MS18687 151 (5.017) Cm (151-36:40)
TOF MS EI+
1.52e5
100
%
0
91.0535
256.1098
257.1118
65.0374
92.0531
151.0386
241.0833
79.0198
109.0628
122.0361
149.0234
166.0611
181.0612
214.0920
213.0845
215.0956
258.1115
288.7410
299.6884
305.1415
326.9845
60
80
100
120
140
160
180
200
220
240
260
280
300
320
m/z

Elemental Composition Report **Page 1**

Single Mass Analysis
Tolerance = 5.0 PPM / DBE: min = -1.5, max = 50.0
Element prediction: Off

Monoisotopic Mass, Odd and Even Electron Ions
3 formula(e) evaluated with 1 results within limits (all results (up to 1000) for each mass)
Elements Used:
C: 0-16 H: 0-16 O: 0-3

19-Feb-2018 BRT-083 School of Chemistry Cardiff University
DB_MS18687 151 (5.017) Cm (151-36:40) TOF MS EI+
1.52e+005

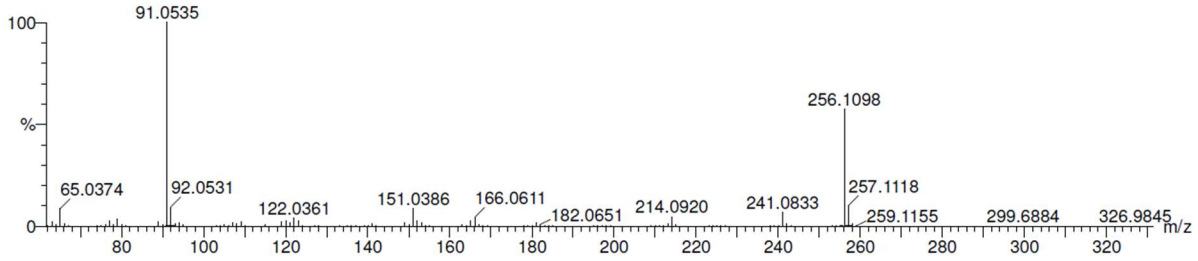

Minimum:				-1.5		
Maximum:		5.0	5.0	50.0		
Mass	Calc. Mass	mDa	PPM	DBE	i-FIT	Formula
256.1098	256.1099	-0.1	-0.4	9.0	16.3	C16 H16 O3

7.6. 1-(4-(benzyloxy)-5-methoxy-2-nitrophenyl)ethan-1-one (3-13)

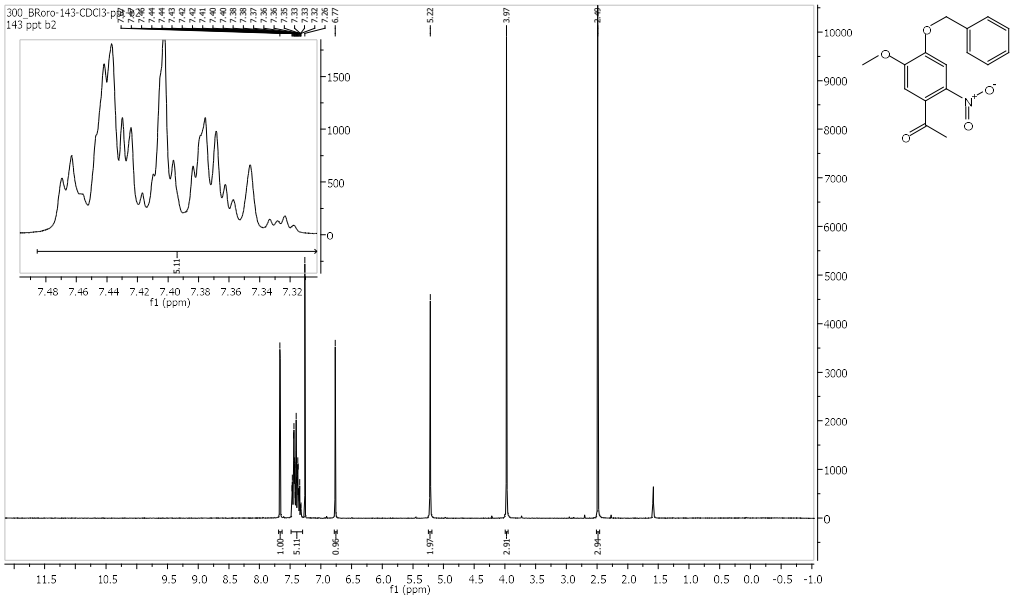

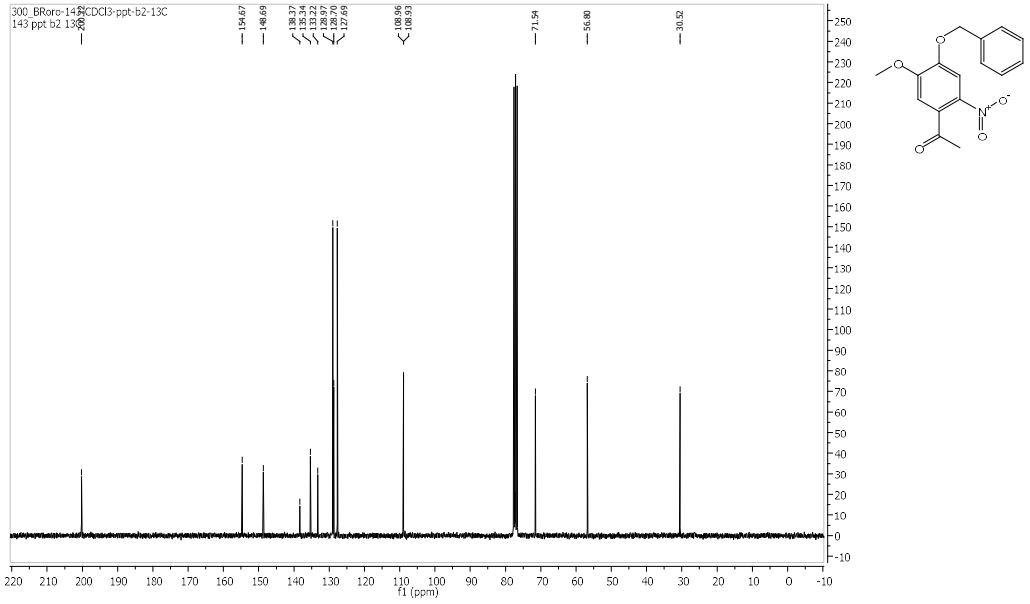

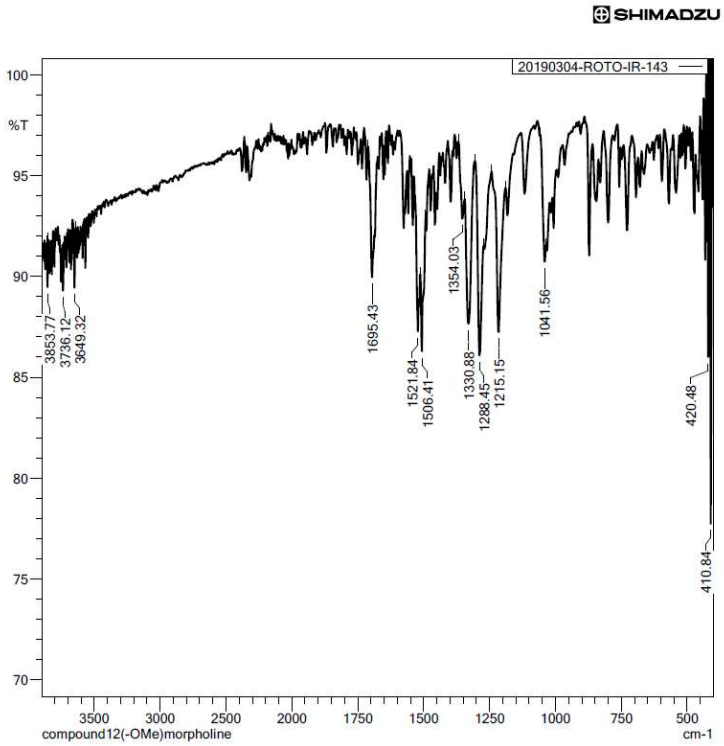
SHIMADZU
20190304-ROTO-IR-143
%T
100
95
90
85
80
75
70
3853.77
3736.12
3649.32
1695.43
1521.84
1506.41
1354.03
1330.88
1288.45
1215.15
1041.56
420.48
410.84
3500
3000
2500
2000
1750
1500
1250
1000
750
500
cm-1
compound12(-OMe)morpholine

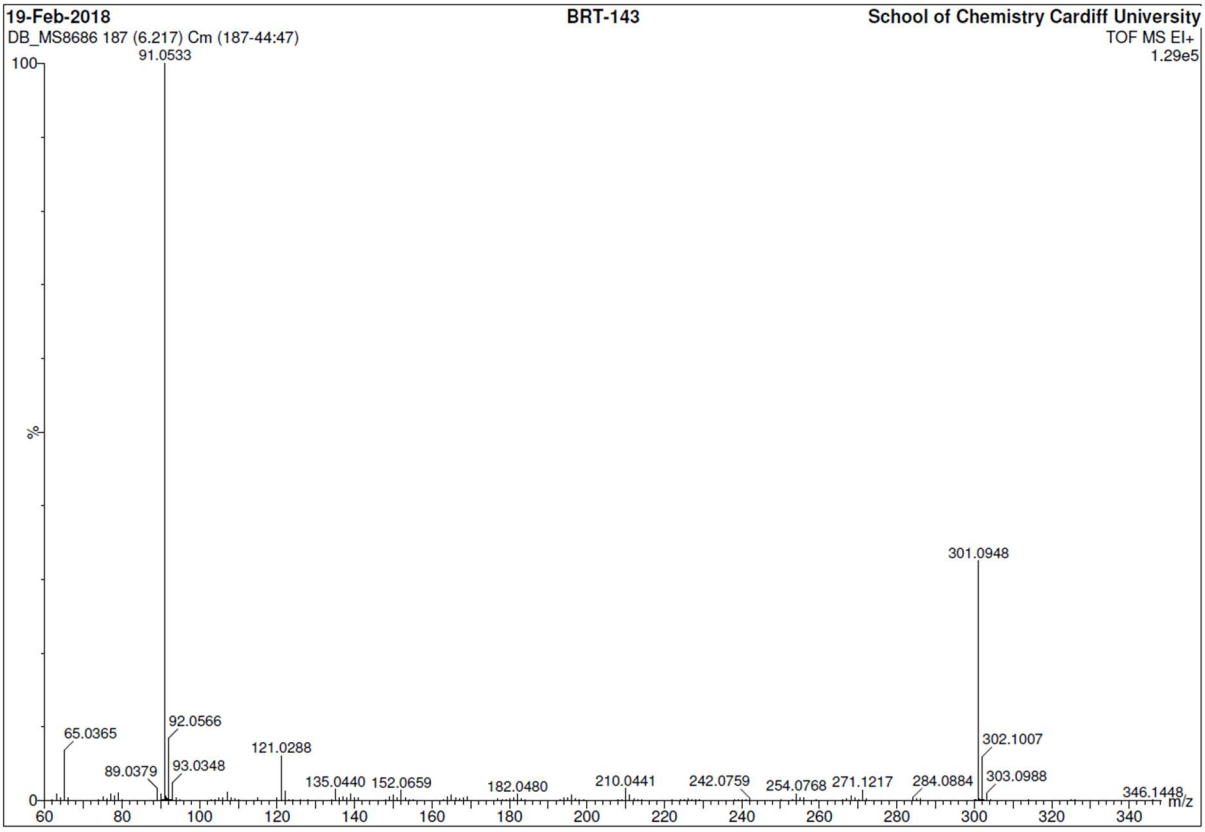
19-Feb-2018
BRT-143
School of Chemistry Cardiff University
DB_MS8686 187 (6.217) Cm (187-44:47)
TOF MS EI+
1.29e5
100
%
0
91.0533
301.0948
65.0365
92.0566
121.0288
89.0379
93.0348
135.0440
152.0659
182.0480
210.0441
242.0759
254.0768
271.1217
284.0884
302.1007
303.0988
346.1448
60
80
100
120
140
160
180
200
220
240
260
280
300
320
340
m/z

Elemental Composition Report **Page 1**

Single Mass Analysis
Tolerance = 5.0 PPM / DBE: min = -1.5, max = 50.0
Element prediction: Off

Monoisotopic Mass, Odd and Even Electron Ions
10 formula(e) evaluated with 1 results within limits (all results (up to 1000) for each mass)
Elements Used:
C: 0-16 H: 0-15 N: 0-1 O: 0-5

19-Feb-2018 BRT-143 School of Chemistry Cardiff University
DB_MS8686 187 (6.217) Cm (187-44:47) TOF MS EI+
1.29e+005

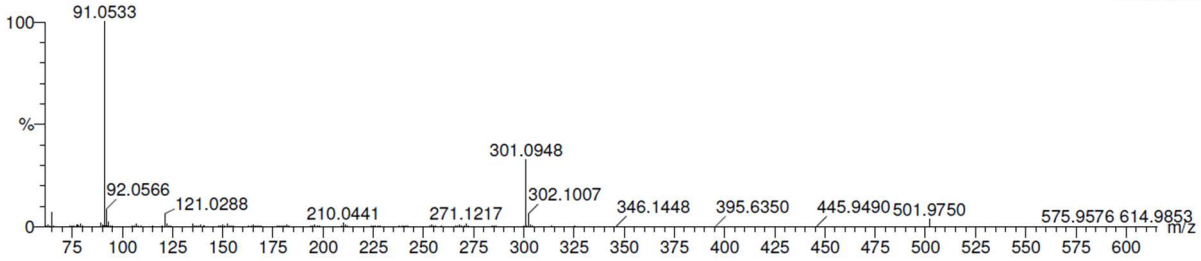

Minimum:				-1.5		
Maximum:		5.0	5.0	50.0		
Mass	Calc. Mass	mDa	PPM	DBE	i-FIT	Formula
301.0948	301.0950	-0.2	-0.7	10.0	8.3	C16 H15 N O5

7.7. 1-(4-hydroxy-5-methoxy-2-nitrophenyl)ethan-1-one (3-14)

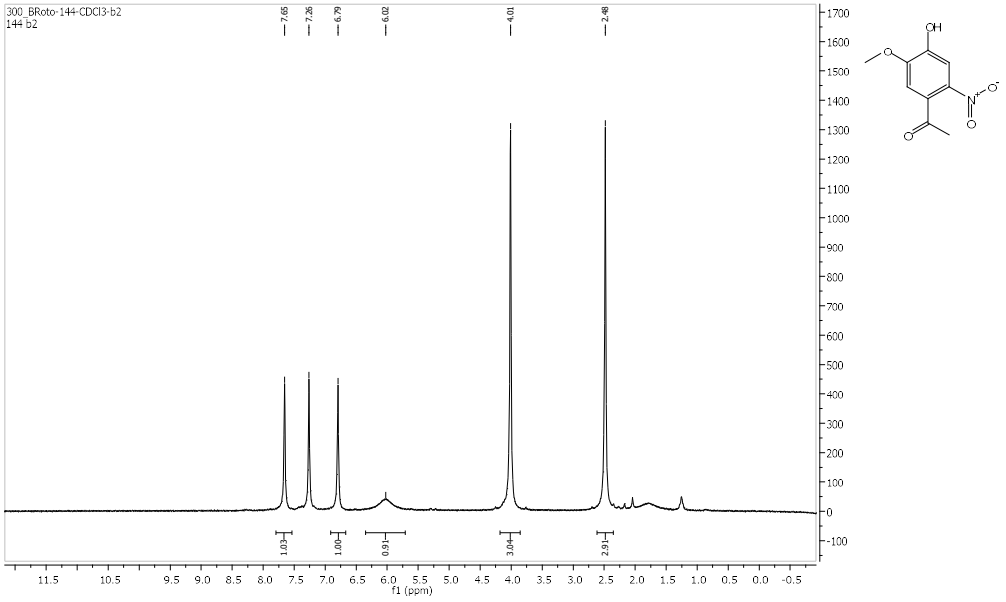

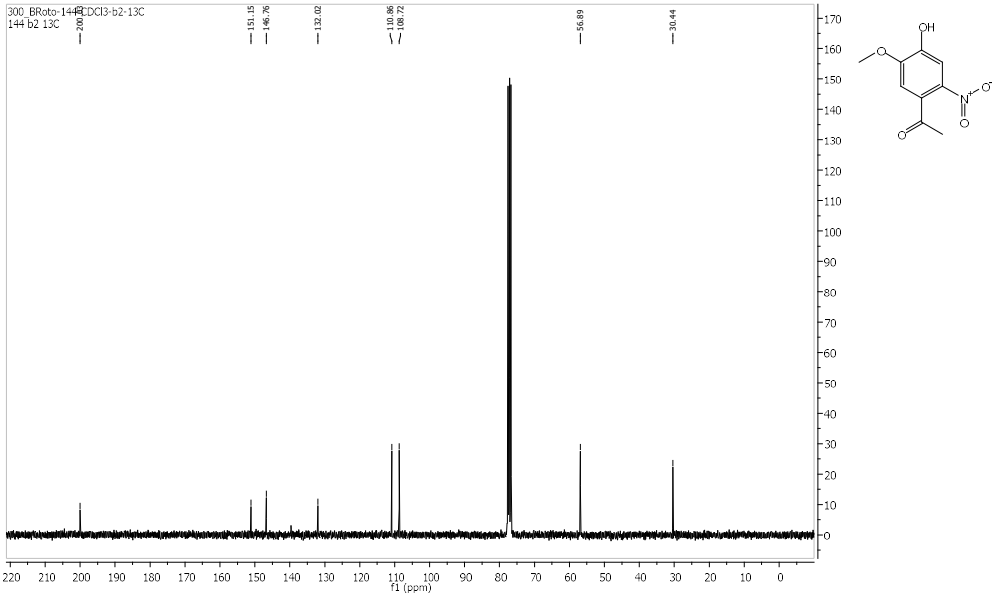

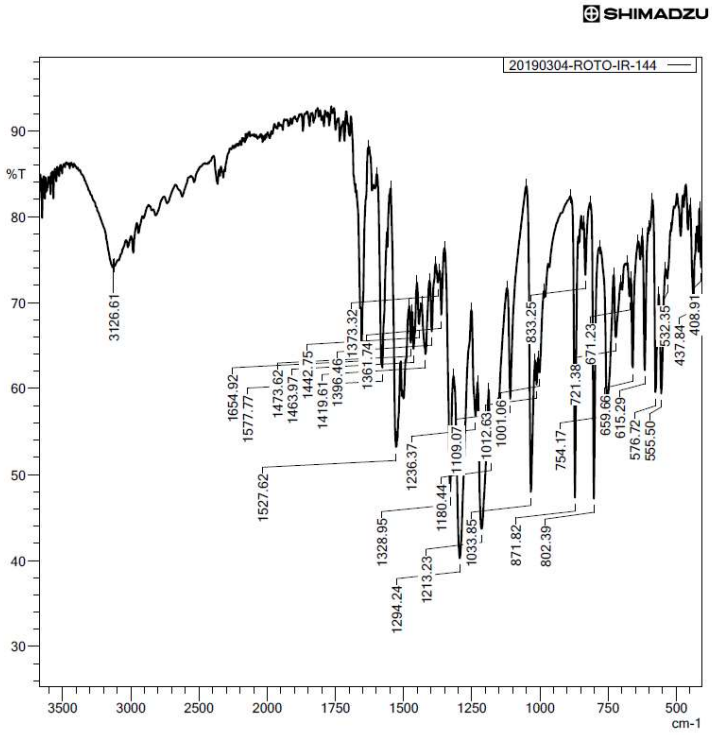
SHIMADZU
20190304-ROTO-IR-144
%T
cm-1
3126.61
1654.92
1577.77
1527.62
1473.62
1463.97
1442.75
1419.61
1396.46
1373.32
1361.74
1328.95
1294.24
1236.37
1213.23
1180.44
1109.07
1033.85
1012.63
1001.06
871.82
833.25
802.39
754.17
721.38
671.23
659.66
615.29
576.72
555.50
532.35
437.84
408.91

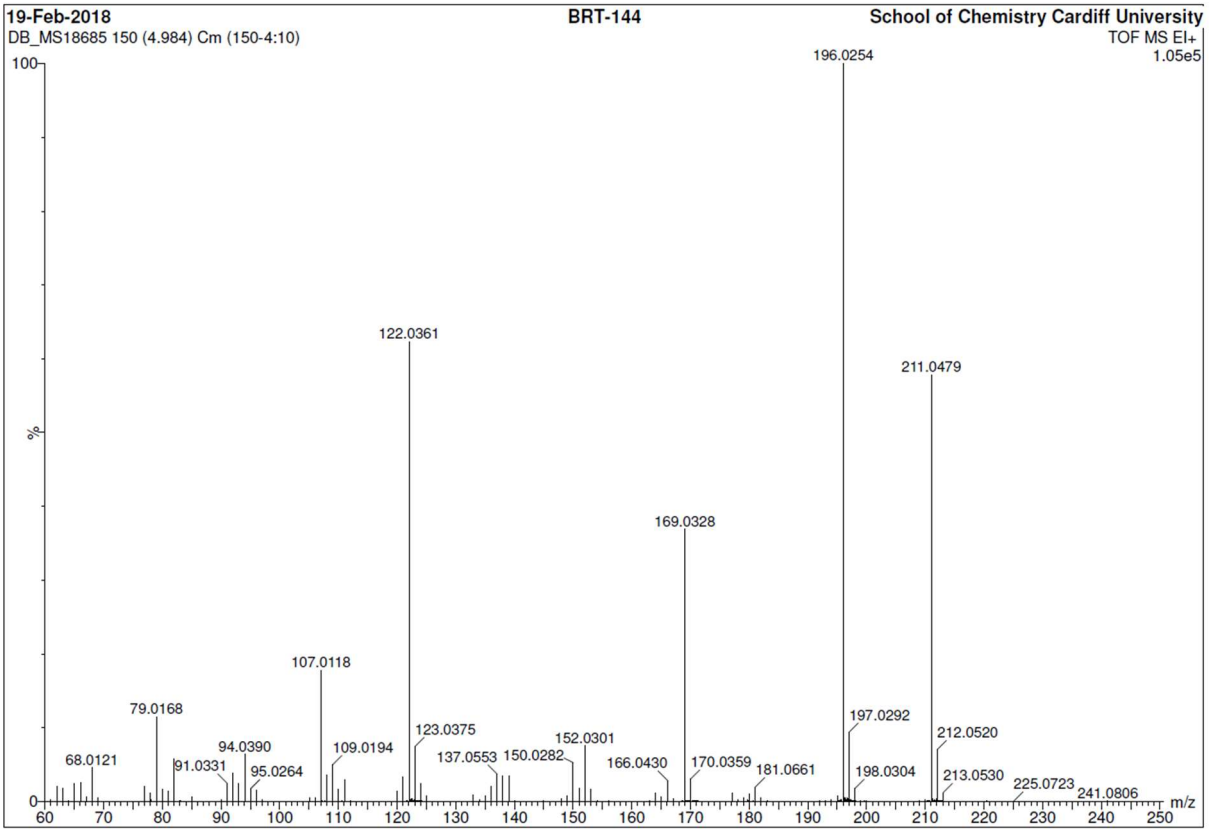
19-Feb-2018
BRT-144
School of Chemistry Cardiff University
DB_MS18685 150 (4.984) Cm (150-4:10)
TOF MS EI+
1.05e5
%
m/z
196.0254
122.0361
211.0479
169.0328
107.0118
79.0168
123.0375
197.0292
212.0520
94.0390
109.0194
152.0301
68.0121
91.0331
95.0264
137.0553
150.0282
166.0430
170.0359
181.0661
198.0304
213.0530
225.0723
241.0806

Elemental Composition Report **Page 1**

Single Mass Analysis
Tolerance = 5.0 PPM / DBE: min = -1.5, max = 50.0
Element prediction: Off

Monoisotopic Mass, Odd and Even Electron Ions
10 formula(e) evaluated with 1 results within limits (all results (up to 1000) for each mass)
Elements Used:
C: 0-9 H: 0-9 N: 0-1 O: 0-5

19-Feb-2018 BRT-144 School of Chemistry Cardiff University
DB_MS18685 150 (4.984) Cm (150-4:10) TOF MS EI+
1.05e+005

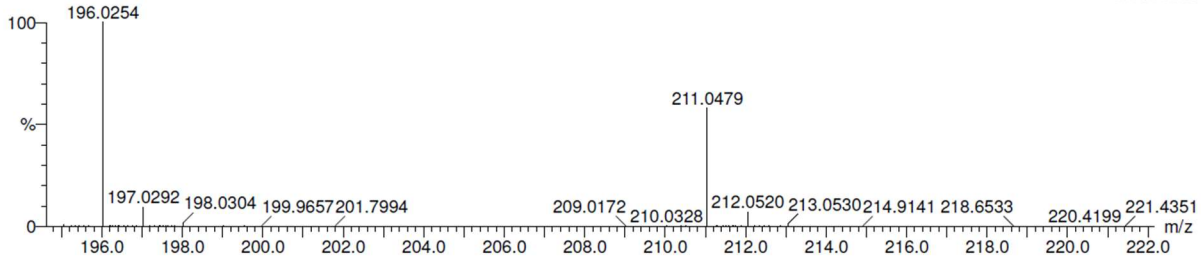

Minimum:				-1.5		
Maximum:		5.0	5.0	50.0		
Mass	Calc. Mass	mDa	PPM	DBE	i-FIT	Formula
211.0479	211.0481	-0.2	-0.9	6.0	82.2	C9 H9 N O5

7.8. *tert*-Butyl-2-(4-acetyl-2-methoxy-5-nitrophenoxy)acetate (3-15)

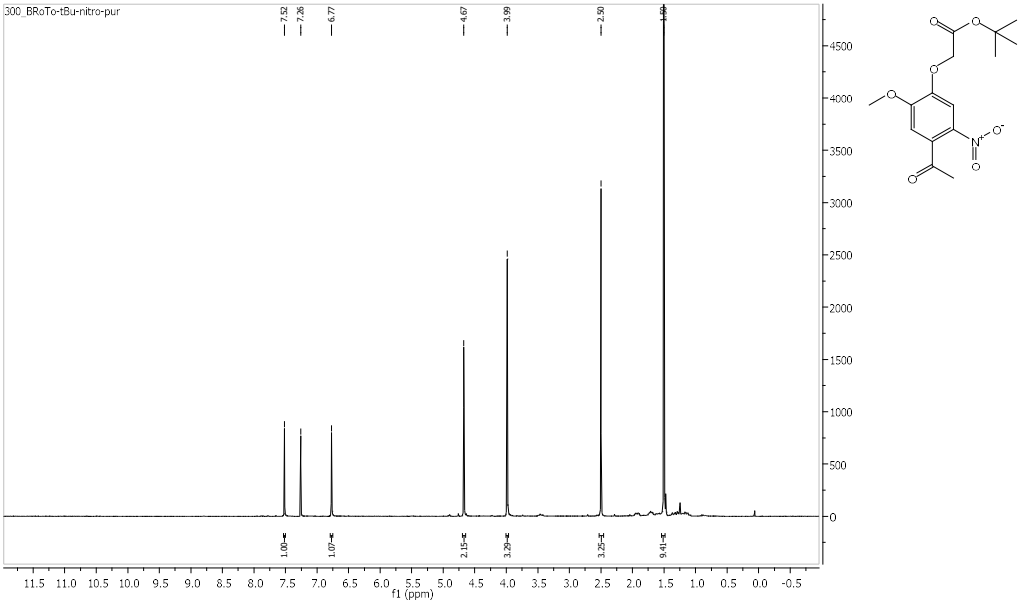

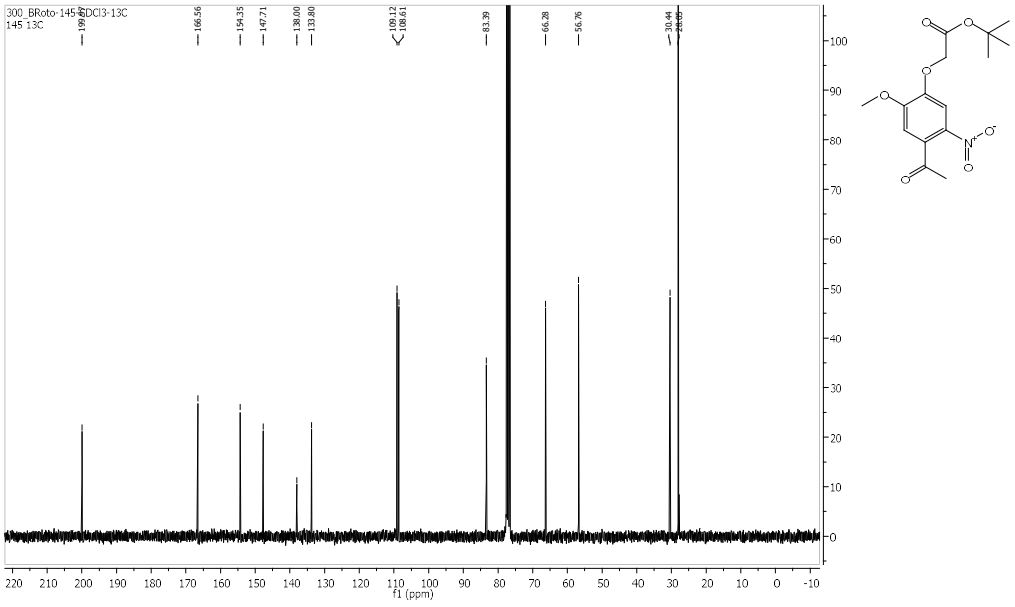

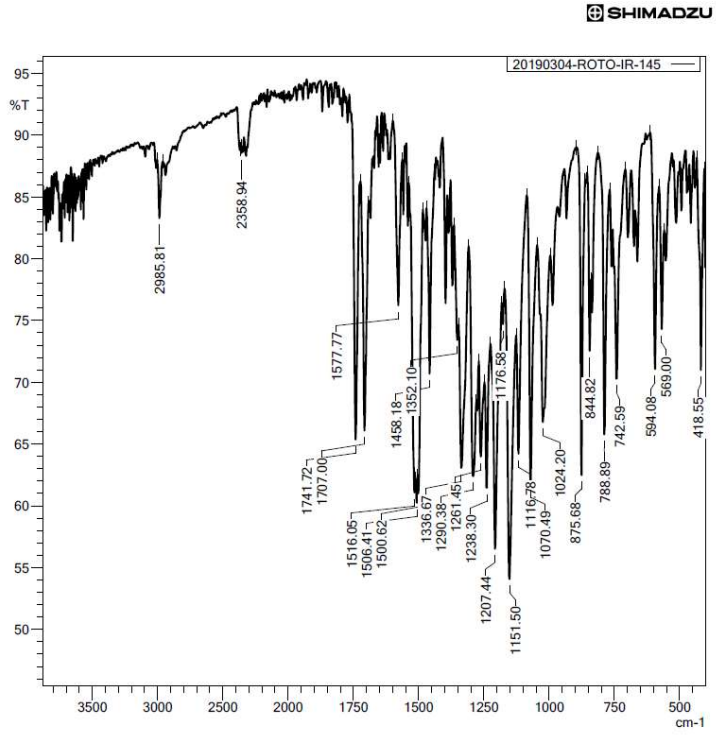
SHIMADZU
20190304-ROTO-IR-145
%T
2985.81
2358.94
1577.77
1458.18
1352.10
1176.58
1741.72
1707.00
1516.05
1506.41
1500.62
1336.67
1290.38
1261.45
1238.30
1207.44
1151.50
1116.78
1070.49
1024.20
875.68
844.82
788.89
742.59
594.08
569.00
418.55
cm-1

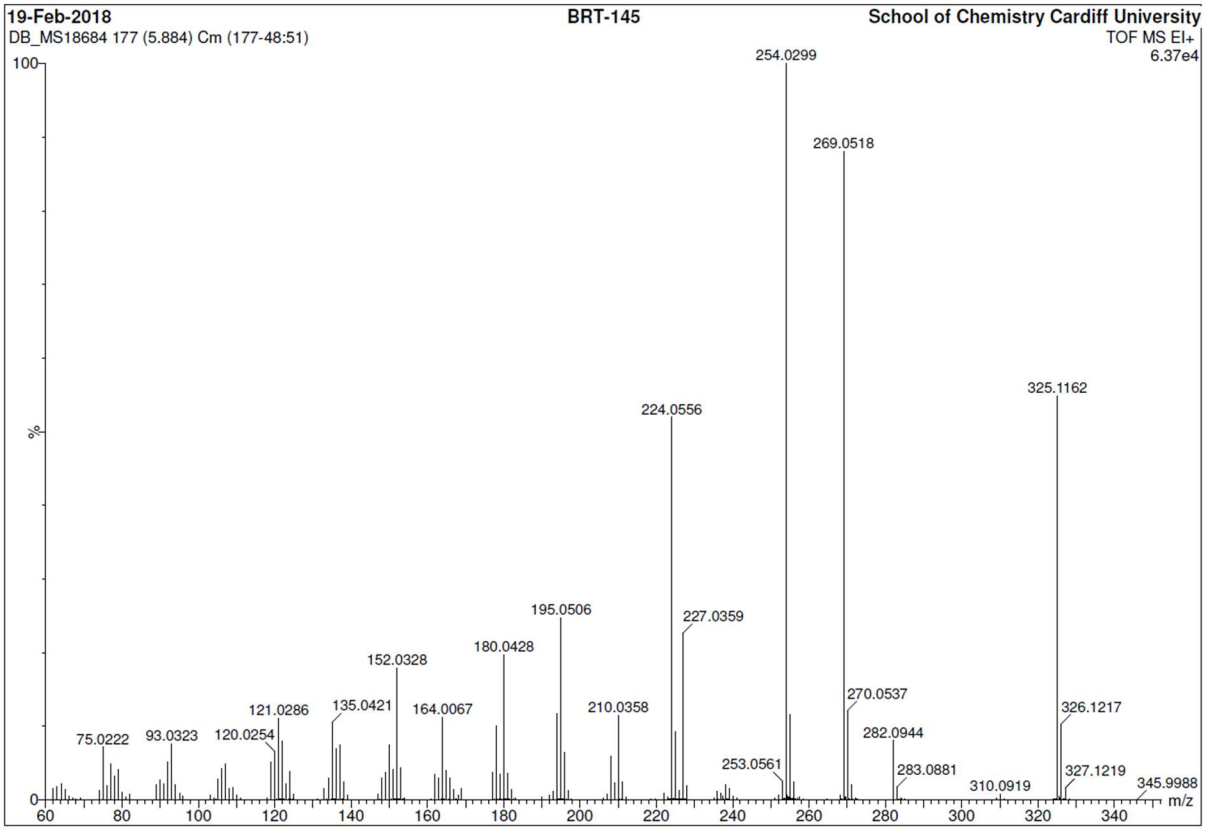
19-Feb-2018
BRT-145
School of Chemistry Cardiff University
DB_MS18684 177 (5.884) Cm (177-48:51)
TOF MS EI+
6.37e4
%
m/z
254.0299
269.0518
325.1162
224.0556
195.0506
227.0359
180.0428
152.0328
270.0537
326.1217
121.0286
135.0421
164.0067
210.0358
282.0944
75.0222
93.0323
120.0254
253.0561
283.0881
310.0919
327.1219
345.9988

Elemental Composition Report **Page 1**

Single Mass Analysis
Tolerance = 5.0 PPM / DBE: min = -1.5, max = 50.0
Element prediction: Off

Monoisotopic Mass, Odd and Even Electron Ions
14 formula(e) evaluated with 1 results within limits (all results (up to 1000) for each mass)
Elements Used:
C: 0-15 H: 0-19 N: 0-1 O: 0-7

19-Feb-2018 BRT-145 School of Chemistry Cardiff University
DB_MS18684 177 (5.884) Cm (177-48:51) TOF MS EI+
3.49e+004

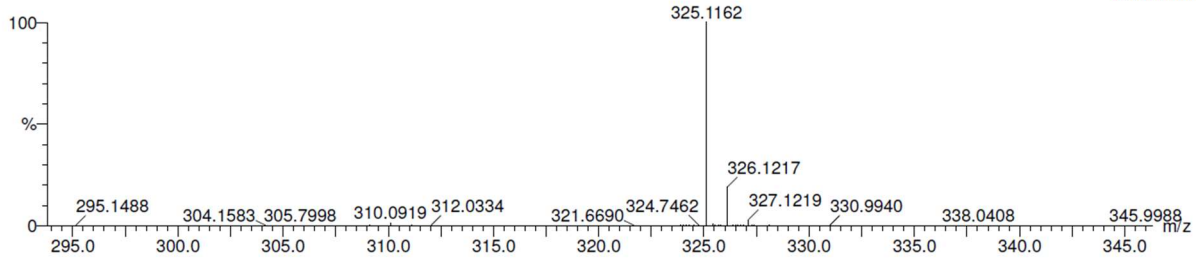

Minimum:				-1.5		
Maximum:		5.0	5.0	50.0		
Mass	Calc. Mass	mDa	PPM	DBE	i-FIT	Formula
325.1162	325.1162	0.0	0.0	7.0	12.5	C15 H19 N O7

7.9. *tert*-Butyl-2-(4-(1-hydroxy-1λ^3-ethyl)-2-methoxy-5-nitrophenoxy)acetate (3-16)

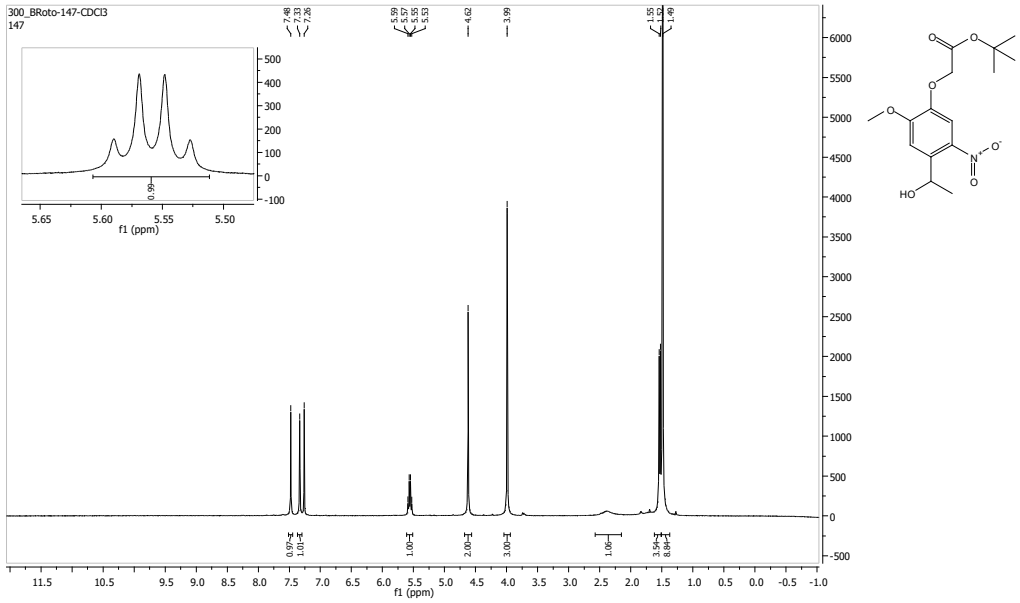

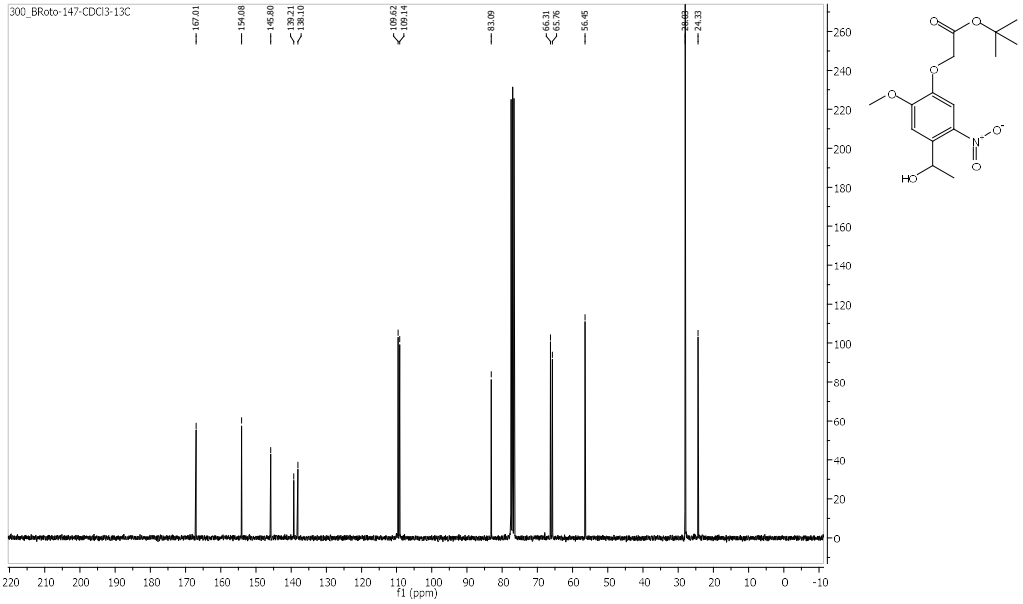

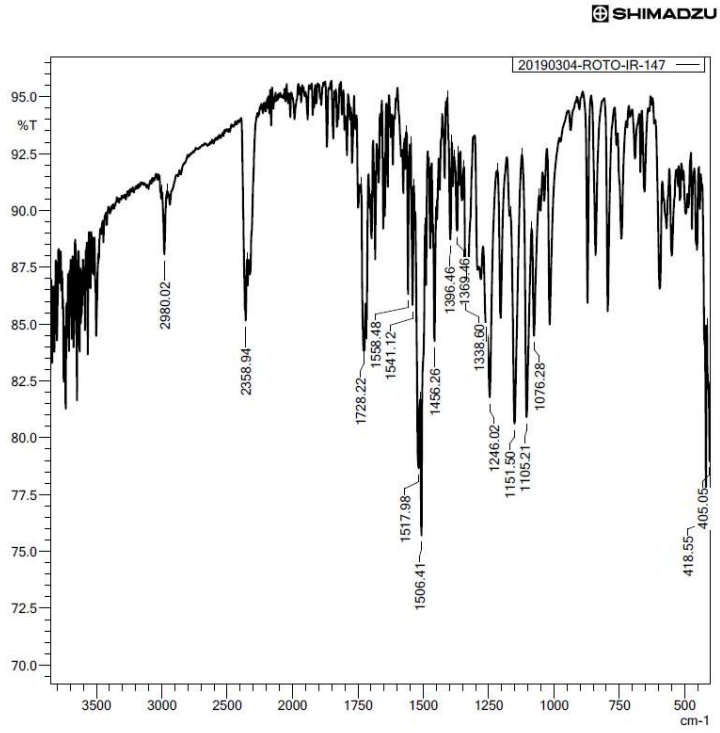
SHIMADZU
20190304-ROTO-IR-147
%T
95.0
92.5
90.0
87.5
85.0
82.5
80.0
77.5
75.0
72.5
70.0
2980.02
2358.94
1728.22
1558.48
1541.12
1517.98
1506.41
1456.26
1396.46
1369.46
1338.60
1246.02
1151.50
1105.21
1076.28
418.55
405.05
3500
3000
2500
2000
1750
1500
1250
1000
750
500
cm-1

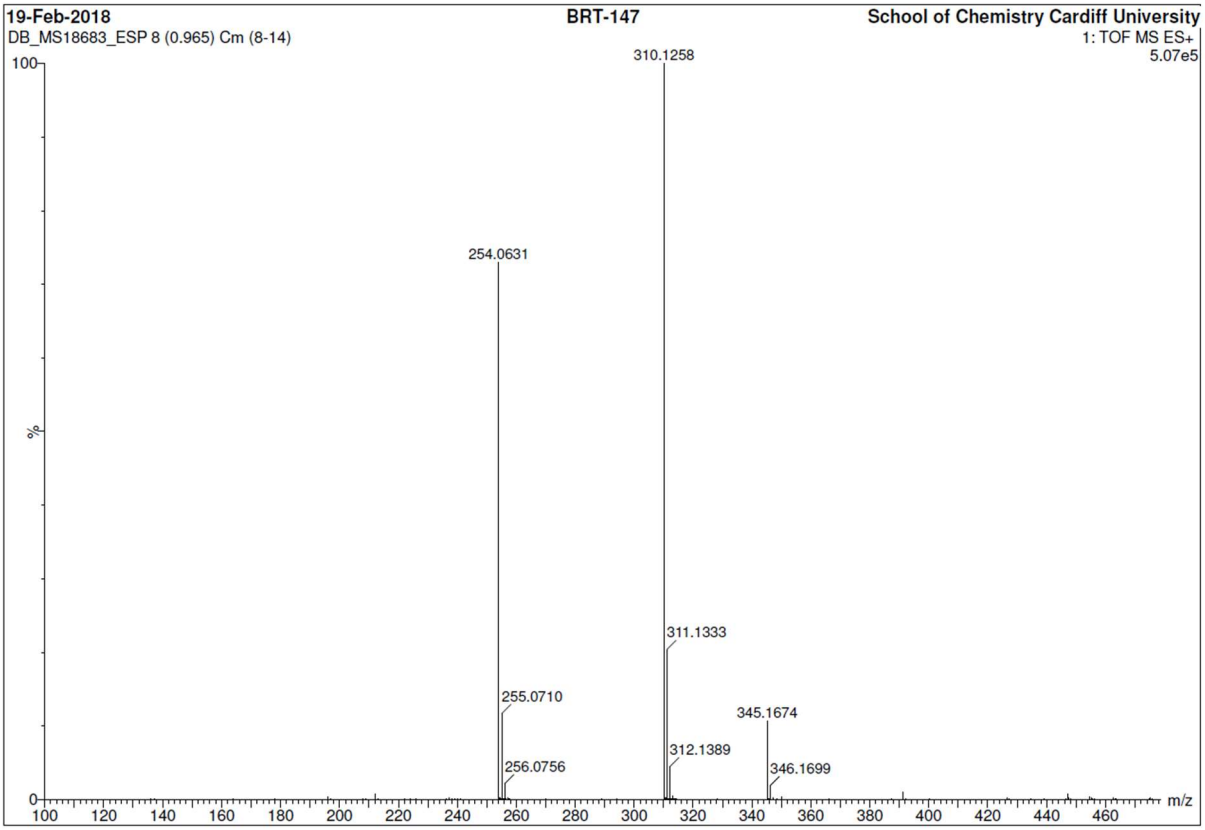
19-Feb-2018
DB_MS18683_ESP 8 (0.965) Cm (8-14)
BRT-147
School of Chemistry Cardiff University
1: TOF MS ES+
5.07e5
100
%
0
310.1258
254.0631
311.1333
255.0710
345.1674
312.1389
256.0756
346.1699
100
120
140
160
180
200
220
240
260
280
300
320
340
360
380
400
420
440
460
m/z

Elemental Composition Report **Page 1**

Single Mass Analysis
Tolerance = 5.0 PPM / DBE: min = -1.5, max = 100.0
Element prediction: Off
Number of isotope peaks used for i-FIT = 9

Monoisotopic Mass, Even Electron Ions
22 formula(e) evaluated with 1 results within limits (up to 50 best isotopic matches for each mass)
Elements Used:
C: 0-15 H: 0-25 N: 0-2 O: 0-7

19-Feb-2018
DB_MS18683_ESP 8 (0.965)

BRT-147

School of Chemistry Cardiff University
1: TOF MS ES+
5.54e+004

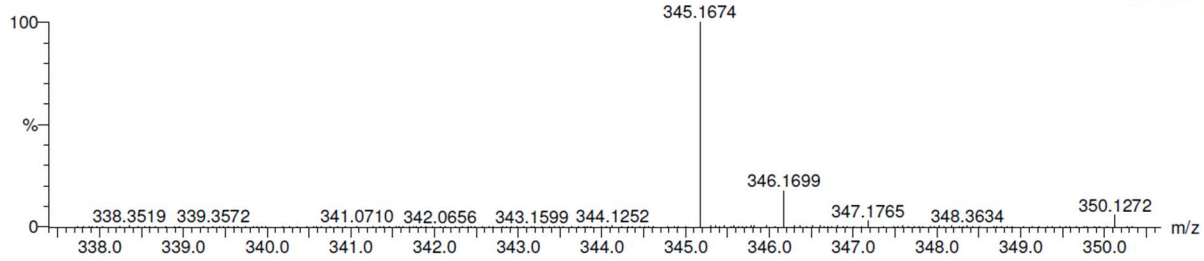

Minimum:				-1.5			
Maximum:		5.0	5.0	100.0			
Mass	Calc. Mass	mDa	PPM	DBE	i-FIT	i-FIT (Norm)	Formula
345.1674	345.1662	1.2	3.5	4.5	465.8	0.0	C15 H25 N2 O7

7.10. 1-(4-(2-(*tert*-butoxy)-2-oxoethoxy)-5-methoxy-2-nitrophenyl)-1λ^3-ethyl (((9H-fluoren-9-yl)methoxy)carbonyl)-L-glutaminate (3-18)

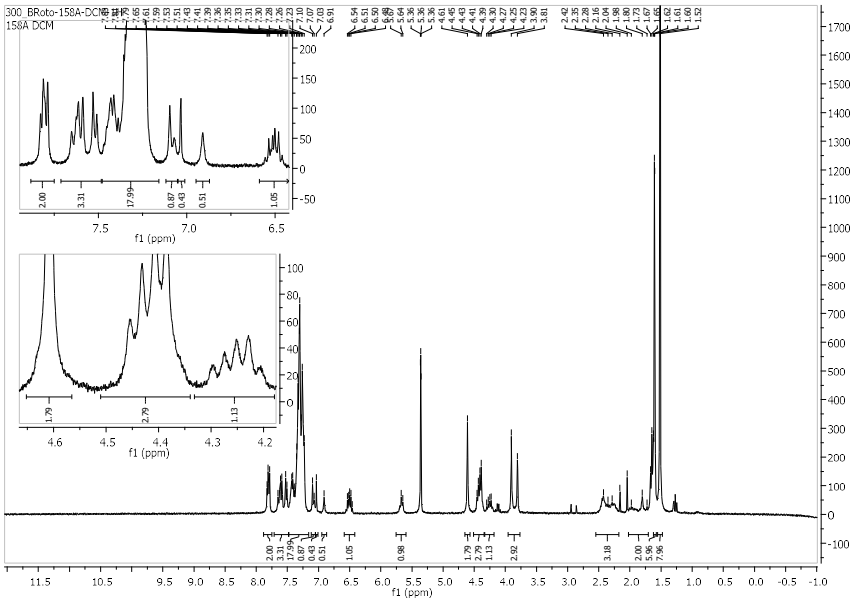

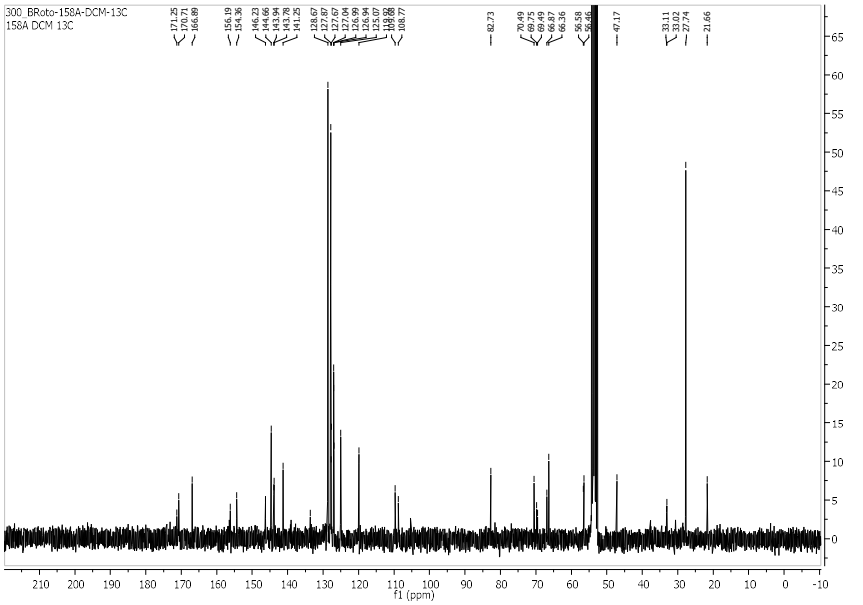

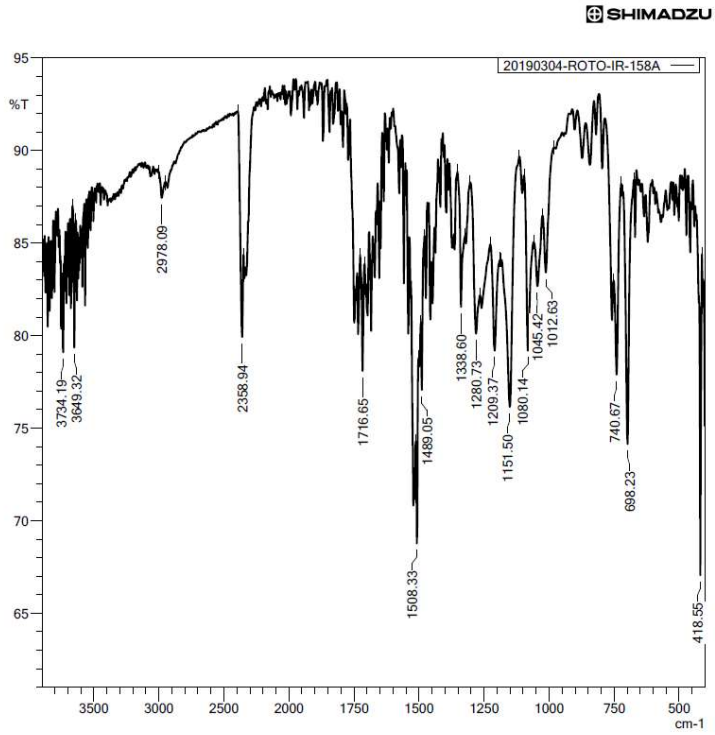
SHIMADZU
20190304-ROTO-IR-158A
%T
95
90
85
80
75
70
65
3734.19
3649.32
2978.09
2358.94
1716.65
1489.05
1508.33
1338.60
1280.73
1209.37
1151.50
1080.14
1045.42
1012.63
740.67
698.23
418.55
3500
3000
2500
2000
1750
1500
1250
1000
750
500
cm-1

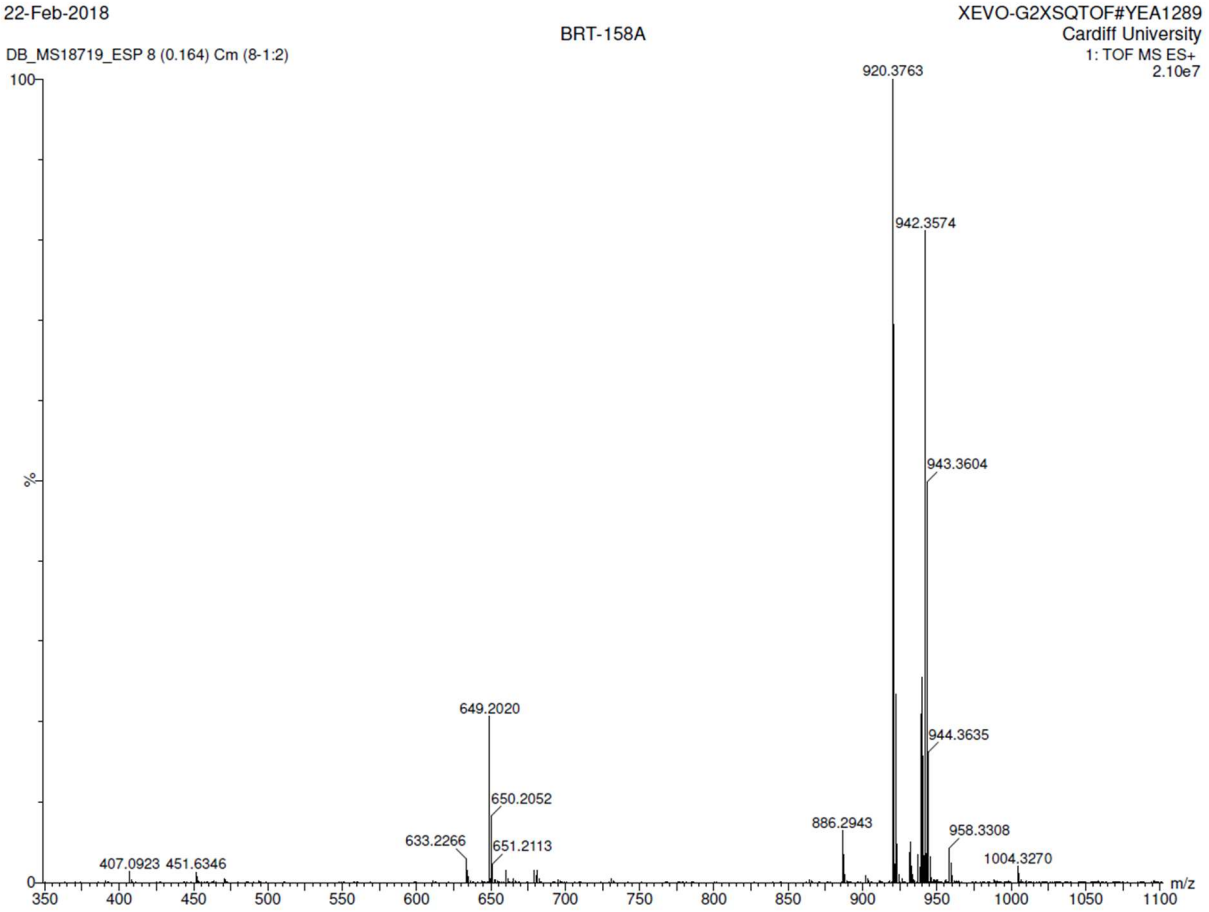
22-Feb-2018
BRT-158A
XEVO-G2XSQTOF#YEA1289
Cardiff University
1: TOF MS ES+
2.10e7
DB_MS18719_ESP 8 (0.164) Cm (8-1:2)
100
%
0
920.3763
942.3574
943.3604
944.3635
649.2020
650.2052
651.2113
633.2266
886.2943
958.3308
1004.3270
407.0923
451.6346
350
400
450
500
550
600
650
700
750
800
850
900
950
1000
1050
1100
m/z

Elemental Composition Report **Page 1**

Single Mass Analysis
Tolerance = 5.0 PPM / DBE: min = -1.5, max = 50.0
Element prediction: Off
Number of isotope peaks used for i-FIT = 3

Monoisotopic Mass, Odd and Even Electron Ions
35 formula(e) evaluated with 1 results within limits (up to 50 best isotopic matches for each mass)
Elements Used:
C: 0-54 H: 0-54 N: 0-3 O: 0-11

Minimum:				-1.5				
Maximum:		5.0	5.0	50.0				
Mass	Calc. Mass	mDa	PPM	DBE	i-FIT	Norm	Conf(%)	Formula
920.3763	920.3758	0.5	0.5	29.5	588.9	n/a	n/a	C54 H54 N3 O11

7.11. 1-(4-(2-(*tert*-butoxy)-2-oxoethoxy)-5-methoxy-2-nitrophenyl)ethyl (((9H-fluoren-9-yl)methoxy)carbonyl)-L-glutaminate (3-17)

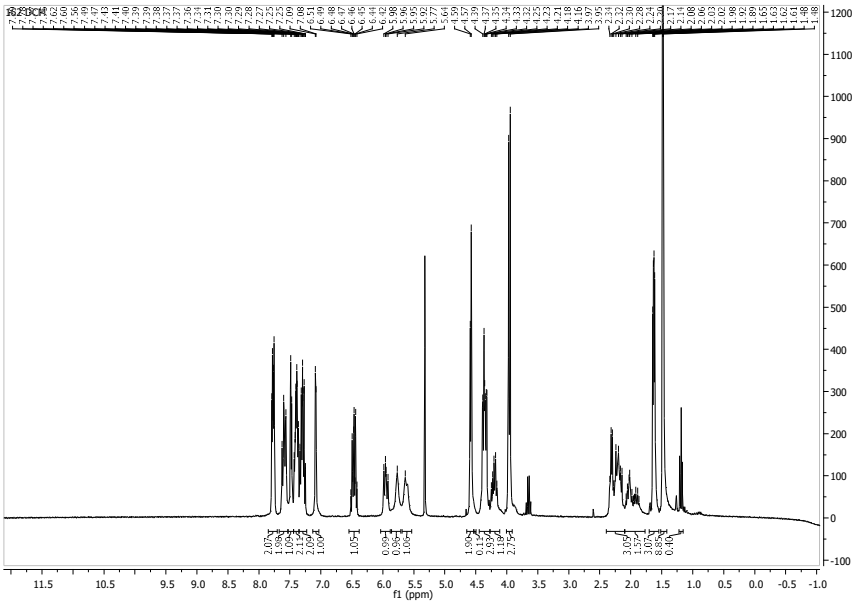

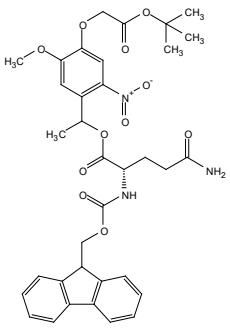

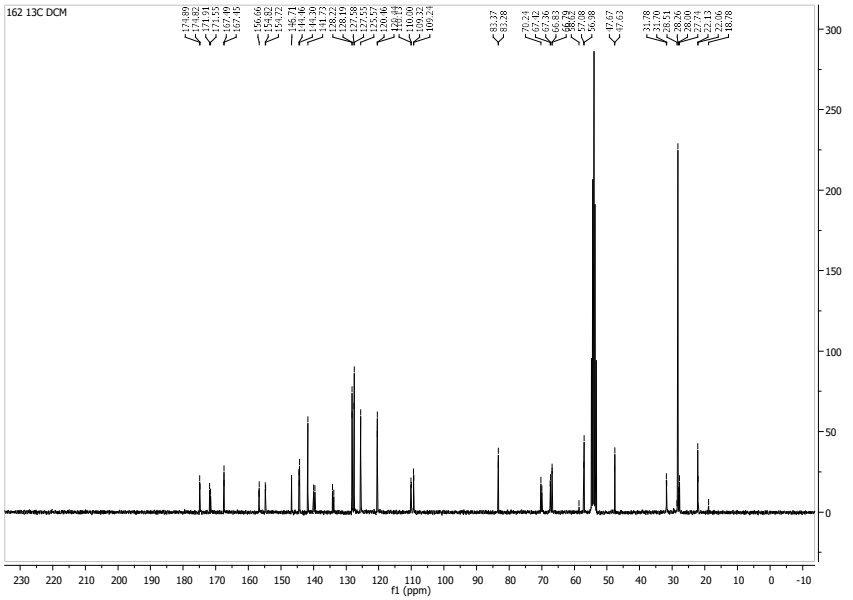

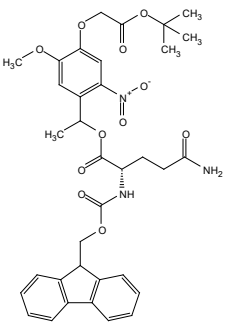

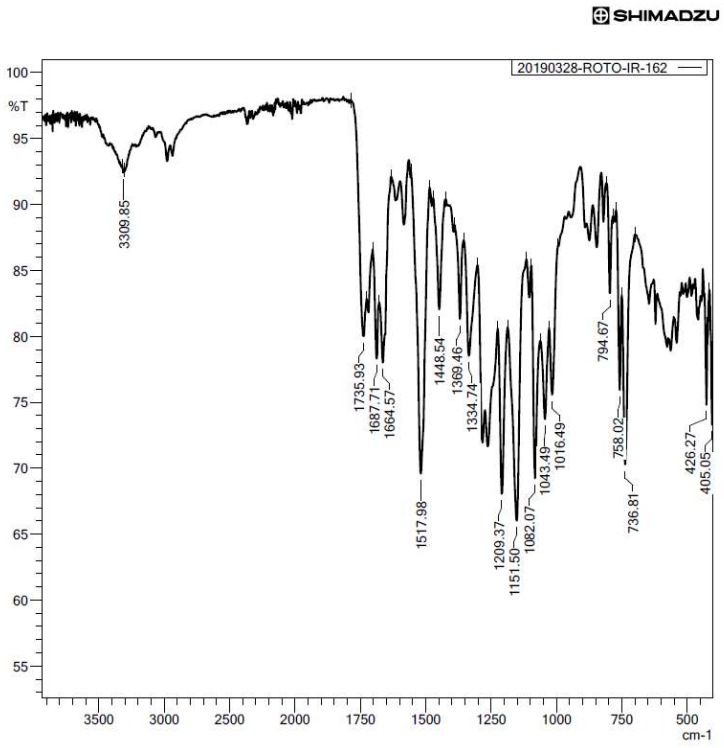
SHIMADZU
20190328-ROTO-IR-162
%T
3309.85
1735.93
1687.71
1664.57
1517.98
1448.54
1369.46
1334.74
1209.37
1151.50
1082.07
1043.49
1016.49
794.67
758.02
736.81
426.27
405.05
cm-1

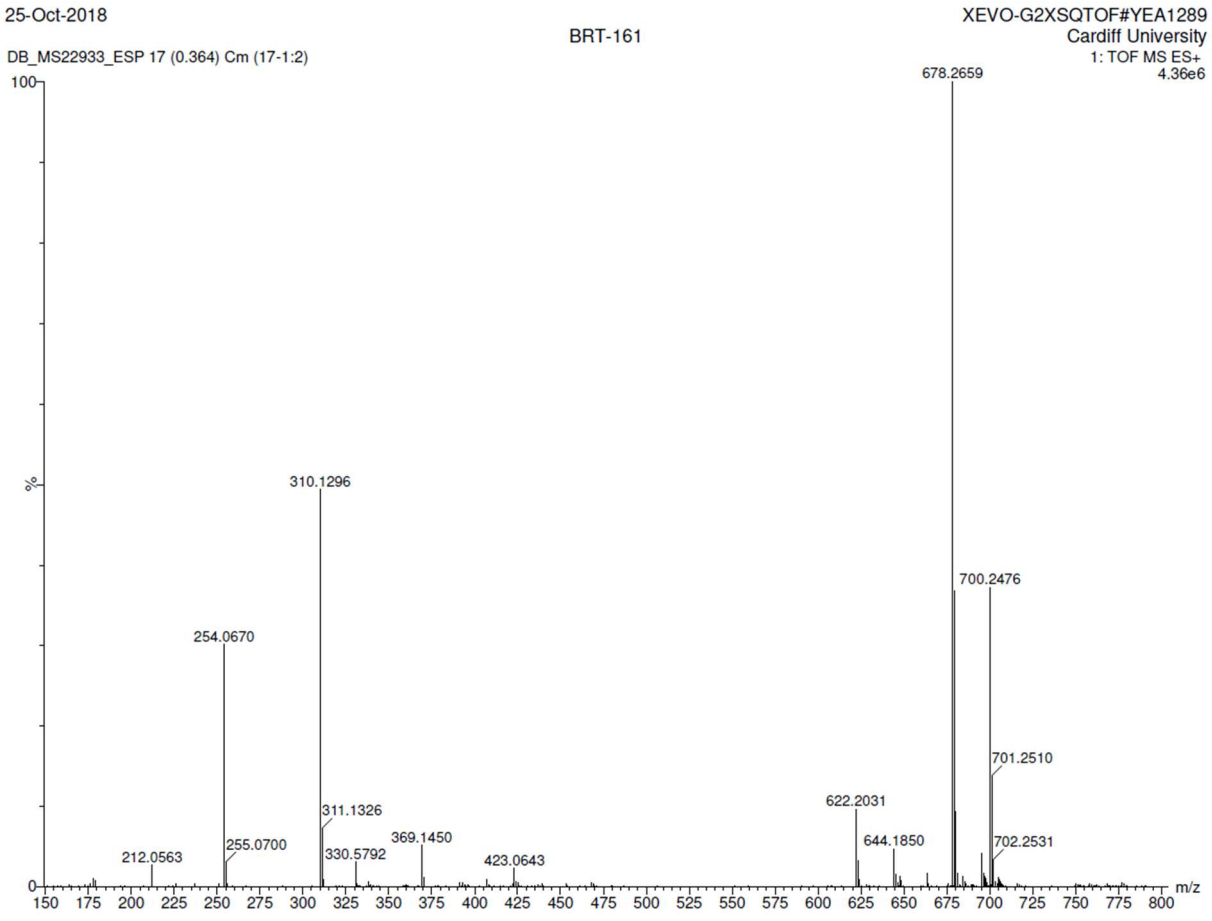
25-Oct-2018
BRT-161
XEVO-G2XSQTOF#YEA1289
Cardiff University
DB_MS22933_ESP 17 (0.364) Cm (17-1:2)
1: TOF MS ES+
4.36e6
678.2659
310.1296
700.2476
254.0670
701.2510
622.2031
311.1326
644.1850
369.1450
702.2531
255.0700
212.0563
330.5792
423.0643
%
m/z

Elemental Composition Report **Page 1**

Single Mass Analysis
Tolerance = 5.0 PPM / DBE: min = -1.5, max = 100.0
Element prediction: Off
Number of isotope peaks used for i-FIT = 3

Monoisotopic Mass, Odd and Even Electron Ions
42 formula(e) evaluated with 1 results within limits (up to 50 closest results for each mass)
Elements Used:
C: 0-35 H: 0-40 N: 0-3 O: 0-11

Minimum:				-1.5				
Maximum:		5.0	5.0	100.0				
Mass	Calc. Mass	mDa	PPM	DBE	i-FIT	Norm	Conf(%)	Formula
678.2659	678.2663	-0.4	-0.6	17.5	229.2	n/a	n/a	C35 H40 N3 O11

7.12. 2-(4-(1-(((((9H-fluoren-9-yl)methoxy)carbonyl)-L-glutaminyl) oxy)-1λ^3-ethyl)-2-methoxy-5-nitrophenoxy)acetic acid (3-19)

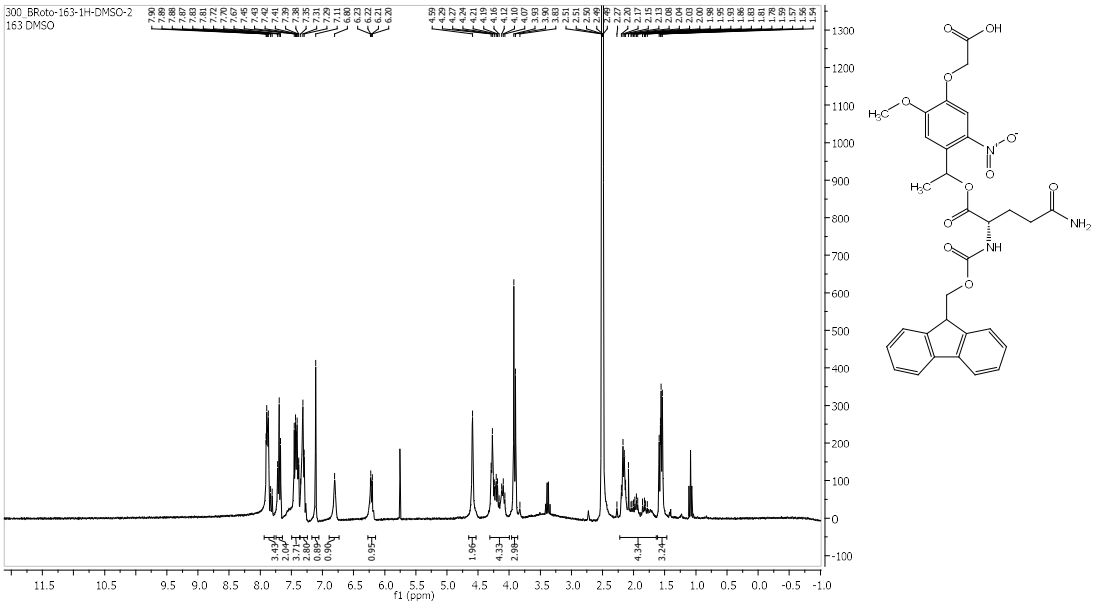

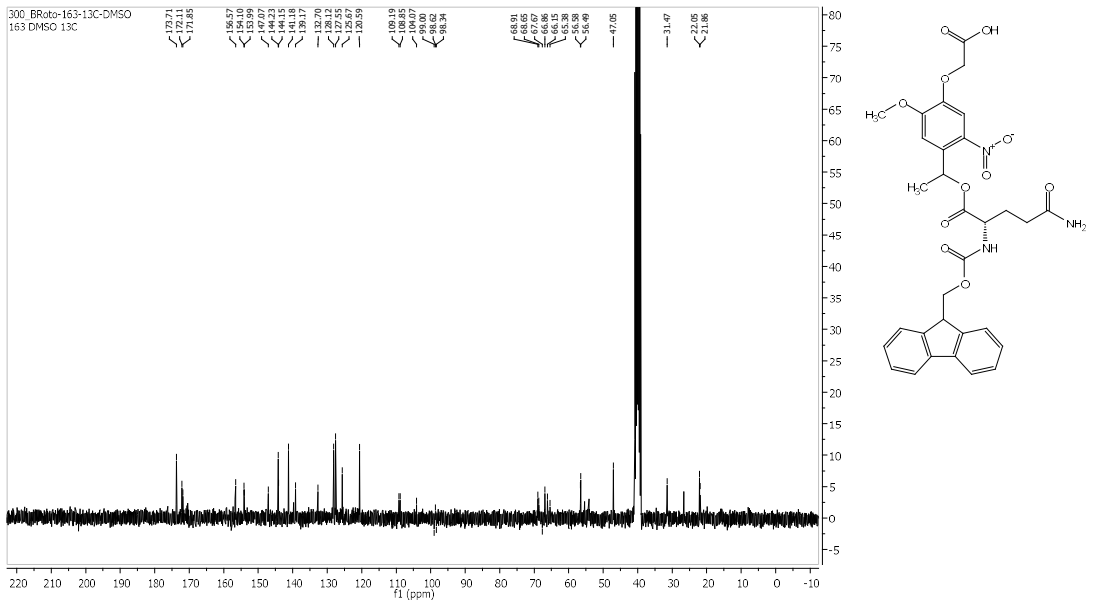

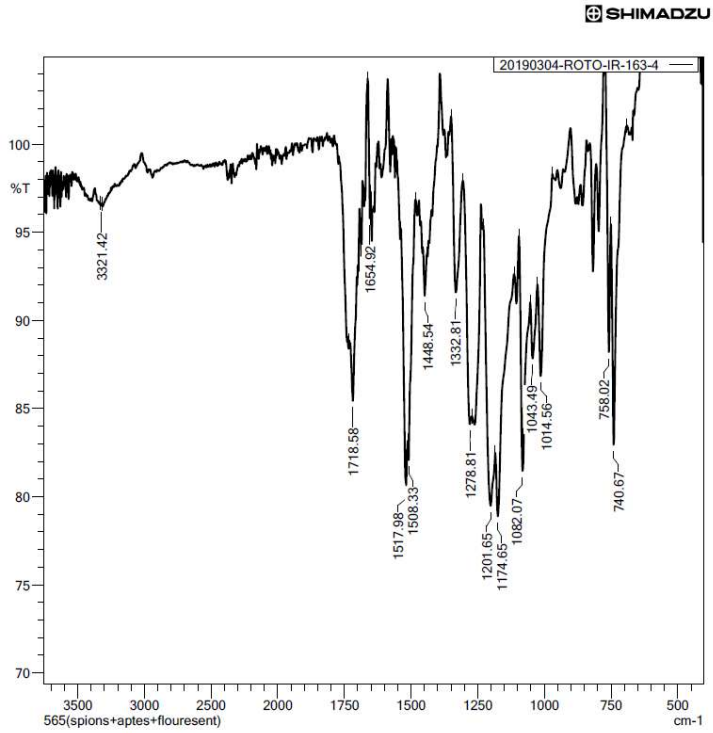
SHIMADZU
20190304-ROTO-IR-163-4
%T
100
95
90
85
80
75
70
3321.42
1654.92
1718.58
1448.54
1332.81
1517.98
1508.33
1278.81
1201.65
1174.65
1082.07
1043.49
1014.56
758.02
740.67
3500
3000
2500
2000
1750
1500
1250
1000
750
500
cm-1
565(spions+aptes+flouresent)

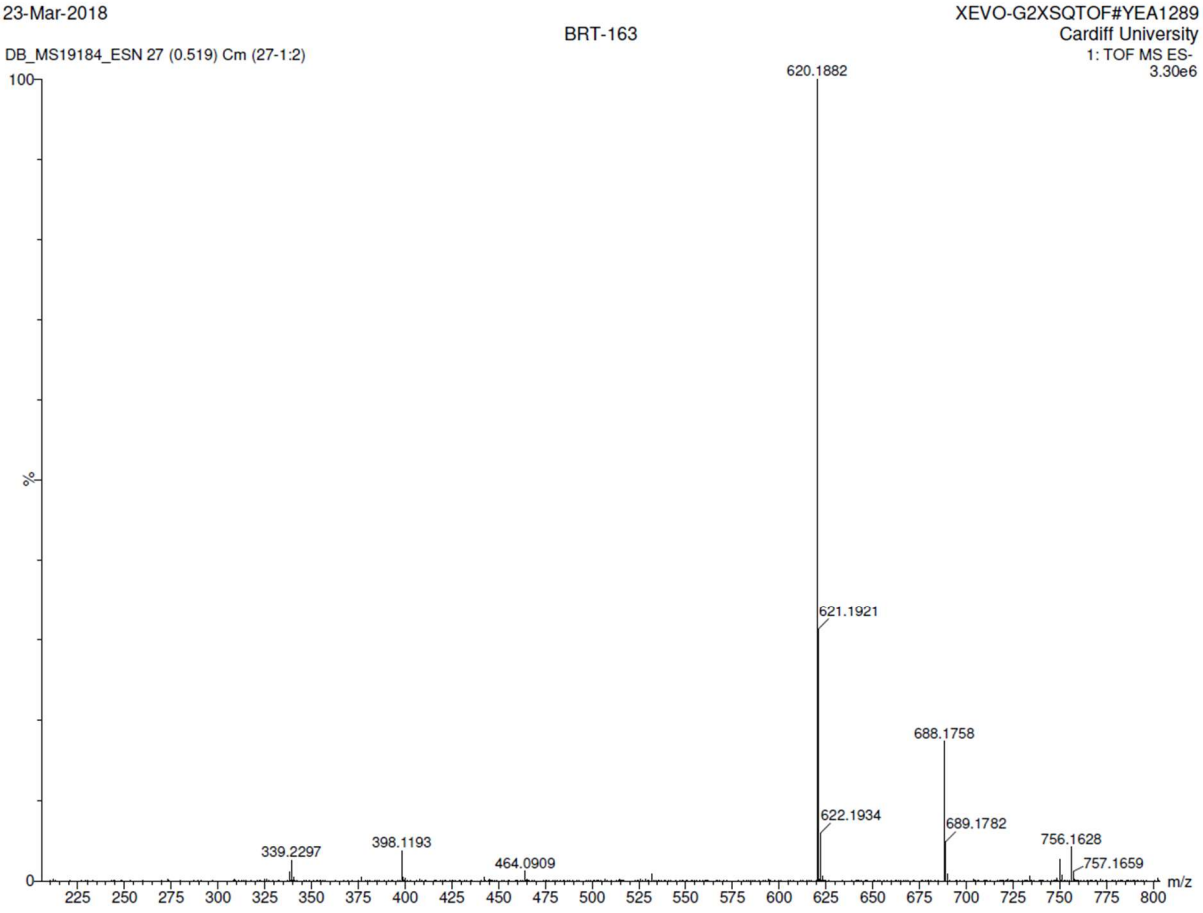
23-Mar-2018
BRT-163
XEVO-G2XSQTOF#YEA1289
Cardiff University
DB_MS19184_ESN 27 (0.519) Cm (27-1:2)
1: TOF MS ES-
3.30e6
100
%
0
620.1882
621.1921
688.1758
622.1934
689.1782
756.1628
757.1659
339.2297
398.1193
464.0909
225
250
275
300
325
350
375
400
425
450
475
500
525
550
575
600
625
650
675
700
725
750
775
800
m/z

Elemental Composition Report **Page 1**

Single Mass Analysis
Tolerance = 5.0 PPM / DBE: min = -1.5, max = 100.0
Element prediction: Off
Number of isotope peaks used for i-FIT = 3

Monoisotopic Mass, Odd and Even Electron Ions
40 formula(e) evaluated with 1 results within limits (up to 50 best isotopic matches for each mass)
Elements Used:
C: 0-31 H: 0-30 N: 0-3 O: 0-11

Minimum:				-1.5				
Maximum:		5.0	5.0	100.0				
Mass	Calc. Mass	mDa	PPM	DBE	i-FIT	Norm	Conf(%)	Formula
620.1882	620.1880	0.2	0.3	18.5	246.5	n/a	n/a	C31 H30 N3 O11

7.13. (S)-4-(((S)-5-amino-1-(1-(4-(((S)-8-carbamoyl-36-mercapto-2,10,26-trioxo-13,16,19,22-tetraoxa-3,9,25-triazahexatriacontyl)oxy)-5-methoxy-2-nitrophenyl)-1λ^3-ethoxy)-1,5-dioxopentan-2-yl)amino)-3-(2-((2S,3S)-2-amino-3-methylpentanamido)acetamido)-4-oxobutanoic acid (3-20)

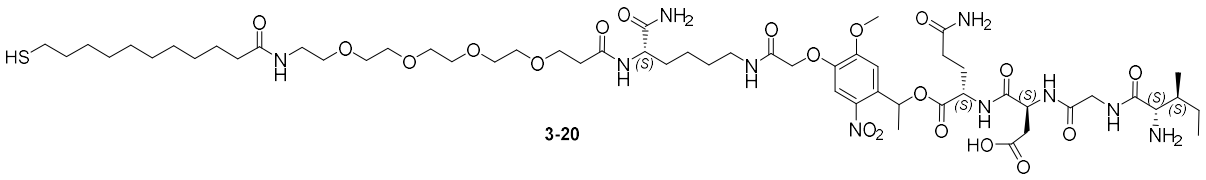

3-20

Chemical Formula: $C_{56}H_{94}N_{10}O_{20}S$
Exact Mass: 1258.6367
Molecular Weight: 1259.4780

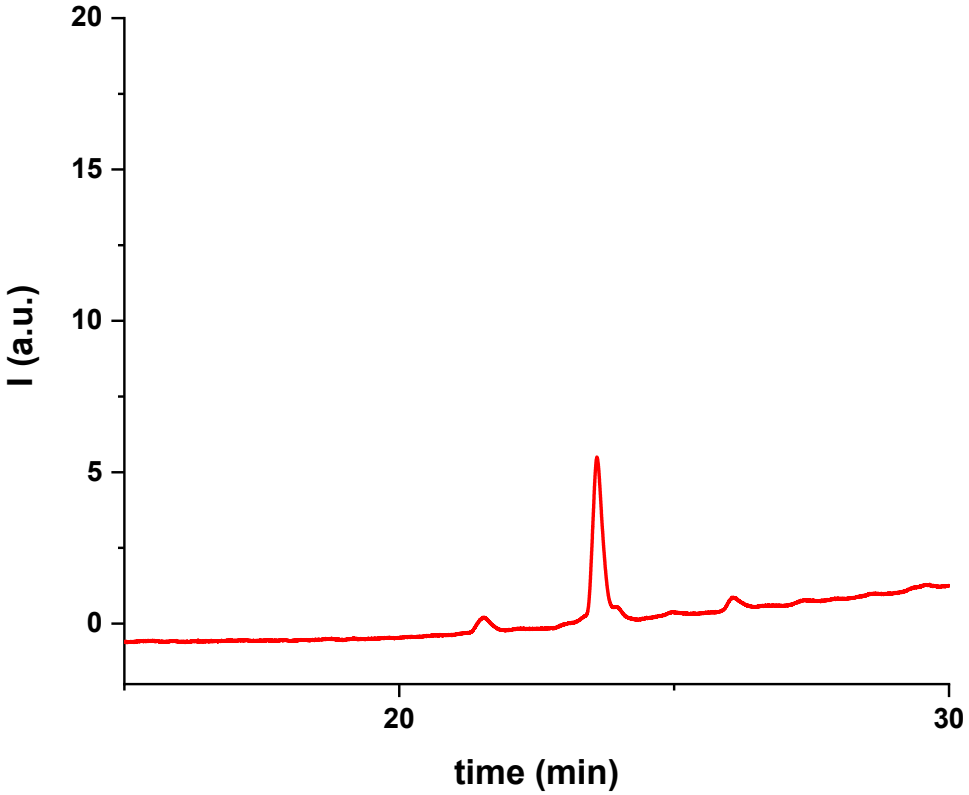

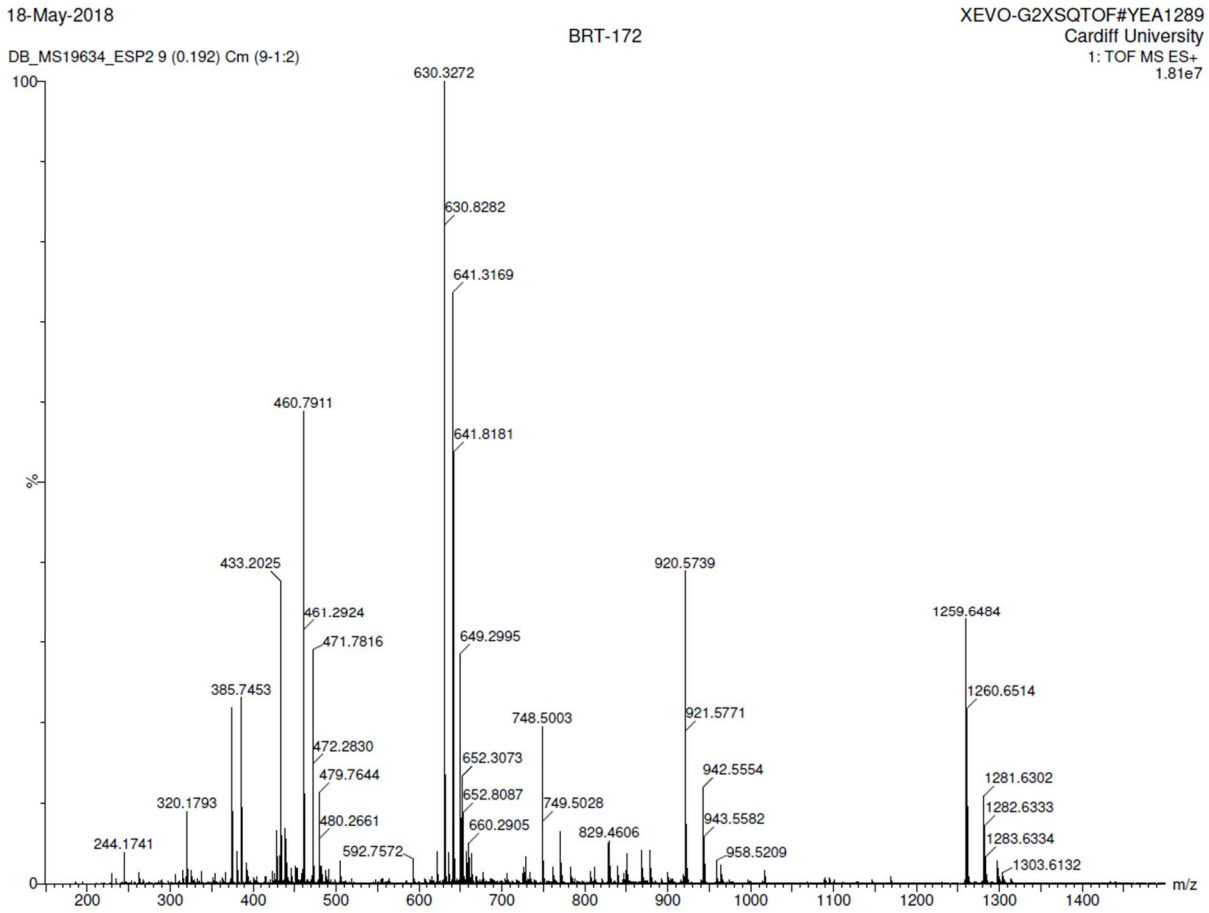

Elemental Composition Report **Page 1**

Single Mass Analysis
Tolerance = 5.0 PPM / DBE: min = -1.5, max = 50.0
Element prediction: Off
Number of isotope peaks used for i-FIT = 3

Monoisotopic Mass, Odd and Even Electron Ions
682 formula(e) evaluated with 1 results within limits (up to 50 best isotopic matches for each mass)
Elements Used:
C: 0-56 H: 0-95 N: 0-10 O: 0-20 S: 0-2

Minimum:				-1.5				
Maximum:		5.0	5.0	50.0				
Mass	Calc. Mass	mDa	PPM	DBE	i-FIT	Norm	Conf(%)	Formula
1259.6484	1259.6445	3.9	3.1	14.5	544.4	n/a	n/a	C56 H95 N10 O20 S

7.14. 4,5-dimethoxy-2-nitrobenzaldehyde (3-22)

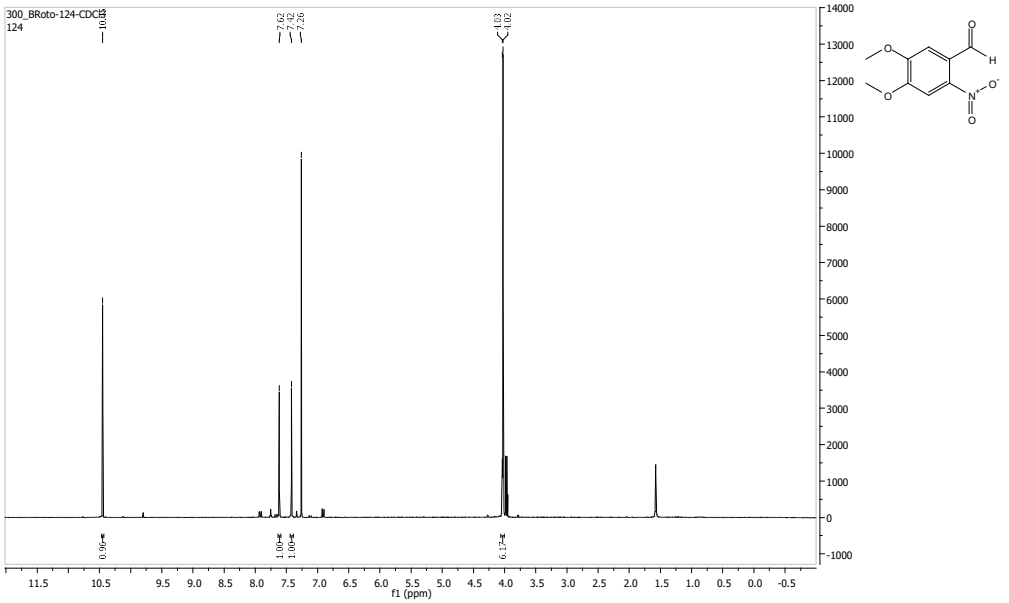

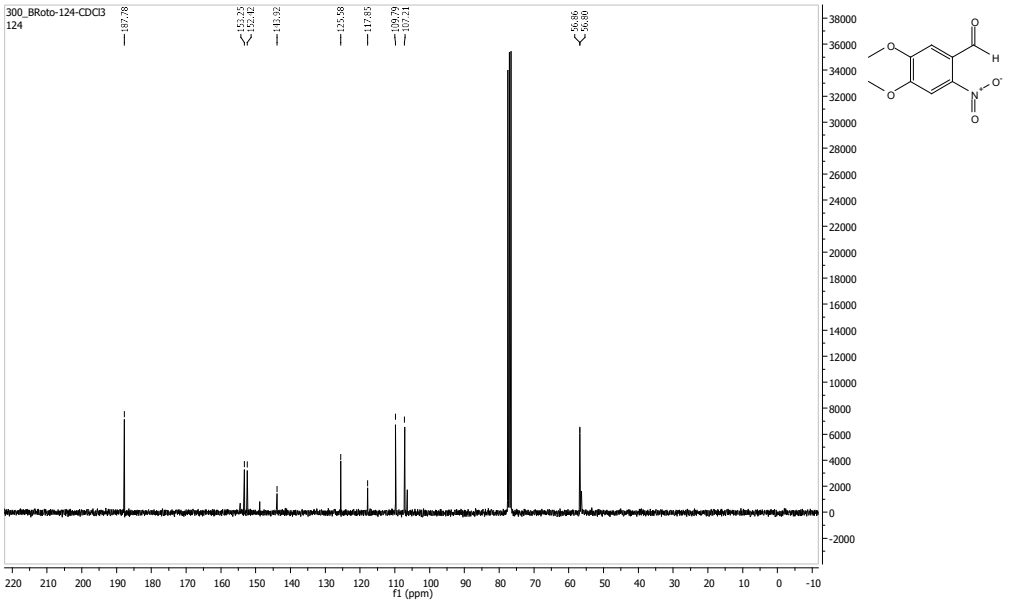

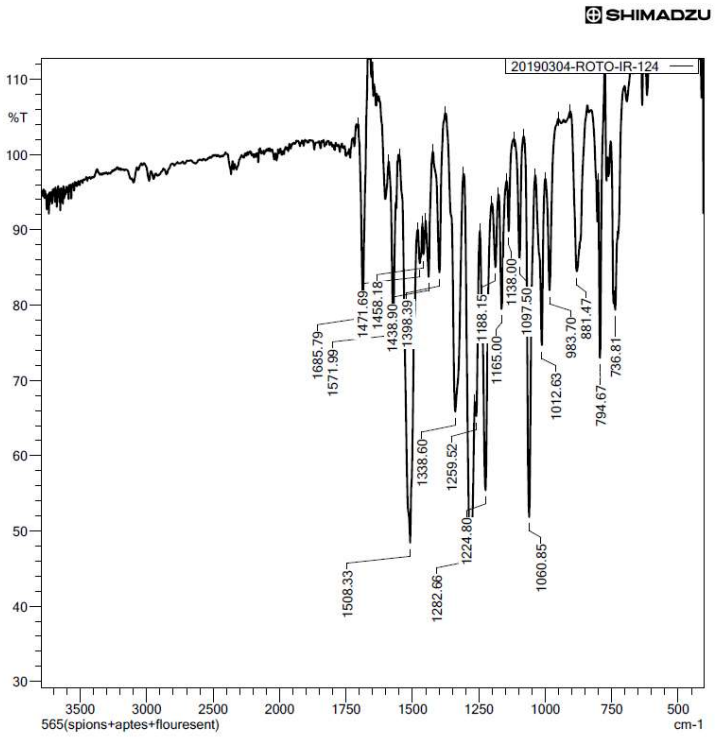
SHIMADZU
20190304-ROTO-IR-124
%T
110
100
90
80
70
60
50
40
30
1685.79
1571.99
1471.69
1458.18
1438.90
1398.39
1338.60
1259.52
1508.33
1282.66
1224.80
1188.15
1165.00
1138.00
1097.50
1060.85
1012.63
983.70
881.47
794.67
736.81
3500
3000
2500
2000
1750
1500
1250
1000
750
500
cm-1
565(spions+aptes+flouresent)

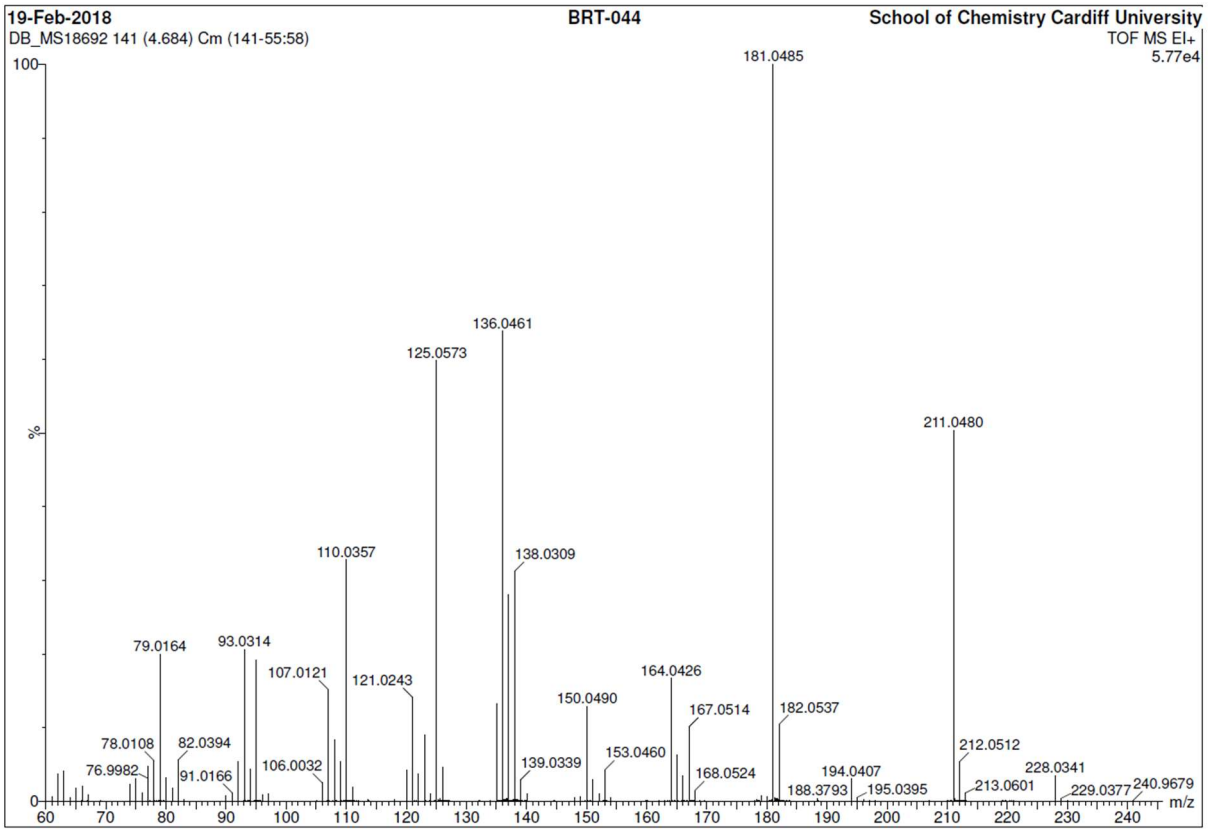
19-Feb-2018
BRT-044
School of Chemistry Cardiff University
DB_MS18692 141 (4.684) Cm (141-55:58)
TOF MS EI+
5.77e4
100
%
0
181.0485
136.0461
125.0573
211.0480
110.0357
138.0309
79.0164
93.0314
107.0121
121.0243
164.0426
150.0490
167.0514
182.0537
78.0108
82.0394
76.9982
91.0166
106.0032
139.0339
153.0460
168.0524
212.0512
194.0407
228.0341
188.3793
195.0395
213.0601
229.0377
240.9679
60
70
80
90
100
110
120
130
140
150
160
170
180
190
200
210
220
230
240
m/z

Elemental Composition Report **Page 1**

Single Mass Analysis
Tolerance = 5.0 PPM / DBE: min = -1.5, max = 50.0
Element prediction: Off

Monoisotopic Mass, Odd and Even Electron Ions
10 formula(e) evaluated with 1 results within limits (all results (up to 1000) for each mass)
Elements Used:
C: 0-9 H: 0-9 N: 0-1 O: 0-5

19-Feb-2018 BRT-044 School of Chemistry Cardiff University
DB_MS18692 141 (4.684) Cm (141-55:58) TOF MS EI+
5.77e+004

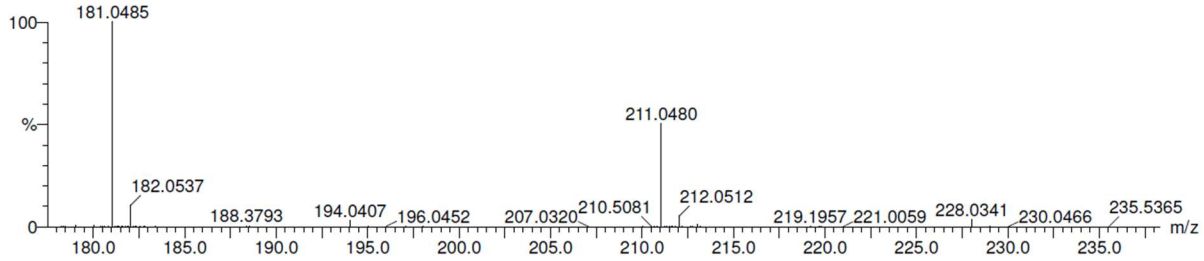

Minimum:				-1.5		
Maximum:		5.0	5.0	50.0		
Mass	Calc. Mass	mDa	PPM	DBE	i-FIT	Formula
211.0480	211.0481	-0.1	-0.5	6.0	33.0	C9 H9 N O5

7.15. (4,5-dimethoxy-2-nitrophenyl)methanol (3-23)

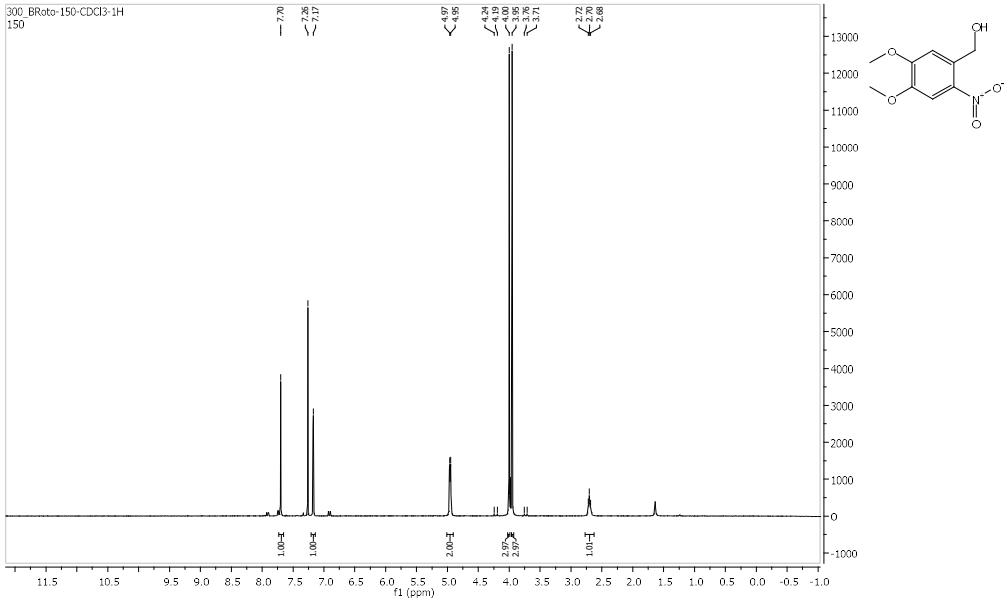

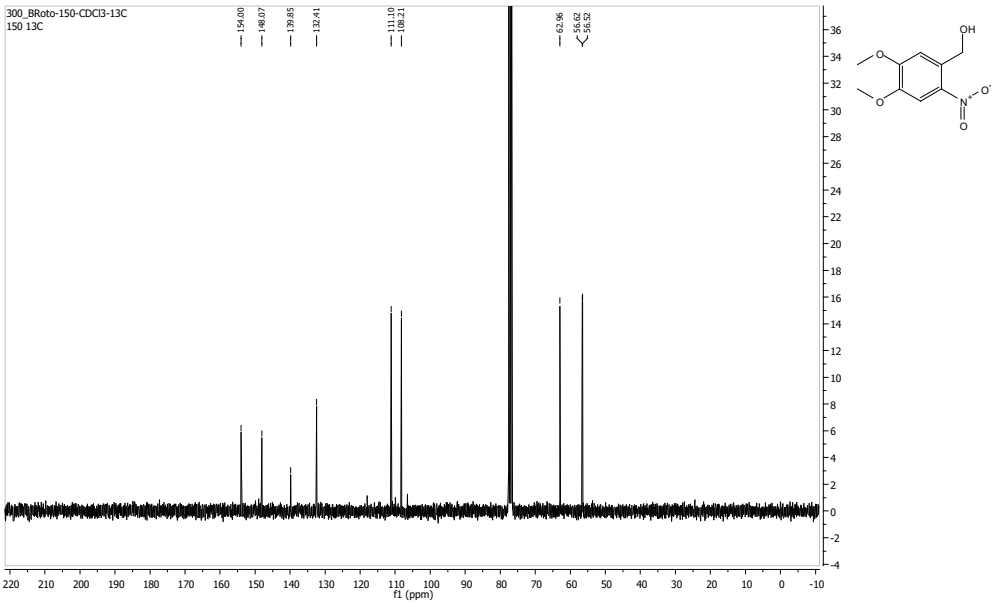

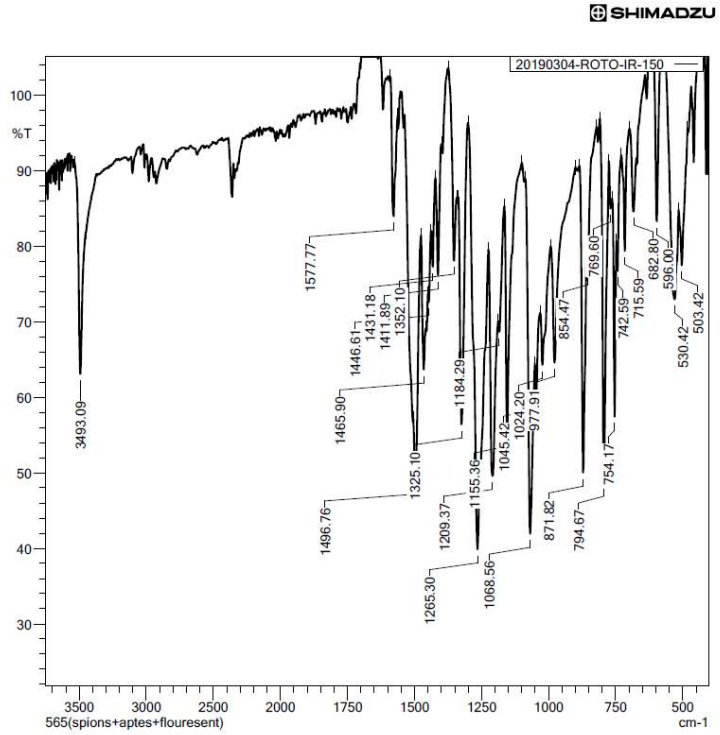
SHIMADZU
20190304-ROTO-IR-150
%T
100
90
80
70
60
50
40
30
3493.09
1577.77
1465.90
1446.61
1431.18
1411.89
1352.10
1325.10
1496.76
1209.37
1184.29
1155.36
1068.56
1265.30
1045.42
1024.20
977.91
871.82
854.47
794.67
769.60
754.17
742.59
715.59
682.80
596.00
530.42
503.42
3500
3000
2500
2000
1750
1500
1250
1000
750
500
cm-1
565(spions+aptes+flouresent)

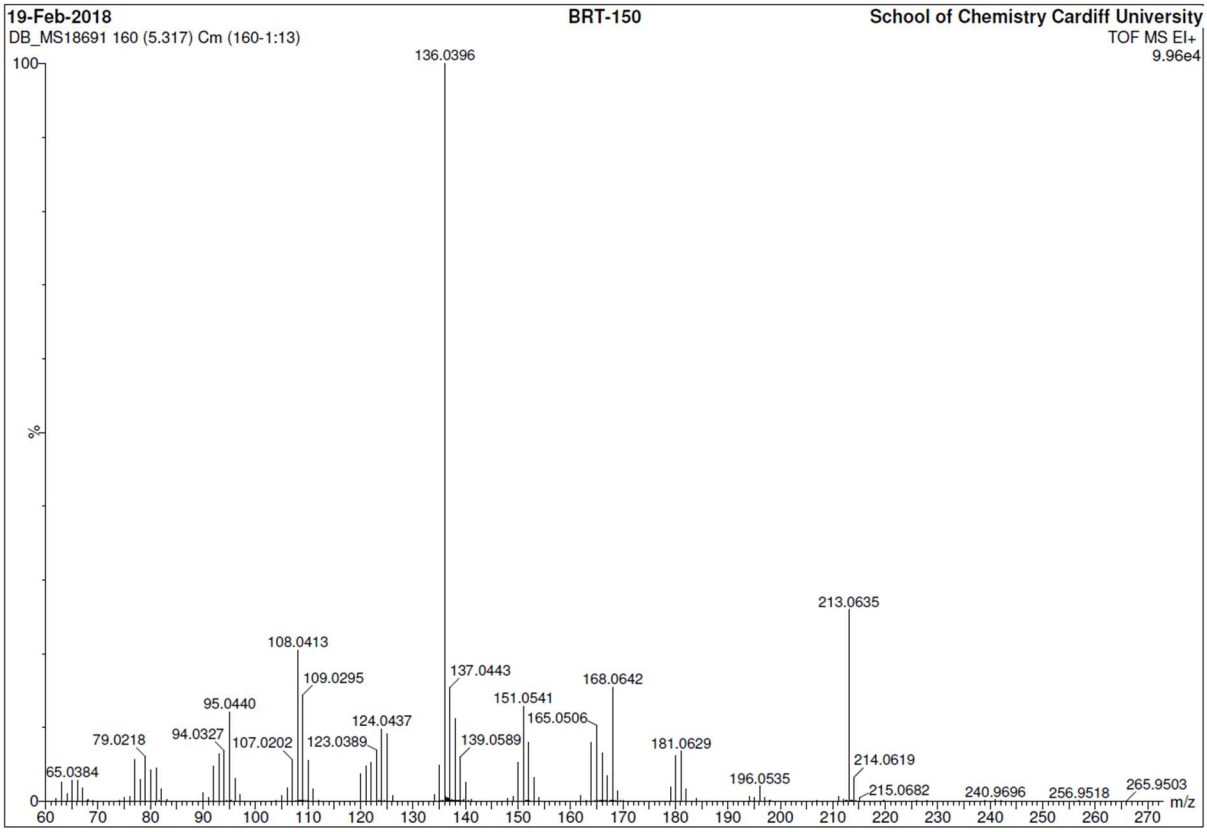
19-Feb-2018
BRT-150
School of Chemistry Cardiff University
DB_MS18691 160 (5.317) Cm (160-1:13)
TOF MS EI+
9.96e4
100
%
0
136.0396
213.0635
108.0413
109.0295
137.0443
168.0642
95.0440
151.0541
165.0506
124.0437
79.0218
94.0327
107.0202
123.0389
139.0589
181.0629
214.0619
65.0384
196.0535
215.0682
240.9696
256.9518
265.9503
60
70
80
90
100
110
120
130
140
150
160
170
180
190
200
210
220
230
240
250
260
270
m/z

Elemental Composition Report **Page 1**

Single Mass Analysis
Tolerance = 5.0 PPM / DBE: min = -1.5, max = 50.0
Element prediction: Off

Monoisotopic Mass, Odd and Even Electron Ions
17 formula(e) evaluated with 1 results within limits (all results (up to 1000) for each mass)
Elements Used:
C: 0-16 H: 0-15 N: 0-1 O: 0-5

19-Feb-2018 BRT-150 School of Chemistry Cardiff University
DB_MS18691 160 (5.317) Cm (160-1:13) TOF MS EI+
9.96e+004

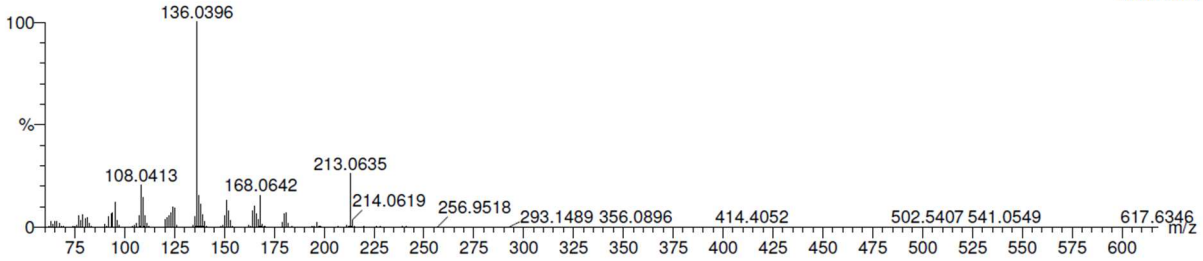

Minimum:				-1.5		
Maximum:		5.0	5.0	50.0		
Mass	Calc. Mass	mDa	PPM	DBE	i-FIT	Formula
213.0635	213.0637	-0.2	-0.9	5.0	34.8	C9 H11 N O5

7.16. *tert*-Butyl (((4,5-dimethoxy-2-nitrobenzyl)oxy)carbonyl)-L-isoleucinate (3-24)

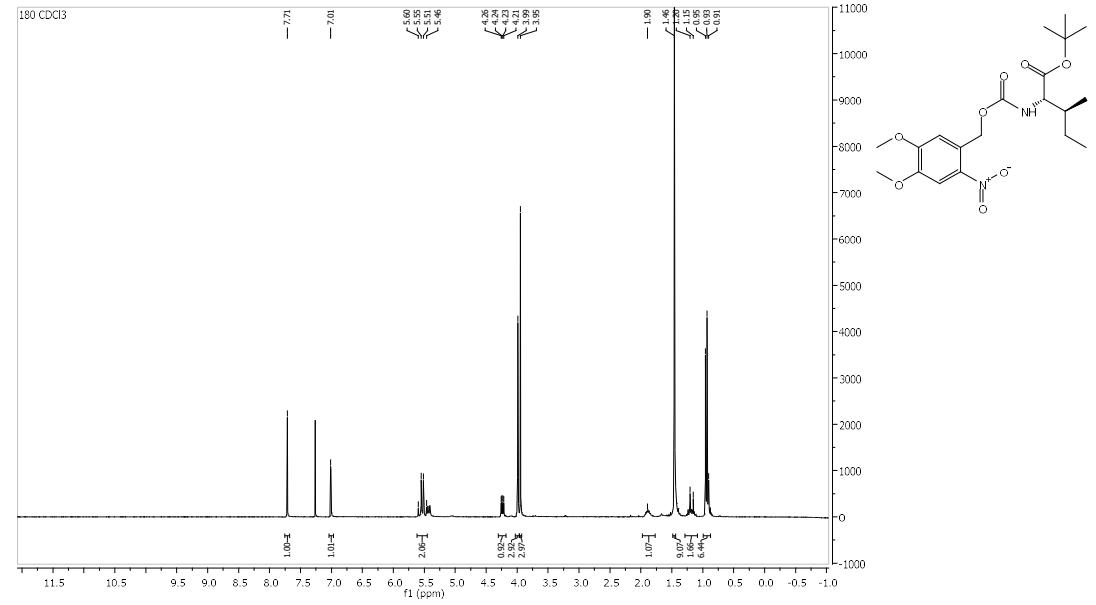

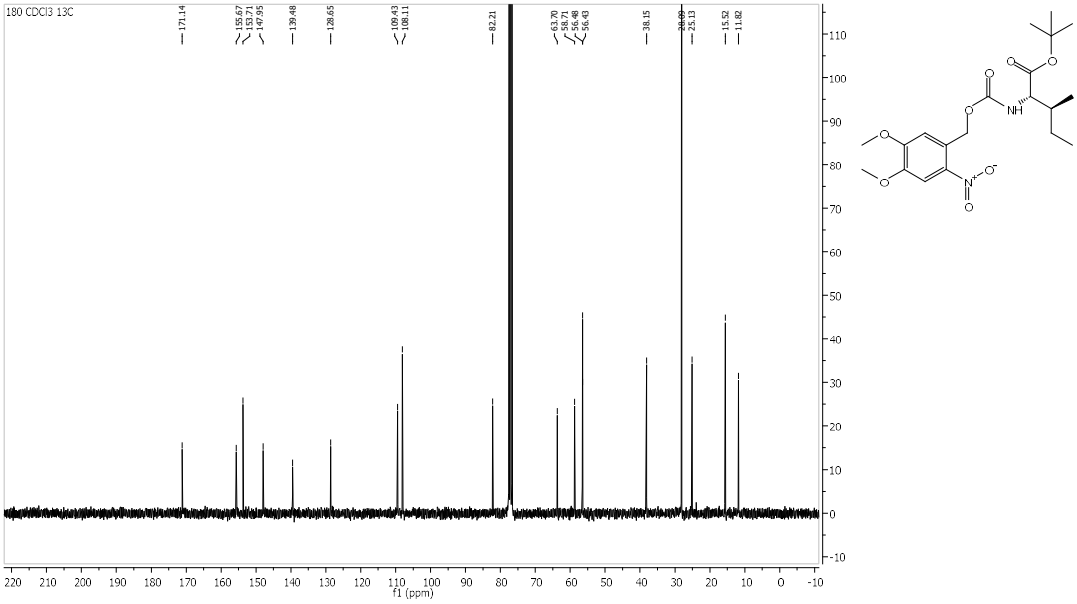

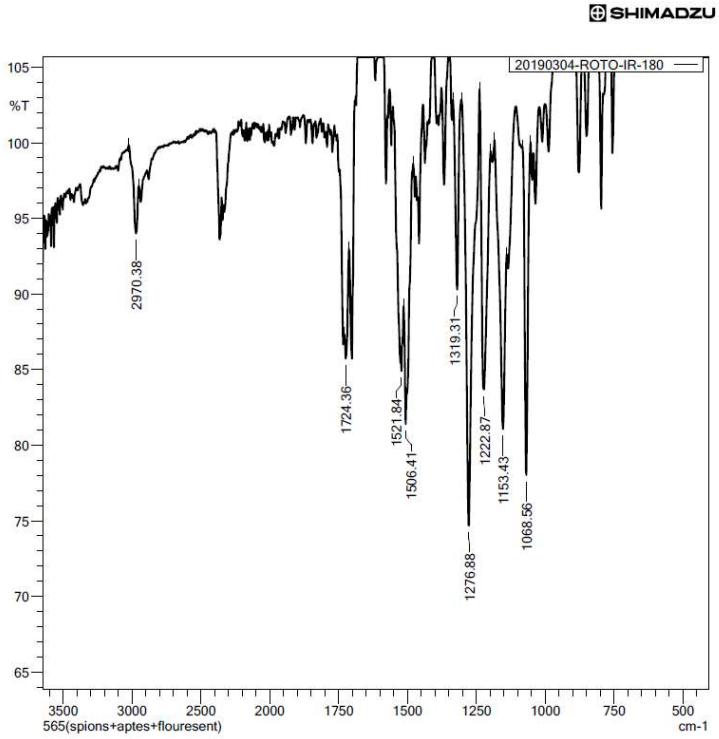
SHIMADZU
20190304-ROTO-IR-180
%T
105
100
95
90
85
80
75
70
65
2970.38
1724.36
1521.84
1506.41
1319.31
1276.88
1222.87
1153.43
1068.56
3500
3000
2500
2000
1750
1500
1250
1000
750
500
cm-1
565(spions+aptes+flouresent)

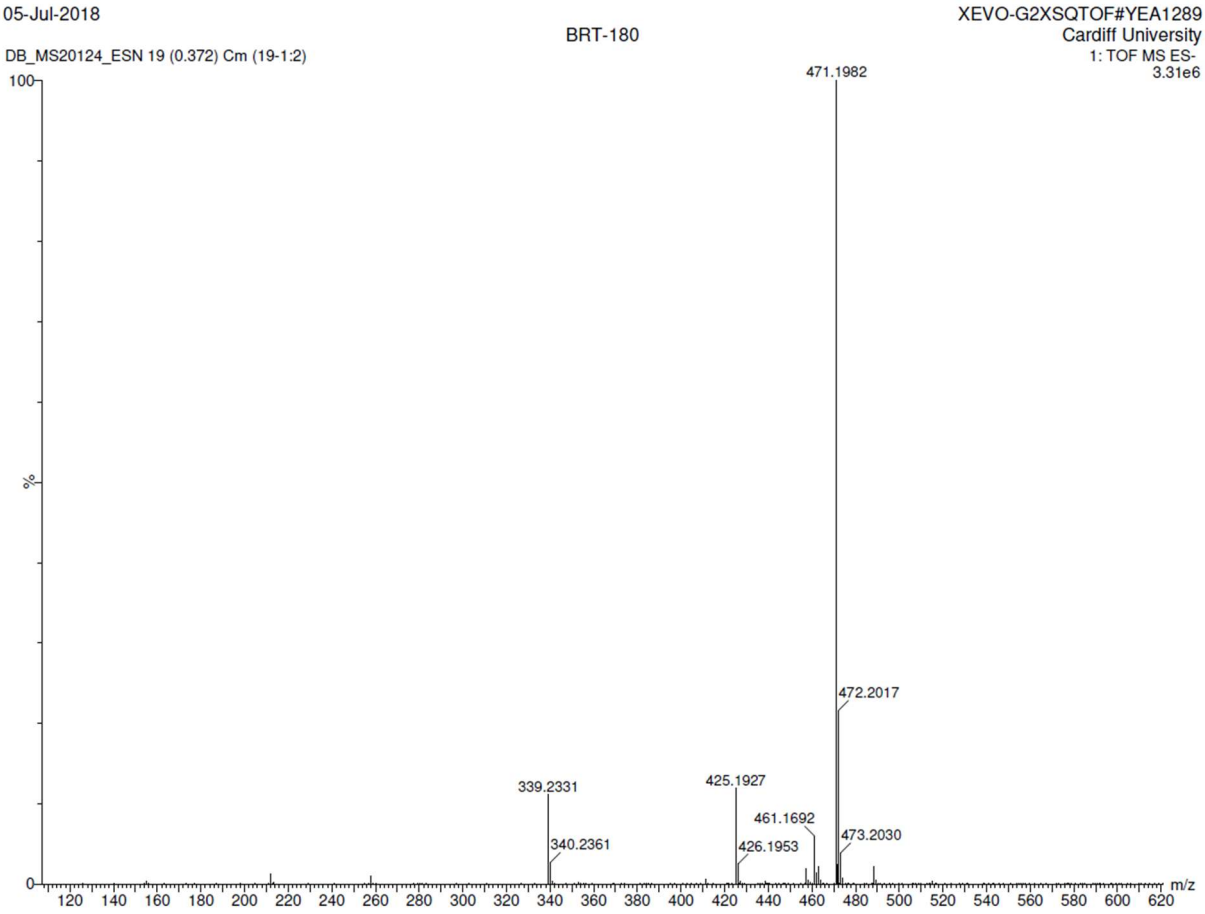
05-Jul-2018
BRT-180
XEVO-G2XSQTOF#YEA1289
Cardiff University
1: TOF MS ES-
3.31e6
DB_MS20124_ESN 19 (0.372) Cm (19-1:2)
100
%
0
471.1982
472.2017
339.2331
425.1927
461.1692
340.2361
426.1953
473.2030
120
140
160
180
200
220
240
260
280
300
320
340
360
380
400
420
440
460
480
500
520
540
560
580
600
620
m/z

Elemental Composition Report **Page 1**

Single Mass Analysis
Tolerance = 5.0 PPM / DBE: min = -1.5, max = 100.0
Element prediction: Off
Number of isotope peaks used for i-FIT = 3

Monoisotopic Mass, Odd and Even Electron Ions
31 formula(e) evaluated with 1 results within limits (up to 50 best isotopic matches for each mass)
Elements Used:
C: 0-21 H: 0-31 N: 0-2 O: 0-10

Minimum:				-1.5				
Maximum:		5.0	5.0	100.0				
Mass	Calc. Mass	mDa	PPM	DBE	i-FIT	Norm	Conf(%)	Formula
471.1982	471.1979	0.3	0.6	7.5	322.8	n/a	n/a	C21 H31 N2 O10

7.17. (((4,5-dimethoxy-2-nitrobenzyl)oxy)carbonyl)-L-isoleucine (3-25)

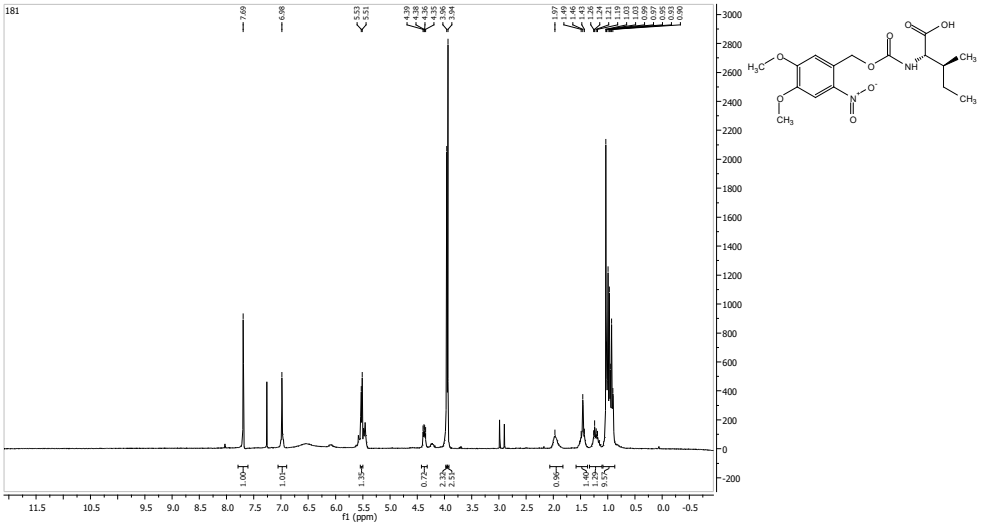

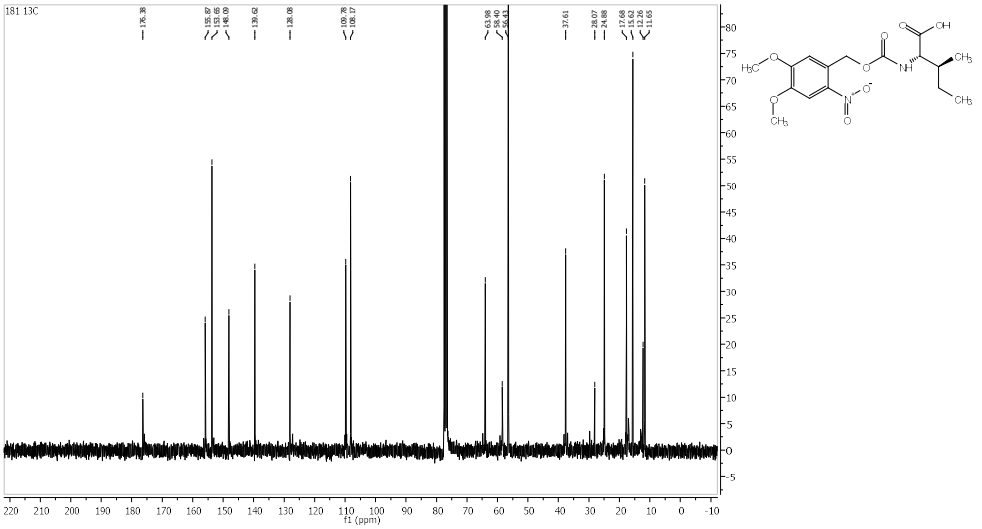

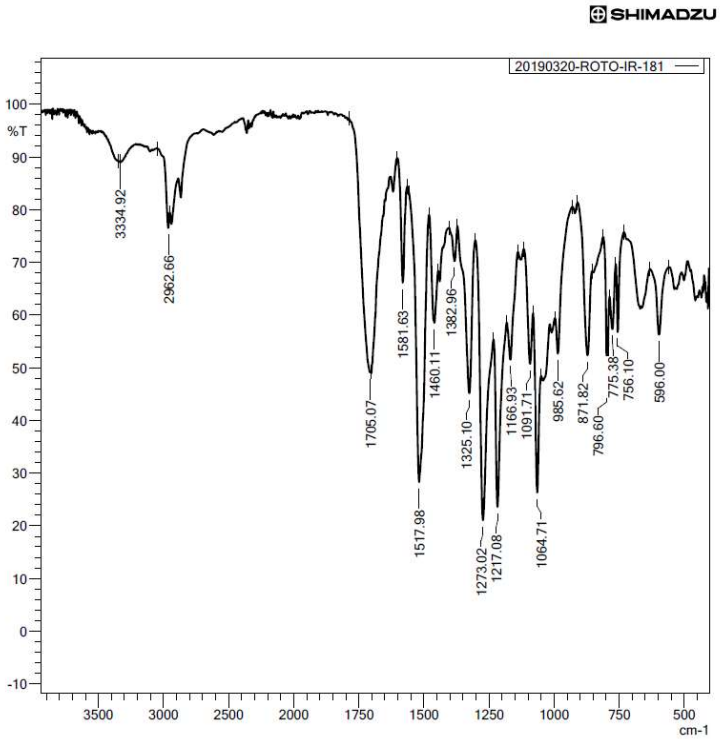
SHIMADZU
20190320-ROTO-IR-181
%T
3334.92
2962.66
1705.07
1581.63
1517.98
1460.11
1382.96
1325.10
1273.02
1217.08
1166.93
1091.71
1064.71
985.62
871.82
796.60
775.38
756.10
596.00
cm-1

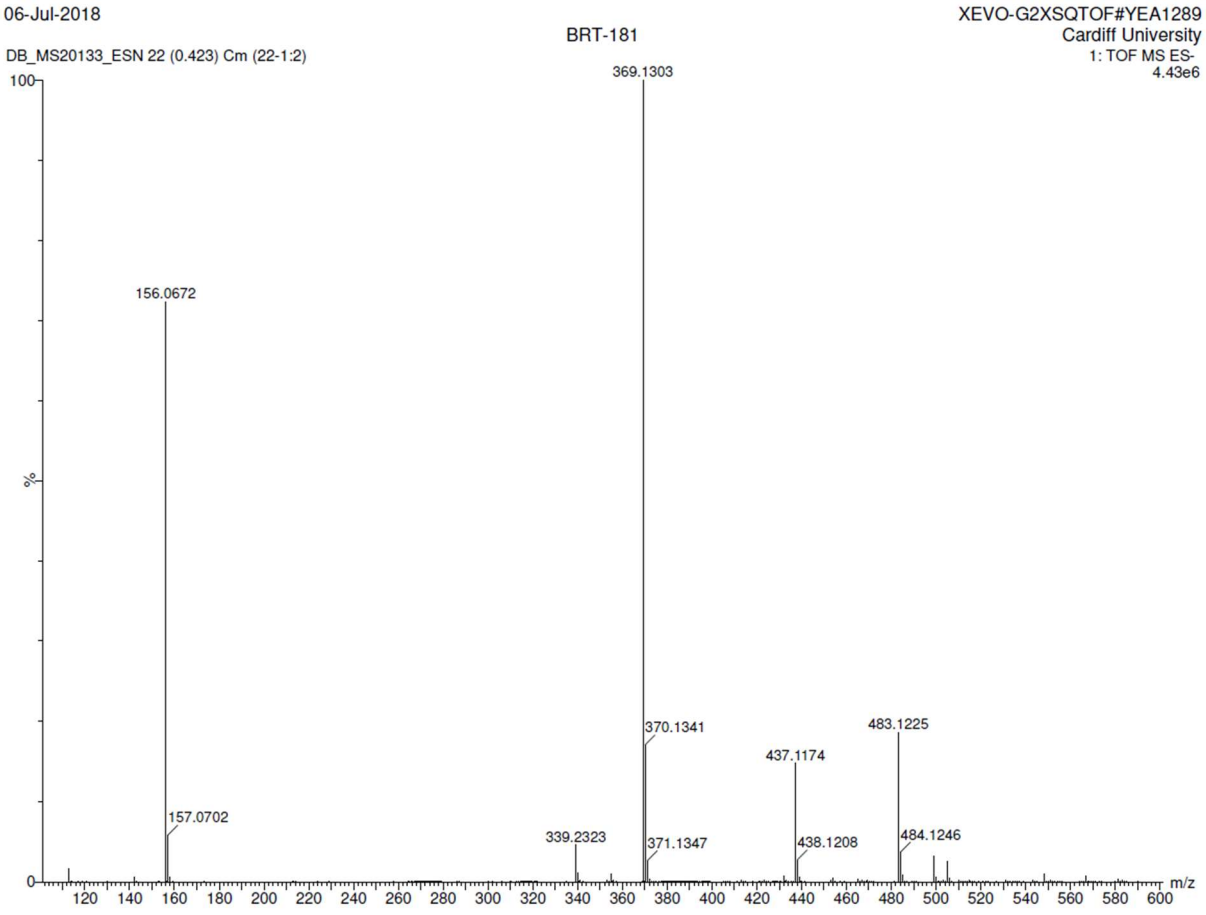
06-Jul-2018
BRT-181
XEVO-G2XSQTOF#YEA1289
Cardiff University
1: TOF MS ES-
4.43e6
DB_MS20133_ESN 22 (0.423) Cm (22-1:2)
%
369.1303
156.0672
370.1341
483.1225
437.1174
157.0702
339.2323
371.1347
438.1208
484.1246
m/z

Elemental Composition Report **Page 1**

Single Mass Analysis
Tolerance = 5.0 PPM / DBE: min = -1.5, max = 100.0
Element prediction: Off
Number of isotope peaks used for i-FIT = 3

Monoisotopic Mass, Odd and Even Electron Ions
25 formula(e) evaluated with 1 results within limits (up to 50 best isotopic matches for each mass)
Elements Used:
C: 0-16 H: 0-21 N: 0-2 O: 0-8

Minimum:				-1.5				
Maximum:		5.0	5.0	100.0				
Mass	Calc. Mass	mDa	PPM	DBE	i-FIT	Norm	Conf(%)	Formula
369.1303	369.1298	0.5	1.4	7.5	522.9	n/a	n/a	C16 H21 N2 O8

7.18. 3S,6S,13S)-6-(3-amino-3-oxopropyl)-13-carbamoyl-3-(2-((2S,3S)-2-((((4,5-dimethoxy-2-nitrobenzyl) oxy)carbonyl)amino)-3-methylpentanamido)acetamido)-41-mercapto-4,7,15,31-tetraoxo-18,21,24,27-tetraoxa-5,8,14,30-tetraazahentetracontanoic acid (3-26)

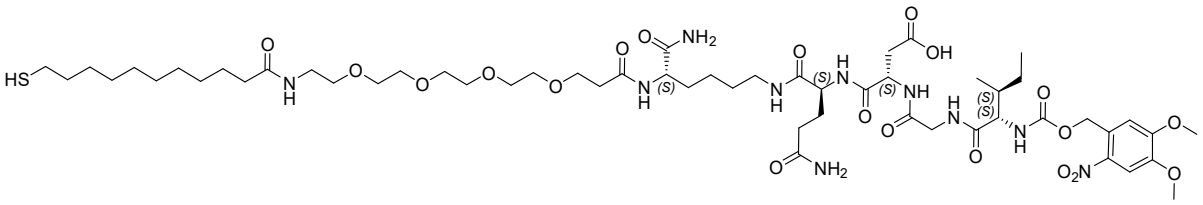

Chemical Formula: $C_{55}H_{92}N_{10}O_{20}S$
Exact Mass: 1244.6210
Molecular Weight: 1245.4510

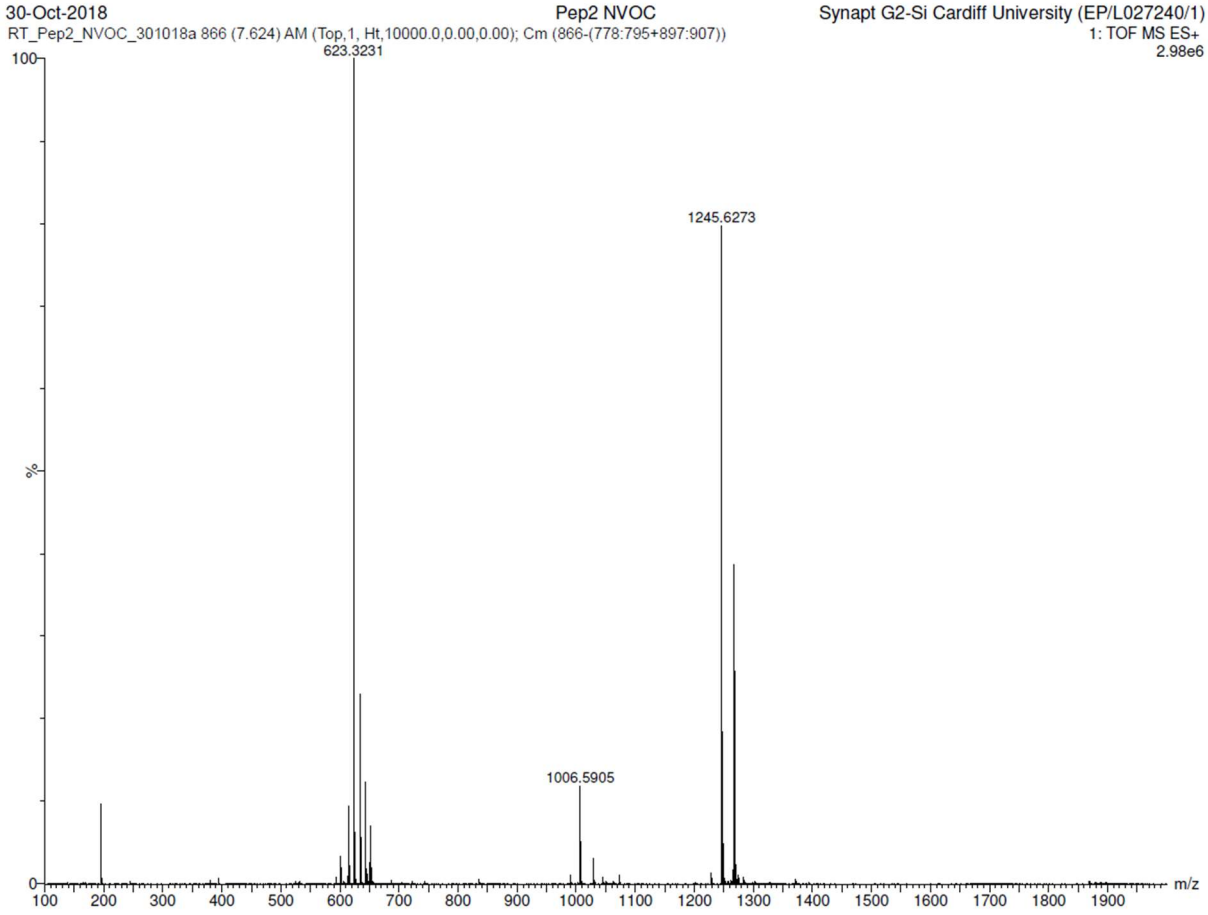

Elemental Composition Report **Page 1**

Single Mass Analysis
Tolerance = 100.0 PPM / DBE: min = -10.0, max = 500.0
Element prediction: Off
Number of isotope peaks used for i-FIT = 3

Monoisotopic Mass, Even Electron Ions
450 formula(e) evaluated with 1 results within limits (up to 50 closest results for each mass)
Elements Used:
C: 0-55 H: 0-93 N: 0-10 O: 0-20 S: 0-1

30-Oct-2018 Pep2 NVOC Synapt G2-Si Cardiff University (EP/L027240/1)
RT_Pep2_NVOC_301018a 866 (7.624) AM (Top,1, Ht,10000.0,0.00,0.00); Cm (866-(778:795+897:907)) 1: TOF MS ES+
2.98e+006

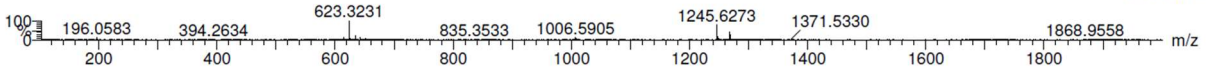

Minimum:				-10.0				
Maximum:		1000.0	100.0	500.0				
Mass	Calc. Mass	mDa	PPM	DBE	i-FIT	Norm	Conf(%)	Formula
1245.6273	1245.6288	-1.5	-1.2	14.5	318.5	n/a	n/a	C55 H93 N10 O20 S

7.19. Nitrobenzyl-peptide irradiation: RP-HPLC chromatogram integration and data processing

Here shown the screened images of the procedure to extrapolate the half-life of a photolinker in an irradiation experiment. Analytical HPLC chromatograms were exported and reprocessed with Origin software. Chromatograms were cropped to exclude everything but the photolinker peak and the internal standard (IS).

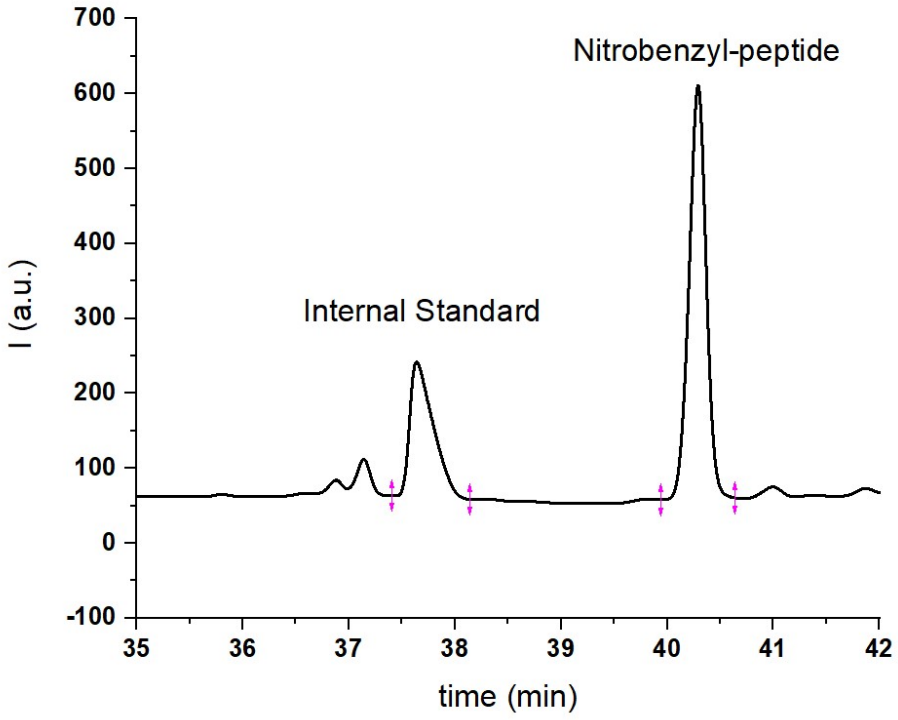

Figure 7-5 - Analytical RP-HPLC chromatogram of nitrobenzyl peptide **3-3**. 220 nm detector. 1 $mg \cdot mL^{-1}$ concentration. H_2O + CH_3CN + 0.1 % TFA gradient.

Photolinker peak and IS peaks were integrated with Origin integration tool. Peak area was exported and plotted again vs. total irradiation time.

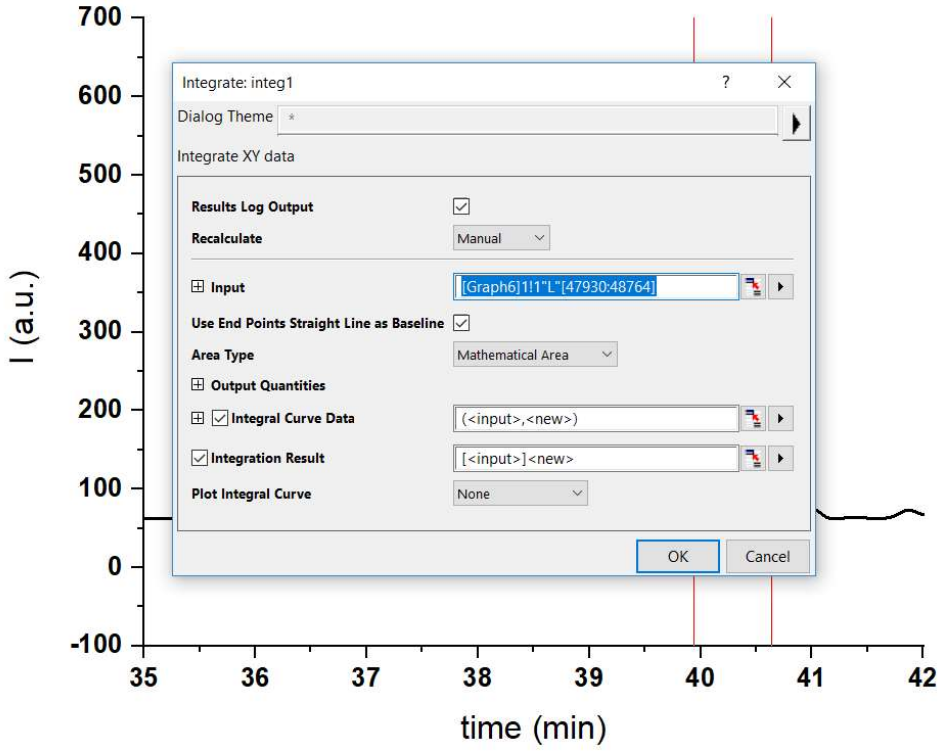

Figure 7-6 - Origin peak integration on an analytical RP-HPLC chromatogram of Nitrobenzyl peptide **3-3** irradiation experiment.

Table 7-4 - Plotted peak areas from nitrobenzyl irradiation experiment.

time	tot time	Area IS	Area NB1	ratio NB1/IS
0	**0**	35.90558	73.29691	**2.041379362**
1	**1**	44.14815	103.6631	**2.348073475**
5	**6**	45.78023	104.1457	**2.274904691**
10	**16**	45.70251	70.64795	**1.5458221**
30	**46**	25.00376	10.96332	**0.438466855**
60	**106**	28.7034	1.02489	**0.035706223**

7.20. General procedure for exponential decay fitting

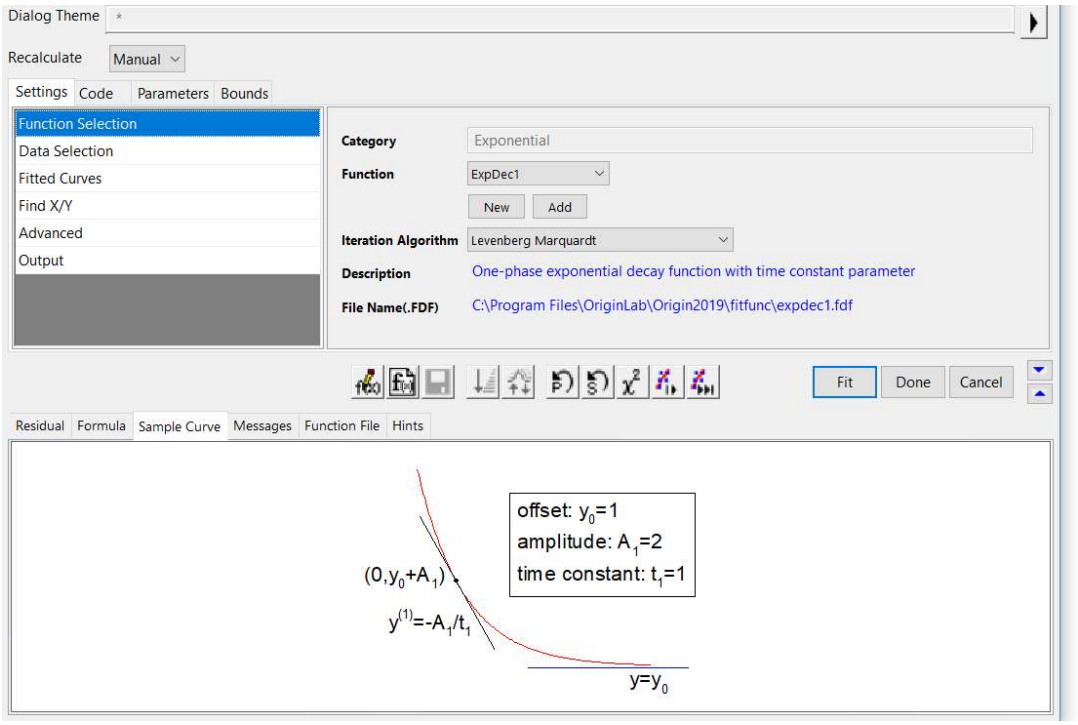

Figure 7-7 - Origin exponential decay selection tool. ExpDec1 was selected in almost all cases, except for NVOC 1 peptide **3-20** where ExpDec2 was chosen.

Nonlinear Curve Fit (ExpDec1) (09/04/2019 17:47:20)

Notes

Input Data

Parameters

		Value	Standard Error	t-Value	Prob>|t|	Dependency
V	y0	-0.21671	0.46447	-0.46657	0.6726	0.94594
	A1	2.55446	0.44748	5.70855	0.01066	0.89281
	t1	40.62389	19.08297	2.1288	0.12315	0.81119
	k	0.02462	0.01156			
	tau	28.15834	13.22731			

Reduced Chi-sqr = 0.0699813296413
COD(R^2) = 0.95688415867333
Iterations Performed = 8
Total Iterations in Session = 8
Fit converged. Chi-Sqr tolerance value of 1E-9 was reached.
Standard Error was scaled with square root of reduced Chi-Sqr.
k, tau are derived parameter(s).

Statistics

	V
Number of Points	6
Degrees of Freedom	3
Reduced Chi-Sqr	0.06998
Residual Sum of Squares	0.20994
R-Square (COD)	0.95688
Adj. R-Square	0.92814
Fit Status	Succeeded(100)

Fit Status Code :
100 : Fit converged. Chi-Sqr tolerance value of 1E-9 was reached.

Summary

	y0		A1		t1		k		tau		Statistics	
	Value	Standard Error	Value	Standard Error	Value	Standard Error	Value	Standard Error	Value	Standard Error	Reduced Chi-Sqr	Adj. R-Square
V	-0.21671	0.46447	2.55446	0.44748	40.62389	19.08297	0.02462	0.01156	28.15834	13.22731	0.06998	0.92814

ANOVA

		DF	Sum of Squares	Mean Square	F Value	Prob>F
V	Regression	2	4.65936	2.32968	33.29	0.00895
	Residual	3	0.20994	0.06998		
	Uncorrected Total	6	17.43896			
	Corrected Total	5	4.8693			

At the 0.05 level, the fitting function is significantly better than the function y=constant.

Figure 7-8 - Origin exponential decay parameter display. Half-life tau parametre can be seen in the first top table.

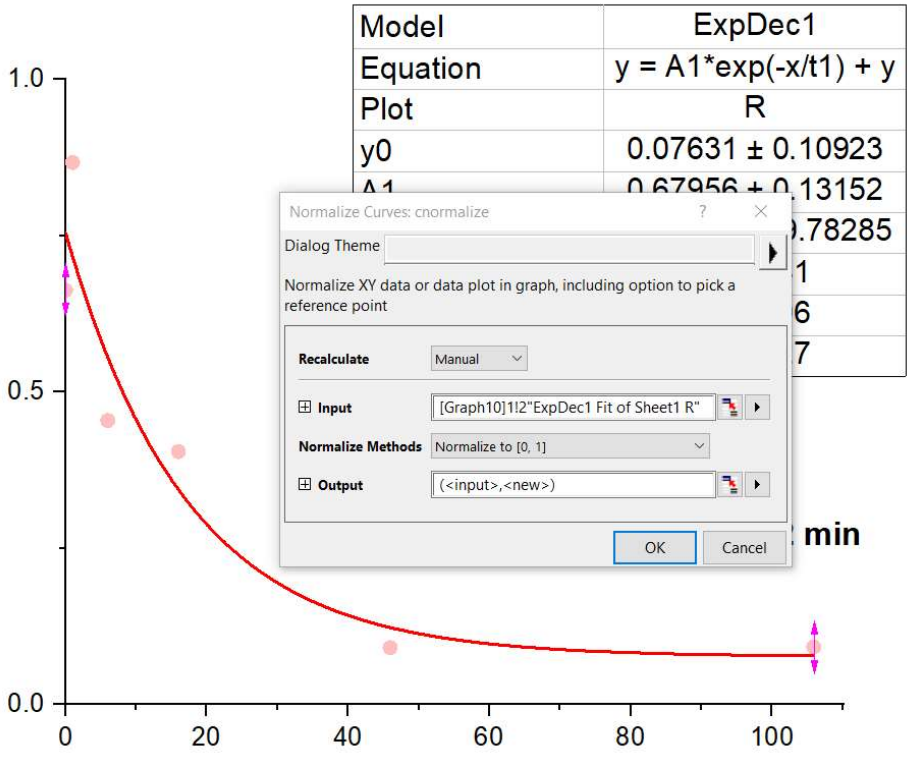

Figure 7-9 - Origin default curve normalization setting.

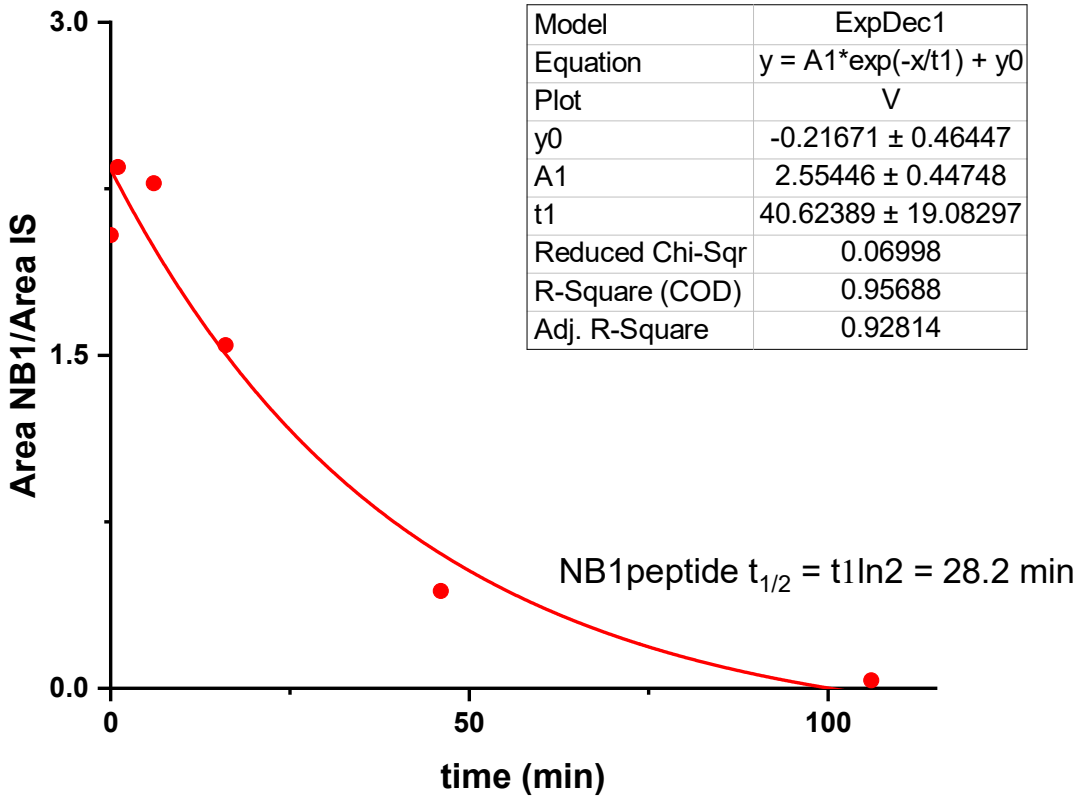

Figure 7-10 - Area vs. time chart for nitrobenzyl-bearing peptide **3-3** irradiation experiment. Exponential decay fitting. Parameters shown on chart.

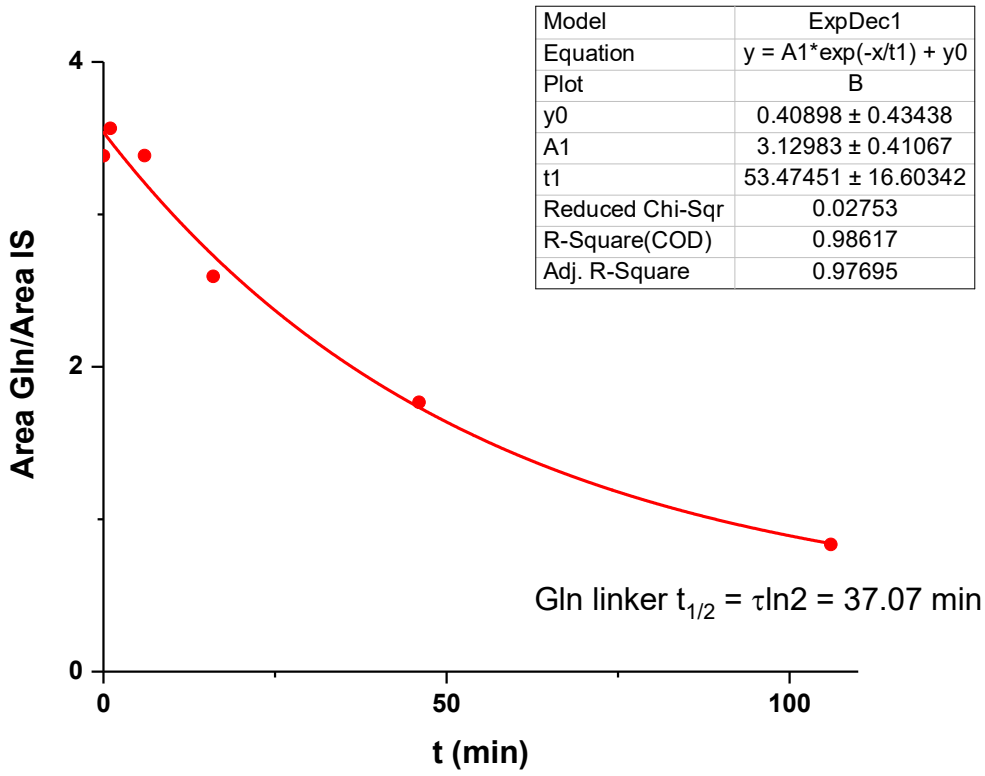

Figure 7-11 Area vs. time chart for nitrobenzyl-bearing linker **3-10** irradiation experiment. Exponential decay fitting. Parameters shown on chart.

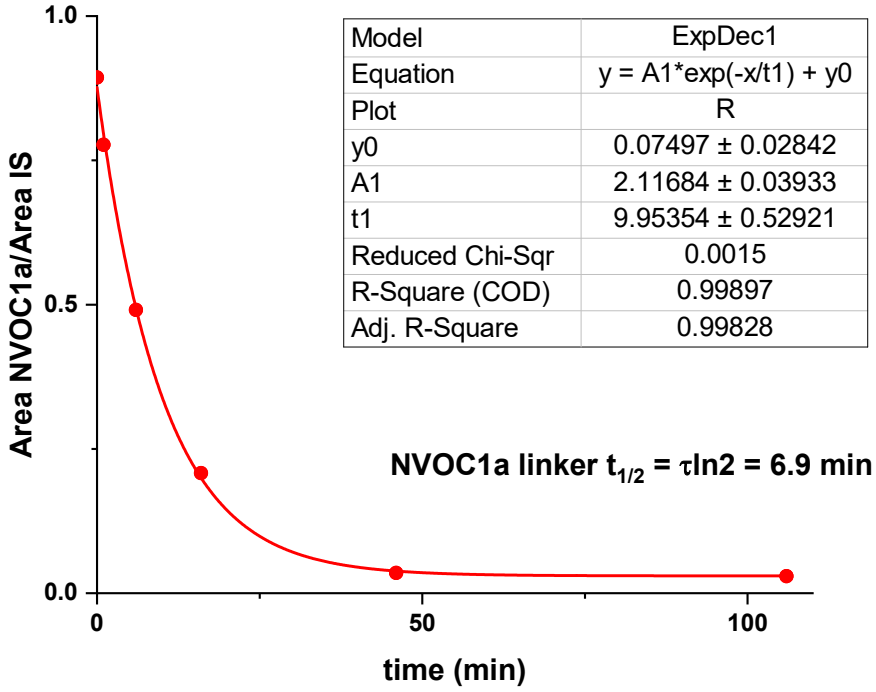

Figure 7-12 - Area vs. time chart for NVOC1a linker **3-19** irradiation experiment. Exponential decay fitting. Parameters shown on chart.

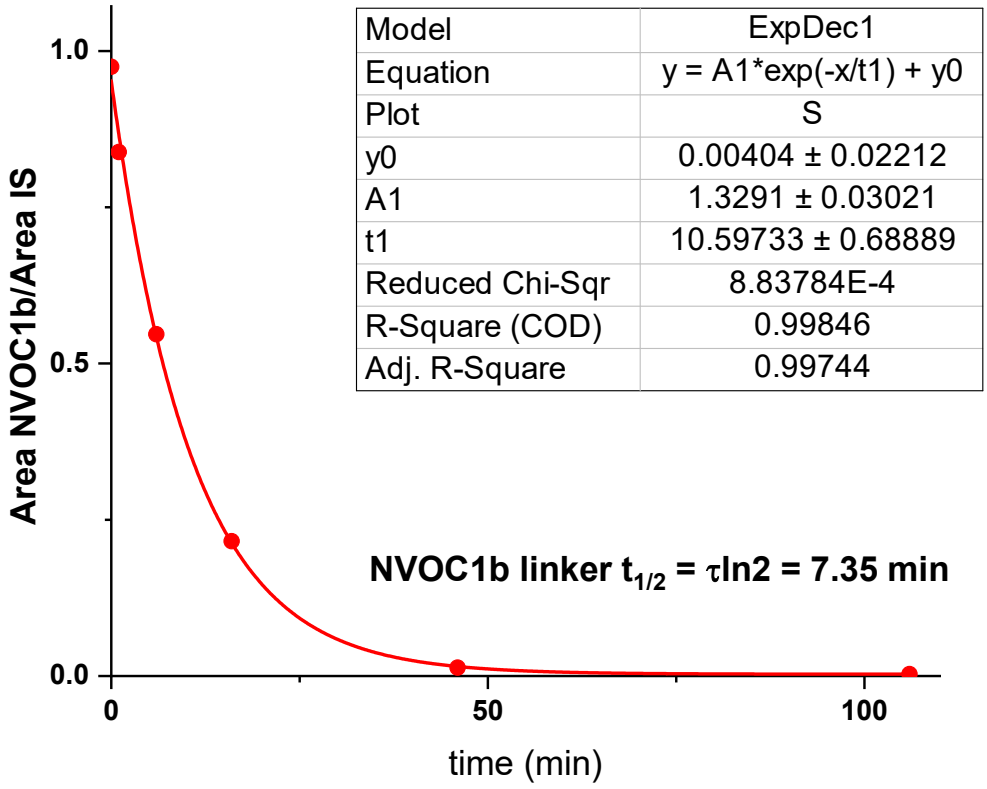

Model	ExpDec1
Equation	y = A1*exp(-x/t1) + y0
Plot	S
y0	0.00404 ± 0.02212
A1	1.3291 ± 0.03021
t1	10.59733 ± 0.68889
Reduced Chi-Sqr	8.83784E-4
R-Square (COD)	0.99846
Adj. R-Square	0.99744

Figure 7-13 - Area vs. time chart for NVOC1b linker **3-19** irradiation experiment. Exponential decay fitting. Parameters shown on chart.

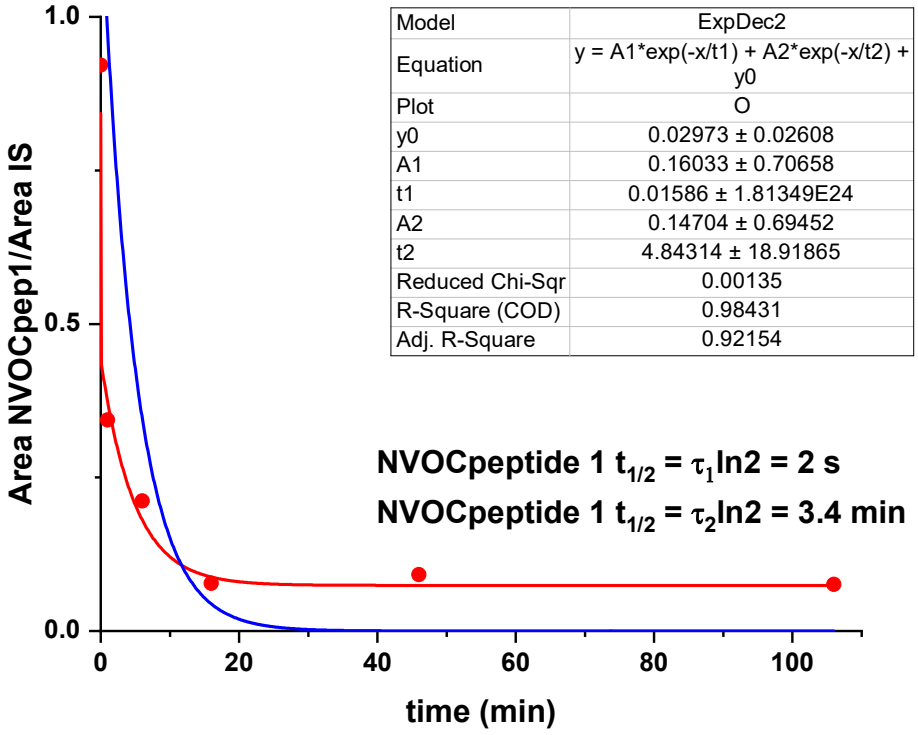

Model	ExpDec2
Equation	y = A1*exp(-x/t1) + A2*exp(-x/t2) + y0
Plot	O
y0	0.02973 ± 0.02608
A1	0.16033 ± 0.70658
t1	0.01586 ± 1.81349E24
A2	0.14704 ± 0.69452
t2	4.84314 ± 18.91865
Reduced Chi-Sqr	0.00135
R-Square (COD)	0.98431
Adj. R-Square	0.92154

Figure 7-14 - Area vs. time chart for NVOC1 peptide **3-20** irradiation experiment. Exponential decay fitting (RED) and normalized fitting (BLUE). Fitting parameters shown on chart.

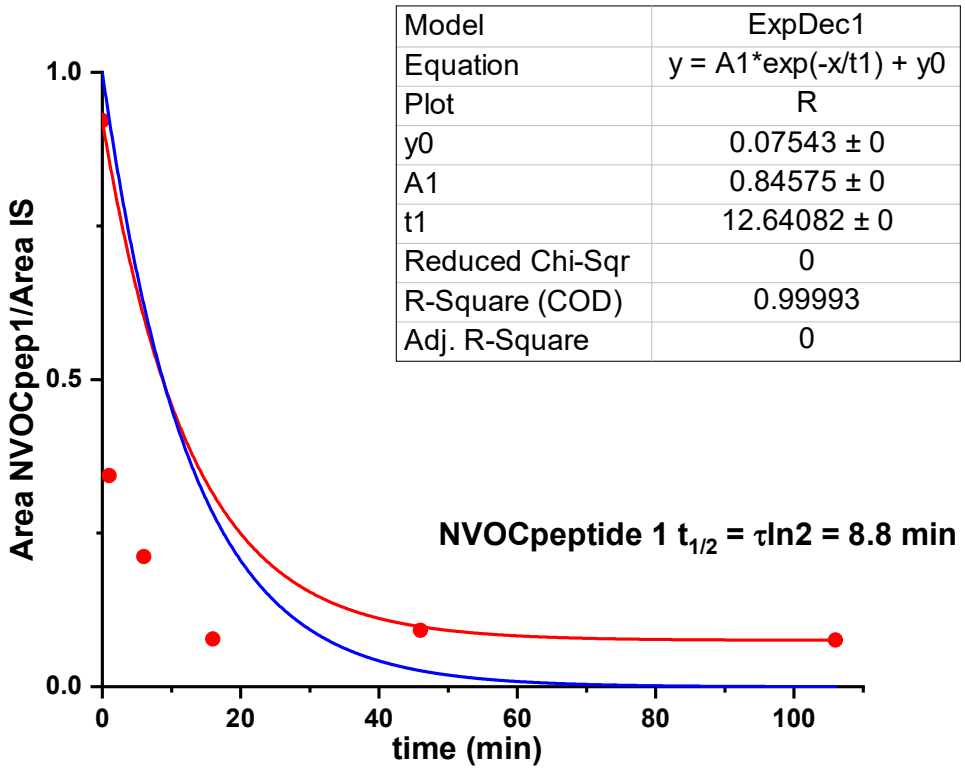

Figure 7-15 - Area vs. time chart for NVOC1 peptide **3-20** irradiation experiment. Exponential decay fitting (RED) and normalized fitting (BLUE). Fitting parameters shown on chart.

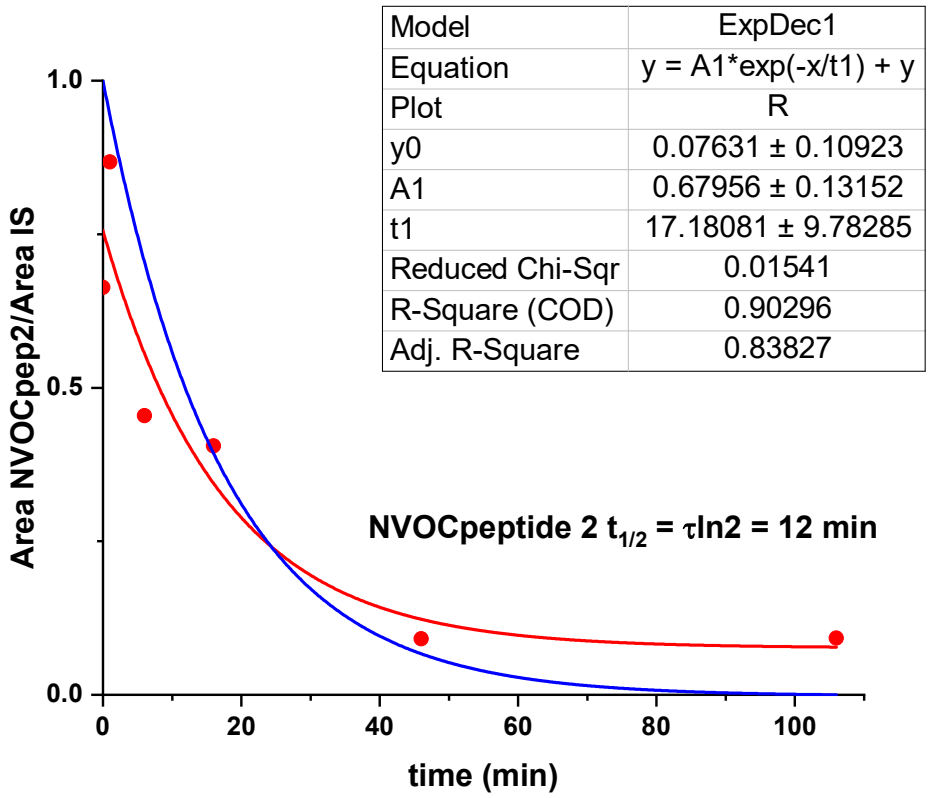

Figure 7-16 - Area vs. time chart for NVOC2 peptide **3-26** irradiation experiment. Exponential decay fitting (RED) and normalized fitting (BLUE). Fitting parameters are shown on chart.